DEVELOPMENT OF AN ELECTROMAGNETIC AND MECHANICAL MODEL FOR A RESONANT COLUMN AND TORSIONAL SHEAR TESTING DEVICE FOR SOILS

by

Inthuorn Sasanakul

A dissertation submitted in partial fulfillment
of the requirements for the degree

of

DOCTOR OF PHILOSOPHY

in

Civil and Environmental Engineering

Approved:

James A. Bay
Major Professor

Loren R. Anderson
Committee Member

Joseph A. Caliendo
Committee Member

Marvin W. Halling
Committee Member

James P. Evans
Committee Member

Laurens H. Smith, Jr.
Interim Dean of Graduate Studies

UTAH STATE UNIVERSITY
Logan, Utah

2005

ABSTRACT

Development of an Electromagnetic and Mechanical Model for a Resonant Column and Torsional Shear Testing Device for Soils

by

Inthuorn Sasanakul, Doctor of Philosophy

Utah State University, 2005

Major Professor: Dr. James A. Bay
Department: Civil and Environmental Engineering

Two weaknesses in resonant column (RC) and torsional shear (TS) tests are the back electromotive force (back emf) created in the typical coil-magnet system of RC/TS equipment and the nonuniform stress-strain that occurs over the radius of specimen in RC/TS tests. This study focused on the developing of methods dealing with these problems more precisely. Methods proposed in this study are the use of electromagnetic model to describe the back emf effect, and the stress integration approach accounting for the nonuniform stress-strain for soil.

The electromagnetic model presents the back emf effect in terms of the equipment spring stiffness (k_{eq}) and equipment viscous damping coefficient (c_{eq}). The model was verified by the measured model parameters. Variation of each model parameter was evaluated over a range of frequencies. In the RC test, the back emf effect increases the resonant frequency and damping, whereas, in the TS test, the model verified that the

effect on the torque measurement could be neglected. The analytical model shows a large effect of back emf on damping measurements. The model predicts equipment generated damping, D_{eq}, as a function of resonant frequency and the polar moment of inertia of the system. The effect of back emf is critical for the low-strain RC test of soil with low resonant frequency because the D_{eq} is high and material damping of soil itself is small.

A stress integration approach was developed to account for the nonuniform stress-strain in RC/TS testing. This involved integration of an assumed soil stress-strain model to develop a theoretical torque (T) and rotation (θ) relationship. The theoretical T-θ relationship was developed using either the closed form or numerical integrations for different soil models, and curve fitting was performed to match the theoretical T-θ relationship to the measured T-θ relationship. The model providing the best fit to the experimental data was selected to represent the stress-strain behavior of the soil. The equivalent radius approach was modified using the stress integration method to improve the damping measurement. The equivalent radius ratio curve based on damping was developed and used to calculate strains for damping curve.

(297 pages)

ACKNOWLEDGMENTS

I would like to thank my dissertation committee members, Dr. Loren R. Anderson, Dr. Marvin W. Halling, Dr. Joseph A. Caliendo, and Dr. James P. Evans, for agreeing to be on my committee and reviewing this dissertation. I really appreciate all their comments and contributions to this work.

Special thanks to Dr. Loren R. Anderson for giving me the opportunity to be at Utah State University with the financial and other support he provided for me. Thanks to Dr. Joseph A. Caliendo for his moral support during the long hard days that happened during my work. He was always around to provide me encouragement to boost my confidence and make me smile.

For my major professor, Dr. James A. Bay, I would like to express my appreciation for everything he has taught me throughout the past four years. I admire his talent and knowledge in the area of geotechnical earthquake engineering as well as electrical engineering. I have had an invaluable learning experience working with him. More than just his input and guidance to help me complete this work, Dr. Bay's encouragement and kindness are some of the best things he has shared with me.

Thanks are also extended to Dr. Kenneth H. Stokoe II for providing me the opportunity to work on part of my research at The University of Texas (UT) at Austin. This work would not have been as interesting if I had not had this great opportunity.

I would like to extend my gratitude to Dr. Dong-Soo Kim for his valuable advisement and contribution to this work.

The support from the U.S.Geological Survey is acknowledged for funding the last stage of this research. Thanks must be extended to UDOT and RB&G for their support on collecting soil samples.

I owe many thanks to Ken Jewkes, the man who can build everything. Ken was always able to transform my ideas and drawings into the real thing. Thanks for building me so many things and indirectly teaching me about machining and electrical work. Without him my research would never have been completed. I will always think of him as one of my professors.

Thank you to the CEE staff. To Becky Hansen for always having answers for me regarding administrative questions, Carolyn Benson for helping out on purchasing equipment, and Marlo Bailey for talking with me and raising my spirits. Thanks to you all for always being there when I needed to talk to someone.

I would also like to thank Wonkyoung Choi for his help when I performed testing at the Soil Dynamics Laboratory at UT. Thanks to many other UT graduate students that I worked with and have not named. Many thanks are due to my good friend Brady Cox for taking care of me when I was in Austin and helping on part of this work when I returned to USU.

Thanks to the USU graduate students who have helped me on this work, to Austin Ball for his help on part of the finite element analysis, and to Jeff Berry for all the help in the lab. Thanks also to all the other geotechnical graduate students who have come and gone over the last four years. Although they were not helping me directly on my dissertation, they were part of my journey. I will always value their friendship.

Thanks to Evans and Butler family for acting as a second family here in United States and helping me to heal my homesickness. Special thanks to Charlie and Kathryn for being my friends here in Logan. They both made me feel that I have never been alone.

Thanks to Allen Evans who is always be there for me. Thanks for his effort on proofreading this dissertation. There is no word to express my appreciation for having him in my life.

Most importantly I would like to thank my family who have always been proud of me and encouraged me. Although we don't really say it often, I love you all. Thank you to my dad for teaching me how to work and study hard when I was a little girl and for teaching me good values. Thanks to my mom for always giving the best to her daughters. She is the one that makes me strong and made it possible for me reach these great heights in my education. My work is dedicated to her.

Inthuorn Sasanakul

CONTENTS

Page

LIST OF TABLES

LIST OF FIGURES

CHAPTER 1

INTRODUCTION

1.1 BACKGROUND

An important task in geotechnical earthquake engineering is the measurement of dynamic soil properties. Although there are a wide variety of field and laboratory methods to measure soil properties, each has different advantages, disadvantages, and limitations. Most field methods, particularly the wave propagation techniques, are limited to measure low-strain soil properties. These tests include reflection, refraction, spectral analysis of surface wave (SASW), crosshole, downhole (and uphole), and seismic cone. In laboratory methods, soil properties can be determined over a wide range of strain levels. However, laboratory tests are performed on a small volume of soil and the in situ stress condition is almost impossible to reproduce. Dynamic soil properties are also influenced by many factors, such as density, soil structure, age, stress and strain history, and cementation, all of which can be easily destroyed by sample disturbance. Cyclic triaxial and cyclic simple shear tests measure high strain behavior. Resonant column, and cyclic torsional shear tests measure low to intermediate strain behavior. Bender element tests measure low-strain behavior. Variations of field and laboratory measurements with strain level are summarized in Table 1.1. Selection of a test method for measuring dynamic soil properties requires careful consideration and understanding of the specific tests.

Table 1.1 Typical Strain Levels Associated with Field and Laboratory Measurements

Strain Level (%)		10^{-5}	10^{-4}	10^{-3}	10^{-2}	10^{-1}	1	10
Field Measurement	Seismic Reflection Test	◄	├					
	Seismic Refraction Test	◄	├					
	SASW Test	◄	├					
	Seismic Crosshole Test	◄	├					
	Seismic Downhole Test	◄	├					
	Seismic Cone Test	◄	├					
Laboratory Measurement	Resonant Column Test	├	─	─	─	├		
	Bender Element Test	◄	─	├				
	Cyclic Triaxial Test				├	─	─	├
	Cyclic Simple Shear Test				├	─	─	├
	Cyclic Torsional Shear Test			├	─	├		

The two soil properties used to describe soil behavior under cyclic loading are stiffness and damping. Stiffness and damping of soils are typically presented in terms of shear modulus, G, and material damping, D. Shear modulus and damping of soils are strain dependent properties. When the strain level is below 10^{-4} %, soil behaves as a linear elastic material and the shear modulus and material damping remain constant with strain amplitude. The shear modulus of soil in the linear range is known as G_{max}. For the range of strain between 10^{-4}-10^{-2}%, the soil behavior becomes nonlinear elastic and the shear modulus decreases and material damping increases as the strain increases. At strain levels above 10^{-2}%, soil behaves nonlinearly and the properties tend to change not only with strain level but also with the loading cycles. The variations of G and D over the entire range of strains are typically presented by the plots of G/G_{max} versus log γ and D versus log γ, where γ is a shearing strain. In geotechnical earthquake engineering problems, the evaluation of dynamic soil properties is required from low to high strains.

As shown in Table 1.1, the resonant column (RC) and torsional shear (TS) tests are the most effective methods for measuring the dynamic properties of soils over a wide range of strains.

Utah State University recently acquired a Stokoe-type resonant column and torsional shear (RC/TS) apparatus. The apparatus was developed in the late 1970's at The University of Texas at Austin and has been improved over the intervening years. The equipment is fix-free type, with the bottom of the specimen fixed and torsional excitation applied to the top. Previous studies reported a problem that occurs in the RC/TS drive system. As the magnet moves through the coil, an electromotive force is induced in the opposite direction to the magnet motion. This force is known as back emf. The back emf effect causes an error in measuring the material damping of soils. The error can be significant because the damping of soil is very small. In the past, empirical approaches have been used to quantify the equipment-generated damping due to the back emf effect. Using this approach, the material damping of soil is simply corrected by subtracting the equipment damping from the measured values. A better approach for predicting the effects of back emf is the use of the electromagnetic model as one developed in this study.

Determination of strain in RC/TS tests is complicated due to the non-uniform stress-strain that varies linearly with the radius in a soil specimen in torsion. Previous work (Chen and Stokoe 1979) used the equivalent radius approach to account for the non-uniform strain problem. This approach is adequate when calculating strain at low to intermediate levels, however, this approach is less accurate when performing the tests at

higher strains. In this study, a stress integration approach was developed to account for the non-uniform strain problem more precisely.

The purpose of this study is to develop approaches to account for the two weaknesses in RC/TS tests. These weaknesses are: (1) the back emf effect created in coil and magnet system of RC/TS equipment, (2) the nonuniform stress-strain that occurs over the radius of specimen. The results from this study provide a simple and reliable method for predicting the equipment generated damping. The stress integration approach was proposed to account for the nonuniform strain effect. These improvements increase the accuracy of measuring the nonlinear stress-strain behavior using the RC/TS testing device.

1.2 OBJECTIVES

The first objective was to develop an electromagnetic model to describe the RC/TS drive system. Electrical, magnetic, and mechanical properties of the RC/TS drive system were used to describe the back emf effect. There are four parameters in the model. These are: (1) the coils resistance, R_c, (2) the coil inductance, L_c, (3) the torque-current factor, k_i, and (4) the back emf-rotational velocity factor, k_B.

The second objective was to develop independent measurements to measure each model parameter and the polar moment of inertia of the drive plate. To perform these measurements, calibration specimens were used. The calibration specimens have a wide range in resonant frequencies. The effect of frequency on the model parameters and polar moment of inertia of the drive plate was investigated using these specimens. In order to minimize the adverse effect of ambient vibrations, this testing was performed on an

isolation table, which was designed and built as part of this study. The model parameters and drive plate calibration were also performed on a drive plate from The University of Texas at Austin. The results of model parameters and drive plate calibration from the USU drive plate and the UT drive plate are compared and discussed.

The third objective was to verify the model prediction of the equipment generated damping by comparing model predictions with actual equipment generated damping. Open and closed circuit tests were performed using the calibration specimens to determine the actual equipment generated damping. The predicted equipment generated was calculated using the model and compared with the measured values. Again, the equipment generated damping for the USU drive plate and the UT drive plates are compared.

The fourth objective was to develop the stress integration approach to account for the nonuniform stress-strain in the RC/TS testing. This approach is used to develop the theoretical relationship between torque (T) and rotation (θ) for an assumed soil stress-strain model. The assumed soil models used in this study are the hyperbolic model, the modified hyperbolic model, and the Ramberg-Osgood model. Either closed form or numerical integration is used to develop these T-θ relationships. Curve fitting techniques are used to match the measured T-θ relationship to the theoretical T-θ relationship. The model providing the best ft to the measured T-θ relationship is used to develop the stress-strain relationship for a soil. The equivalent radius approach (Chen and Stokoe 1979) was modified using the stress integration approach to account for the nonuiform strains in damping.

The fifth objective was to apply the electromagnetic model and the stress integration approach in RC/TS testing of Bonneville clay. The RC/TS testing was performed on Bonneville clay to develop the modulus reduction and damping curves. In this test, the electromagnetic model was used to correct for equipment generated damping and the stress integration approach was used to calculate stresses and strains. The modulus and damping curves for Bonneville clay are compared with generic modulus reduction and damping curves.

1.3 ORGANIZATION OF DISSERTATION

Chapter 2 contains a literature review of RC/TS testing. The review is divided into four sections; the behavior of soil during cyclic loading, the normalized modulus reduction and damping curves, the nonuniform stress-strain in torsional testing, and the effect of equipment generated damping in RC/TS equipment.

Chapter 3 contains an overview description of RC/TS test equipment and method of analysis. The basic analysis methods used for analyzing results for both RC and TS tests are presented.

Chapter 4 presents the two basic calibration of the RC/TS equipment. These calibrations are the drive plate calibration and the deformation sensors calibration. The drive plate is calibrated to determine the polar moment of inertia of the drive plate. Results of drive plate calibration for the USU and UT are presented. Finite element method was used for the analysis of nonrigid body motion of the USU drive plate. Results of this analysis are discussed and compared with the results from calibrations. The deformation sensors are also calibrated. The deformation sensors used in RC/TS

testing are proximitors, accelerometers, and the linear voltage displacement transducers (LVDT). The calibration factors used for each sensor are summarized and discussed.

Chapter 5 presents the electromagnetic model development. The basic concepts of electromagnetism are used to describe toque and the back electromotive force (back emf) generated in the RC/TS drive system. The development of the electromagnetic model is then presented. The behavior and effects of back emf in RC/TS tests are discussed.

Chapter 6 presents the measurements of electromagnetic properties of the RC/TS drive system. These properties are the model parameters described the electromagnetic model. An independent measurement was made of each parameter. Factors affecting the value of each model parameters were correlated to the strength of drive plate magnets. These measurements and the evaluation of the model parameters were performed for both the USU drive plate and the UT drive plates. Differences and similarities of both drive plate are discussed. Calculations of the drive plate efficiency are also included.

Chapter 7 presents the verification of the electromechanical model. Comparisons of the predicted and measured equipment damping are included. Limitations of the proposed model are discussed. An explanation of discrepancies in the literature between predictions of equipment generated damping in RC and TS tests is presented.

Chapter 8 presents the development of stress integration approach used to account for the nonuniform stress-strain in RC/TS tests. Closed form and numerical procedures for integrating stress-strain models are presented. Curve fitting technique used for the stress integration approach is discussed. An evaluation of the equivalent radius approach

is presented. An improvement of the equivalent radius for determining strain in damping measurements is also presented.

Chapter 9 presents RC/TS testing performed on Bonneville clay to develop modulus reduction curves and damping curves. Index properties of the soil specimens tested in this study are summarized. The RC/TS testing procedures are presented. The analysis procedures developed in this study are applied to the RC/TS testing of Bonneville clay. These analysis procedures are the correction of equipment generated damping and the application of stress integration approach are presented. Finally, the factor affecting the modulus reduction and damping of Bonneville clay are compared with generic modulus and damping curves. Results are discussed.

Chapter 10 contains a summary and the conclusions of this work. Recommendations for further research are also presented.

CHAPTER 2

LITERATURE REVIEW

2.1 INTRODUCTION

The literature reviews presented in this chapter are separated into four sections, (1) behavior of soil during cyclic loading, (2) normalized modulus reduction and damping curves, (3) nonuniform stress-strain effects in torsional testing, and (4) effects of equipment generated damping in RC/TS equipment.

The behavior of soil during cyclic loading is first described in detail. Three nonlinear stress-strain soil models are presented. Basic aspects of these models are discussed.

The normalized reduction and damping curves for soils developed empirically by the past research studies are summarized. Factors affecting these two curves are presented and discussed.

The nonuniform stress-strain in torsional testing is presented. Approaches accounting for this problem are presented and discussed in details.

Finally, the effects of equipment generated damping in RC/TS equipment are presented. A summary of research works on the equipment generated damping is presented and discussed.

2.2 BEHAVIOR OF SOIL DURING CYCLIC LOADING

When soil experiences strain in the medium range, approximately between 10^{-3} % and 10^{-1} %, it behaves as an elastoplastic material. Shear modulus tends to decrease as the

shear strain increases and hysteresis cause energy dissipation during loading cycles. Damping is used to represent the energy absorbing properties of soils and the cyclic behavior of soils is commonly described using the theory of viscoelasticity. However, unlike viscoelastic materials, the energy dissipation in soil is nearly independent of loading frequency. A typical nonlinear hysteresis loop for soil is shown in Figure 2.1.

The hysteresis loop representing the stress-strain path during cyclic loading is related to the monotonic loading stress-strain path called the backbone curve. The rules for constructing a hysteresis loop using the backbone curve are called the Masing rules. These rules are illustrated in Figure 2.1. Suppose loading is increased from point O to a level indicated by point A, with a stress reversal occuring at point A. The unloading path is obtained by enlarging the loading path or backbone curve, OA, by a factor of two. The curve is then folded and the initial point, O, is translated to the point of stress reversal. The unloading curve extends to point B, which is axis-symmetrical to point A. The reloading path is obtained by enlarging the backbone curve in the same manner as for the unloading curve. The reloading curve starts at point B and intersects the backbone curve at point A, which was the point of initial stress reversal. These unloading and reloading curves complete the hysteresis loop which represents the nonlinear stress-strain behavior and energy dissipating characteristics of the soil.

The nonlinear stress-strain relation is usually described by the secant shear modulus, G. This parameter can be defined as the slope of a line connecting the origin and a point on the backbone curve. For nonlinear soil, the shear stress is expressed as a function of shear strain thus the secant modulus can be obtained from:

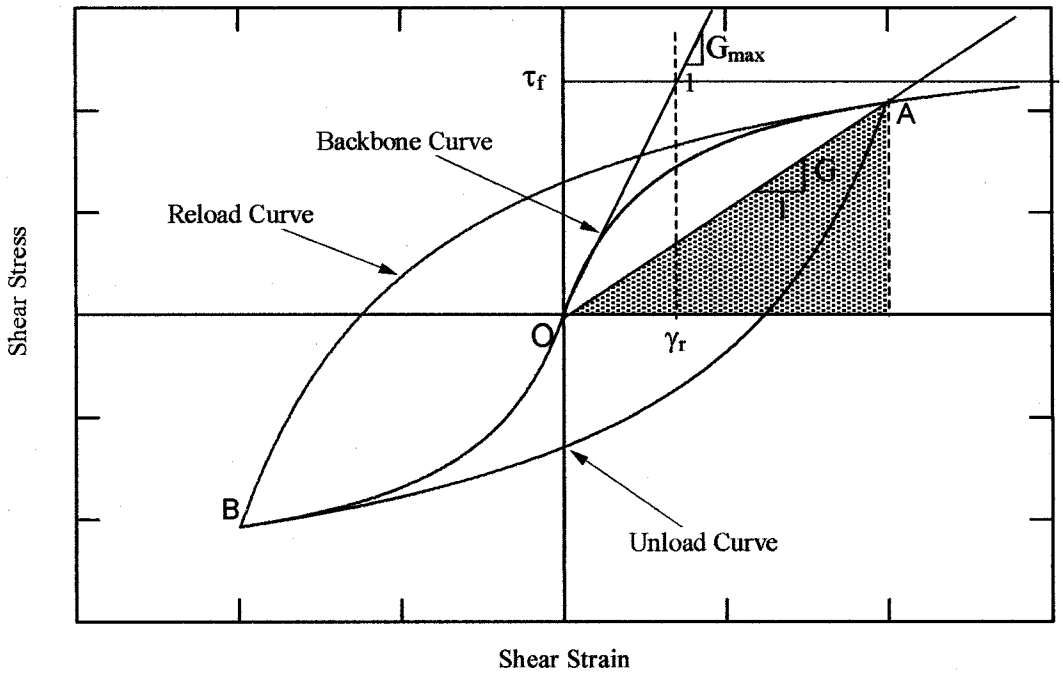

Figure 2.1 Nonlinear hysteresis loop

$$G = \frac{\tau}{\gamma} = \frac{f(\gamma)}{\gamma}. \tag{2.1}$$

The energy dissipated per cycle is proportional to the area enclosed by the hysteresis loop, ΔW. Damping ratio is defined as the ratio of the energy dissipated per cycle to the maximum stored energy, W. Thus the damping can be expressed as:

$$D = \frac{1}{4\pi}\frac{\Delta W}{W}. \tag{2.2}$$

For nonlinear soil behavior, the maximum stored energy, W, is assumed to be equal to the area of the triangle bounded by a straight line defining the secant modulus as shown in Figure 2.1 and obtained from:

$$W = \frac{1}{2}\gamma f(\gamma). \tag{2.3}$$

The area of the hysteresis loop (ΔW) representing the energy loss per cycle can be obtained from:

$$\Delta W = 8\left[\int_0^{\gamma} f(\gamma)d\gamma - W\right]. \tag{2.4}$$

By substitution and rearranging, the damping ratio can be written as:

$$D = \frac{2}{\pi}\left[\frac{2\int_0^{\gamma} f(\gamma)d\gamma}{\gamma f(\gamma)} - 1\right]. \tag{2.5}$$

The damping obtained from the Masing behavior is considered as the frequency independent and hysteretic in nature. There is another type of energy loss due to viscosity that can be modeled using a linear spring-dashpot model. The simplest and most widely used model is called Kevin model consisting of a spring representing the elastic soil properties and a dashpot representing the damping connected in parallel. The loss of energy or damping generated in this model increases linearly with increasing frequency regardless of the strain amplitude. However, the damping properties of soil are practically frequency independent. Therefore, the application of the spring-dashpot model to soils requires judgment and should be restricted to special cases (Ishihara 1996).

As the basic derivations for the secant modulus and damping ratio (G and D) are established, it is obvious that these two parameters are strongly related to the backbone curve and expressed as a function of shear strain amplitude. The backbone curve is the key characteristic of the nonlinear stress-strain relationship for soil under cyclic loading. Two models have been commonly used to describe the backbone curve are the hyperbolic

model and a four-parameter model known as the Ramberg-Osgood model (R-O model). Recently, Darendeli has proposed a modified hyperbolic model as an improvement over the conventional hyperbolic model (Darendeli and Stokoe 1997, and Darendeli 2001). The basic aspects of these models are discussed in following sections.

2.2.1 Hyperbolic Model

The hyperbolic model is the most widely used model to described nonlinear stress-strain relationship of soils. The stress-strain curve is bound by two straight lines; the first line is a tangent at small strains and second line is a tangent at large strains, as illustrated in Figure 2.1. The slope of the first line represents the small-strain elastic shear modulus known as G_{max}. The second line is horizontal asymptote indicating the upper limit of the shear stress or shear strength, τ_f. The strain level where these two lines intersect is called reference strain, γ_r, which defined as:

$$\gamma_r = \frac{\tau_f}{G_{max}}. \tag{2.6}$$

The hyperbolic model can be expressed in the following equation:

$$\tau = \frac{G_{max}\gamma}{1+\frac{\gamma}{\gamma_r}}, \tag{2.7}$$

where G_{max} = small-strain shear modulus.

The normalized modulus, G/G_{max} calculated using:

$$\frac{G}{G_{max}} = \frac{1}{1+\frac{\gamma}{\gamma_r}} \tag{2.8}$$

can be substituted into Equation 2.5 to obtain the following equation for damping (Ishihara 1996):

$$D = \frac{4}{\pi}\left[1 + \frac{1}{\gamma/\gamma_r}\right]\left[1 - \frac{\ln(1+\gamma/\gamma_r)}{\gamma/\gamma_r}\right] - \frac{2}{\pi}. \quad (2.9)$$

It should be noted that the damping ratio calculated from Equation 2.9 has limitations for predicting damping at very small and very high strain amplitude. When the shear strain becomes infinitely large, the damping ratio tends to converge to the value of $2/\pi = 0.637$. The calculated damping ratio deviates from the actual soil behavior at very high strain hence overestimating the damping ratio. On the other hand, at very small strain the damping ratio gradually decreases as the strain decreases and converges to zero. Numerous measurements on soils have shown that the small stain damping is usually higher than the damping calculated from Masing behavior, thus it underestimates the actual damping of soil at small strains.

Only two parameters, G_{max} and γ_r, are required to define the hyperbolic model. In many cases, these two parameters are insufficient to characterize shear modulus and damping ratio of soil. As a result, numerous researchers have attempted to adjust and refine the model to achieve a good fit to experimental data for different soil types (e.g., Hardin and Drenevich 1972a, 1972b, Seed et al. 1986, Vucetic and Dobry 1991, Darendeli and Stokoe 1997)

2.2.2 *Modified Hyperbolic Model*

The modified hyperbolic model has been proposed by Darendeli and Stokoe (1997). The two-parameter hyperbolic model was modified by simple approach in order to obtain the normalized reduction curves for all soil types. In addition to the two parameters (G_{max} and γ_r) the parameter, a so called a curvature coefficient, a, was added into the conventional hyperbolic model as shown below:

$$\tau = \frac{G_{max}\gamma}{1+\left(\frac{\gamma}{\gamma_r}\right)^a}. \tag{2.10}$$

As discussed by Darendeli (2001), the advantage of the curvature coefficient, a is that the stress-strain curve can be calculated even if the strain level is far below failure thus the value of τ_f is not identified. In this approach, the reference strain, γ_r is assumed to be the strain amplitude at shear modulus equal to one half of G_{max} ($\gamma_r = \gamma_{G/Gmax=0.5}$). This approach simplifies and provides better approximation for the modulus reduction curves obtained from experimental data.

For the damping curve, Darendeli (2001) also proposed the modified model using two additional parameters (b and D_{min}) as expressed as:

$$D = b\left(\frac{G}{G_{max}}\right)^{0.1} D_{masing} + D_{min}, \tag{2.11}$$

where D_{masing} = Masing behavior damping described the damping of soils at high strain.

It is noted that D_{masing} for coefficient of curvature, a, equal to 1.0 is the damping obtained from conventional hyperbolic model and derived in similar method as discussed earlier, thus it can be calculated from Equation 2.9. In Derendeli approach, D_{masing} for

any value of coefficient of curvature, a, is assumed to be a polynomial function of $D_{masing,a=1.0}$. The numerical integration was used to determine the polynomial function terms (c_1, c_2 and c_3) using sixty damping curves of soils and they were assumed to be functions of curvature coefficient. D_{masing} is determined from the expression below:

$$D_{masing} = c_1 D_{masing,\,a=1.0} + c_2 D_{masing,\,a=1.0} + c_3 D_{masing,\,a=1.0} \tag{2.12}$$

where $c_1 = -1.1143a^2 + 1.8618a + 0.2523$,

$c_2 = 0.0805a^2 - 0.0710a - 0.0095$, and

$c_3 = -0.0005a^2 + 0.0002a + 0.0003$.

The additional two parameters are the scaling coefficient, b and the small-strain material damping ratio, D_{min}. The scaling coefficient, b is used to adjust the damping at high strains where the Masing behavior tends to overestimate the damping value. The small-strain damping ratio, D_{min} represents the damping of soil at small strains. This modified hyperbolic model proposed by Darendeli (2001) was called the four-parameter model. The parameters γ_r, a, b, and D_{min} are used to describe the model. The empirical relationships for these parameters were developed using statistical analysis based on the experimental data of four different soil types; clean sands, sands with high fine content, silts, and clays (Darendeli 2001). The factors affecting these model parameters are confining pressure, soil plasticity, overconsolidation ratio, loading frequency, and number of loading cycles. The relationships are shown below:

$$\gamma_r = \left[\varphi_1 + \varphi_2(PI)(OCR)^{\varphi_3}\right]\sigma_o'^{\varphi_4}, \tag{2.13}$$

$$a = \varphi_5, \tag{2.14}$$

$$D_{min} = \left[\varphi_6 + \varphi_7(PI)(OCR^{\varphi_8})\right]\sigma_o'^{\varphi_9}\left[1 + \varphi_{10}\ln(frq)\right], \tag{2.15}$$

$$b = \varphi_{11} + \varphi_{12}\ln(N), \tag{2.16}$$

where σ_o' = mean effective confining pressure (atm),

PI = soil plasticity index (%),

OCR = overconsolidation ratio,

frq = loading frequency,

N = number of loading cycles, and

ϕ_1 through ϕ_{12} = model parameters tabulated in Table 2.1.

Although the damping ratio at very high strains and very small strains has been adjusted in this model using the parameters, b and D_{min}, the model does not accurately predict damping at small strains at very low loading frequencies. Neither hysteretic damping nor the viscous damping can explain the soil damping behavior for this special case. A complete model describing the actual damping behavior for soils has not yet been developed.

Table 2.1 Mean Values and Variances of the Model Parameters after Darendeli (2001)

Model Parameters	Mean	Variance
ϕ_1	3.52E-02	9.99E-07
ϕ_2	1.01E-03	4.16E-09
ϕ_3	3.25E-01	2.85E-03
ϕ_4	3.48E-01	2.20E-04
ϕ_5	9.19E-01	6.78E-05
ϕ_6	8.01E-01	1.73E-03
ϕ_7	1.29E-02	3.82E-06
ϕ_8	-1.07E-01	2.49E-03
ϕ_9	-2.89E-01	4.96E-04
ϕ_{10}	2.92E-01	7.66E-04
ϕ_{11}	6.33E-01	2.23E-04
ϕ_{12}	-5.66E-03	5.02E-06

2.2.3 *Ramberg-Osgood Model*

The four-parameter model was originally proposed by Ramberg and Osgood in 1943 and modified for soil (Streeter et al. 1974) into the form of:

$$\frac{\gamma}{\gamma_y} = \frac{\tau}{\tau_y}\left[1+\alpha\left|\frac{\tau}{\tau_y}\right|^{r-1}\right], \tag{2.17}$$

where τ_y = shear stress,

γ_y = shear strain,

α = constant, and

r = constant.

Idriss et al. (1978) applied the model to soil by defining τ_y and γ_y as the shear strength, τ_f and reference strain, γ_r, respectively. The reference strain is the same as the reference strain used in the hyperbolic model. Making this substitution, Equation 2.17 can be written as:

$$\tau = \frac{G_{max}\gamma}{1+\alpha\left|\frac{\tau}{G_{max}\gamma_r}\right|^{r-1}}. \tag{2.18}$$

Unlike the hyperbolic model, the Ramberg-Osgood model is calculates shear strain as a function of shear stress, $\gamma = g(\tau)$. The damping can be determined as the function of shear stress (Ishihara 1996) using:

$$D = \frac{2}{\pi}\left[1-\frac{2\int_0^{\tau} g(\tau)d\tau}{\tau g(\tau)}\right]. \tag{2.19}$$

Substitution of Equation 2.18 into Equation 2.19 gives:

$$D = \frac{2r-1}{\pi r+1}\alpha \frac{\left|\frac{\tau}{G_{max}\gamma_r}\right|^{r-1}}{1+\alpha\left|\frac{\tau}{G_{max}\gamma_r}\right|^{r-1}}, \tag{2.20}$$

where $\alpha = \frac{\gamma_f}{\gamma_r} - 1$, and (2.21)

γ_f = shear strain at failure.

If the shear modulus at failure, G_f, and damping at failure, D_f, are known, the parameter, r can be determined from:

$$r = \frac{1+\frac{\pi D_f}{2}\frac{1}{1-G_f/G_{max}}}{1-\frac{\pi D_{max}}{2}\frac{1}{1-G_f/G_{max}}}. \tag{2.22}$$

The four parameters of the Ramberg-Osgood model are G_{max}, γ_r, α, and r. Values for the α and r parameters are usually obtained from curve fitting laboratory data. The empirical relationships correlated between these parameters and soil properties are not in the literature.

2.3 NORMALIZED MODULUS REDUCTION AND DAMPING CURVES

The nonlinear cyclic behavior of soil can be characterized using normalized modulus reduction curves (G/G_{max} versus γ) and damping curves (D versus γ). Over the past three decades, several researchers have investigated the soil properties that effect the shape of these curves. The factors affecting these two curves are characterized into two categories; nature of the soil and loading conditions. The first category includes type of

soil, plasticity index, overconsolidation ratio (OCR), void ratio, degree of saturation, grain characteristics, mineralogy, and soil structure. The second category includes strain amplitude, mean effective confining pressure, number of loading cycles, and loading frequency.

The earliest work on the factors affecting the shear modulus and damping of soils was conducted by Hardin and Drenevich (1972a, 1972b). They were the first to propose the hyperbolic function for stress-strain relationship of soils. They also proposed an empirical relationship for predicting G_{max} was also proposed as a function of void ratio, e, plasticity index, PI, overconsolidation ratio, OCR, and mean effective confining pressure, σ_o'. They developed approximate shapes of material damping curves using two additional parameters; the maximum damping ratio of soil, D_{max}, and the hyperbolic strain, γ_h. These vary with soil type, mean effective confining pressure, σ_o', number of loading cycle and loading frequency.

Seed proposed a series of normalized modulus reduction and damping curves for sand (Seed and Idriss 1970, Iwasaki et al. 1978, Seed et al. 1986). The curves shown in Figure 2.2 represent the culmination of that series (Seed et al. 1986). The upper and lower ranges in the curves are attributed to variability in the characteristics of the granular particles (shape, size, gradation, and mineralogy), variability of nonlinear soil behavior, effect of confining pressure and accuracy in measurement. These curves represent the behavior of clean silty sand with confining pressure ranging from 0.25 atm to 4 atm.

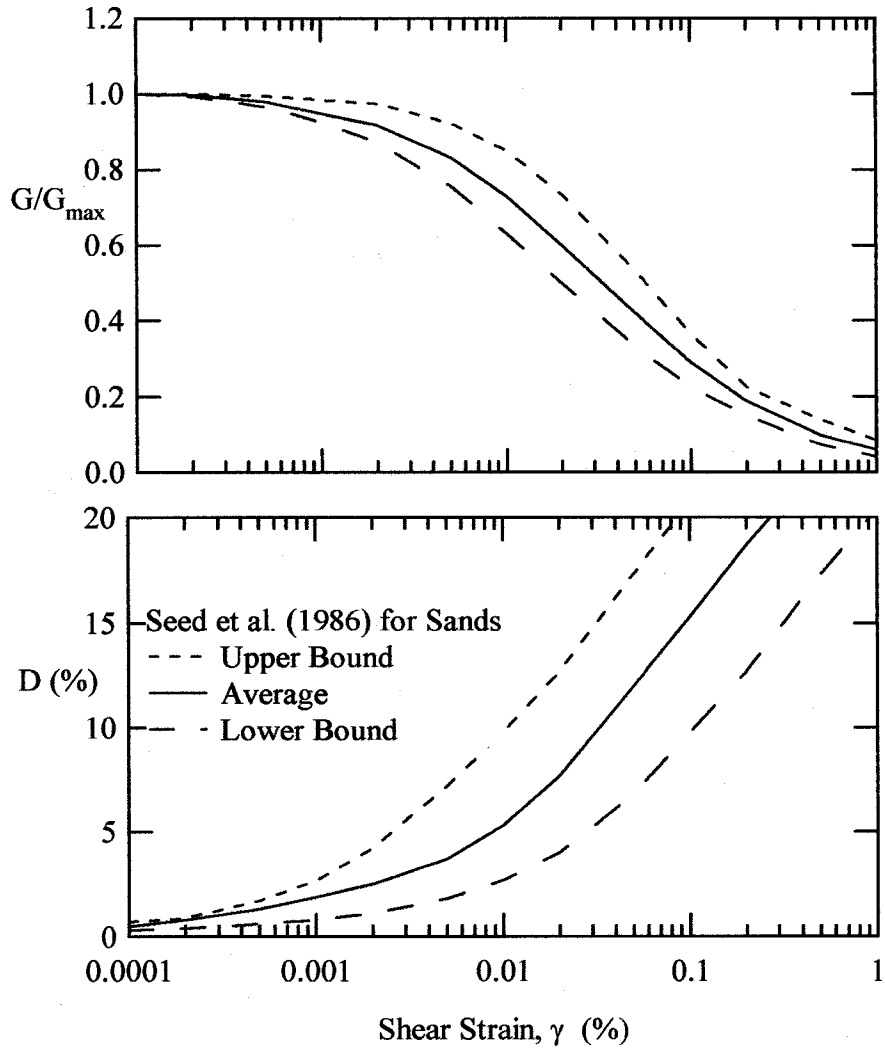

Figure 2.2 Empirical relationships for normalized modulus reduction and material damping for sand after Seed et al. (1986)

Sun et al. (1988) proposed the curves for soils with plasticity as shown in Figure 2.3. Their normalized modulus reduction curves account for the effect of plasticity on nonlinear soil behavior while material damping curves are presented in terms of one mean curve and an upper and lower bound for all soils within the total range of soil plasticities.

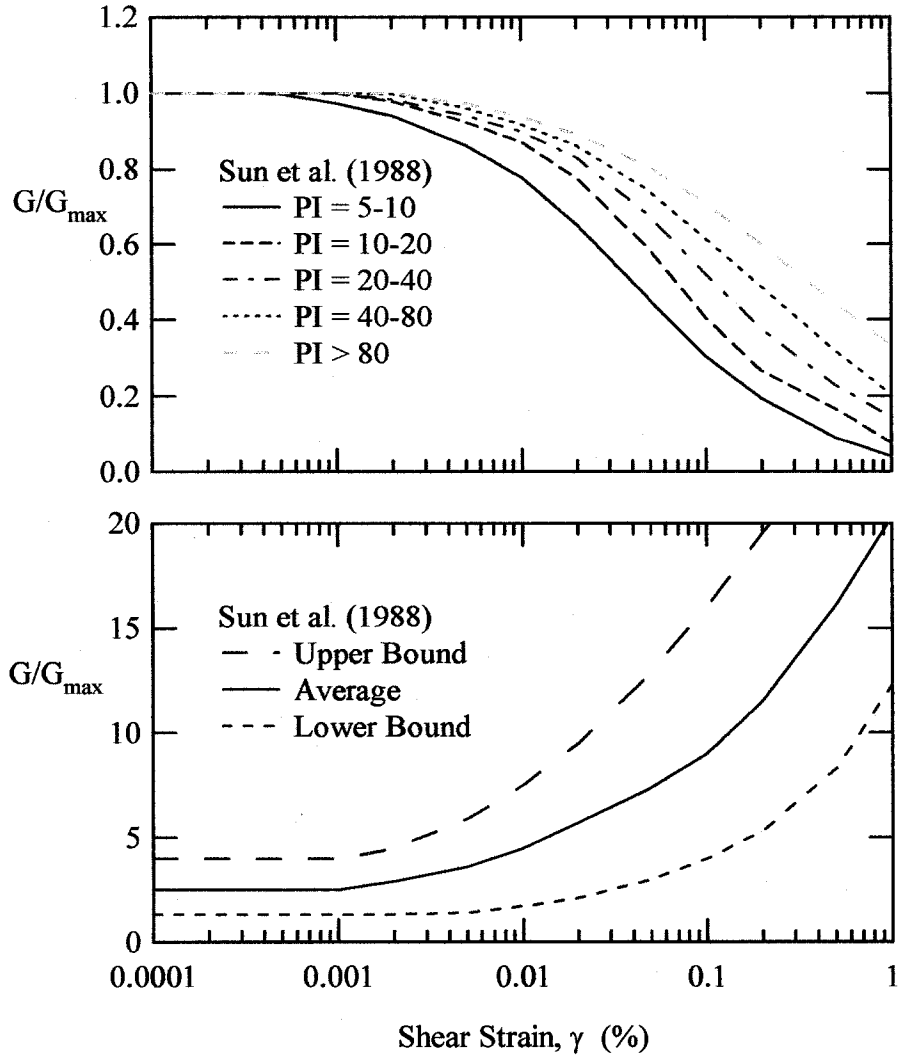

Figure 2.3 Empirical relationships for normalized modulus reduction and material damping for clay after Sun et al. (1988)

Idriss (1990) proposed two "average" normalized modulus reduction curves for sands and clays and a single material damping curve for all soil types.

Vucetic and Dobry (1991) proposed normalized modulus reduction and material damping curves accounting for the effect of plasticity on both modulus and damping as shown in Figure 2.4. However, the values of damping at low strain have been left

undefined due to the lack of data. The data used by Vucetic and Dobry (1991) were obtained from soils tested at confining pressures ranging from 0.25 to 4 atm.

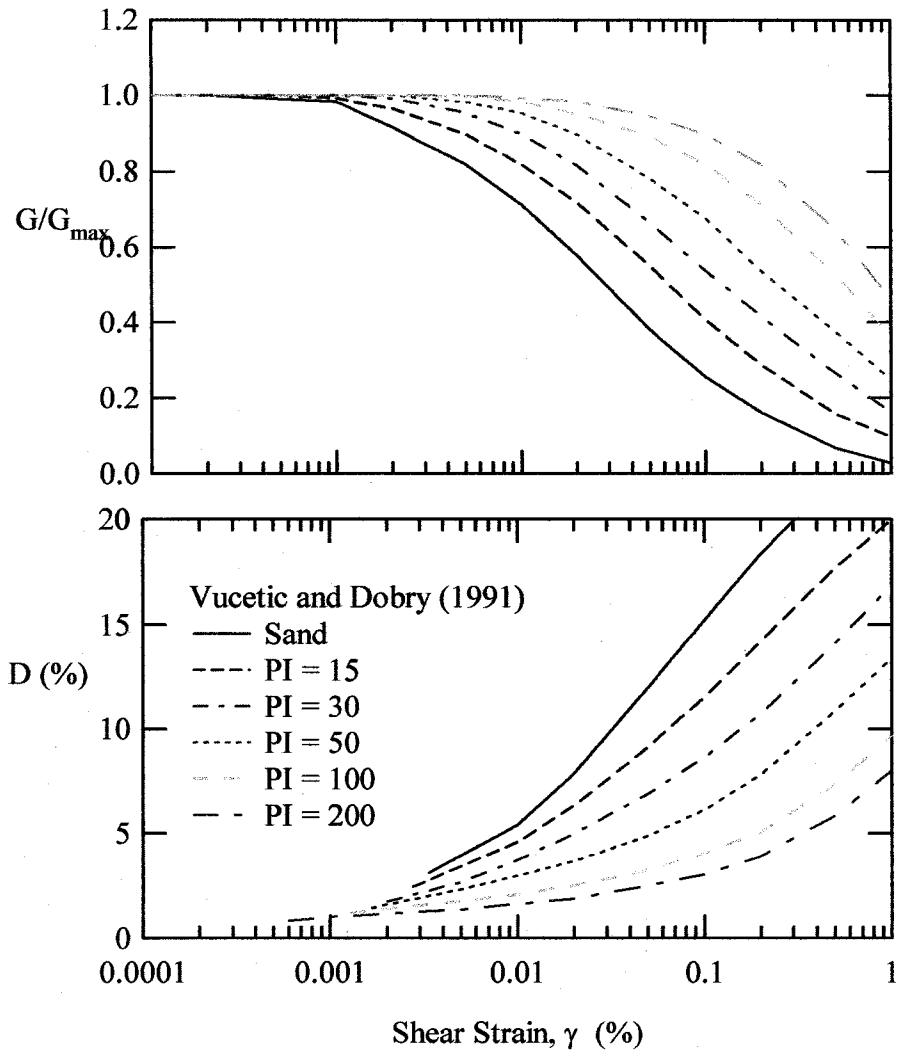

Figure 2.4 Empirical relationships for normalized modulus reduction and material damping after Vucetic and Dobry (1991)

Ishibashi and Zhang (1993) proposed a set of equations generate normalized modulus reduction and material damping curves accounting for confining pressure, $\bar{\sigma}_o$, and soil plasticity, PI. The equations proposed by Ishibashi and Zhang (1993) are:

$$\frac{G}{G_{max}} = K(\gamma, PI)\bar{\sigma}_o^{m(\gamma,PI)-m_o}, \text{ and} \tag{2.23}$$

$$D = \frac{0.333(1+e^{-0.0145PI^{1.3}})}{2}\left\{0.586\left(\frac{G}{G_{max}}\right)^2 - 1.547\left(\frac{G}{G_{max}}\right)+1\right\}, \tag{2.24}$$

where $$m(\gamma, PI) - m_o = 0.272\left[1-\tanh\left\{\ln\left(\frac{0.000556}{\gamma}\right)^{0.4}\right\}\right]e^{-0.0145PI^{1.3}},$$

$$K(\gamma, PI) = 0.5\left[1+\tanh\left\{\ln\left(\frac{0.000102+n(PI)}{\gamma}\right)^{0.492}\right\}\right], \text{ and}$$

$$n(PI) = \begin{cases} 0.0 & \text{for} \quad PI = 0 \\ 3.37\times10^{-6}PI^{1.404} & \text{for} \quad 0 < PI \le 15 \\ 7.00\times10^{-7}PI^{1.976} & \text{for} \quad 15 < PI \le 70 \\ 2.70\times10^{-5}PI^{1.115} & \text{for} \quad PI > 70 \end{cases}$$

The normalized modulus reduction and damping curves generated by the equations proposed by Ishibashi and Zhang (1993) are presented in Figures 2.5-2.7. Significant effect of confining pressure are observed on sand and clay as shown in Figure 2.5 and 2.6, respectively. The data used to develop these curves are the results of tests performed at confining pressure less than 10 atm. Unrealistic relationships are observed at high confining pressure as shown in Figures 2.5 and 2.6, where the normalized shear modulus value begins to exceed 1.0. Figure 2.7 shows the effect of PI on normalized modulus reduction and damping curve at a confining pressure of 1 atm. Unrealistic values (greater

than 1.0) of normalized shear modulus are obtained for PI = 15 and 30 in the intermediate strain level. More realistic values are obtained for PI = 50, 100, and 200. The equations proposed by Ishabashi and Zhang (1993) do not accurately represent the normalized shear modulus and damping of soils at high confining pressures or the range of PI's from 0-40.

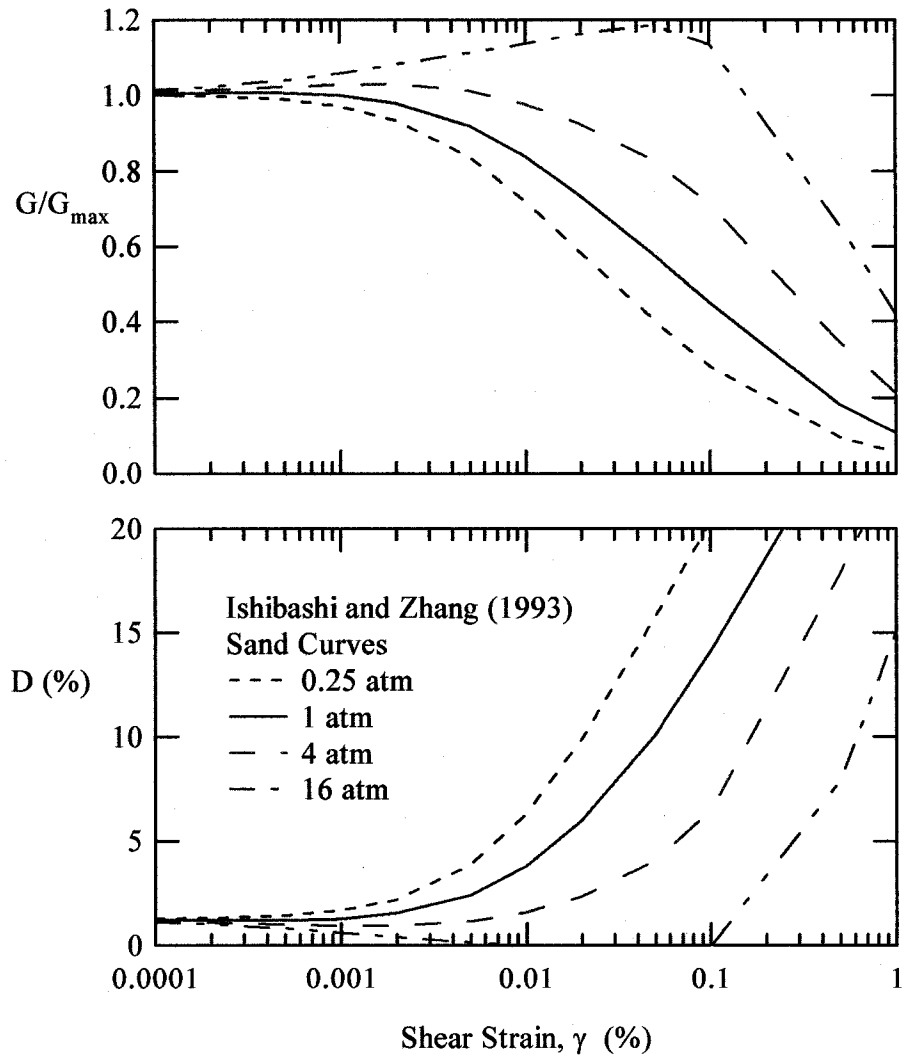

Figure 2.5 Empirical relationships for normalized modulus reduction and material damping for sand after Ishibashi and Zhang (1993)

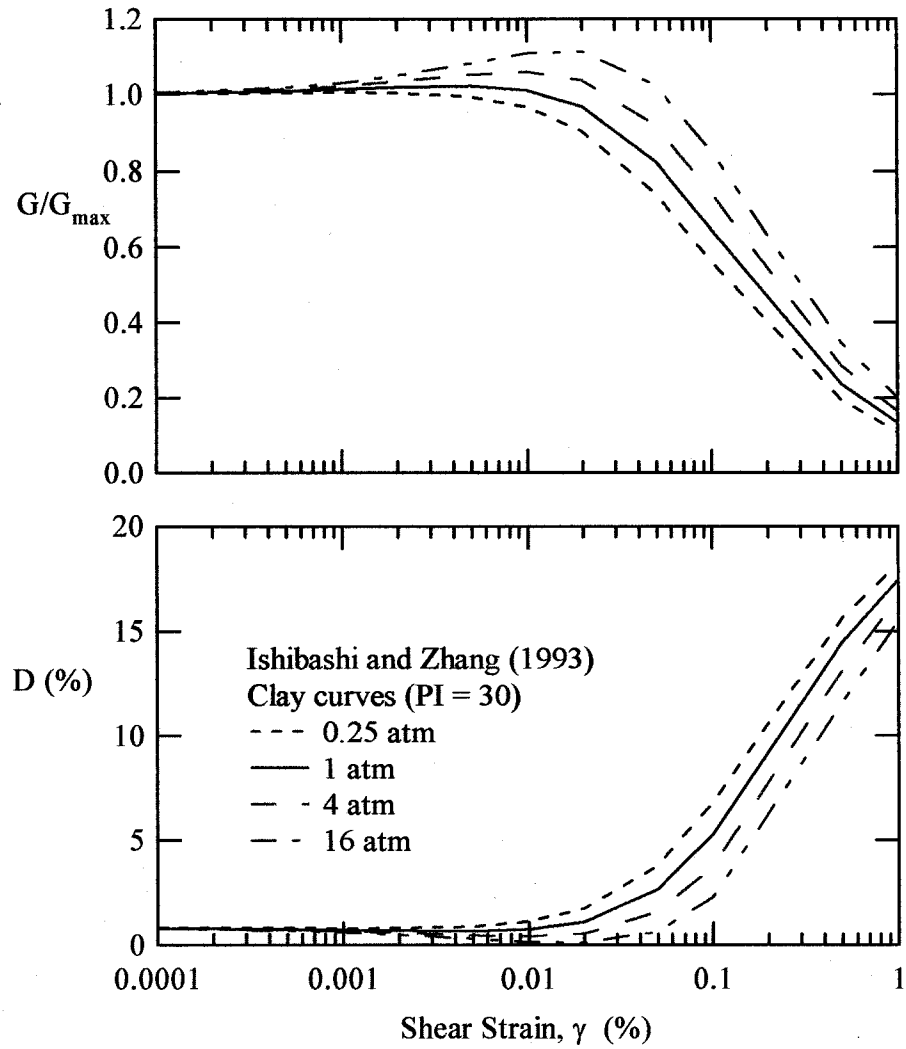

Figure 2.6 Empirical relationships for normalized modulus reduction and material damping for clay after Ishibashi and Zhang (1993)

As discussed in the previous section, Darendeli (2001) proposed a modified hyperbolic model to characterize normalized modulus reduction and material damping. Curves generated using Darendeli's equations are shown in Figures 2.8-2.10. Soil specimens used in Darendeli (2001) database were taken from Northern California, Southern California, South Carolina and Lotung, Taiwan. The curves proposed by

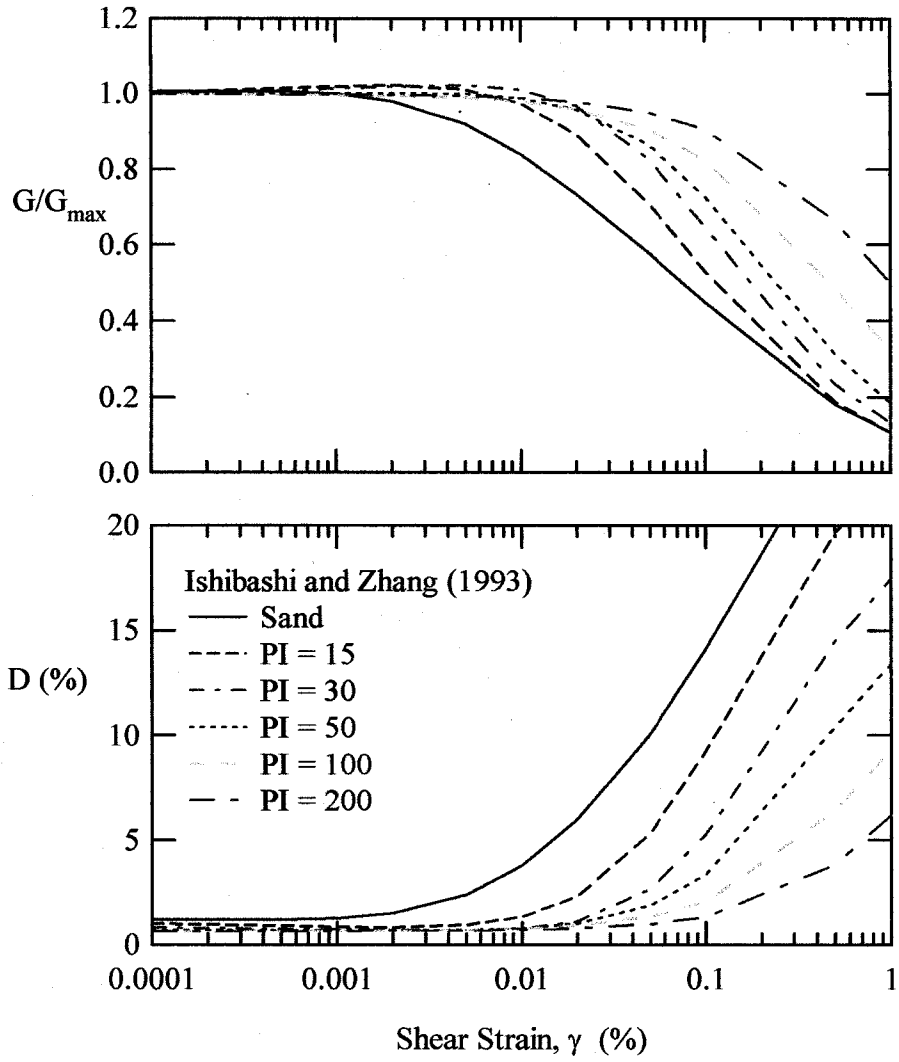

Figure 2.7 Empirical relationships for normalized modulus reduction and material damping show the effect of plasticity index after Ishibashi and Zhang (1993)

Darendeli (2001) show larger effect of confining pressure than the curves proposed by Ishibashi and Zhang (1993). The material damping curves at small strain account for the effect of confining pressure. The effect of plasticity index is shown in Figure 2.10. Darendeli shows that the damping at low strains for soil with high plasticity tends to be higher than soils with low plasticity.

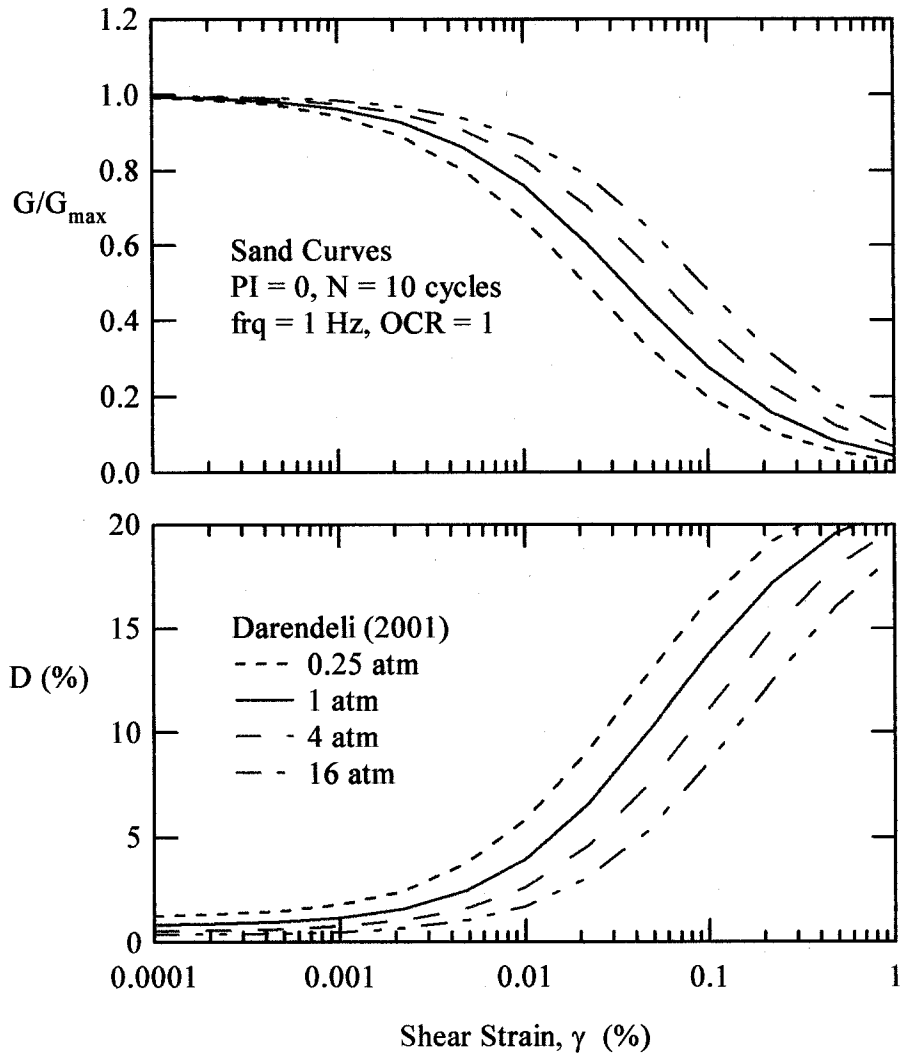

Figure 2.8 Empirical relationships for normalized modulus reduction and material damping for sand after Darendeli (2001)

2.4 NONUNIFORM STRESS-STRAIN IN TORSIONAL TESTING

One of the weaknesses of resonant column and torsional shear method is the fact that stress-strain distribution is not uniform in the radial direction of the horizontal plane of a soil specimen during torsional loading. Theory of elasticity was utilized originally because the torsional shear test was developed to measure the small strain soil behavior.

As described earlier, soils behave nonlinearly when subjected to strain levels as small as 10^{-3} %. The nonuniform stress-strain effect becomes significant when testing on soil at medium to high strain levels. Using hollow rather than solid specimen can minimize this effect however the hollow specimens are not commonly used because of trimming and handling difficulties.

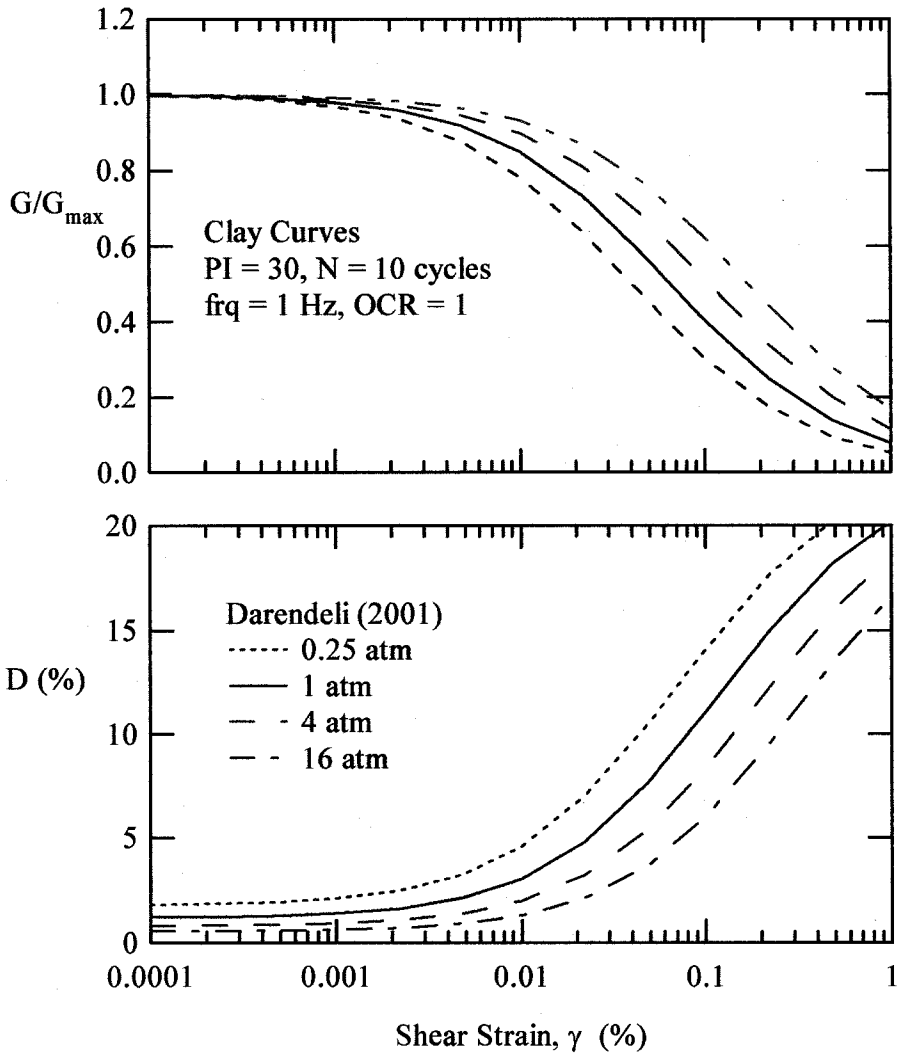

Figure 2.9 Empirical relationships for normalized modulus reduction and material damping for clay after Darendeli (2001)

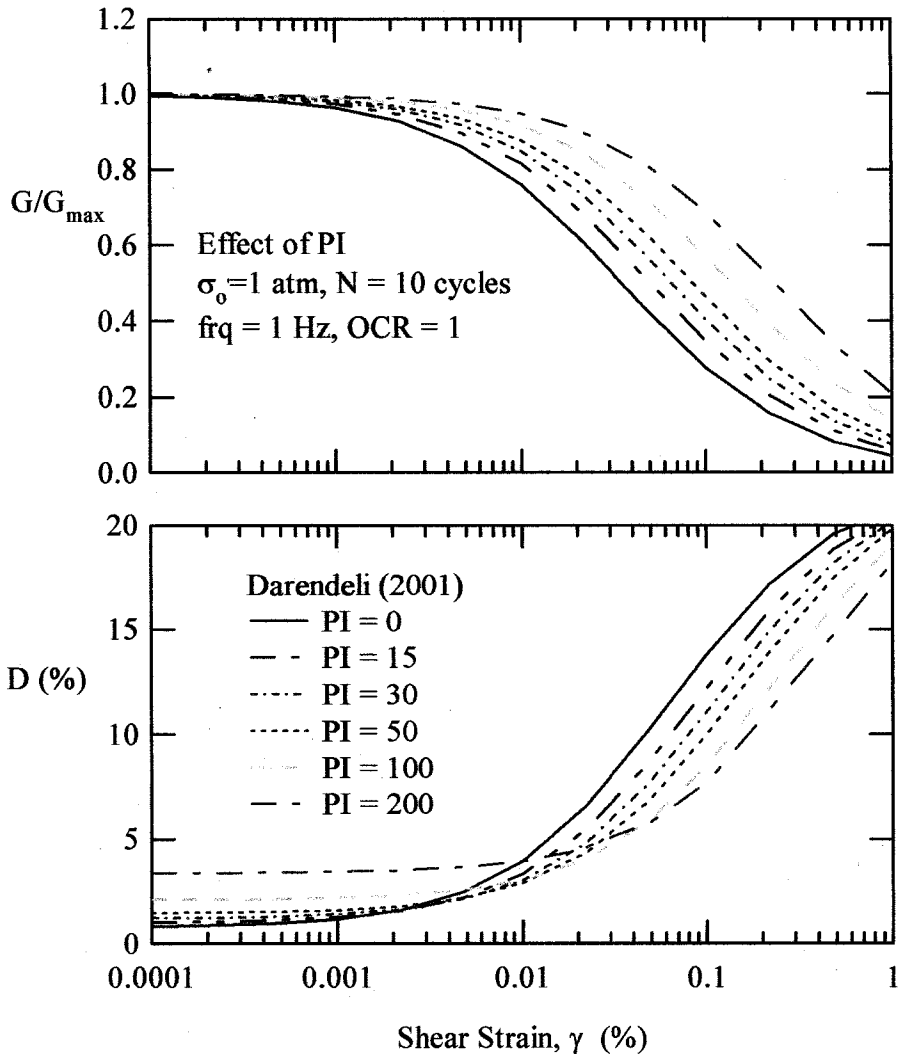

Figure 2.10 Empirical relationships for normalized modulus reduction and material damping show the effect of plasticity after Darendeli (2001)

In torsional testing, measurements are made of torque (T) and rotation angle (θ). Several approaches have been proposed to correlate the measured T-θ relationship to the stress-strain relationship of the soils (Hardin and Drenevich 1972a, Taylor and Parton 1973, Chen and Stokoe 1979).

Hardin and Drnevich (1972a) recommended using the average stress and strain in the soil specimen. For a cylindrical soil specimen with the height of L, the average strain, γ_{av} can be expressed as:

$$\gamma_{av} = \frac{\int_A \gamma \, dA}{\int dA} = \frac{2}{3}\frac{\theta}{L}\left(\frac{R_o^3 - R_i^3}{R_o^2 - R_i^2}\right), \tag{2.25}$$

where θ = rotation angle,

R_o = outside diameter of the specimen, and

R_i = inside diameter of the specimen.

In the case of solid specimen, $R_i = 0$, and the average shear strain occurs at a radius of 0.667 times the sample radius. Therefore, the average shear stress and strain are obtained from following equation:

$$\gamma \approx \frac{\theta}{L} 0.667R, \tag{2.26}$$

$$\tau \approx \frac{T}{I_p} 0.667R, \tag{2.27}$$

where T = torque, and

I_p = area moment of inertia of soil specimen.

This approach is based on the summation of linear variation of strain over the radius of soil specimen but does not account for the nonlinear stress-strain soil behavior.

The equivalent radius approach dealing with the nonuniform distribution of strain in soil specimen was developed by Chen and Stokoe (1979). The hyperbolic model and Ramberg-Osgood model were used as known stress-strain relationship for soils and used to calculated T-θ relationship using the following equations:

$$\theta = \frac{\gamma L}{r}, \text{ and} \tag{2.28}$$

$$T = \int_A \tau r \, dA = 2\pi \int_0^R \tau r^2 dr. \tag{2.29}$$

Chen and Stokoe developed T-θ curves by dividing the cross section of a theoretical soil cylinder equally into N concentric rings. The cross-sectional area (A) of each ring was equal, therefore the width of the rings varied with the distance from the center of the soil cylinder. For a given rotation angle, the average shear strain on each ring was calculated using Equation 2.28. Using the hyperbolic or Ramberg-Osgood stress-strain relationship, an average shearing stress was determined on each ring. The total torque was obtained from Equation 2.29. This procedure was repeated for different rotation angles using the results of this analysis, normalized plots of T versus θ were developed as shown in Figure 2.11. The normalized values of T_r and θ_r, are defined as:

$$T_r = JG_{max}\theta_r, \text{ and} \tag{2.30}$$

$$\theta_r = \frac{\gamma_r L}{R}, \tag{2.31}$$

where γ_r is the reference strain from Equation 2.6.

Figure 2.11 shows three different curves; one generated from the hyperbolic model, the other two from the Ramberg-Osgood model. For the hyperbolic model, the parameters G_{max} and γ_r are equal to 50,000 kPa, and 0.2%, respectively. The Ramberg-Osgood model is used for the other two curves use the parameters of $\alpha = 0.7$, $r = 5.5$, and $\alpha = 1.2$, $r = 4.1$, respectively. The values T and θ from these computed normalized T-θ

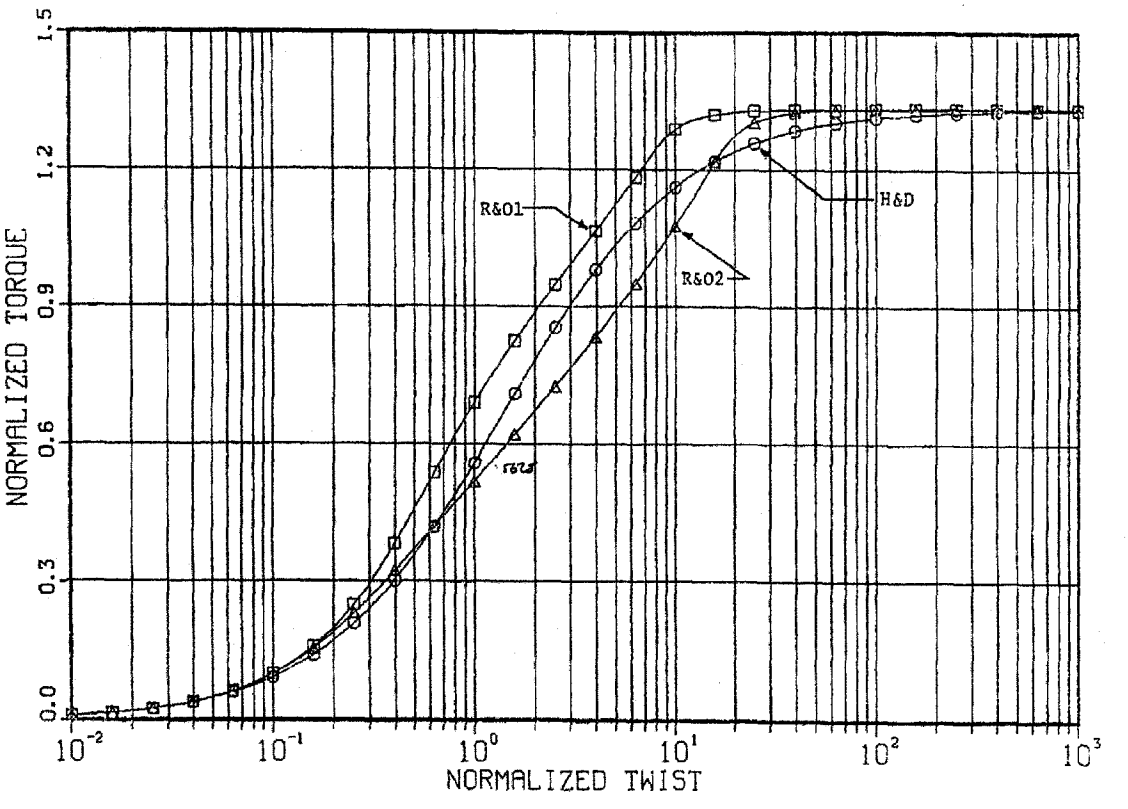

Figure 2.11 Normalized torque-twist relationship from Chen and Stokoe (1979)

curves were used to calculate the corresponded effective shear modulus (G_{eff}) using a basic torsion equation. Each value of G_{eff} was then matched with the value of G generated by the theoretical stress-strain relationship. The corresponded θ from G_{eff} and γ from G were compared and a correction is applied to radius of specimen to achieve the best match of γ from experimental and theoretical relationships. This correction is expressed in term of the equivalent radius ratio (R_{eq}) or the ratio of the equivalent radius, r_{eq} and the radius of specimen, R.

Figure 2.12 shows plots of the R_{eq} with normalized θ generated by Chen and Stokoe (1979). The value of R_{eq} is as high as 1.0 for R-O model case and 0.8 for hyperbolic model at small strain. The value of R_{eq} decreases to about 0.75 for very large strain for both models. Based on this study, the R_{eq} is recommended to be varied from 0.82 for shearing strain less than 0.001% to 0.79 for shearing strain equals to 0.1%. Therefore, the nonuniformity of strain can be minimized by a simple correction of the radius of soil specimen. This approach is considered reasonable in practice however the calculation of strain for damping is still in question.

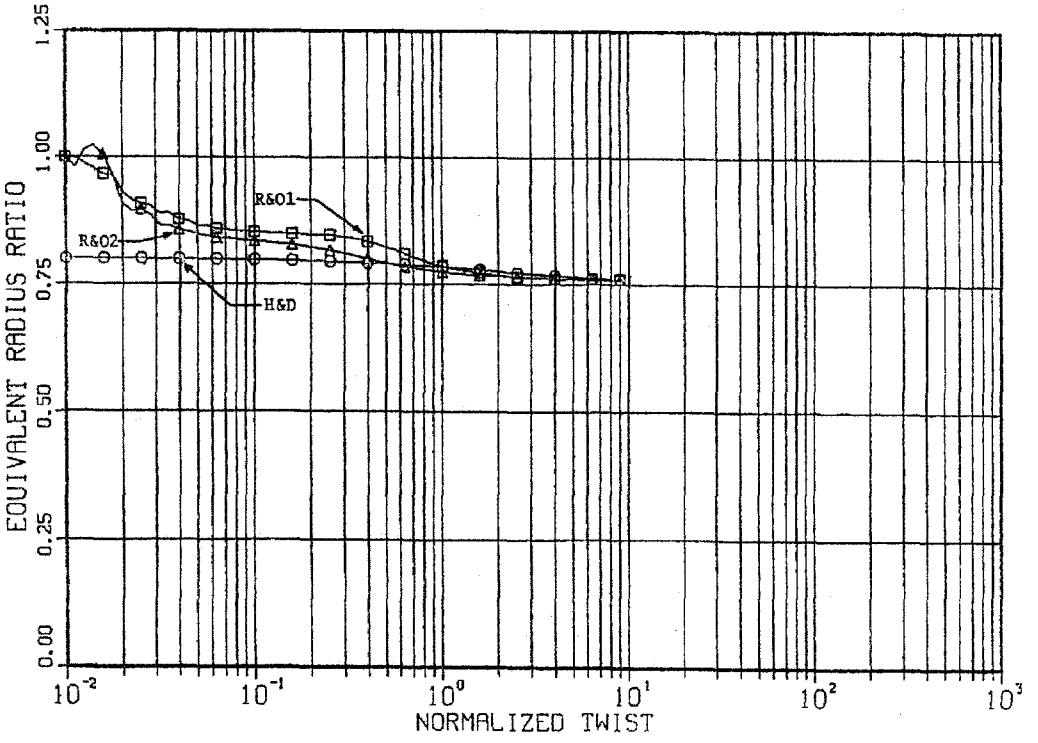

Figure 2.12 Variation of equivalent radius ratio with normalized twist in solid specimen from Chen and Stokoe (1979)

2.5 EFFECT OF EQUIPMENT GENERATED DAMPING IN RC/TS EQUIPMENT

Numerous laboratory experiments have shown that the material damping of soils increases with the strain amplitude. The damping values range from below 1% at very low strains to above 20% at very high strains. Accurate measurements of material damping are challenging, especially at low strains where the soil damping is very small. The resonant column and torsional shear methods are typical used to measure the material damping of soils. There are several potential sources of error in resonant column and torsional shear damping measurements and many researchers have proposed some procedures to mitigate these problems.

One of the major problems is related to the equipment generated additional damping due to the drive system. Typical drive systems in the resonant column and torsional shear device use a coil and magnet system. The additional damping is created from the movement of the magnet in the coil inducing an electromotive force (emf) opposing the driving motion called back emf. Kim (1991) and Hwang (1997) performed calibrations to determine the magnitude of this equipment generated damping and developed correction procedure for resonant column and torsional shear tests.

Kim's and Hwang's calibrations were made by performing the tests on metal specimens that have resonant frequencies range from 14 Hz to 150 Hz. The method is based on the assumption that the material damping of the metal specimens is very small, and thus can be neglected. Results from the resonant column calibration tests indicate that the equipment generated damping can be as large as 4% at low resonant frequencies and decreases to as low as 0.3% at high resonant frequencies. Figure 2.13a shows the

plot of the measured equipment damping versus different resonant frequency (Hwang 1997). The material damping of soil specimen at the same resonant frequency is corrected by subtracting the equipment damping at the same frequency (Hwang 1997).

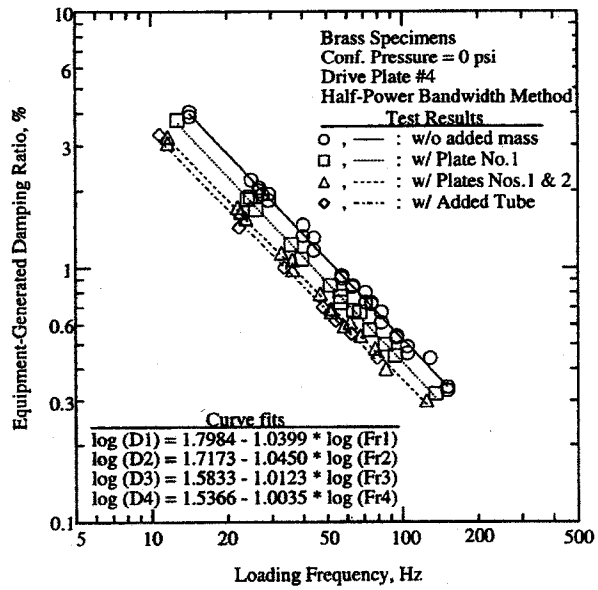

a) Resonant column test

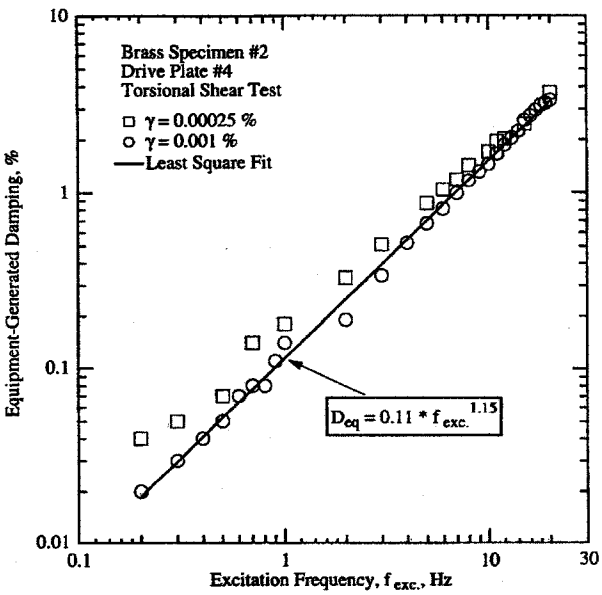

b) Torsional shear test

Figure 2.13 Equipment generated damping ratio using metal specimens from Hwang (1997)

In the torsional shear test, the equipment generated damping was measured at the loading frequencies from 0.2 Hz to 20 Hz. The results show a trend opposite to the resonant column results, with the damping increasing with frequency as shown in Figure 2.13b.

Recently, other researchers have proposed alternatives to these empirical corrections for the resonant column method. Li et al. (1998) proposed an alternative testing method using the energy-injecting virtual mass resonant column system. The main idea of this approach is to maintain the resonant frequency and damping of testing material at a pre-specified values using a feedback system, thus minimal the back emf effect. The new system was verified by performing the test on the aluminum rod with known properties. This system works reasonably well however it is complicated and required a special control system.

Cascante et al. (2003) presented a current-based measurement as an alternative to the conventional voltage-based measurement to minimized the back emf effect in resonant column test. The derivation of new transfer functions for voltage and current measurement were introduced and expressed as:

$$H_v(\omega)=\frac{A(\omega)}{V_T(\omega)}=\frac{-\left[\frac{Blr_m a}{J}\right](\omega/\omega_o)^2}{(R+\omega Li)+\left[(1-(\omega/\omega_o)^2+(c_E r_m^2+d_s)\frac{(\omega/\omega_o)i}{\omega_o J}\right]+Bl^2 r_m^2\frac{(\omega/\omega_o)i}{\omega_o J}}, \quad (2.32)$$

and

$$H_I(\omega)=\frac{A(\omega)}{I(\omega)}=\frac{-\left[\frac{Blr_m a}{J}\right](\omega/\omega_o)^2}{(1-(\omega/\omega_o)^2+(c_E r_m^2+d_s)\frac{(i\omega/\omega_o)}{\omega_o J}}, \quad (2.33)$$

where ω = angular frequency,

ω_o = resonant angular frequency,

i = imaginary unit,

$A(\omega)$ = spectral density of the acceleration,

$V_T(\omega)$ = spectral density of the total voltage,

$I(\omega)$ = spectral density of the current,

r_m = distance from the center of the specimen to the magnet,

r_a = distance from the center of the specimen to the accelerometer,

J = rotational mass moment of inertia of the specimen and drive plate,

Bl = magnetic-force factor of the coils,

c_E = damping coefficient due to the eddy-current forces,

d_s = viscous damping of the specimen,

R = resistance of the coil, and

L = inductance of the coil.

This method was evaluated by testing three aluminum specimens and comparing the results between the current and voltage measurement. Results showed that the damping measured by the voltage measurement was as much as 50 times higher than that measured using current measurements. The damping measurement in dry sand using the voltage measurement was also observed to be up to 300% of the damping measured using the current measurement. Cascante et al. (2003) recommended using the current-base measurement for the resonant column test and analyzing results using the current transfer function. This study used the curve fitting processes to obtain the model parameters.

Meng and Rix (2003) developed an electromechanical model to derive the equipment generate damping which is expressed as:

$$D_{eq} = \frac{c_{eq}}{c_c} = \frac{2k_i k_b}{R_s + R_c} \frac{1}{2J\omega_r}, \tag{2.34}$$

where D_{eq} = equipment generated damping ratio,

c_{eq} = equipment generated damping term,

c_c = critcal damping,

k_i = torque against current calibration factor,

k_b = induced voltage against angular velocity,

R_s = resistance of source,

R_c = resistance of coil,

J = total mass polar moment of inertia of the drive system and specimen,

and ω_r = resonant angular frequency.

Meng and Rix (2003) also proposed a solution to reduce equipment generated damping in resonant column testing using an instrumentation operational amplifier circuit to convert the voltage-mode source into a current-mode source. From this study, the equipment generated damping is reduced by more than three orders of magnitude compared with the voltage-mode source. However, the current limitations of the operational amplifier will limit testing at high strain levels.

Wang et al. (2003) proposed the electromechanical model used for presenting the back emf effect in terms of the "virtual inertia," I_{EMF} and the additional electrical damping, c_{EMF}. The electromechanical model derived by Wang et al. (2003) was presented in form of:

$$(I_t - I_{EMF})\ddot{\varphi} + (c_{soil} + c_{EMF})\dot{\varphi} + K_t\varphi = T_o e^{i\omega t}, \quad (2.35)$$

$$I_{EMF} = \frac{\alpha\beta L}{R^2 + \omega^2 L^2}, \text{ and} \quad (2.36)$$

$$c_{EMF} = \frac{\alpha\beta R}{R^2 + \omega^2 L^2}, \quad (2.37)$$

where I_t = rotational moment of inertia of the system,

ϕ = angular displacement,

c_{soil} = lumped viscosity for the soil,

K_t = torsional stiffness,

$T_o e^{i\omega t}$ = applied torque, and

α and β = proportionality constants.

Development of the electromechanical model proposed by Wang et al. (2003) is very similar to model proposed in this study, however, the effect of back emf was presented using a different formulation. Frequency effects for α and β were not investigated by Wang et al. (2003).

CHAPTER 3

TEST EQUIPMENT AND METHOD OF ANALYSIS

3.1 INTRODUCTION

A Stokoe-type resonant column and torsional shear (RC/TS) apparatus was employed in this study. This equipment is one of the most widely used to perform the dynamic testing on soils for research and commercial purposes. The equipment has been developed and modified to operate both resonant column (RC) and torsional shear (TS) testing (Isenhower 1979, Lodde 1982, Ni 1987, Hwang 1997, Darendeli 2001). A detailed description of the RC/TS testing method and equipment are presented in this chapter. The theoretical basis used for analyzing results for both RC and TS tests are included.

3.2 OVERVIEW OF RESONANT COLUMN AND TORSIONAL SHEAR TESTS

There are several versions of the resonant column test apparatus employing different conditions to constrain the top and bottom of specimen. The fixed-free type, where the soil specimen is fixed in place at the bottom and driving force is applied at the top, is the method most commonly used. The vibration response is monitored at the top of specimen. The ideal fixed-free configuration is shown Figure 3.1a. For actual testing, a torque must be applied to the top of soil specimen, thus a drive plate as well as deformation sensors must be attached to the specimen at the top. As a result, the top of soil specimen is not in the ideal free condition. The approach dealing with this complication is to lump the attachments into one mass and the boundary condition for the

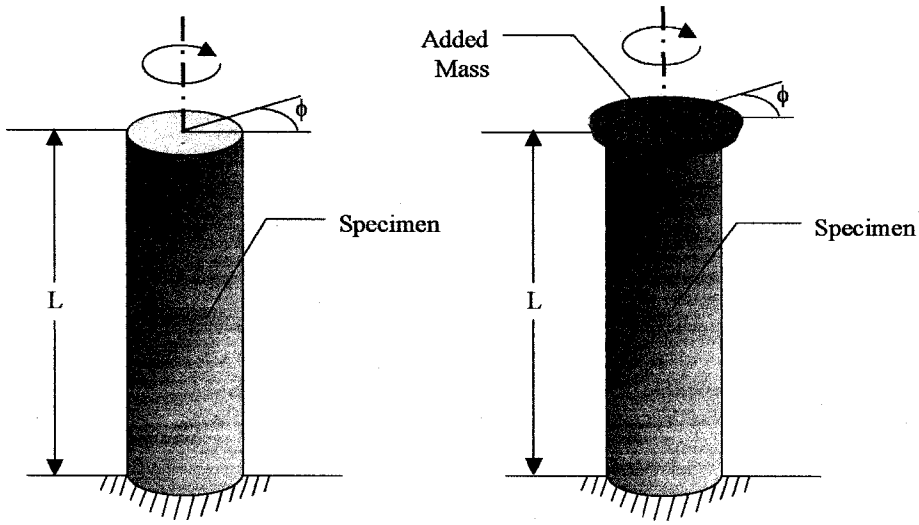

a) Fixed Free Type-No Mass b) Fixed Free Type-Added Mass

Figure 3.1 Fixed-free configurations for RC/TS test

ideal fix-free configuration must be modified. Consequently, the vibration response of a soil specimen in RC/TS test is modeled as a cylindrical rod with one end fixed and an attached rigid mass on the other end as shown in Figure 3.1b.

Two different types of testing can be performed on the same soil specimen in RC/TS apparatus. The first type of test is the resonant column (RC) test. The general principle employed in the RC test is to excite the soil specimen with a steady-state torsional motion over a range of frequencies to identify the first mode resonant frequency. The shear modulus can then be evaluated utilizing the well-defined boundary conditions and the specimen geometry and mass. Material damping is determined by one of two methods; the free vibration decay method or the half power bandwidth method.

The second type of test is the torsional shear (TS) test. The difference between the TS test and the RC test is mainly in the excitation frequency. In the TS test, a slow cyclic

loading in the range of 0.01 to 10 Hz is applied to the specimen. Shear modulus and damping are determined based on the characteristic of the hysteresis loop.

3.3 OVERVIEW OF RESONANT COLUMN AND TORSIONAL SHEAR EQUIPMENT

Figure 3.2 shows a drawing of the RC/TS equipment. The RC/TS equipment is capable of testing a solid or hollow cylindrical specimen and a variety of specimen sizes by using interchangeable top platens and base pedestals. The equipment consists of three basic components. First, the drive system used to apply a torsional cyclic load at the top of soil specimen. Second, the deformation monitoring system for measure the rotational and vertical displacements of the top of the specimen. Third, the confinement system used to apply isotropic confining pressure to specimen during consolidation and testing. RC/TS testing is performed on a specially designed isolation table to minimize the effects of ambient vibration on the measurements. A schematic diagram of the RC/TS drive system and deformation monitoring system is presented in Figure 3.3. Details of each component are described as below.

3.3.1 The RC/TS Drive System

The drive system in RC/TS equipment consists of a drive plate and eight drive coils. The drive plate is a four-armed aluminum plate that has rectangular shaped magnets attached to the end of each arm as shown in Figure 3.2. The drive coil is a long copper wire wound in multiple elliptical loops. The drive plate is positioned such that each end of magnet is at the center of a coil loop. When current passes through the coils, the interaction between coil and magnet behaves similarly to an electrical motor creating

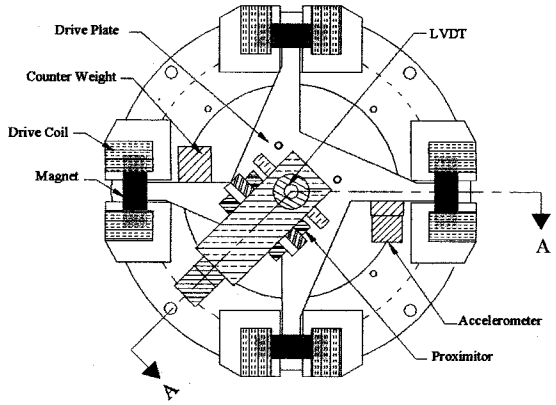

Top view of the drive plate

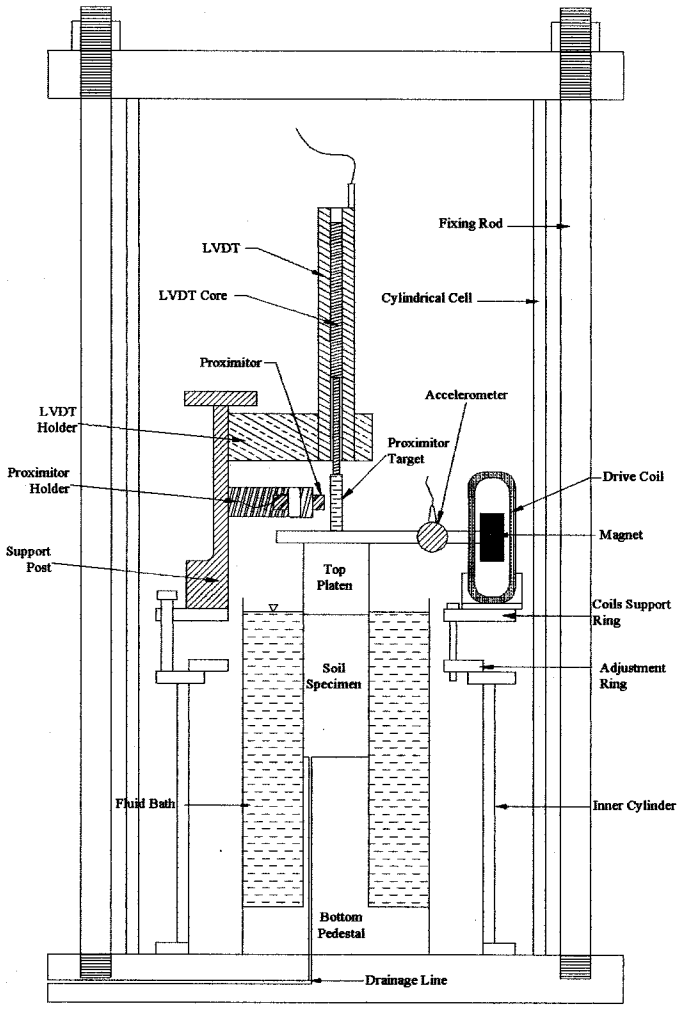

Section A-A with confinement system

Figure 3.2 The RC/TS equipment configuration

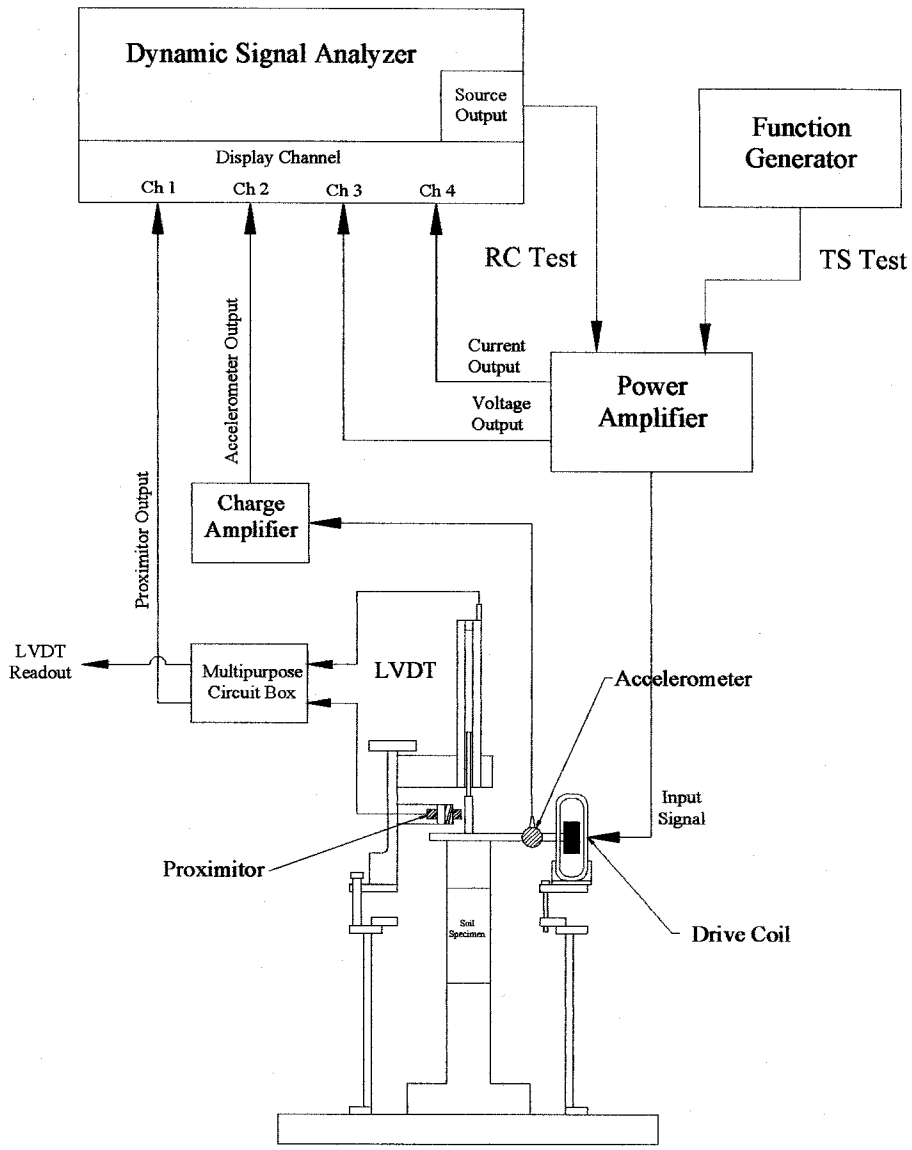

Figure 3.3 Drive system and deformation monitoring diagram for RC/TS equipment

torsion on the drive plate. More details on coil and magnet interaction are presented in Chapter 4.

A harmonic sinusoidal function is sent to the drive coils from a function generator. For the RC test, a constant amplitude signal is generated over a range of frequency by a dynamic signal analyzer (Hewlett Packard Model 35670A). For the TS test, the signal frequency, number of cycles, and amplitude are controlled by a function generator (Hewlett Packard Model 3314A). For both tests, the signal is transmitted through a power amplifier before being sent to the drive coils. The power amplifier used for this study is AE Techron Linear Amplifier (Model LVC 608). There are two advantages to using a power amplifier. First, the signal can be amplified up to about 25 times when performing a high amplitude tests. Second, the power amplifier has special features for monitoring voltage and current it outputs. This feature is useful for torque calculations in TS test. The voltage and current signals monitored by the power amplifier are then sent to the dynamic signal analyzer to be recorded and analyzed.

3.3.2 The RC/TS Deformation Monitoring System

The second component of the RC/TS apparatus is the deformation monitoring system which includes the rotational and vertical displacement monitoring devices. The rotational monitoring device consists of both accelerometer and proximitors.

In the RC test, the accelerometer is used for monitoring the rotation of the drive plate. Typically, the RC test is performed over frequency ranges of 10-400 Hz. An accelerometers perform well in this frequency range. The accelerometer is mounted on the drive plate so it senses the motion of the drive plate. The signal from the

accelerometer is transmitted through a charge amplifier for amplification and signal conditioning. The output signal from the charge amplifier is then sent to the dynamic signal analyzer. The real time record is converted into frequency domain by Fast Fourier Transform (FFT) and the frequency response is displayed on the dynamic signal analyzer.

For the TS test, torque is applied at much lower frequencies than those used in RC testing (0.01-10Hz). Accelerometers are not suitable for this low frequency range so displacement transducers known as a proximitor is used to monitor rotation. The system consists of two proximity probes and a metal target as shown in Figure 3.2. The two proximity probes are fixed to a rigid post and the metal targets are mounted on top of the drive plate. Two proximity probes are used in the system to minimize the effect of bending on rotation measurements. The output time of the proximitor system is monitored using the dynamic signal analyzer.

A linear vertical displacement transducer (LVDT) is used as a vertical displacement monitoring device for RC/TS equipment. The LVDT monitors the settlement when soil specimen as it consolidates. The LVDT is rigidly mounted to the same post used for the proximitor system and positioned at the center of the dive plate as shown in Figure 3.2. The output from LVDT is recorded manually using the multipurpose circuit box explained below.

The multipurpose circuit box was designed and built for two different purposes. The first purpose of the box is to condition the proximitor signals. The box has a subtraction circuit used to subtract a predetermined proximitor center voltage from the output voltage from each proximitor. The signal out of the subtraction circuit can be used for adjusting the gap between the proximitor and target. The gap distance is adjusted

until the circuit output is zero volts. The proximitor is then at the center of its linear range. During the test, a signal proportional to the difference between the two proximitor signals is generated using an instrumentation quality differential amplifiers. The signal from this amplifier is sent to the dynamic signal analyzer. The subtraction circuit for the proximitor signals developed in this study is presented in Figure 3.4. The second purpose of the box is to excite and monitor the LVDT. The LVDT output voltage is displayed using a 4 ½ digit voltage monitor.

3.3.3 The RC/TS Confinement System

The third component of RC/TS equipment is the confinement system. As shown in Figure 3.2b, the RC/TS equipment is enclosed inside a cylindrical cell where the isotropic pressure is applied to a soil specimen. Air pressure is applied inside the cell through the air line located at the bottom plate of the cell. The pressure is controlled and maintained by an air regulator. The cell is made from stainless steel and has the capacity to withstand pressure up to at least 150 psi. Inside the cell, the specimen is surrounded by a fluid bath which minimizes air defusing into the specimen. The fluid bath is a cylindrical plastic sleeve fixed to the base pedestal and filled with fluid such as silicone oil. During consolidation, soil specimen is drained using the two drainage lines located in the bottom pedestal.

3.3.4 Isolation Table

An isolation table was designed and constructed in this study to accommodate the RC/TS equipment as well as to isolate the measurement system from building vibrations. The table is isolated vertically and horizontally by a combination of cables suspension

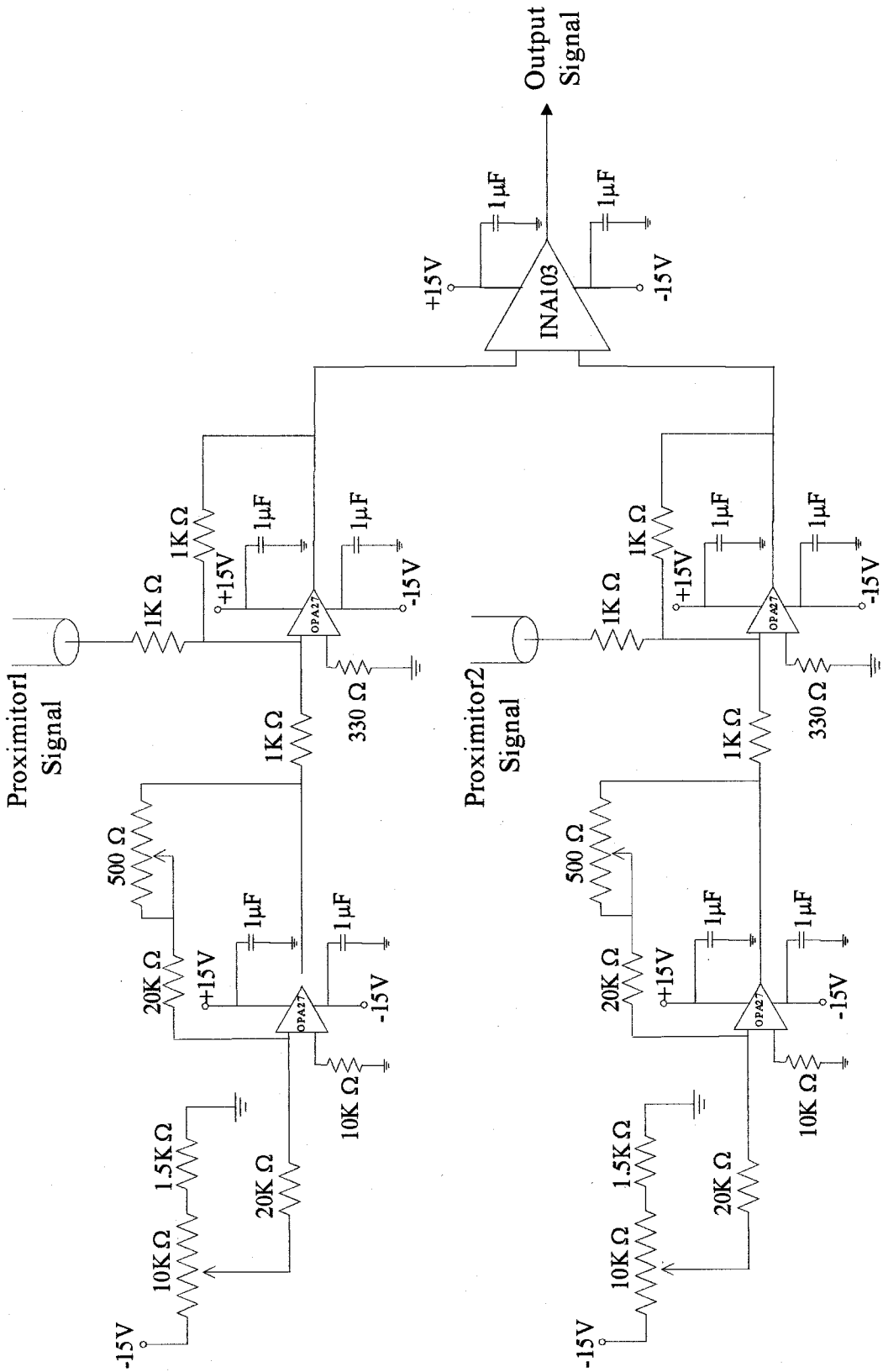

Figure 3.4 Subtraction circuit for the proximitor signa

and an air spring system. The isolation is triangular in shape and suspended from ceiling beams by three cables with the lengths of about 8 ft. The table is made from steel and filled with mill scale. Total weight of the isolation table is about 3000 lb. Three air springs are used to support the three corners of the tabletop. Air pressure in each air spring is controlled by valve system so that the table remains level. The isolation table was designed to have a natural frequency in vertical displacement of about 1 Hz and in horizontal displacement of about 0.3 Hz. Figures 3.5 and 3.6 show a photograph and drawing of the isolation table.

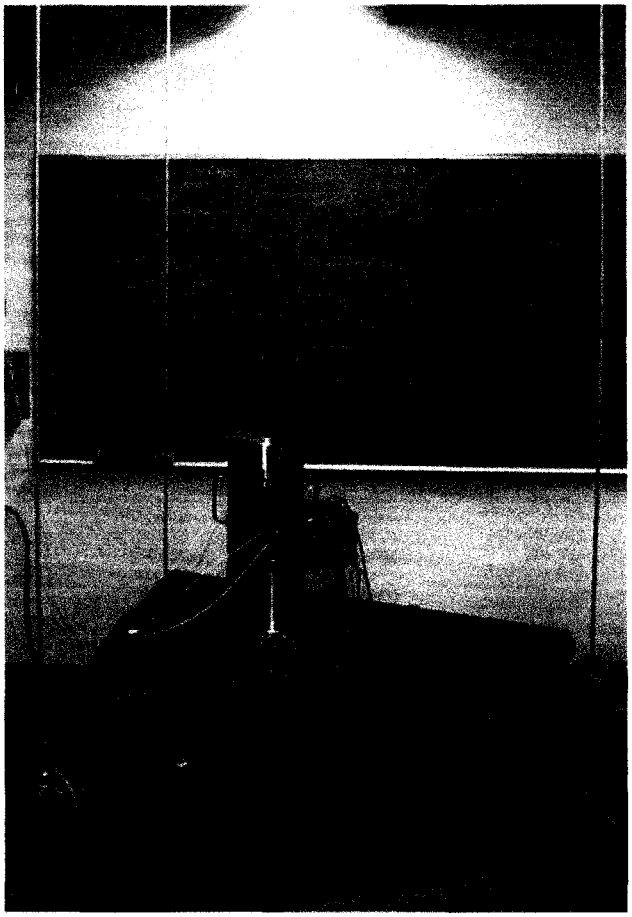

Figure 3.5 Photograph of the isolation table

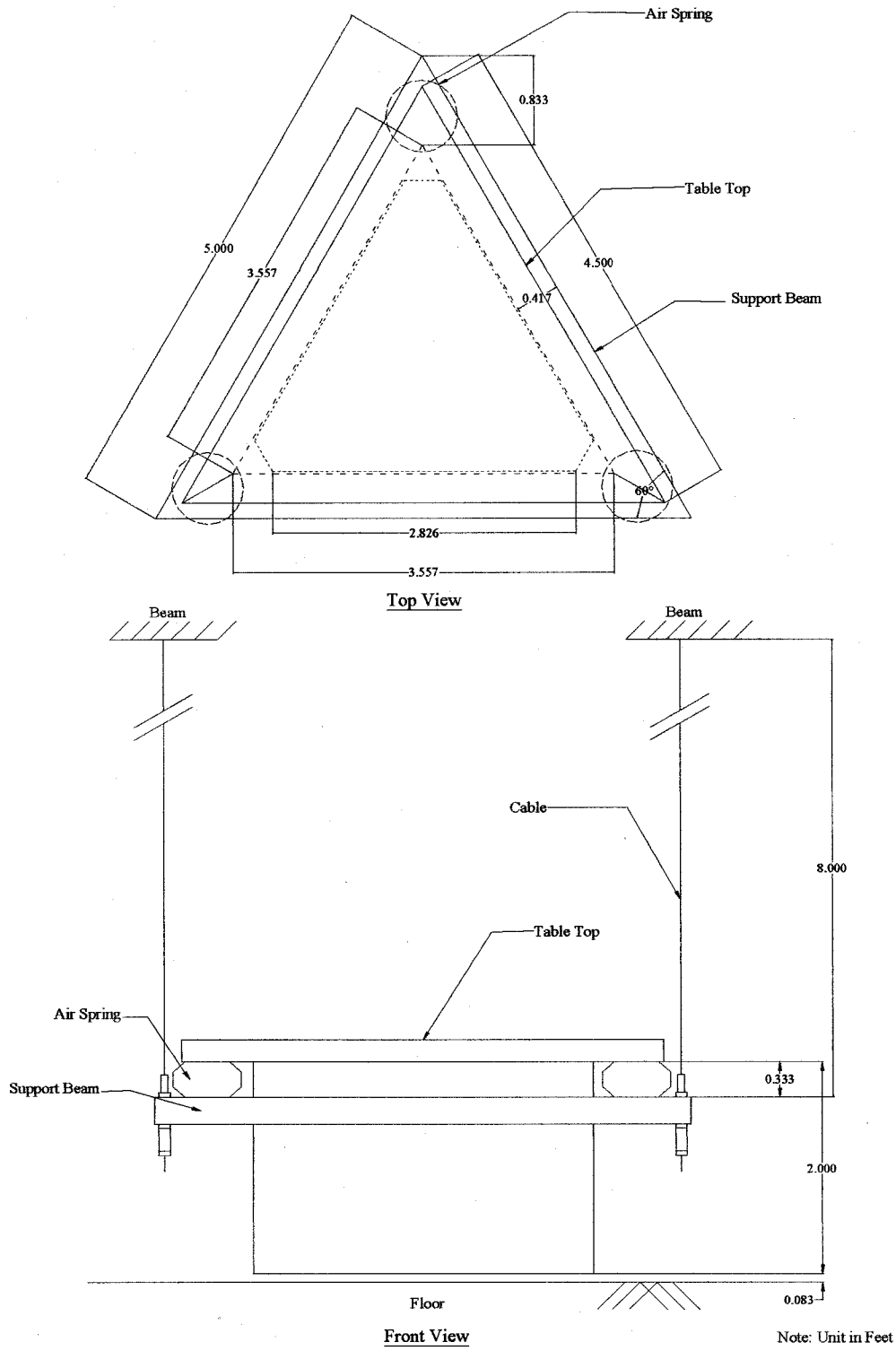

Figure 3.6 Drawing of the isolation table

3.4 METHOD OF ANALYSIS

Different analysis methods are required for RC and TS testing. The RC test analysis procedure is based on the wave propagation in elastic media. The TS test analysis assumes static behavior to measure is the hysteretic behavior of elastroplastic material. Both tests are complicated by nonuniform stress- strain in the soil specimen. The nonuniform stress- strain effect is taken into account more precisely using a stress integration approach developed in this study. This approach is presented in Chapter 8. In this section, the basic analysis methods used in RC and TS testing is presented.

3.4.1 The RC Test Analysis

In RC test, a cylindrical soil specimen is excited torsionally in its first resonant mode. The wave velocity is determined from the resonant frequency and from dimensions and mass of the soil specimen. The test configuration is the fixed-free type with added mass applied on top of the specimen as shown in Figure 3.1b. Torque is exerted on top of soil specimen is equal to the inertia force of the added mass. This torque can be expressed as:

$$T = GI_p \frac{\partial \theta}{\partial x} = -J_o \frac{\partial^2 \theta}{\partial t^2}, \tag{3.1}$$

where G = shear modulus of specimen,

I_p = area moment of inertia of specimen,

$\left(= \frac{\pi R^4}{2} \right.$ for a solid cylindrical specimen with radius, R),

J_o = mass polar moment of inertia of added mass, and

θ = rotational angle.

By applying the fix-free end condition, the governing equation for torsional vibration of soil column can be written as:

$$\frac{J}{J_o} = \frac{\omega_n L}{v_s} \tan \frac{\omega_n L}{v_s}, \tag{3.2}$$

where ω_n = undamped natural circular velocity ($=2\pi f_n$),

f_n = undamped natural frequency $\left(= \frac{f_m}{\sqrt{1-2D^2}} \right)$,

f_m = resonant frequency for constant force amplitude,

J = mass polar moment of inertia of specimen,

$(= \frac{1}{32} mR^2$ for a solid cylindrical specimen with mass, m),and

D = damping ratio of specimen,

v_s = shear wave velocity of specimen, and

L = length of specimen.

The right hand side of Equation 3.2 can be written in the form of $\beta\tan\beta$, where $\beta = \omega_n L/v_s$. By applying the predetermined values of the polar moment of inertia of specimen and added mass, the value of β can be solved graphically by plotting a curve of β versus J/J_o. Once an appropriated value of β is selected, the shear wave velocity of specimen can be determined from:

$$v_s = \frac{2\pi f_n L}{\beta}. \tag{3.3}$$

Shear modulus (G) is then calculated using the following equation:

$$G = \rho v_s^2, \tag{3.4}$$

where ρ = mass density of the specimen.

The resonant column test produces the response curve that provides the information regarding the dynamic properties of the test specimen. The response curve is the transfer function presented in term of the ratio of the displacement (or rotation) and force (or torque) amplitude. For a single degree of freedom system, the transfer function is expressed as:

$$H = \frac{\theta}{T} = \frac{1}{\sqrt{\left[1-(\frac{\omega}{\omega_n})^2\right]^2 + \left[2D\frac{\omega}{\omega_n}\right]^2}}, \text{ and} \tag{3.5}$$

$$\tan\varphi = \frac{2D\frac{\omega}{\omega_n}}{1-(\frac{\omega}{\omega_n})^2}. \tag{3.6}$$

where H = transfer function amplitude, and

φ = phase angle between torque and rotation.

For constant force amplitude, the frequency at maximum amplitude, f_m is given by:

$$f_m = f_n\sqrt{1-2D^2}. \tag{3.7}$$

and maximum transfer function amplitude, H_{max} is given by:

$$H_{max} = \frac{1}{2D\sqrt{1-D^2}} \approx \frac{1}{2D} \text{ for small D (<10\%).} \tag{3.8}$$

Utilizing the shape of the response curve, damping ratios can be determined using the half-power bandwidth method. The method is applied by selecting two points on the

response curve at H is equal to $\frac{1}{\sqrt{2}}H_{max}$. These points are called f_1 and f_2 as presented in Figure 3.7. The amplitude at f_1 and f_2 can be expressed as:

$$\frac{1}{\sqrt{2}}H_{max} = \frac{1}{\sqrt{2}}\cdot\frac{1}{2D} = \frac{1}{\sqrt{\left[1+(\frac{f_{1,2}}{f_n})^2\right]^2 + \left[4D\frac{f_{1,2}}{f_n}\right]^2}}. \tag{3.9}$$

Squaring and rearranging Equation 3.9 gives:

$$\left(\frac{f_{1,2}}{f_n}\right)^4 - 2\left(\frac{f_{1,2}}{f_n}\right)^2(1-2D^2) + (1-8D^2) = 0. \tag{3.10}$$

Roots of Equation 3.10 become:

$$\left(\frac{f_{1,2}}{f_n}\right)^2 = (1-2D^2) \pm 2D\sqrt{1-D^2}\,. \tag{3.11}$$

The second-order term of D is negligible since the D is small. Equation 3.11 reduces to:

$$\left(\frac{f_{1,2}}{f_n}\right)^2 \approx 1 \pm 2D. \tag{3.12}$$

Subtracting the roots from Equation 3.12 gives:

$$\left(\frac{f_2}{f_n}\right)^2 - \left(\frac{f_1}{f_n}\right)^2 \approx 4D. \tag{3.13}$$

Rearranging gives:

$$D \approx \frac{(f_2 - f_1)(f_2 + f_1)}{4f_n^{\,2}}. \tag{3.14}$$

Assuming that the response curve is symmetric, (f_2+f_1) is equal to $2f_n$. Equation 3.14 reduces to:

$$D \approx \frac{f_2 - f_1}{2f_n}. \tag{3.15}$$

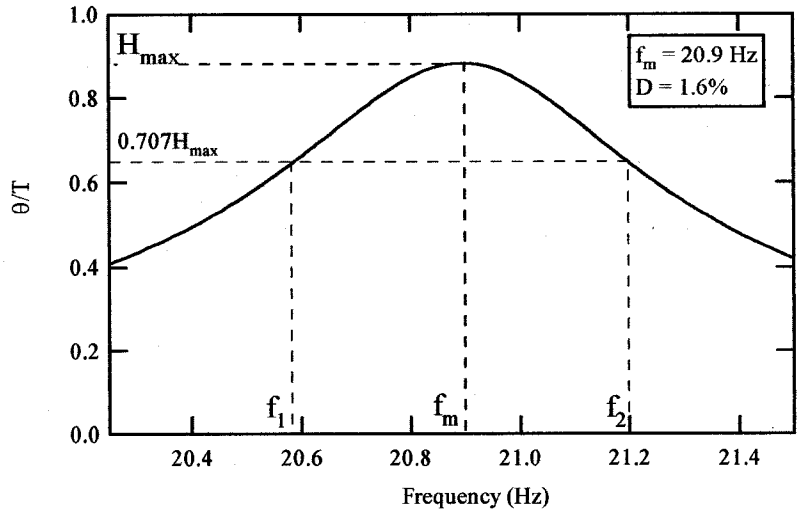

Figure 3.7 Typical response curve for soil from the RC test

Equation 3.15 is widely used to determine the damping ratio of soil in the resonant column test. It should be noted that the half power bandwidth method is based on the assumptions that D is small (less than 10%) and the response curve is symmetrical. However, when performing the resonant column test at high strain level, the response curve becomes distorted and is no longer has a symmetrical shape. Many researchers recommended using the free vibration decay method to evaluate damping of soil for high strain test (Kim 1991, Hwang 1997). Details regarding to the free vibration decay method are briefly described below.

Free vibration decay is the method used to determine damping utilizing the decay of vibration. One of the properties of viscous damping is that the magnitude of the decay of vibration of any two successive peaks is a constant ratio. The natural logarithm of two successive amplitude of motion is called the logarithmic decrement, δ expressed as:

$$\delta = \ln \frac{z_n}{z_{n+1}}, \tag{3.16}$$

where z_n and z_{n+1} = two successive peak amplitudes.

The ratio of peak amplitudes is given by:

$$\frac{z_n}{z_{n+1}} = \exp(f_n D \frac{2\pi}{f_m}). \tag{3.17}$$

Substitution of Equation 3.7 gives:

$$\delta = \frac{2\pi D}{\sqrt{1-D^2}}. \tag{3.18}$$

Therefore, Equation 3.18 can be used for calculating the material damping, D in the free vibration decay method. The weakness of the free vibration decay method is that there is an uncertainty in determining the associated strain level. Typically, the strain level is estimated from the first three cycles of the free vibration decay curve (Hwang 1997) and this method is used at higher strain level (> 0.01%) when the half power bandwidth is not applicable. A typical free vibration decay curve is shown in Figure 3.8.

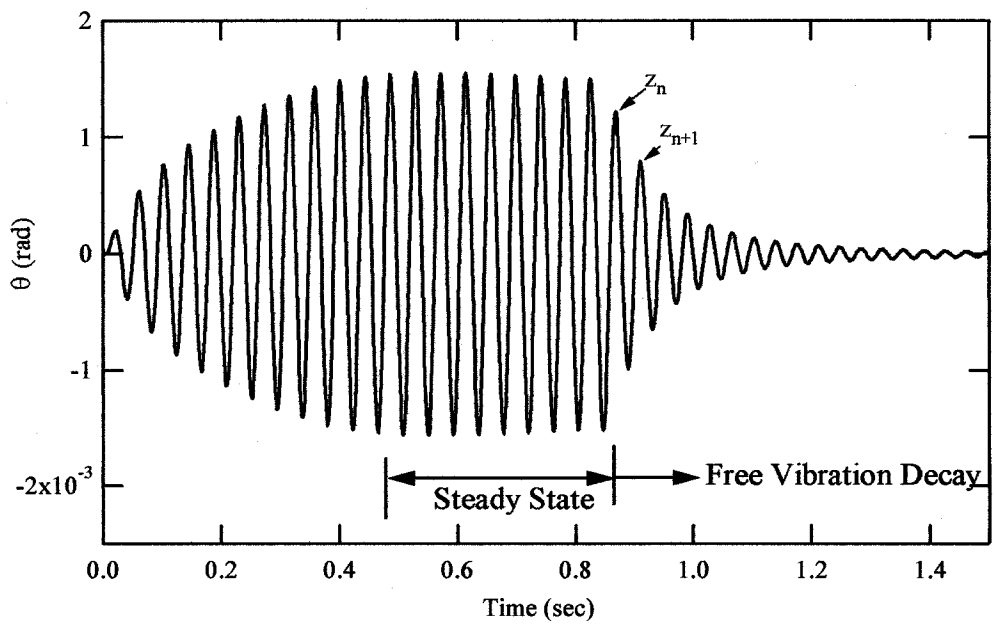

Figure 3.8 Typical free vibration decay curve for soil

3.4.2 The TS Test Analysis

In the TS test, torque is applied to soil specimen at a very low frequency where inertia is insignificant. Current flowing through the coils is measured and converted into torque using calibration factor. In this study, this calibration factor is called torque-current factor, k_i. More details on the measurement of the k_i value are included in Chapter 6. Rotation is measured by the proximitor system and calculated using a calibration factor presented in Chapter 4. The relationship between torque and rotation is then transformed into the stress-strain hysteresis loop as shown in Figure 3.9. As discussed in Chapter 2, the nonuniform stress-strain effect occurs in both the RC and TS tests. For TS test, the nonuniform stress-strain effect has an impact on the determination of both shear stress and shear strain. The equivalent radius approach (Kim 1991, Hwang 1997) has been used to calculate stress and strain that correspond to the measured torque and rotation. A more precise method called the stress integration approach will be presented in Chapter 8.

When the stress-strain (τ–γ) hysteresis loop as illustrated in Figure 3.9 is developed, shear modulus is simply calculated from the secant slope of any point on the loop. This secant modulus can be expressed as:

$$G = \frac{\tau}{\gamma}. \tag{3.19}$$

The damping in the torsional shear test is determined from the characteristics of the hysteresis loop. As described in Chapter 2, the damping is the ratio of the energy loss per cycle to the maximum stored energy. An example of hysteresis loop is illustrated in

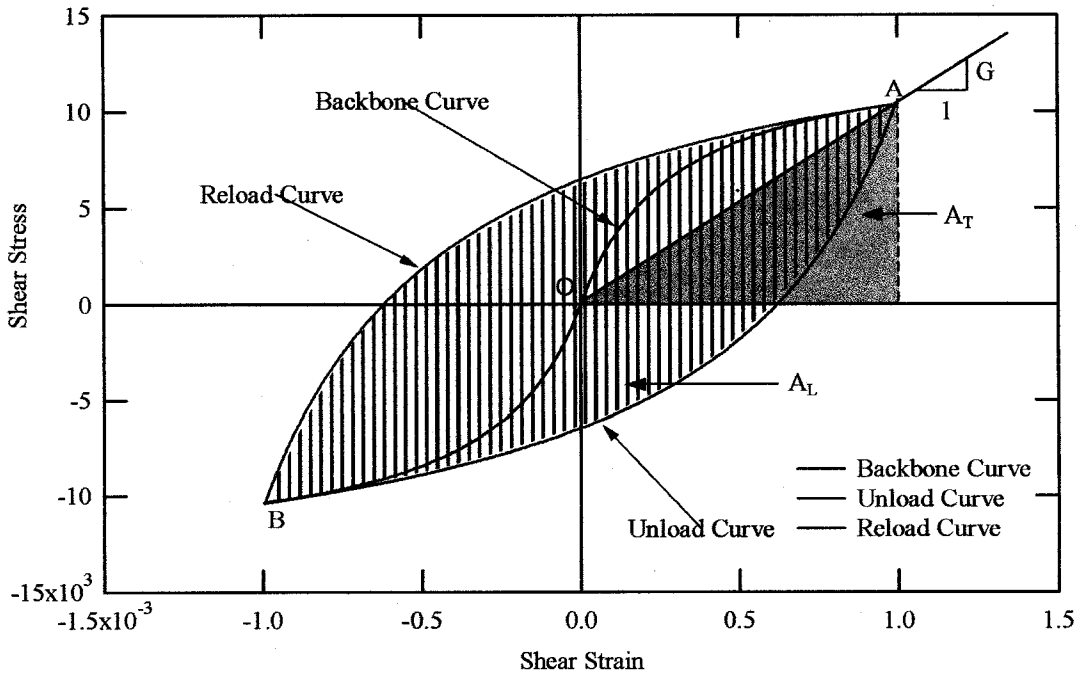

Figure 3.9 Hysteresis loop measured in the TS test

Figure 3.9. The area of triangle represents the maximum stored energy. The area of hysteresis loop represents the energy loss per cycle. The damping is then calculated from:

$$D = \frac{1}{4\pi}\frac{A_L}{A_T}, \tag{3.20}$$

where A_L = area of hysteresis loop, and

A_T = area of triangle.

It should be noted that damping could also be determined from torque-rotation (T-θ) hysteresis loop. The damping from T-θ relation is calculated using the same concept as the damping from τ–γ relation therefore Equation 3.20 is also applied in both cases. Differences between two methods are discussed in Chapter 8.

CHAPTER 4

DRIVE PLATE AND DEFORMATION SENSORS CALIBRATION

4.1 INTRODUCTION

Like any other laboratory testing equipment, the RC/TS equipment needs to be calibration prior to performing tests. This chapter presents the basic calibrations of the RC/TS equipment. Two basic calibrations are presented in this chapter. The first is the drive plate calibration to determine the mass polar moment of inertia of the drive plate. The second is the deformation sensors calibration to determine the calibration factor for each deformation sensor.

The mass polar moment of inertia of the drive plate is an important parameter in the analysis of RC tests. In this chapter, an experimental measurement was used to calibrate the polar moment of inertia of the drive plate. The calibration was performed for the USU drive plate and the drive plate No. 9 at The University of Texas at Austin (UT). Calibration of results for each drive plate are compared and discussed.

The calibration specimens are used to measure the polar moment of inertia of a drive plate. Details on the calibration specimens are also included in this chapter.

The finite element method was used for an analysis of nonrigid body motion of the USU drive plate. Results of this analysis are discussed and compared with the results from the calibration.

Deformation sensors are used for monitoring the torsional rotation and vertical deformation of soil specimens in the RC/TS apparatus. These sensors are proximitors, an

accelerometer, and a LVDT. In this study, the proximitors and the LVDT were calibration. The calibration factor of the accelerometer provided by the manufacturer was used in this study. The rotation measured from the proximitors and the accelerometer is compared and discussed.

4.2 CALIBRATION SPECIMENS

Calibration specimens were designed and built for the drive plate calibration and for measurement of electromagnetic properties of the drive system presented in Chapter 6. Requirements for the calibration specimens as well as their design and construction are presented.

The calibration specimens have three requirements; (1) the specimens can be tested repeatedly without changing properties, (2) each specimen is designed to have a specific resonant frequency, and (3) the specimens must have linear frequency independent stress-strain behavior. In this study, the frequency range of interest is from 0-200 Hz. Four metal specimens were designed to have resonant frequencies at about 14 Hz, 62 Hz, 128 Hz, and 188 Hz. Each specimen was custom fabricated at Civil and Environmental Engineering Department (CEE) machine shop, Utah State University.

The specimen with resonant frequency of 14 Hz was built from a solid steel rod. Figure 4.1a shows a drawing of this specimen. The top and bottom of the rod were rigidly welded to circular steel plates. There are four threaded holes at each top and bottom plates so the specimen could be screwed tightly to the drive plate and the bottom platen of RC/TS apparatus. Although the top plate is rigidly welded to the steel rod, the

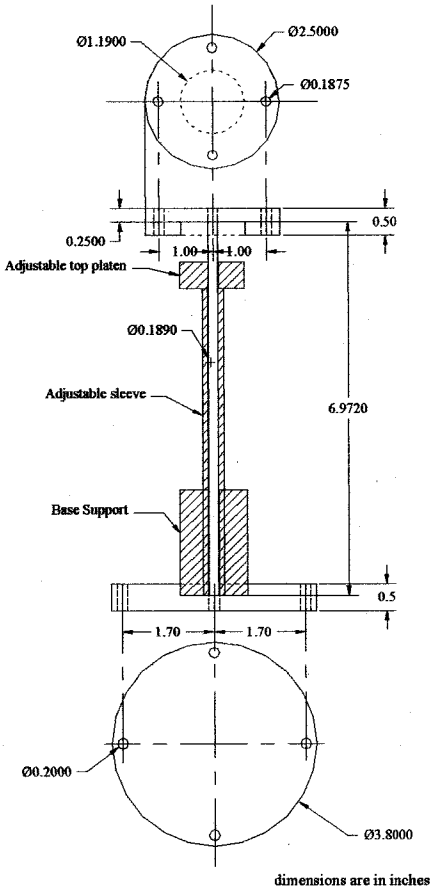

a)

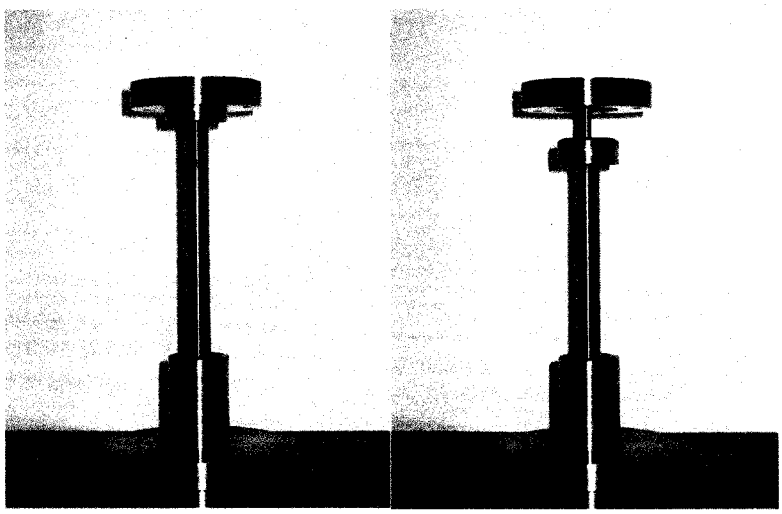

b)

Figure 4.1 Drawing and photo of 14-Hz calibration specimen

weld is relatively weak because the steel rod diameter is only 0.189 in. To protect the welded joints, and to prevent the rod from bending during set-up, a support system was built for this specimen. The supporting system was built from a hollow, steel, threaded rod with a top platen attached to it as shown in Figure 4.1a. This top platen can be adjusted up and down. During setup, the top platen is adjusted to be against the top plate of the specimen. The supporting system during setup is shown in left photograph of Figure 4.1b. Once the installation is finished the supporting top platen is lowered so it does not interfered with the specimen during testing. The photograph on the right in Figure 4.1b shows the specimen of 14 Hz in testing position.

The 62 Hz, 128 Hz, and 188 Hz calibration specimens were made from brass tube with different diameter as shown in Figures 4.2-4.4. The top and bottom plate of these specimens are built from circular brass plate connected to the tube by welding. There are four threaded screw holes at the top and bottom similar to the specimen of 14 Hz. Size and dimension of these specimens are presented in Figures 4.2b, 4.3b, and 4.4b.

For accuracy in determining the mass polar moment of inertia of the calibration specimens, each part was precisely machined in geometric shape and weighed before assembly. Dimensions were carefully measured. The mass polar moment of inertia of each part was calculated accounting for all screw holes. These values are presented in Table 4.1.

4.3 DRIVE PLATE CALIBRATION

As explained in Chapter 3, the analysis method for the RC test is based on the theory of wave propagation in a finite rod under the fixed-free conditions. In RC/TS

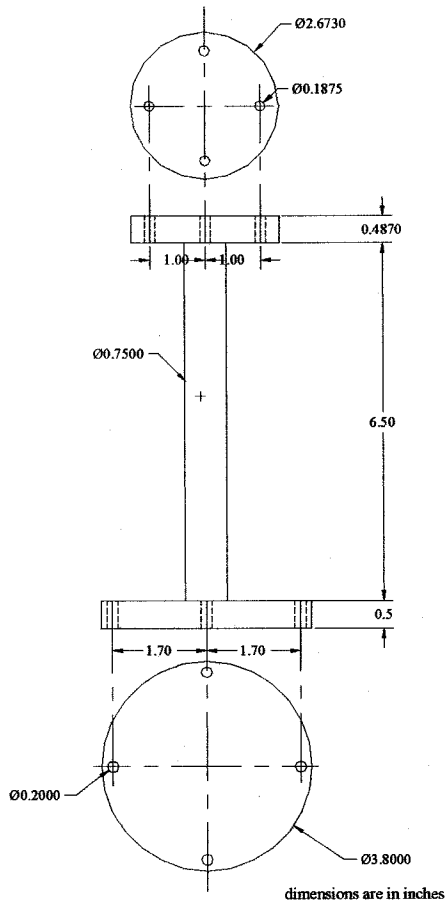

a)

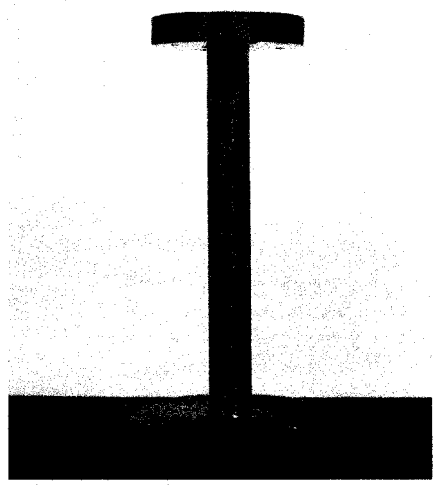

b)

Figure 4.2 Drawing and photo of 62-Hz calibration specimen

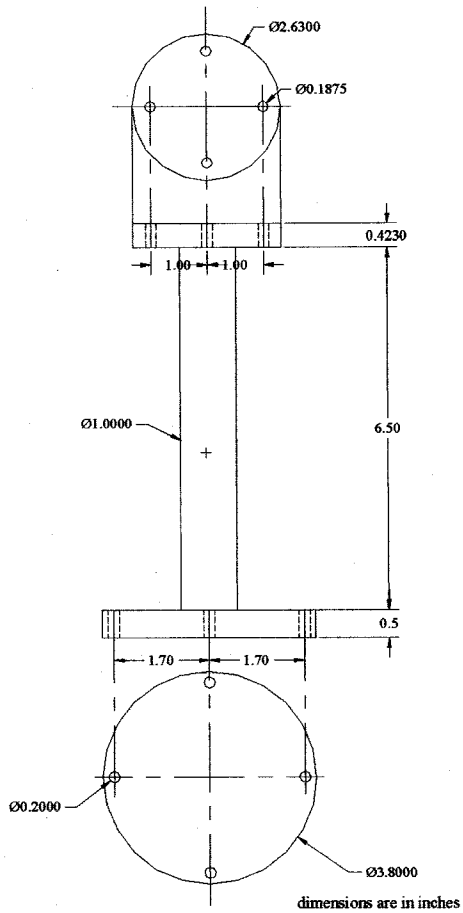

a)

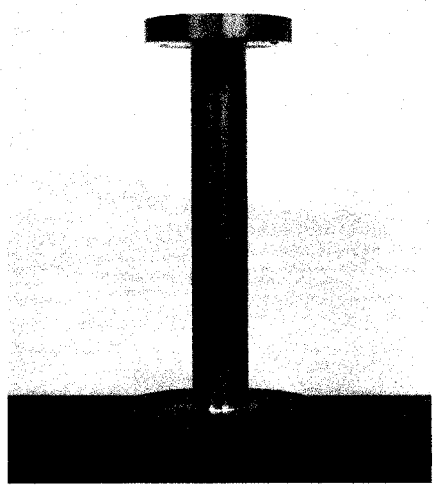

b)

Figure 4.3 Drawing and photo of 128-Hz calibration specimen

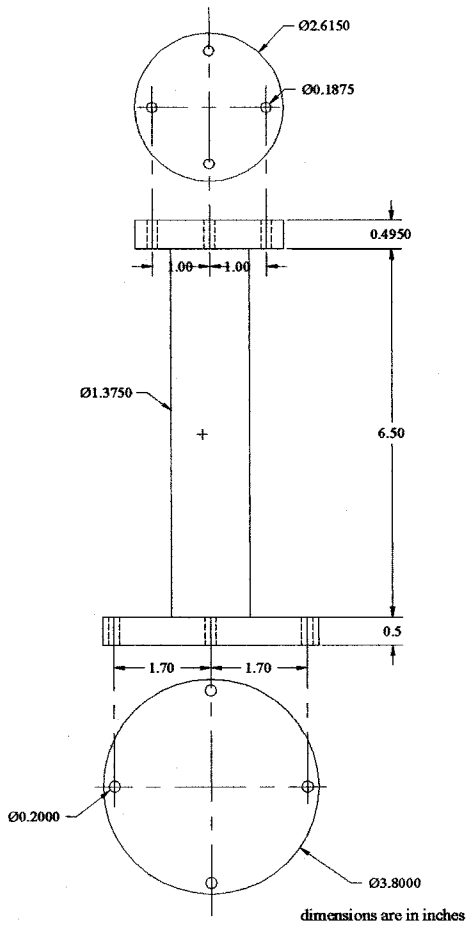

a)

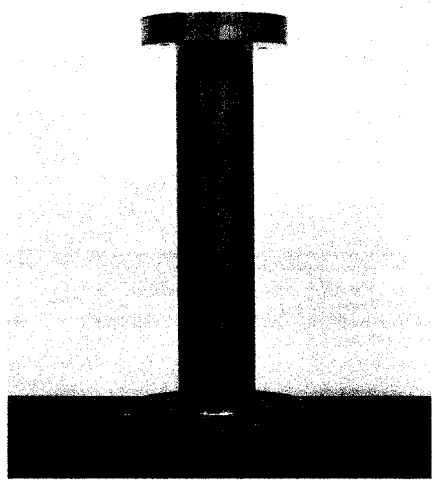

b)

Figure 4.4 Drawing and photo of 188-Hz calibration specimen

Table 4.1 Properties of Calibration Specimens

Specimen of Resonant Frequency (Hz)	Material	Density (lb/in^3)	Mass Polar Moment of Inertia ($lb\text{-}ft\text{-}sec^2$)	
			Rod or Tube (J)	Top Plate (J_t)
14	Steel	0.283	5.268E-8	1.121E-4
62	Brass	0.313	1.924E-6	1.661E-4
128	Brass	0.313	8.862E-6	1.361E-4
188	Brass	0.313	2.119E-5	1.548E-4

equipment, a soil column is fixed at the bottom and torque is applied at the top of specimen. The torque is applied to the specimen through the drive plate and top platen that are fixed to the top of the specimen. As a result, the top of soil specimen is not completely free because of the drive plate and top platen attached to it. This attachment becomes an added mass that exerts an inertial torque on top of soil specimen. Accounting for this inertial torque requires the mass polar moment of inertia of the top platen and drive plate. Therefore, it is necessary to carefully measure the mass polar moment of inertia of the added mass for the RC test.

The assembly at the top of the soil column in the RC/TS equipment consists of two different added masses. First the drive plate, which consists of four-armed drive plate with magnets and all of the equipment attached to it such as the accelerometer, the counter weight, the proximitor target, and screws. And, second the top platen, which is attached to the drive plate contacts with the top of soil column.

The mass polar moment of inertia of the top platen can be determined directly by calculation because it has a simple geometric shape. However, the shape of the drive plate is much more complex making a direct calculation for the polar moment of inertia impractical. Instead, the mass polar moment of inertia of the drive plate is determined experimentally. Method for this experimental determination is described below.

4.3.1 Drive Plate Calibration Method

One of the complications in using the RC/TS equipment is the back-electromotive force generated in the coil and magnet in the drive system. This is typically called back emf effect. The back emf induces a current in opposite direction to the applied current. The typical method of testing is using forced vibration, hence the coil circuit is closed, allowing the flow of back-emf induced current. This current affects the resonant frequency and damping of the system. More details regarding the back emf effect is presented in Chapters 5-7. For this study, the drive plate calibration method was modified to eliminate the back emf effect. Rather than performing the test using a closed drive circuit, an open drive coil circuit was employed. This allows no current to flow through the circuit, hence no back emf effect.

The electrical circuit for the open drive circuit test is shown in Figure 4.5. A fuse is connected between the voltage source and the drive system. Instead of driving the coil by applying a sinusoidal forcing function, the current is increased linearly resulting in increasing of torque on the drive plate. The current is increased until it blows the fuse, opening the coil circuit. The torque on the drive plate instantly decreases to zero, and the system freely oscillates at its resonant frequency without generating any back emf.

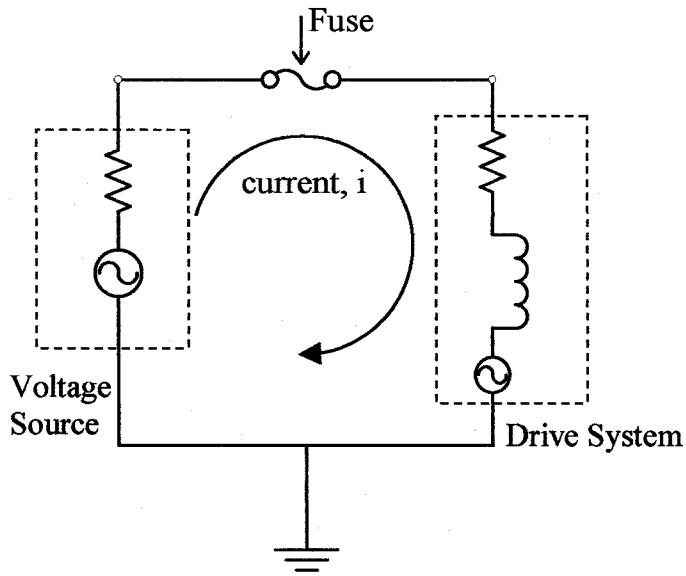

Figure 4.5 Electrical circuit for the open circuit drive plate calibration

The drive plate calibration system can be modeled as a single-degree-of-freedom, spring-mass system. The calibration specimen represents the massless spring with torsional spring stiffness, K_θ, and the top plate of calibration specimen and the drive plate represent the mass in the system. Additional analyses were performed accounting for the mass of the calibration specimen. These yielded nearly identical to the simpler single-degree-of-freedom assumption. Therefore, only the single-degree-of-freedom results are presented.

In torsional mode, the natural frequency, f_n can be expressed as:

$$f_n = \frac{1}{2\pi}\sqrt{\frac{K_\theta}{J_o + J_t}}, \tag{4.1}$$

where K_θ = torsional spring stiffness of the calibration specimen,

J_o = mass polar moment of inertia of the drive plate and the assembly, and

J_t = mass polar moment of inertial of the top plate of the calibration specimen.

In free vibration, the resonant frequency, f_m is:

$$f_m = f_n\sqrt{1-D^2}\,, \tag{4.2}$$

where D = damping ratio of calibration specimen.

Substitution of Equation 4.2 into Equation 4.1 gives:

$$f_m = \frac{1}{2\pi}\sqrt{\frac{K_\theta}{J_o + J_t}}\sqrt{1-D^2}\,. \tag{4.3}$$

The K_θ and J_o are two unknowns presented in Equation 4.3. Solving for these unknowns requires at least one more equation. To obtain additional equations, the test was repeated on the same calibration specimen with additional masses of known mass polar moment of inertia is fixed on top of the drive plate as shown in Figure 4.6. The resonant frequency, and damping, D is then measured and Equation 4.3 is modified to become:

$$f_m = \frac{1}{2\pi}\sqrt{\frac{K_\theta}{J_o + J_t + \Delta J}}\sqrt{1-D^2}\,, \tag{4.4}$$

where ΔJ = mass polar moment of inertia of an added mass.

With two equations and two unknowns, the value K_θ and J_o can be calculated from Equations 4.3 and 4.4.

In this study, three added masses were built for the drive plate calibration. They are steel circular disks with different thickness as shown in Figure 4.7. Dimension and density of the added masses were carefully determined. The polar moment of inertia of the added masses were calculated and tabulated in Table 4.2. The calibration was

Figure 4.6 Test setup for the drive plate calibration with added mass

performed using the four calibration specimens described in the previous section. Tests without added mass and tests with added masses were performed on each specimen. Therefore, there were four equations to solve for K_θ and J_o. These equations are shown below:

$$f_{mo} = \frac{1}{2\pi}\sqrt{\frac{K_\theta}{J_o + J_t}}\sqrt{1 - D_o^{\,2}}, \tag{4.5}$$

$$f_{m1} = \frac{1}{2\pi}\sqrt{\frac{K_\theta}{J_o + J_t + \Delta J_1}}\sqrt{1 - D_1^2}, \tag{4.6}$$

$$f_{m2} = \frac{1}{2\pi}\sqrt{\frac{K_\theta}{J_o + J_t + \Delta J_2}}\sqrt{1 - D_2^2}, \tag{4.7}$$

$$f_{m3} = \frac{1}{2\pi}\sqrt{\frac{K_\theta}{J_o + J_t + \Delta J_3}}\sqrt{1 - D_3^2}, \tag{4.8}$$

where $f_{m0,1,2,3}$ = measured resonant frequency of the calibration specimen for the test with no added mass, mass no.1, 2, 3, respectively,

$D_{0,1,2,3}$ = measured damping ratio of the calibration specimen for the test with no added mass, mass no. 1, 2, 3, respectively, and

$\Delta J_{1,2,3}$ = polar moment of inertia of the added mass no. 1, 2, 3, respectively.

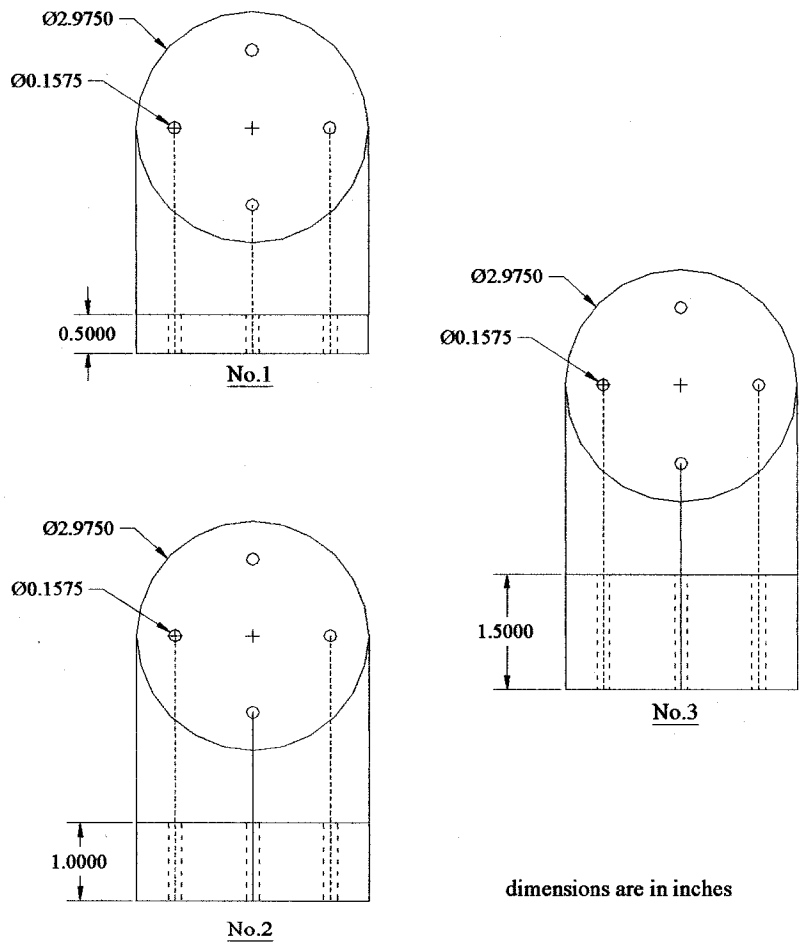

Figure 4.7 Drawing for added masses for the drive plate calibration

Table 4.2 Properties of Added Masses for Drive Plate Calibration

Added Mass No.	Material	Density (lb/in^3)	Polar Moment of Inertia, ΔJ ($lb\text{-}ft\text{-}sec^2$)
1	Steel	0.283	2.384E-4
2	Steel	0.283	4.739E-4
3	Steel	0.283	7.077E-4

4.3.2 Drive Plate Calibration Results

Solutions to Equations 4.5-4.8 give six solutions for values of K_θ and J_o for each calibration specimen. Table 4.3 presents the measured resonant frequency and damping of the system from each test. The damping ratio is very small because there is no additional damping from the back emf effect.

Solutions for K_θ and J_o can be solved graphically by plotting all possible values of J_o versus K_θ for each test. These plots are shown in Figure 4.8. The intersection point represents a solution of two equations and each solution has an average resonant frequency for the two equations associated with it. All of the solutions for values of J_o versus K_θ are presented in Table 4.4. It can be seen that solutions based upon tests with large differences in resonant frequency result in outlying values of J_o. This deviation is more significant in the stiffest specimen because it has the most difference in resonant frequency between two tests. An average value of K_θ was calculated from the average of the three of the closest resonant frequencies and this value was used to determine electromagnetic properties presented in Chapter 6.

Table 4.3 Drive Plate Calibration Results

Added Mass No.[1]	14-Hz Specimen		61-Hz Specimen		128-Hz Specimen		188-Hz Specimen	
	f_m (Hz)	D (%)	f_m (Hz)	D (%)	f_m (Hz)	D (%)	f_m (Hz)	D (%)
No Added Mass	14.314	0.020	61.861	0.018	128.418	0.010	188.079	0.023
1	13.603	0.013	58.902	0.009	122.718	0.008	117.564	0.019
2	12.988	0.020	56.317	0.008	180.775	0.007	173.917	0.017
3	12.463	0.011	54.064	0.013	113.029	0.007	167.797	0.015

Note: 1. Top plate is considered as part of specimen

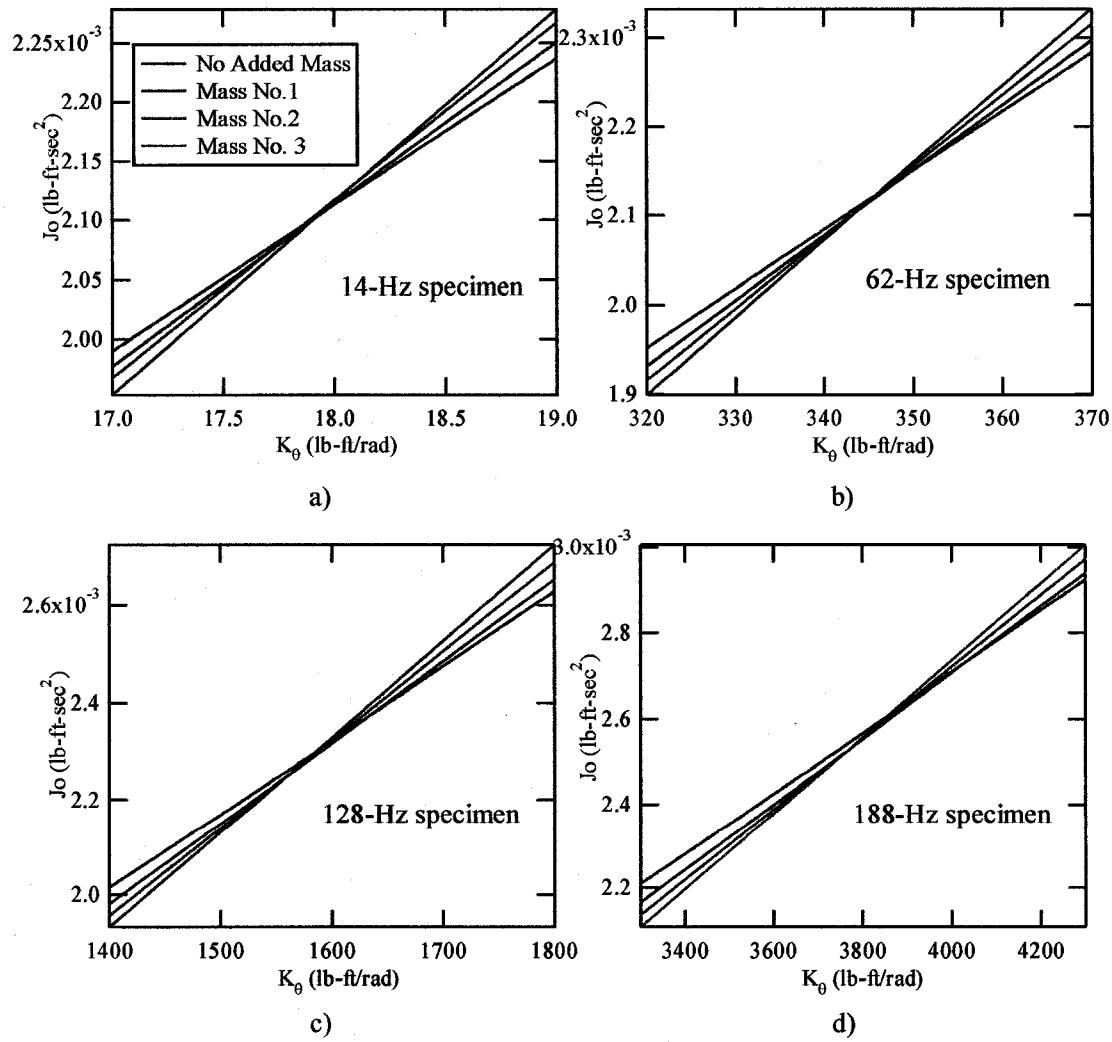

Figure 4.8 Solutions for K_θ and J_o for the calibration specimens

Table 4.4 All Solutions for Values of K_θ and J_o Obtained from Drive Plate Calibration

Specimen	Average Resonant Frequency, f_m (Hz)	Polar Moment of Inertia of Drive Plate, J_o (lb-ft-sec^2)	Torsional Stiffness, K_θ (lb-ft/rad)	Average K_θ[1] (lb-ft/rad)
14 Hz	12.725	2.132E-3	18.102	**17.942**
	13.033	2.103E-3	17.919	
	13.295	2.078E-3	17.740	
	13.388	2.105E-3	17.936	
	13.651	2.095E-3	17.856	
	13.958	2.110E-3	17.970	
62 Hz	55.208	2.109E-3	344.22	**343.80**
	56.493	2.106E-3	343.80	
	57.617	2.102E-3	343.38	
	57.972	2.123E-3	345.78	
	59.097	2.128E-3	346.55	
	60.382	2.149E-3	349.74	
128 Hz	115.305	2.247E-3	1558.8	**1560.6**
	117.88	2.250E-3	1560.6	
	120.143	2.253E-3	1562.4	
	120.730	2.297E-3	1584.2	
	122.993	2.317E-3	1597.1	
	125.568	2.372E-3	1632.9	
188 Hz	170.857	2.520E-3	3759.6	**3768.53**
	174.296	2.528E-3	3768.4	
	177.346	2.535E-3	3777.6	
	177.938	2.606E-3	3855.2	
	180.998	2.641E-3	3904.4	
	184.427	2.737E-3	4038.4	

Note: 1. An Average K_θ is calculated from three of the closest values represented by the values in shading area

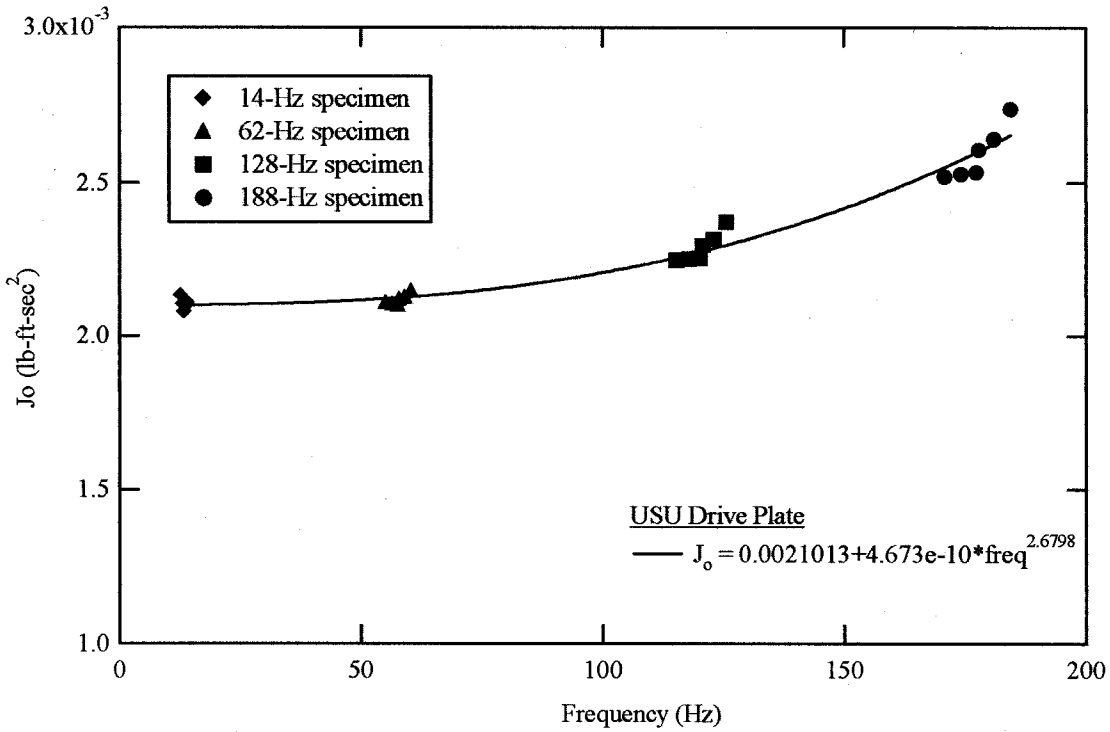

Figure 4.9 Variation of J_o with frequency

From Table 4.4, the solutions of J_o for pair of tests are plotted versus the average resonant frequencies in Figure 4.9. Results show a trend of increasing J_o with frequency. The equation presented in Figure 4.9 represents the average trend of the data. The increase of J_o is about 28% from 14 Hz to 188 Hz. The increasing of J_o with frequency found in this study will cause an error of the calculated shear wave velocity, V_s, if it is not accounted for. If too low a value of J_o is used for calculating V_s in a high frequency test, the error can be as high as 12%. Therefore, the increasing J_o should be taken into account.

Theoretically, J_o of the drive system should be independent of frequency if the drive plate moves as a rigid body. This assumption may not be realistic.

4.3.3 Finite Element Analysis of the Drive Plate

Increasing values of J_0 of the drive plate with increasing frequency may be due to non-rigid body motion of the drive plate. As described in Chapter 3, the drive plate consists of four aluminum arms plate with a magnet attached to each arm. The non-rigid body motion of the drive plate possibly occurs at the connection between the arm and each magnet. To verify this assumption, finite element analysis, using a program called RISA –2D, was performed to prove this assumption. The drive plate and boundary condition were modeled to replicate the experiment setup of the drive plate calibration. The stiffness of the connection between the drive plate and magnet was investigated.

The shape and dimensions of drive plate were modeled with a finite element meshes were generated using rectangular plate elements as shown in Figure 4.10. Material properties of drive plate and magnet are those of aluminum and steel, respectively. The calibration specimen was modeled as four springs. Each spring rotated freely in x and y direction and each of them has stiffness of one fourth of the stiffness of the calibration specimen. The springs were attached to the drive plate at position of screw hole where the drive plate is fixed on top of the calibration specimen. The accelerometer and the counter weight were also modeled as a round bar with steel material properties.

The connection between the aluminum plate and magnet was assumed to cause the non-rigid body motion. For the RC/TS equipment used at USU, the magnet is connected to the drive plate as shown in Figure 4.11. The steel rod is epoxied into the magnet and connected to the drive plate with a setscrew. In the finite element analysis, the connection was modeled using very thin plate element. The stiffness for this

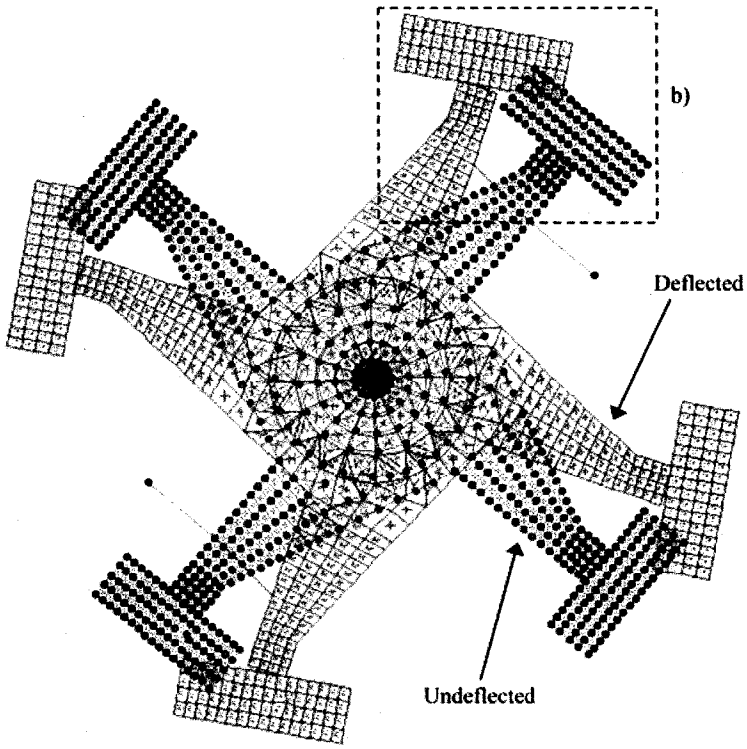

a)

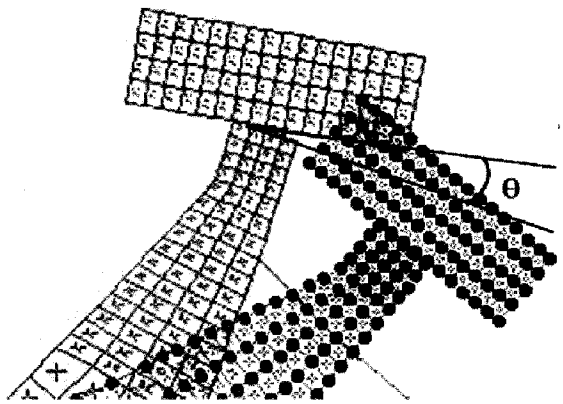

b)

Figure 4.10 Finite element analysis results of the drive plate (exaggerated deflection)

connection was adjusted literately in the analysis until the finite element results match with the experimental results. The finite element analysis was performed with different spring stiffness representing each calibration specimen. The best match value of stiffness for this connection was found to be equal to about 220 ksi. This value is much lower than the stiffness of the aluminum plate which is about 10^4 ksi. Results of the resonant frequency and calculated value of J_o are presented in Table 4.5.

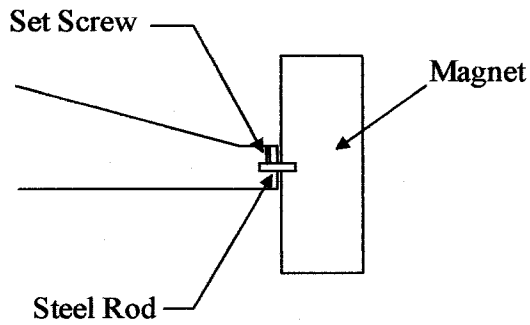

Note: Not To Scale

Figure 4.11 Connection of the drive plate and magnet

Table 4.5 Results of the Finite Element Analysis of the Drive Plate

Specimen	f_m for FEM (Hz))	Polar Moment of Inertia of Drive Plate, J_o (lb-ft-sec^2)
14 Hz	14.104	2.173E-3
61 Hz	61.374	2.146E-3
128 Hz	128.971	2.240E-3
188 Hz	187.891	2.549E-3

In the finite element analysis, a deflection was observed at the connection between the magnet and the drive plate. As shown in Figure 4.10b, the magnet tends to rotate independently with the drive plate and the rotation angle was observed to be larger at higher frequencies. At higher frequencies, the movement of the drive plate and the magnets system no longer behave as a rigid body.

The calculated values of J_o from the finite element analysis are plotted along with with the experimental results shown in Figure 4.12. The agreement between results from both methods verifies that the non-rigid body motion of the drive plate causes increasing J_o with frequency.

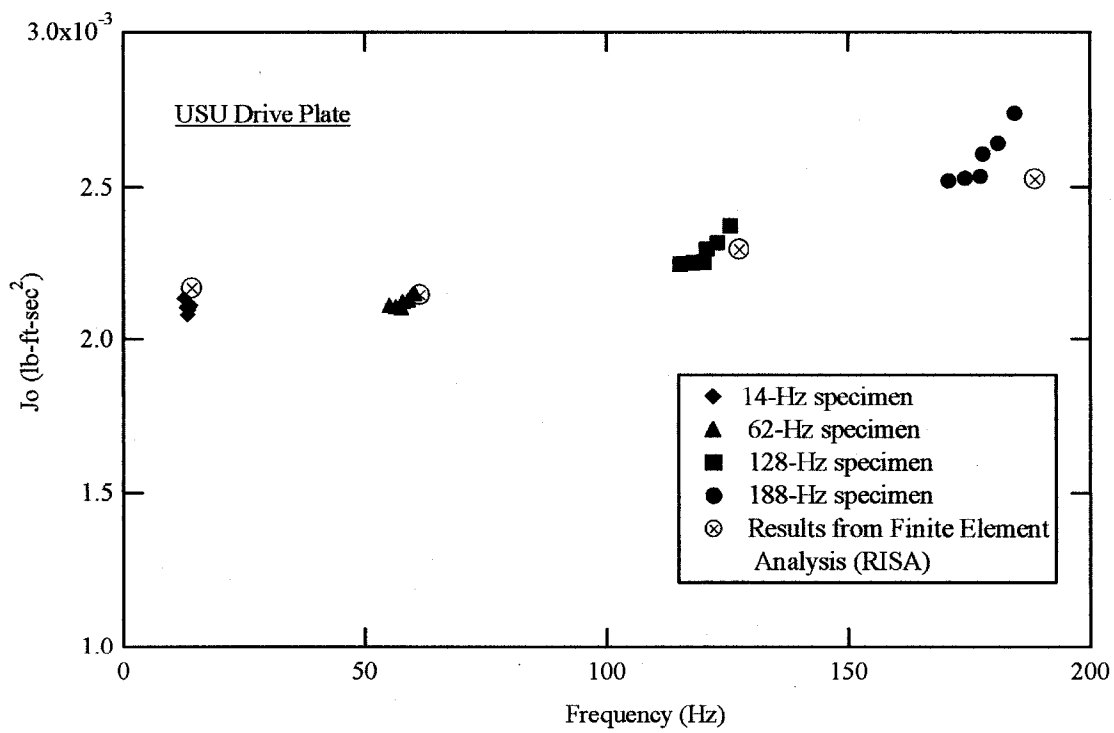

Figure 4.12 Comparison of results from the experiment and the finite element analysis for the drive plate calibration

It should be noted that the results of this analysis apply only to the USU drive plate. Other RC/TS equipment may behave differently depending on the type of connection between the magnet and drive plate.

4.3.4 Comparison of Drive Plate Calibration of the USU and UT Drive Plate

To investigate the effect of frequency on the polar moment of inertia for other drive plates, the same calibration method was performed using the same calibration specimens using drive plate No. 9 of The University of Texas at Austin (UT). The comparison between the USU and UT drive plate calibration is shown in Figure 4.13.

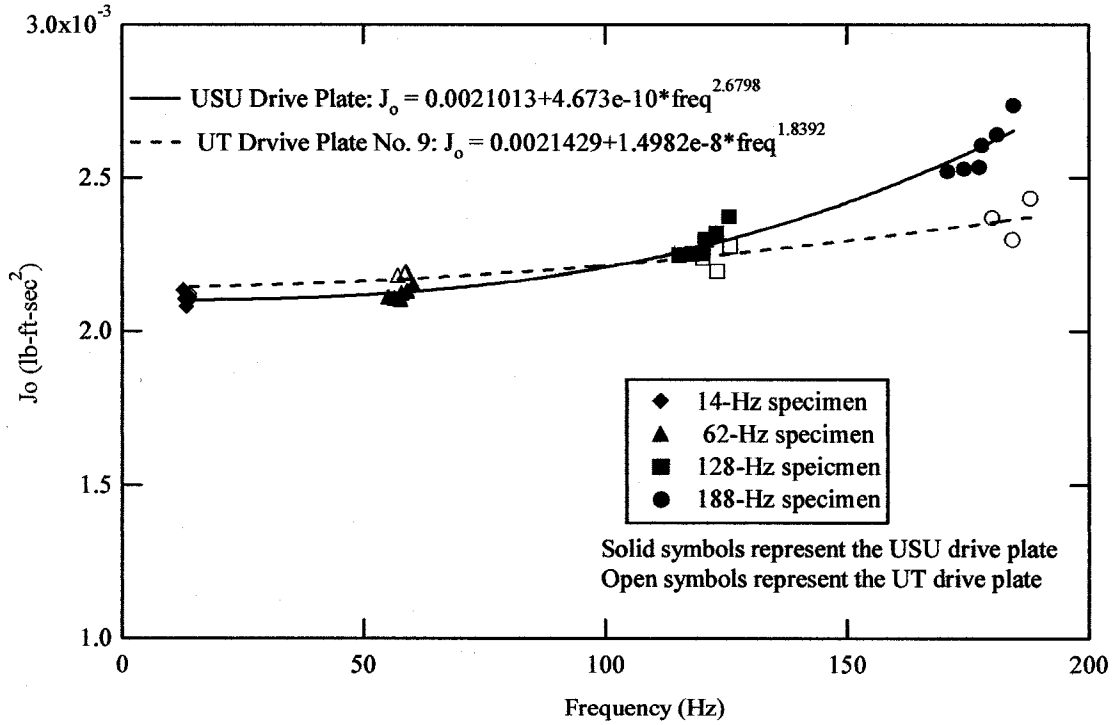

Figure 4.13 Comparison of the drive plate calibration for the USU and UT drive plate

Only a slight increase in J_0 with increasing frequency was observed in the UT drive plate. The error in calculated shear wave velocity due to the increasing of J_0 with frequency for the UT drive plate would be less than 5%.

A physical difference between the two drive plates was observed at the connection between the drive plate and the magnet. The USU drive plate uses a steel rod and a set screw to connect the magnet to the drive plate. Figure 4.14 shows the connection of the USU drive plate. The UT drive plate is connected to the magnet using an adhesive as shown in Figure 4.15. The difference in connection method explains the difference in behavior of these two drive plates.

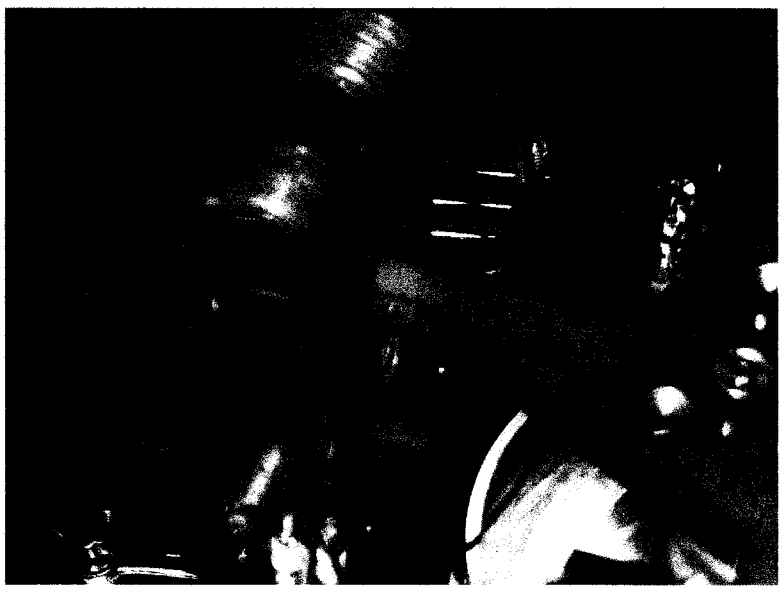

Figure 4.14 Photo of drive plate and magnet connection for the USU drive plate

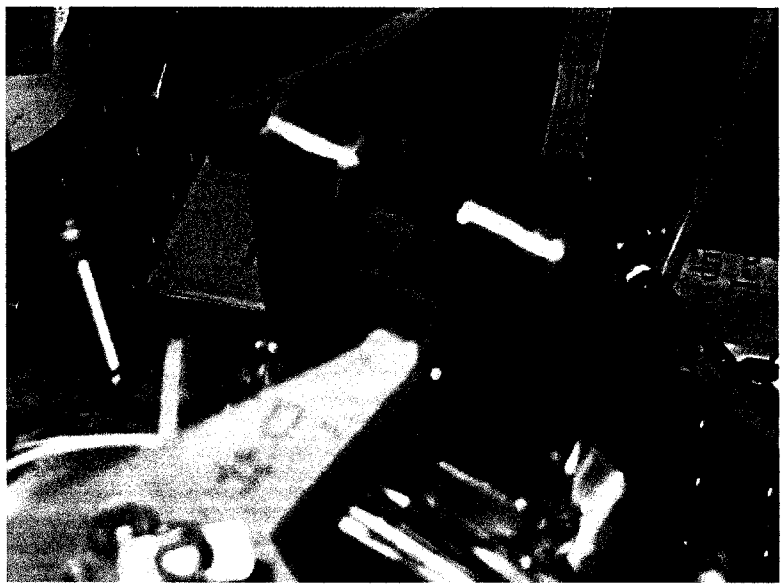

Figure 4.15 Photo of drive plate and magnet connection for the UT drive plate No. 9

4.4 DEFORMATION SENSORS CALIBRATION

4.4.1 Proximitor Calibration

The proximitors are mainly used to measure the rotation at low frequency for the TS test. The proximitor system for RC/TS equipment consists of two proximitors and targets. The proximitor system is a non-contacting measurement. The proximitor probe generates a voltage proportional to the distance between the probe and the target. Although there is a calibration factor provided by the manufacturer, the calibration is required because the calibration factor and linear range vary with the target material.

In this study, the proximitor calibration was performed using a milling machine to obtain an accurate measurement of the gap between the proximitor and target. The proximitor was mounted to the machine table and the target was fixed to the mill head.

The proximitor output voltage was measured at 5 mils (0.005 in) intervals as the mill head was moved away from the table.

The results of the proximitor calibrations are presented in Figure 4.16. The average linear range for the two proximitors is about 0.085 in. Hence, the proximitors can measure strain levels up to about 1.5% for soil specimens with a 1:2 (diameter: length) aspect ratio. The slopes of the plots for two proximitors and the average value are also shown in Figure 4.16.

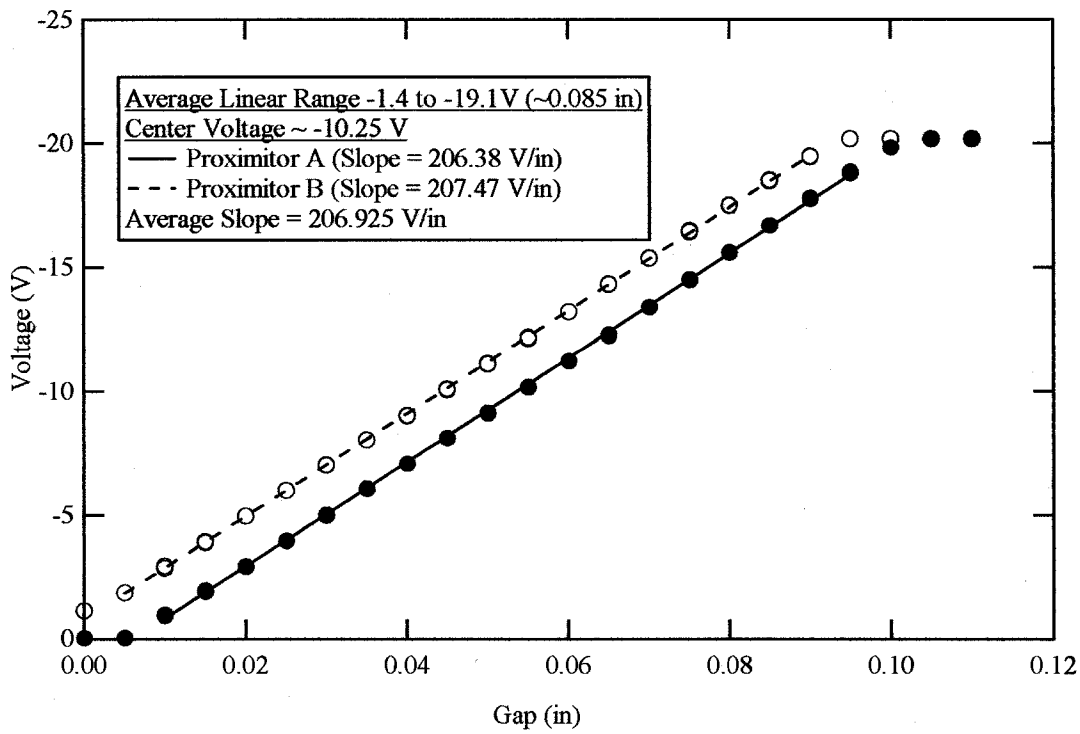

Figure 4.16 Results for the proximitors calibration

To confirm the measured proximitor calibration factors, swept sine test was performed on the 14 Hz calibration specimen. A constant amplitude torque was applied to the specimen over a frequency range of 0 to 155 Hz. The resulting rotation was then measured with both the proximitors and the accelerometer. Using the accelerometer calibration factor supplied by the manufacturer, a proximitor calibration factor was calculated. This calibration factor is plotted versus frequency in Figure 4.17.

As seen in Figure 4.17, the results were noisy at low frequencies because the accelerometer output is very low at low frequencies. At higher frequencies, the plot is smoother and the calculated calibration factor is constant. An average value for the calculated proximitor calibration factor of 215.02 V/in was obtained from the best quality measurement frequency band of 50-120 Hz as shown in Figure 4.17. This value is about 4% higher than the measured value of 206.925 V/in from the calibration presented previously.

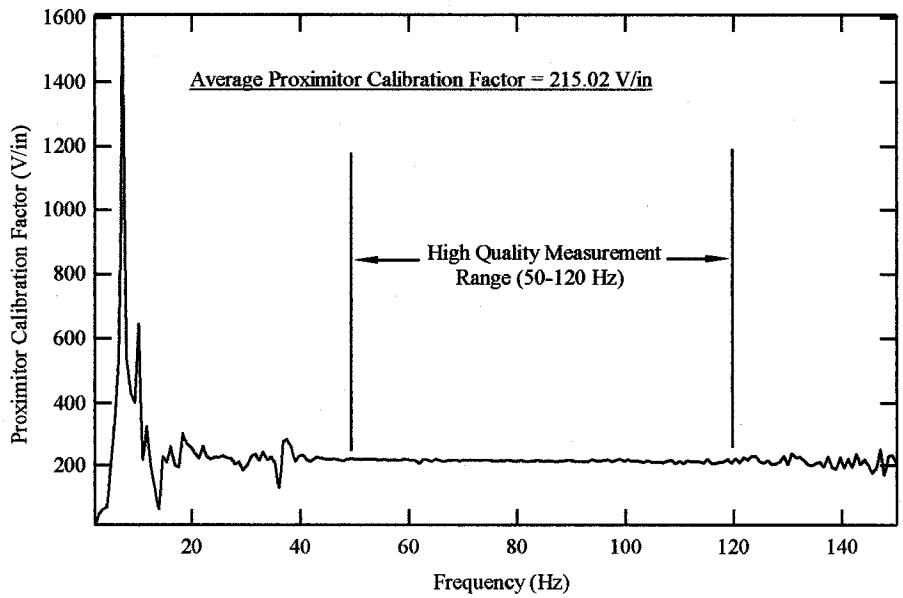

Figure 4.17 Proximitor calibration factor calculated from rotation using accelerometer

The difference of the proximitor calibration factors from both methods is as expected. The proximitor calibration on the milling machine is based on the assumption that the proximitor probe and target are perfectly parallel. In the actual measurement, the specimen is deformed in torsion, therefore, the target is rotated and no longer paralleled to the proximitor probe. An improvement for this method is to measure the output voltage with the rotation angle. However, this requires an accurate measurement of very small rotational angle. In this study, the proximitor calibration factor determined from the accelerometer measurement is considered more accurate. Therefore, the proximitor calibration factor of 215.02 V/in (0.003322 rad/V) is used.

4.4.2 Linear Voltage Displacement Transducer (LVDT) Calibration

The LVDT used in this study is Schaevitz Model HR500, which can measure vertical displacements up to one inch. The LVDT consists of two parts: the transformer, and the core. The core is inserted inside the transformer and the LVDT circuitry outputs a voltage proportional to the core position in the transformer. In RC/TS equipment, the steel rod is threaded to the core and positioned at the center of the drive plate.

As in the proximitor calibration, the milling machine was used for the LVDT calibration. The core was mounted to the mill head and the housing was mounted to the machine table. The output voltage at 5 mils (0.005 in) intervals was measured as the table was move away from the mill head. The resulting calibration is plotted in Figure 4.18. The line represents the best least square fit to the data. The calibration factor for LVDT used for this study is 0.151256 in/V.

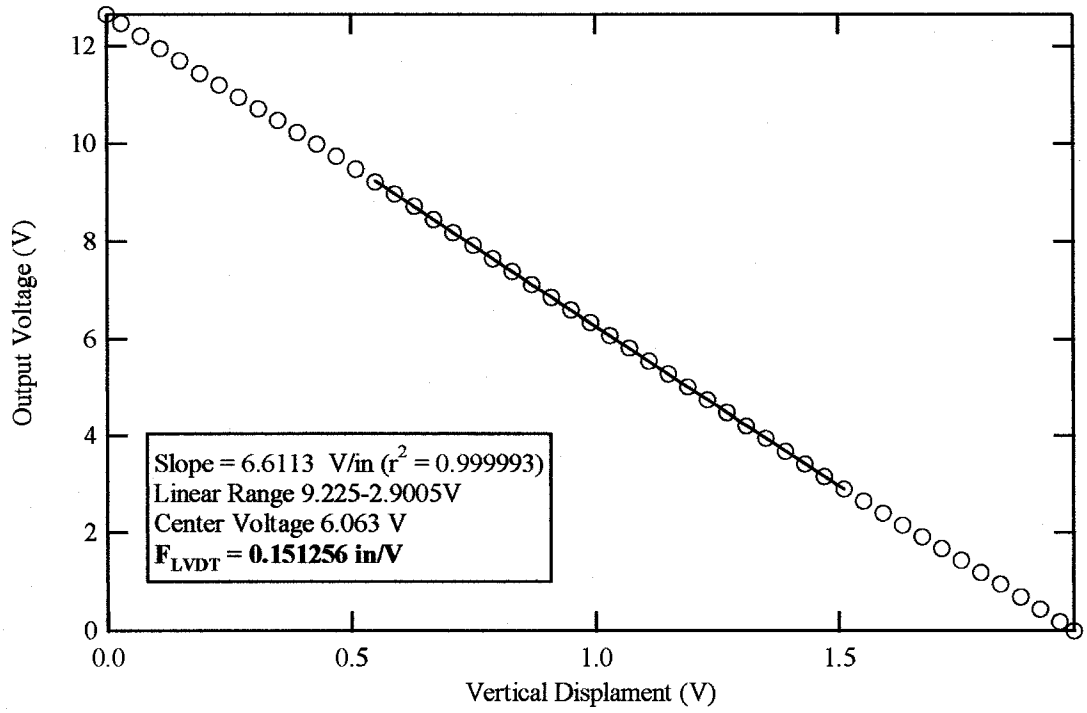

Figure 4.18 Results for the LVDT calibration

CHAPTER 5

ELECTROMAGNETIC MODEL DEVELOPMENT

5.1 INTRODUCTION

This chapter presents the basic concepts of electromagnetism that describe how torque is generated in the RC/TS drive system. These same basic concepts also explain how back emf effects RC/TS measurements. These back emf effects are quantified.

Once the back emf problem has been identified, an electromagnetic model is developed to mathematically describe the RC/TS drive system. This model can be used to describe, predict, and correct for the back emf effect is the RC/TS tests. An approach for using this model to correct RC/TS measurements is presented.

5.2 DRIVE SYSTEM IN THE RC/TS EQUIPMENT

Torque in the RC/TS drive system is generated from reaction force between coils and magnets. As shown in Figure 5.1, each of the four arms of the RC/TS drive plate is attached to a magnet. A coil encircles each end of the magnet. The eight coils are in series with the coils at either end of magnet wound in opposite directions. When energized, the coils generate magnetic fields. These magnetic fields interact with the fields from the magnets to generate forces of attraction or repulsion. The torque is transmitted from the drive plate through the top platen to the top of soil specimen. The magnitude and direction of force is quantified in next section.

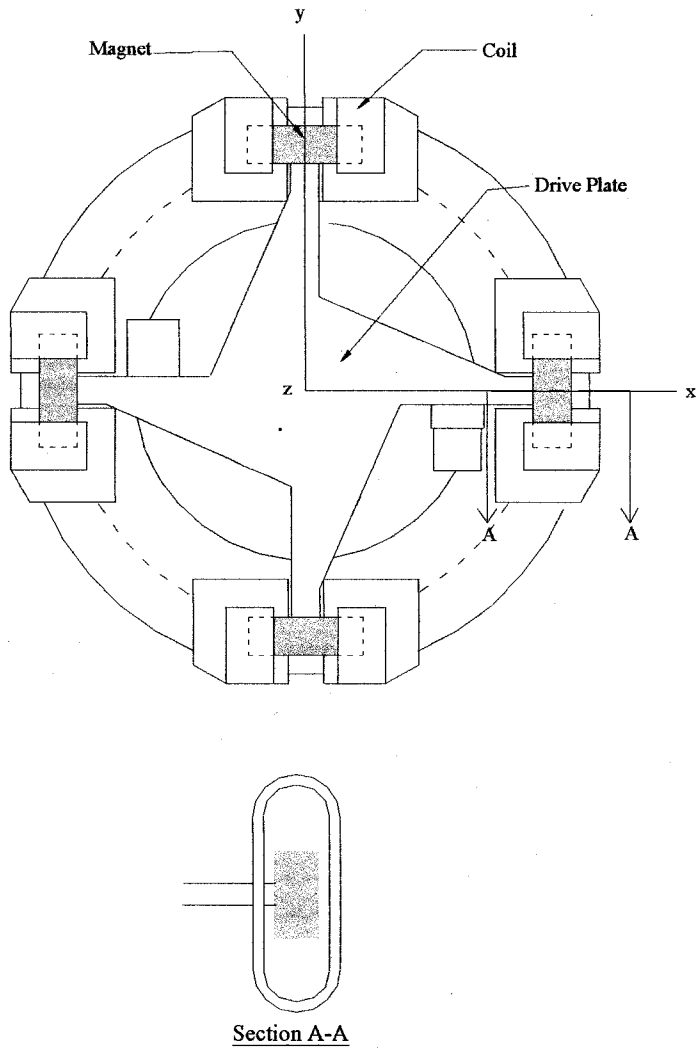

Figure 5.1 Drive system in the RC/TS equipment

5.3 BASIC MAGNETISM

Understanding the torque created in the RC/TS drive system requires knowledge of the concept of magnetism (Halliday and Resnick 1981) including magnetic fields, magnetic forces and electromotive forces. These concepts are presented in following sections, with specific application to the RC/TS drive system.

5.3.1 Magnetic Field

When a current flows through a wire it creates the magnetic field in the direction given by the right hand rule. Ampere's law is used to determine the strength of this magnetic field:

$$\oint \mathrm{Bdl} = \mu_0 i, \tag{5.1}$$

where B = magnetic field (tesla = 10^4 Gauss),

l = length of the wire (m),

i = current in the wire(A), and

μ_o = permeability constant = $4\pi \times 10^{-7}$ (tesla-m/A).

Equation 5.1 can be applied to a coil, which is a long wire wound into loops. Figure 5.2 shows the lines of the magnetic field in a loosely wound coil. The magnetic fields tend to cancel each other between the wires. At points inside of the coil and far from the coil, the magnetic field is parallel to the axis of the coil. For the case of coil with tightly packed wires, the coil becomes a cylindrical current sheet. The right end, from which the magnetic lines emerge, behaves like the north pole of a magnet and left end behaves like the south pole of a magnet, as shown in Figure 5.3. Ampere's law applies to a coil is:

$$B = N\mu_0 i, \tag{5.2}$$

where N is the number of loops.

An additional term that needs to be defined is the magnetic flux, Φ_B. The magnetic flux is defined as the number of the magnetic lines that pass through a given surface, S and it is expressed as:

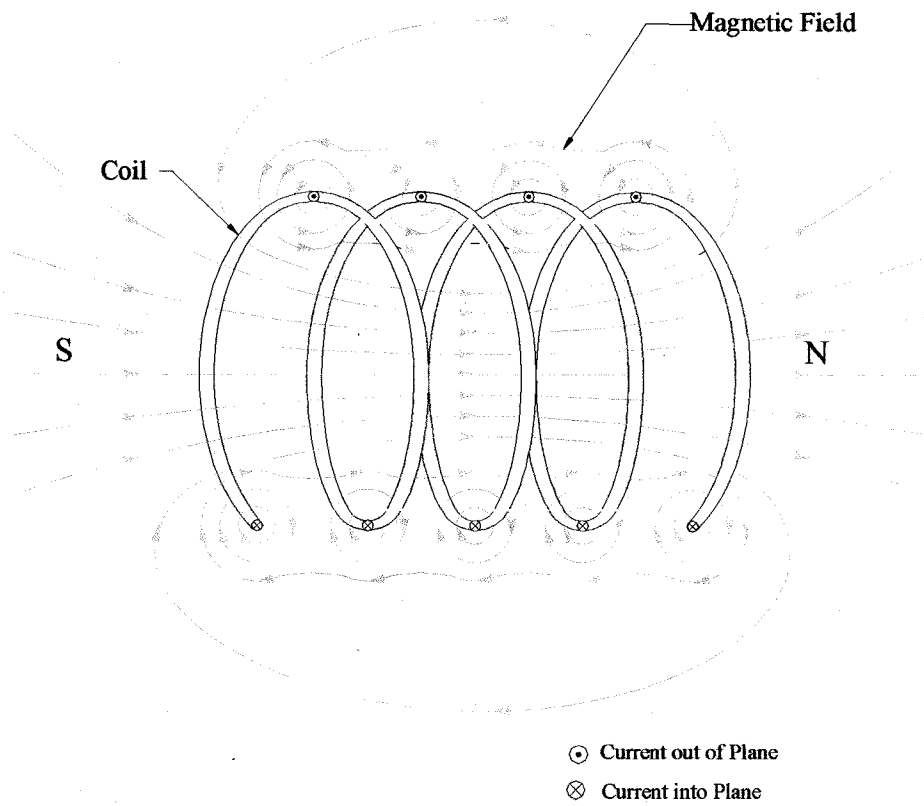

Figure 5.2 Magnetic field of a loosely wound coil

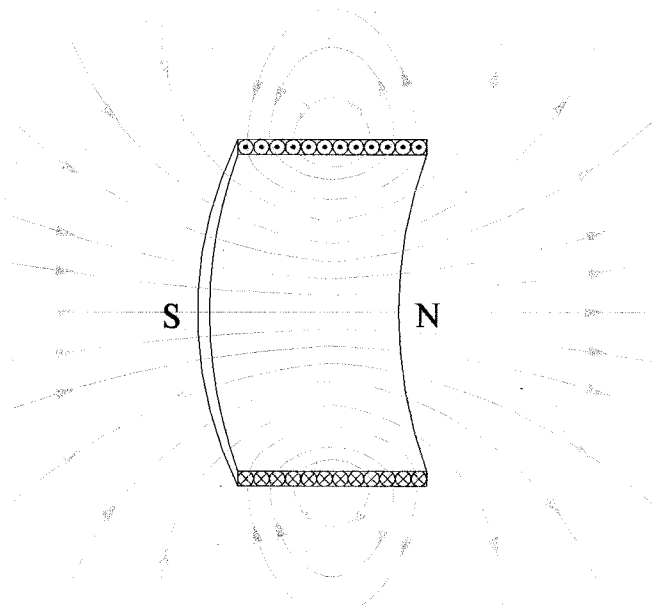

Figure 5.3 Magnetic field of a coil of finite length

$$\Phi_B = \int B \cdot dS. \tag{5.3}$$

The magnetic flux has units of tesla-m^2 or weber (Wb). If the magnetic field is constant, and at right angles to all point on a planar surface of area, A, then Φ_B becomes:

$$\Phi_B = BA = Blx, \tag{5.4}$$

where l = length of the coil loop, and

x = width of the coil loop.

A coil carrying currents behaves like a permanent magnet with a north pole at one end and a south pole at the other end. A permanent magnet can be modeled as an identically shaped coil that has an equivalent surface current flowing around it. Figure 5.4 shows the current loops on the cross section of the permanent magnet. In the interior of a magnet, the currents are in opposite directions and cancel each other, leaving the net current loop at the surface as shown in Figure 5.4. Although these currents are imaginary, they satisfy Ampere's law. Therefore, Equations 5.1 – 5.4 are applicable to a permanent magnet.

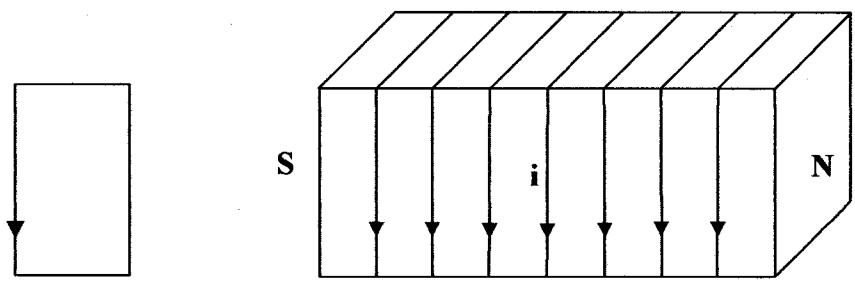

Figure 5.4 Equivalent surface current in a permanent magnet

5.3.2 Magnetic Force

The basic equation for magnetic force describes the force between two parallel wires carrying current as shown in Figure 5.5. The force exerted to the wire a can be expressed as:

$$F_a = i_a l \times B_b . \tag{5.5}$$

Equation 5.5 shows that the force vector is the cross product between the current vector in wire a, i and magnetic field vector from wire b, B_b. The magnetic field, B_b is calculated using Equation 5.1. The magnetic field created due to a current on a long straight wire at distance, x can be expressed as:

$$B_b = \frac{\mu_o i_b}{2\pi x}. \tag{5.6}$$

Therefore, the magnitude of force in two parallel wires is:

$$F_a = i_a l B_b = \frac{\mu_o l i_a i_b}{2\pi x}. \tag{5.7}$$

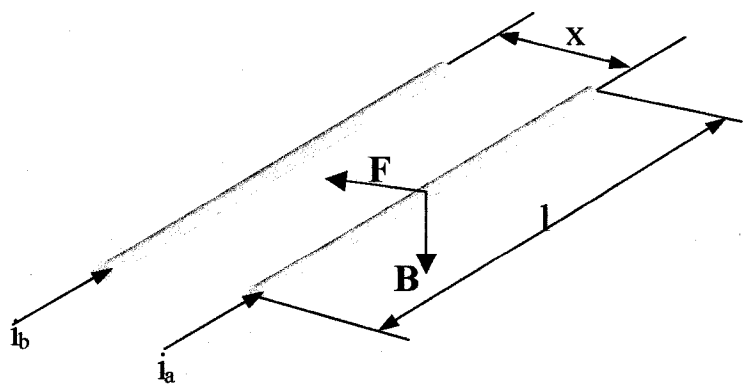

Figure 5.5 Force on two parallel wires carrying currents

As explained earlier, a permanent magnet behaves the same as a coil carrying current. Therefore, it is possible to describe the force on the magnet due to a nearby coil as the force between two coils interacting with each other: one is carrying apparent current and another is carrying real current. As shown in Figure 5.6, the magnet has equivalent surface current flowing around it and the coil sets up a magnetic field due to the real current. Force is applied to the side of the magnet due to the vertical line of the magnetic field from the coil with the vector B is at a right angle to the vector i. The cross product of the current and magnetic field vectors is the force vector having direction shown in Figure 5.6. In addition, vertical forces are also created due to nonvertical lines of the magnetic field. However, these forces cancel each other out.

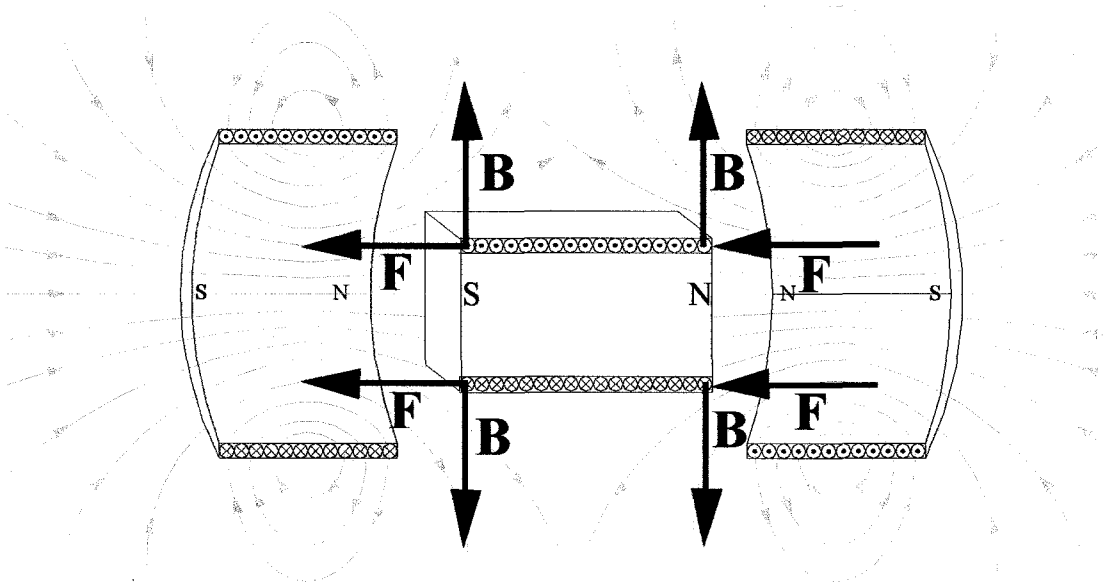

Figure 5.6 Reaction force between a magnet and coils

In RC/TS drive system, the direction of the current is opposite for a pair of coils because they are wound in the opposite directions. According to the right hand rule, magnetic fields set up by the two coils are in opposing directions. One coil produces a repulsive force with the magnet and the other produces an attractive force with the magnet as shown in Figure 5.6. The net force moves the magnet in one direction depending on the direction of the applied current. Similar results occur for each magnet and coils because they are set up in the same north-south pole arrangement all around the drive plate. All four magnets are subjected to the same direction of magnetic force thus they move in phase with each other creating torque on the drive plate as shown in Figure 5.7.

The equivalent surface current of the magnet was only used to verify the direction of the torque, it is not a real current that can be measured in the laboratory. Rather than calculating the force acting on the magnet due to the magnetic field of the coil, in this the force was found by calculating the force acting on the coil due to the magnetic field of the magnet, which is measurable. Considering only the lines of magnetic field at right angle to the direction of current flowing through the coil, the magnitude of the force is:

$$F = i N l_c B, \tag{5.8}$$

where i = current in the coil,

l_c = circumference length of coil loop,

N = total number of loops in the coil in x and y direction ($N = N_x N_y$) illustrated in Figure 5.9, and

B = magnetic field of the permanent magnet.

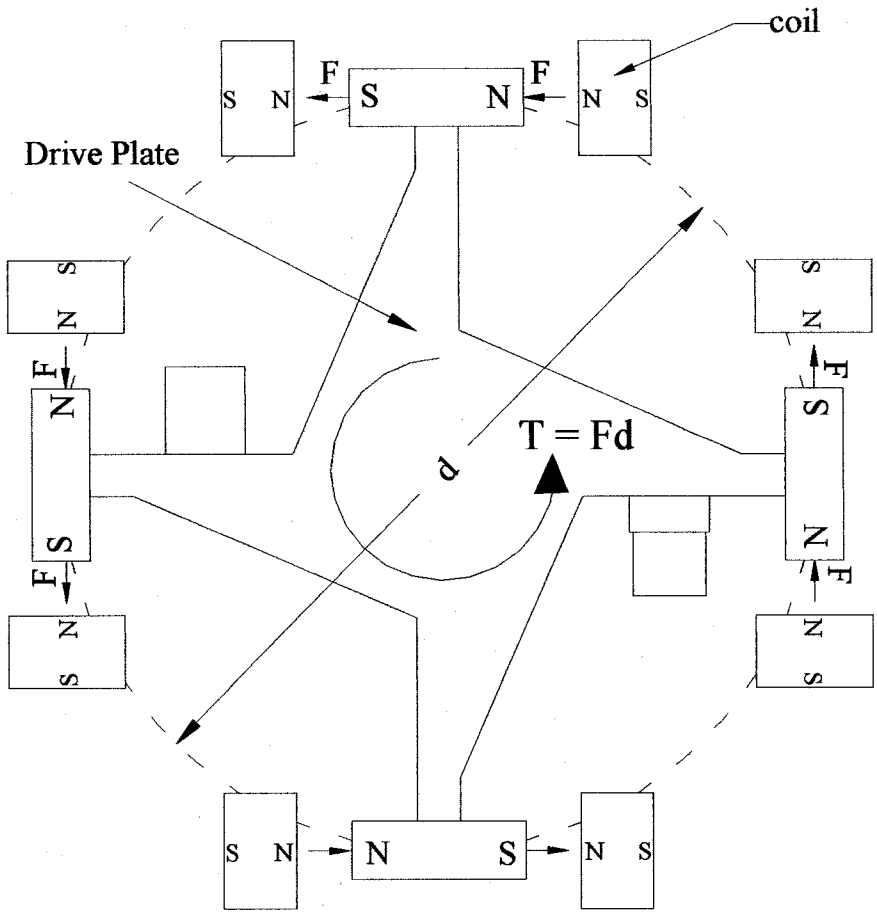

Figure 5.7 Torque generated on the drive plate

From Equation 5.8, it can be seen that the force created in the RC/TS drive system is proportional to the current flowing through coils. Torque created in the system can be determined by introducing the moment arm of the drive plate, d, and modifying Equation 5.8 to:

$$T = (N_x N_y) l_c B d i = k_i i \,, \tag{5.9}$$

where k_i = torque-current factor . And,

$$k_i = N_x N_y l_c B d \,. \tag{5.10}$$

The factor k_i is an important factor used for calculating torque generated in the torsional shear test. As shown in Equation 5.10, if the circumference length of the coil loop and the moment arm of the drive plate are constant, the value k_i is proportional to the numbers of loops in the coil and strength of the magnetic field of the magnet. This implies that torque in RC/TS system can be easily increases if either the numbers of turn increase or a stronger magnet is used. The second option is practical. However, there is also a disadvantage to using a stronger magnet to create more torque. The disadvantage is discussed in next section. Calculations of k_i value using Equation 5.10 is also presented in Chapter 6.

5.3.3 Electromotive Force

When the magnet moves axially inside the coil, the movement of the magnet also induces an electromotive force (emf) according to Faraday's law. The induced electromotive force in a circuit is equal to the rate at which the flux through the circuit is changing:

$$\varepsilon_{emf} = -\frac{d\Phi_B}{dt}. \tag{5.11}$$

The emf is a potential difference between two points in a circuit therefore it has a unit of joule/coulomb or volts.

The direction of the induced emf is specified by Lenz's law using the conservation of energy principle. Lenz's law states that: the direction of the induced current will appear in such a direction that it opposes the change that produces it. Notice that Faraday's law also suggests this opposition by using minus sign as presented in Equation 5.11. Lenz's law refers to induced current (i_{emf}), which means that it applies to

closed circuits such as that shown in Figure 5.8. If the north pole of the magnet is pushed toward the coil, an induced current sets up a magnetic field that opposes to the motion of the magnet. As shown in Figure 5.8, the side of the coil which the north pole of the magnet is moved toward becomes a north pole, and the two north poles will repel each other. The right hand-rule shows that the for the magnetic field setup by the coil to emerge to the right side of the coil, the induced current must be in the direction in Figure 5.8. In RC/TS equipment, this phenomenon is called "back emf."

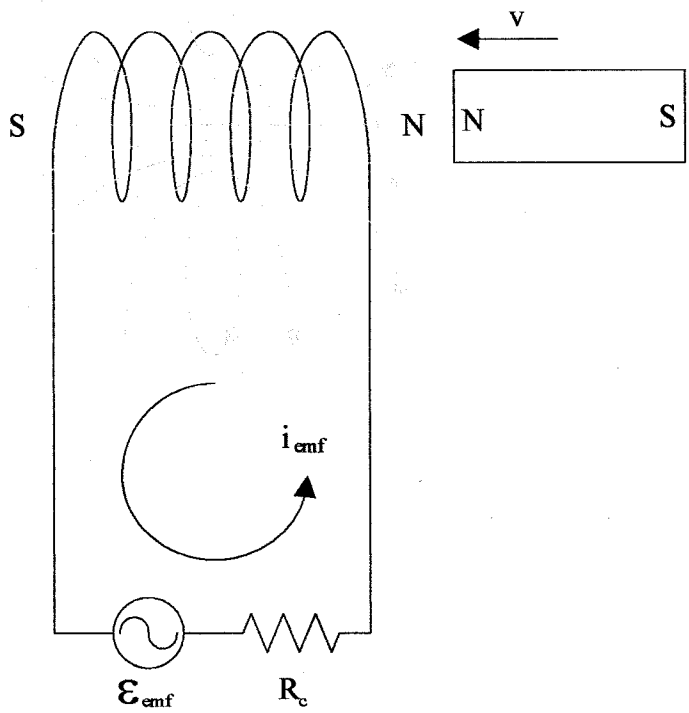

Figure 5.8 Electromotive force induced by the movement of magnet

The induced current due to the back emf always counteracts with the applied current in the coil. The back emf is a source of energy loss in the drive circuit. This energy loss acts as damping generated by the RC/TS equipment, therefore is it is called equipment generated damping. The equipment generated damping is combined with the material damping of the soil during RC/TS measurements. An error in soil material damping due to the back emf effect has been one of the weaknesses in the RC/TS test.

To quantify the back emf effect in the RC/TS drive system, the cross sections of a coil in the x, y, and z planes is illustrated in Figure 5.9. Assuming that the magnetic lines created by the magnet passes through the area of the coil loop, A_c, the flux Φ_B enclosed by the loop for every turns of the coil is equal to:

$$\Phi_B = BA_c . \tag{5.12}$$

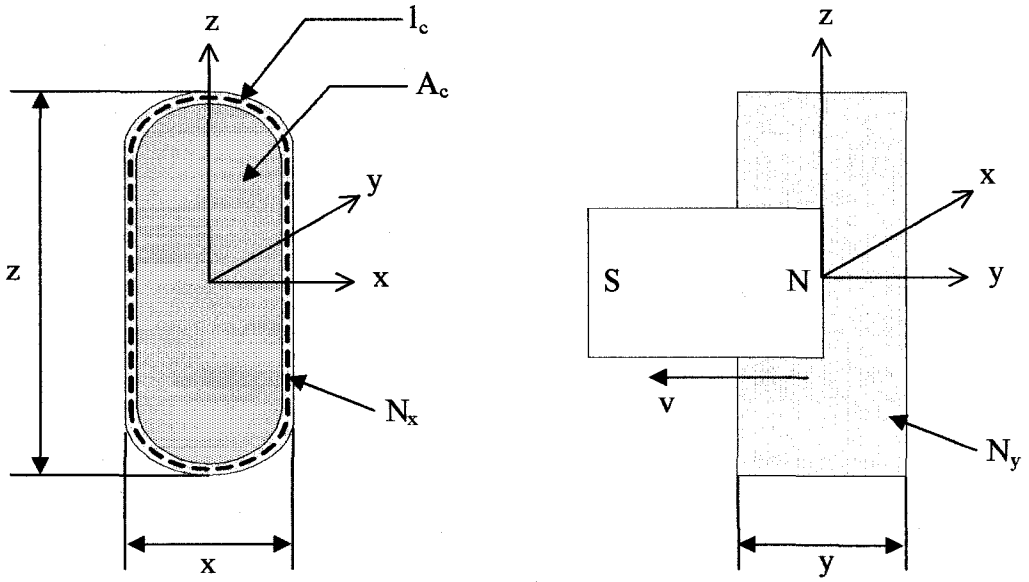

Figure 5.9 Cross sections of coil loop

Applying Faraday's law to the coil, an emf appears for every loop of the coil. With the assumptions that the flux through every loop of the coil is added and that the coil is an ideal coil, the induced emf is given by:

$$\varepsilon_{emf} = \frac{d(N\Phi_B)}{dt} = \frac{d(N_x N_y B A_c)}{dt}. \tag{5.13}$$

For the case of coil and magnet in RC/TS drive system, the magnetic flux changes as the magnet moves. This change is the increase or decrease in total Φ_B through the coil loop caused by moving the magnet toward or away from the coil. The total Φ_B is represented by the terms $N\Phi_B$ or $N_xN_y\Phi_B$ in Equation 5.13. Since the magnet is only moved in y direction, the change in Φ_B, therefore, is only caused by a change of N_y. Equation 5.13 can be rearranged as:

$$\varepsilon_{emf} = BA_cN_x\frac{dN_y}{dt}. \tag{5.14}$$

The change of N_y or dN_y is directly related to a moving distance dy as shown in the relationship below:

$$dN_y = \frac{N_y}{y}dy, \tag{5.15}$$

where y = total width of the coil loop in y-direction as shown in Figure 5.8.

Substitution of Equation 5.13 into Equation 5.12 gives:

$$\varepsilon_{emf} = \frac{BA_cN_xN_y}{y}\frac{dy}{dt} = \frac{BA_cN_xN_y}{y}v, \tag{5.16}$$

where v = velocity of the magnet.

Equation 5.16 implies that emf is proportional to the velocity of the magnet. In the RC/TS system, it is more useful to express the emf in relation to the rotational velocity of the magnet. Equation 5.16 then becomes:

$$\varepsilon_{emf} = \frac{2}{d}\frac{BA_c N_x N_y}{y}\frac{d\theta}{dt} = k_B \frac{d\theta}{dt}, \tag{5.17}$$

where $\frac{d\theta}{dt}$ = rotational velocity of the magnet, and

k_B = back emf-rotational velocity factor which is equal to,

$$k_B = \frac{2}{d}\frac{BA_c N_x N_y}{y}. \tag{5.18}$$

The factor k_B derived in Equation 5.18 is an electromagnetic property of the RC/TS drive system. This factor represents the amount of back emf created in the drive system, hence higher value of k_B means higher effect of back emf. From Equation 5.18, the factor k_B is proportional to the number of loops in the coil and the magnetic field of the magnet which are the same as factors affecting the value of k_i. More back emf is expected if numbers of loops in the coil are increased, or a stronger magnet is used. As presented in the previous section, increasing the numbers of loops in the coil and using a stronger magnet increases capacity of the RC/TS drive system in generating torque. Consequently, more back emf effect is also generated and resulting in higher equipment generated damping. However, if the back emf effect can be predicted and the equipment generated damping is taken into account precisely, the problem with the back emf is then solved. In this study an electromagnetic model of the RC/TS drive system is developed to describe the back emf effect that can be used to predict the equipment generated damping.

5.4 ELECTROMAGNETIC MODEL

An electromagnetic model was developed using the combined electrical, magnetic and mechanical properties of the RC/TS apparatus. The purpose of the model is to describe the behavior of the system including the effect of the back emf. The model is used to predict the equipment generated damping due to the back emf allowing a precise measurement for the material damping of soil. This section presents the step-by-step development of the electromagnetic model. The effect of the back emf in the model is described. In addition, the effects of back emf effect in the RC and the TS tests are considered separately. Methods are presented to account for the back emf effect in each test.

Figure 5.10 shows the RC/TS drive circuit. A voltage source with internal resistance of R_s generates voltage potential, V_s. The resistor R_c and inductor L_c represent the total resistance and total inductance of the eight drive coils, respectively. The back emf (ε_{emf}) appears in the circuit as an additional voltage source. The circuit is connected to ground at point b. Current, i, is assumed to flow through the circuit in the clockwise direction, as shown in Figure 5.10. At point a, the voltage potential V_a is given by:

$$V_a = V_s - iR_s. \tag{5.19}$$

Applying Kirchhoff's voltage law to the drive circuit, starting at the voltage source and going around the circuit in the clockwise direction results in:

$$V_s - iR_s - iR_c - L_c\frac{di}{dt} - \varepsilon_{emf} = 0, \tag{5.20}$$

where $L_c(di/dt)$ = drop in voltage potential due to the coil inductance.

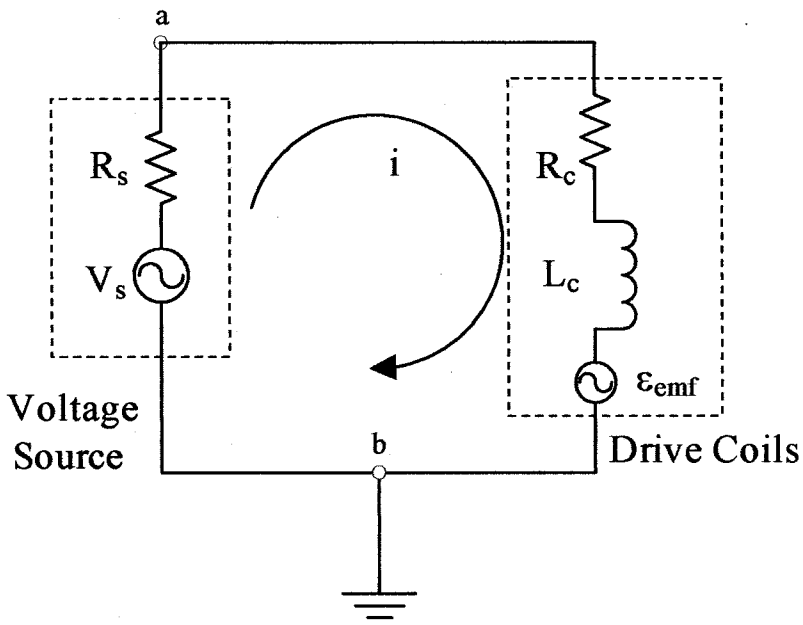

Figure 5.10 Drive circuit of the RC/TS equipment

Substitution of Equation 5.18 and Equation 5.19 into from Equation 5.20 and gives:

$$V_a - i(R_c + sLc) = s\theta k_B, \tag{5.21}$$

where s = Laplace variable ($s = j\omega$),

ω = circular velocity.

Solving for the current in the coil yields:

$$i = \frac{V_a - s\theta k_B}{R_c + sL_c}. \tag{5.22}$$

As derived in previous section, the torque is proportional to the current. An expression for torque can be obtained by substituting Equation 5.22 into Equation 5.9:

$$T = k_i i = k_i \frac{V_a - s\theta k_B}{R_c + sL_c}. \tag{5.23}$$

Soil in the RC/TS system can be described as a viscoelastic material represented as a single degree of freedom system. In this type of system, the elastic property is represented by a spring with stiffness, k_θ and the damping is represented by a dashpot with damping coefficient, c_θ. The simplest and most widely used model to predict the viscoelastic behavior is called the Kevin model. The drive system of the RC/TS equipment is represented by a mass with mass polar moment of inertia, J attached to the model. Torque is applied to the system as shown in Figure 5.11.

From the assumed single degree of freedom system, torque is evaluated from the following differential equation:

$$T = k_\theta\theta + c_\theta s\theta + Js^2\theta \qquad (5.24)$$

where k_θ = torsional spring stiffness,

c_θ = torisonal viscous damping coefficient, and

J = polar moment of inertia of the system.

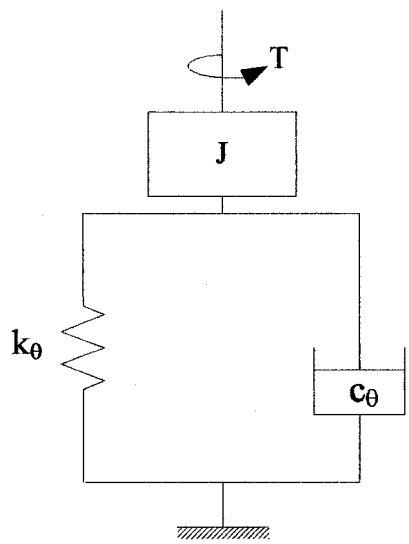

Figure 5.11 Kevin model

Substitution of the torque obtained from the drive circuit (Equation 5.23) gives:

$$k_i\left(\frac{V_a - s\theta k_B}{R_c + sL_c}\right) = k_\theta\theta + c_\theta s\theta + Js^2\theta\,. \tag{5.25}$$

Division by θ and rearrangement gives:

$$\frac{V_a}{\theta}\left(\frac{k_i}{R_c + sL_c}\right) = k_\theta + c_\theta s + s^2 J + s\frac{k_i k_B}{R_c + sL_c}\,. \tag{5.26}$$

The complex terms $\frac{k_i k_B}{R_c + sL_c}$ in Equation 5.26 can be expanded and rearranged into a form a+sb as follows:

$$\frac{k_i k_B}{R_c + sL_c}\left(\frac{R_c - sL_c}{R_c - sL_c}\right) = \frac{k_i k_B R_c - s k_i k_B L_c}{R_c^2 + \omega^2 L_c^2}\,. \tag{5.27}$$

By substituting Equation 5.27 into Equation 5.26, and jω for s, Equation 5.26 becomes:

$$\frac{V_a}{\theta} = \frac{R_c + j\omega L_c}{k_i}\left[\left(k_\theta + \frac{\omega^2 k_i k_B L_c}{R_c^2 + \omega^2 L_c^2}\right) + j\omega\left(c_\theta + \frac{k_i k_B R_c}{R_c^2 + \omega^2 L_c^2}\right) - \omega^2 J\right]. \tag{5.28}$$

Therefore, the voltage transfer function, H_v for the rotation and applied voltage is expressed as:

$$H_v = \frac{\theta}{V_a} = \frac{\dfrac{k_i}{R_c + j\omega L_c}}{\left[\left(k_\theta + k_{eq}\right) + j\omega\left(c_\theta + c_{eq}\right) - \omega^2 J\right]}, \tag{5.29}$$

where k_{eq} = equipment spring stiffness,

c_{eq} = equipment viscous damping coefficient, and

ω = angular velocity (ω = 2πf).

The terms k_{eq} and c_{eq} are:

$$k_{eq} = \frac{\omega^2 k_i k_B L_c}{R_c^2 + \omega^2 L_c^2}, \text{ and} \tag{5.30}$$

$$c_{eq} = \frac{k_i k_B R_c}{R_c^2 + \omega^2 L_c^2}. \tag{5.31}$$

The current transfer function for rotation and current, H_i can be expressed as:

$$H_i = \frac{\theta}{i} = \frac{k_i}{\left[k_\theta + j\omega c_\theta - \omega^2 J\right]}. \tag{5.32}$$

Equation 5.29 is the transfer function developed to predict the response curve for soil including the back emf effect in RC testing using a voltage measurement. The voltage measurement for RC test is commonly used because the amplitude of sinusoidal signal generated by the source generator is quantified in terms of voltage. Equation 5.29 shows that an increase of the stiffness and viscosity of the system due to the back emf are expected as presented by the terms k_{eq} and c_{eq}, respectively. The term k_{eq} and c_{eq} are function of frequency and four parameters: coil resistance, R_c, coil inductance, L_c, torque-current factor, k_i, and back emf-rotational velocity, k_B. The value of k_{eq} tends to increases as the frequency increases while the value of c_{eq} tends to decrease as the frequency increases. The frequency effect on value of k_{eq} and c_{eq} is investigated experimentally in Chapter 7.

Equation 5.32 shows that there is no back emf effect in RC/TS testing when using a current rather than a voltage source. The back emf effect can also be eliminated by measuring current in RC/TS tests using voltage sources.

5.4.1 Behavior of Back Emf in RC/TS Drive System

The single degree of freedom system composed of a spring-dashpot system called the Kevin model can be used to represent the RC/TS system. The same model can be used to describe the effect of back emf.

In Equation 5.29, the additional terms k_{eq}, and c_{eq} were introduced to the transfer function for voltage measurement due to the back emf effect. The back emf is therefore can be described as an additional spring and an additional dashpot connected in parallel with the original spring and dashpot representing a soil specimen in the system as shown in Figure 5.12. The spring-dashpot system with back emf effect can be described with the following equation:

$$T = (k_\theta + k_{eq})\theta + (c_\theta + c_{eq})s\theta + Js^2\theta \,. \tag{5.33}$$

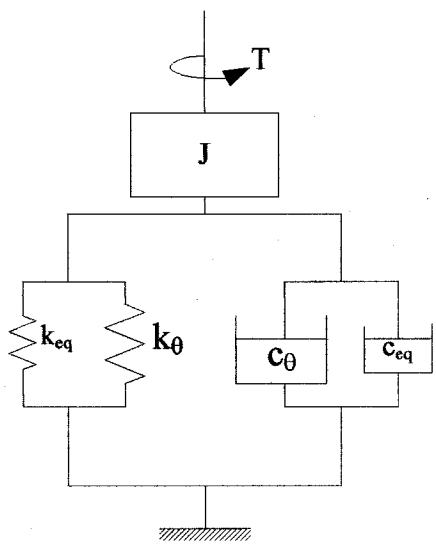

Figure 5.12 Modified Kevin model including the back emf effect

In Figure 5.12, the k_θ and c_θ in parallel with k_{eq} and c_{eq} implies that an applied torque generated in the RC/TS drive system is not all transferred to k_θ and c_θ because it is partially transferred to k_{eq} and c_{eq}. Consequently, the measured k_θ and c_θ of the system does not represent the stiffness and damping of the soil behavior but a combination of the soil and the back emf. As a result, the soil stiffness and damping are overestimated if the back emf is not taken into account. Methods used to account for the back emf effect in RC and TS tests are presented in next section.

5.4.2 Back Emf Effect in RC/TS Tests

As described in Chapter 3, the RC and TS tests are performed at different loading frequencies. The RC test is performed at first mode resonance, which is typically higher than 10 Hz while the TS test is performed at very low frequencies usually in the range of 0.01-1Hz. Therefore, the effects of back emf in the RC and TS tests are taken into account differently.

In the RC test, Equation 5.29 can be applied directly to the response curve measured in the RC test using voltage source. To account for the back emf effect, the terms k_{eq} and c_{eq} can be calculated if the model parameters, R_c, L_c, k_i, k_B are known. The effect of back emf in resonant frequency and damping can be predicted using the following equations:

$$\Delta f_m = \frac{1}{2\pi}\left[\sqrt{\frac{k_\theta + k_{eq}}{\Sigma J}}\sqrt{1-2(D+D_{eq})^2} - \sqrt{\frac{k_\theta}{\Sigma J}}\sqrt{1-2D^2}\right], \text{ and} \tag{5.34}$$

$$D_{eq} = \frac{c_{eq}}{c_c}. \tag{5.35}$$

where D = damping of system,

c_c = critical damping coefficient ($c_c = 4\pi f_n \Sigma J$),

f_n = undamped natural frequency of specimen ($f_n = \frac{f_m}{\sqrt{1-2D^2}}$), and

ΣJ = total polar moment of inertia of the system including such as drive plate (J_o), top plate (J_t).

The Δf_m and D_{eq} are the effects of back emf on resonant frequency and damping due to the equipment spring stiffness, k_{eq}, and the equipment viscous damping coefficient, c_{eq} described by the model. The Δf_m is an increasing of resonant frequency and the D_{eq} is an equipment generated damping.

In TS test, soil behavior is analyzed based on characteristics of the hysteresis loop. The hysteresis loop is constructed from a measured torque and rotation. Torque applied to the soil specimen is partially transmitted to the k_{eq} and c_{eq} as shown in Figure 5.12. The torque can be corrected by rearranging of Equation 5.31 as shown below:

$$T_c = T_m - (k_{eq}\theta + c_{eq}s\theta) = k_\theta\theta + c_\theta s\theta + Js^2\theta\,, \qquad (5.36)$$

where T_c = corrected torque, and

T_m = measured torque.

Equations 5.34-5.35 and 5.36 can be used to account for the back emf effect for RC and TS test, respectively, if the terms k_{eq} and c_{eq} are known. In order to determine the k_{eq} and c_{eq}, the model parameters: R_c, L_c, k_i and k_B must be evaluated. These parameters are the electromagnetic properties of the RC/TS drive system that can be measured experimentally using the measurement method developed in this study. Details on the measurement method used for each parameter and results are presented in Chapter 6.

CHAPTER 6

CALIBRATIONS OF DRIVE PLATE ELECTROMAGNETIC PROPERTIES

6.1 INTRODUCTION

This chapter presents measurements of the electromagnetic properties of the RC/TS drive system. These properties are the parameters of the electromagnetic model developed in this study. The testing methods and analysis procedures used to evaluate each parameter are described. All measurements were performed on both the USU and the UT drive plates. A comparison of the USU and UT drive plates are included at the end of each section. The experimental procedures developed in this study are simple and use readily available equipment. Where possible, measurements were performed over a range of frequencies and amplitudes to evaluate frequency effects and nonlinearity.

Additionally, the magnetic field strength of the drive plate magnet was measured. These magnetic field were then used to determine the theoretical values of the electromagnetic properties measured in this chapter. The theoretical value of the magnetic properties and the measured value were compared and the ratio was used to calculated efficiency of the drive plate.

6.2 MODEL PARATMETERS

As derived in Chapter 5, the proposed electromagnetic model consists of four parameters, coil resistance, R_c, coil inductance, L_c, torque-current factor, k_i, and back emf-rotational velocity factor, k_B. In order to verify and apply the model, these parameters need to be determined. An independent measurement is used to measure the model parameters. The measured model parameters are then used to predict the

equipment generated stiffness, k_{eq} and equipment generated viscosity, c_{eq}. These independent measurements are presented in the following sections.

6.2.1 Coil Resistance and Inductance

The coil resistance, R_c, and inductance, L_c, can be measured directly using an ohmmeter and an inductance meter. The ohmmeter measures the resistance under D.C. conditions, while the inductance meter measures the inductance at a single high frequency (typically 5-10 kHz). This study focused on measuring R_c and L_c over the range of frequencies typically encountered in RC/TS testing. The measurements were performed using a stiff aluminum specimen so that the drive plate rotation was negligible. This eliminated back emf effects. Figure 6.1 shows a drawing and a photo of the stiff specimen developed for the measurement of R_c and L_c.

The drive system of the RC/TS drive system was modified in this study so that R_c and L_c could be measured in the same test. The modified circuit is shown in Figure 6.2. A reference resistor, R_{ref}, was connected in series with the source and the coils. The measurement was performed using swept sine test or applying a sinusoidal voltage signal over a frequency range of 0 to 400 Hz to the drive coil circuit. Measurements were made of voltage, V_1 and V_2 , as shown in Figure 6.2. The current flowing through the circuit is:

$$i = \frac{V_1 - V_2}{R_{ref}}, \tag{6.1}$$

where V_1-V_2 = voltage potential drop across the R_{ref};

V_1 = voltage output from the source, and

V_2 = input voltage to the coils.

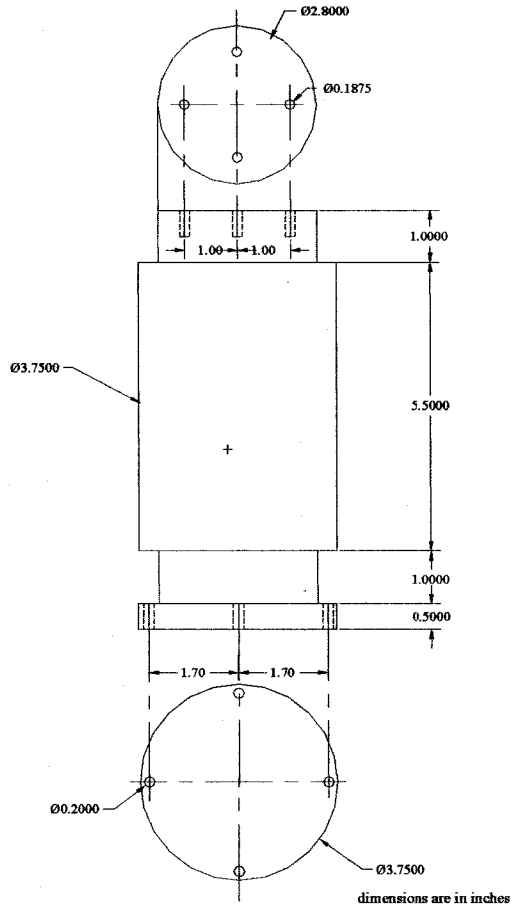

a)

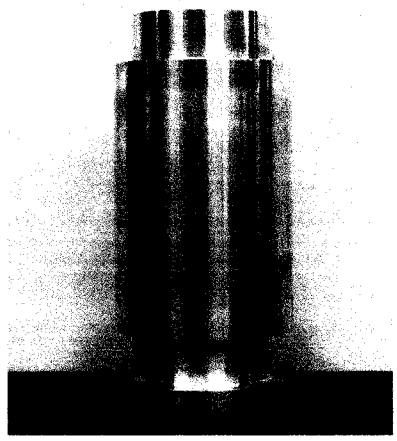

b)

Figure 6.1 Drawing and photo of stiff aluminum specimen

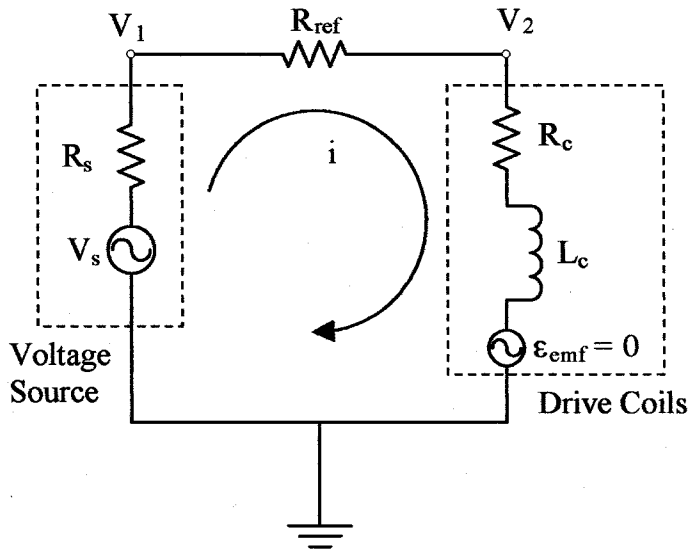

Figure 6.2 Electrical drive circuit for R_c and L_c, measurements

All the coils are connected to ground, therefore V_2 can be obtained from:

$$V_2 = i(R_c + j\omega L_c). \tag{6.2}$$

Substitution of the current, i, and expansion gives:

$$V_2 = \frac{V_1 - V_2}{R_{ref}}(R_c + j\omega L_c). \tag{6.3}$$

In this equation, the coil resistance, R_c is in the real part of the equation and the coil inductance, L_c is in the imaginary part of the equation. As the value of V_1 and V_2 are measured a any given R_{ref}, the coil resistance, R_c and inductance, L_c can be obtained from:

$$R_c = \text{real}\left(\frac{V_2}{V_1 - V_2}R_{ref}\right), \text{ and} \tag{6.4}$$

$$L_c = \frac{1}{\omega}\text{imag}\left(\frac{V_2}{V_1 - V_2}R_{ref}\right). \tag{6.5}$$

Units of R_c and L_c are ohm (Ω) and henry (H), respectively. The tests were performed with reference resistor, R_{ref}, of 25, 50, 100 ohms. R_{ref} was varied to evaluate any nonlinearities with current. The linearity of the current was also evaluated by using the source voltage of 0.01, 0.1, 0.5, 2 volts.

Measurements of coil resistance and coil inductance for the USU drive plate are shown in Figures 6.3-6.5. Results for the coil resistance show a slight increase with frequency, about 3% over the measured frequency band. Measurements using different reference resistors and source voltages show no significant nonlinearity in the coil resistance.

Inductance measurements for the USU drive plate are also shown in Figures 6.3-6.5. There is no variation of coil inductance with frequency. There is a slight source voltage effect with the maximum effect observed in the tests at a voltage of 2 volts with R_{ref} = 25 and 50 ohms. The outlying results have slightly higher inductance values, however, similar results were not observed at the test of 2 volts with R_{ref} = 100 ohms. There is no adequate explanation of this effect, but the variations are very small and can be neglected.

The resistance and inductance of the coils was estimated by averaging of all the results. The average value of coil resistance, R_c, is 45.6 ohms. The average value of coil inductance, L_c, is 0.0256 henries. These values are used for the predicting the equipment generated damping using the electromagnetic model.

Rotation of the drive plate was also measured during the coil resistance and inductance measurements. The accelerometer and proximitors were used to measure this rotation. The results are shown in Figure 6.6. Generally, accelerometers do not perform

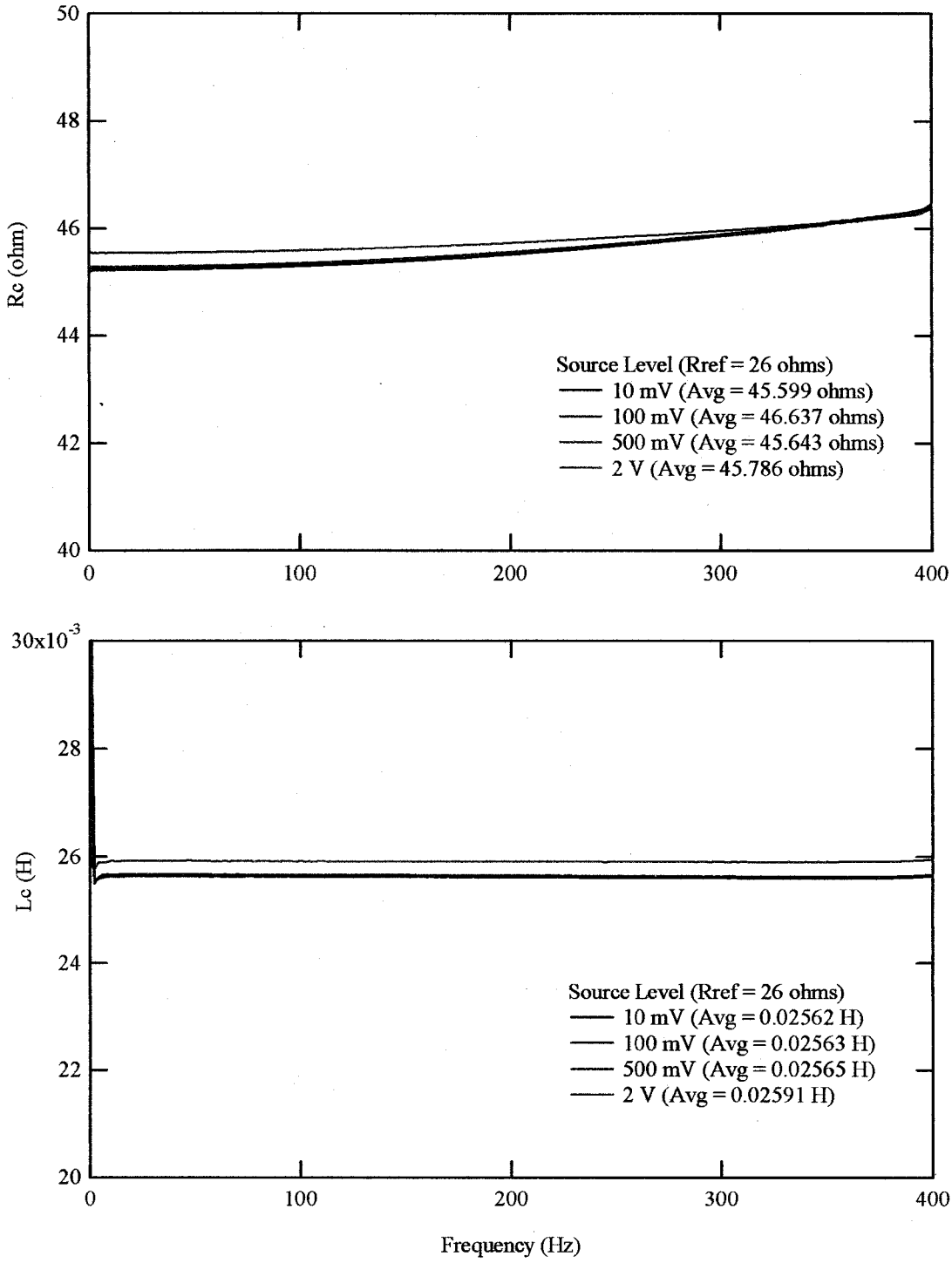

Figure 6.3 Coil resistance and inductance for R_{ref} of 26 ohms at different source voltage levels for the USU drive plate

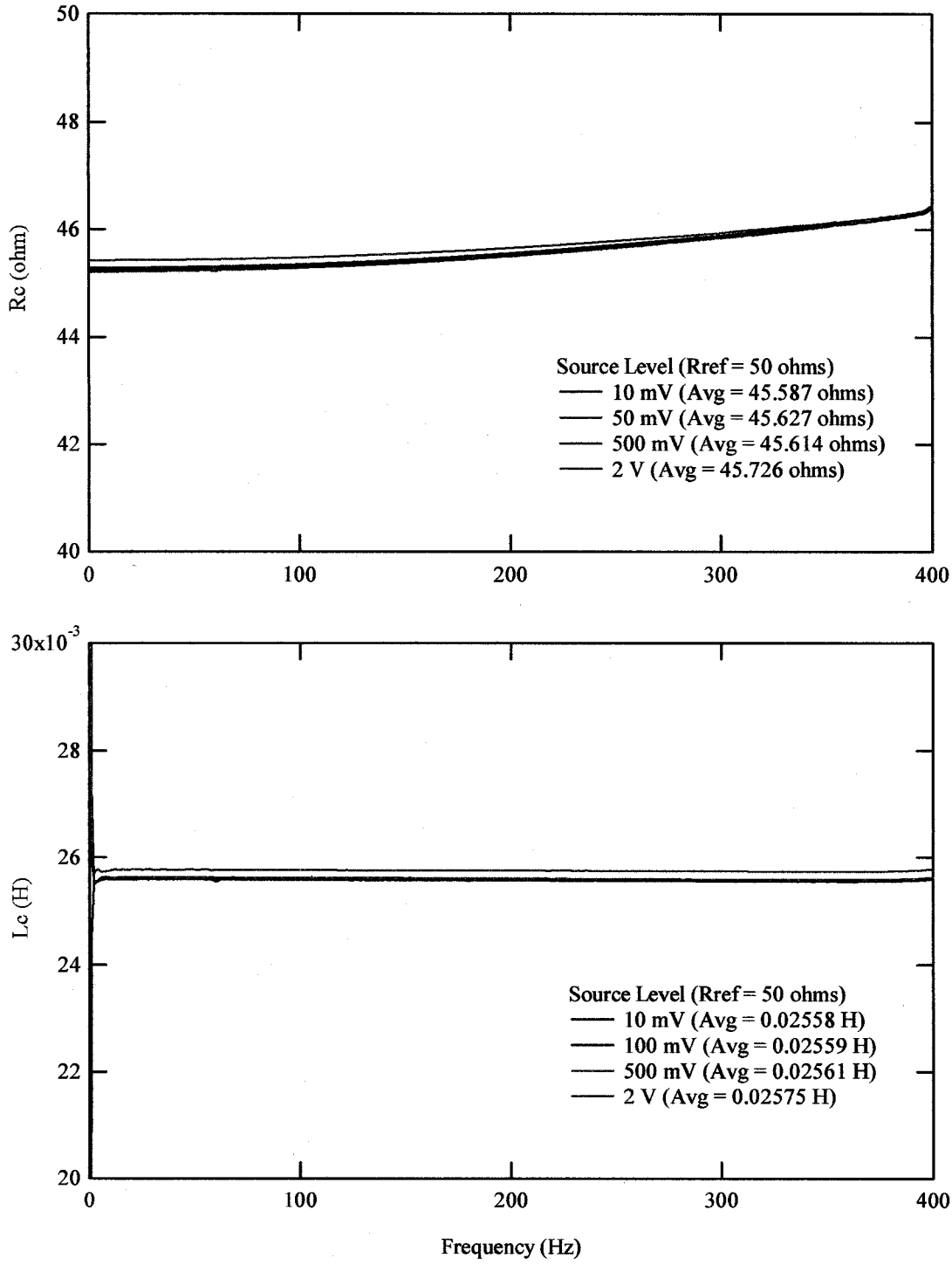

Figure 6.4 Coil resistance and inductance for R_{ref} of 50 ohms at different source voltage levels for the USU drive plate

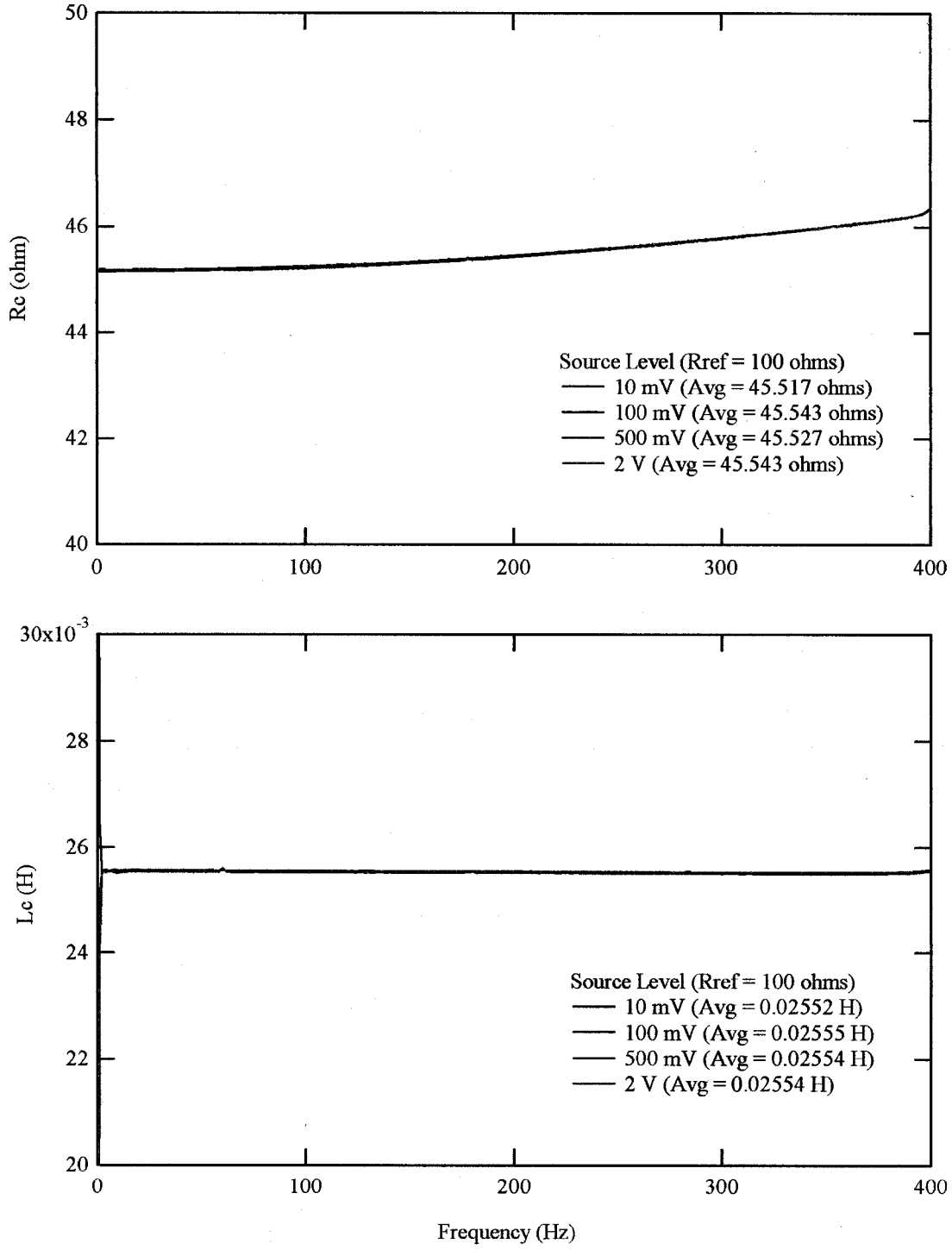

Figure 6.5 Coil resistance and inductance R_{ref} of 100 ohms at different source voltage levels for the USU drive plate

well at very low frequencies, thus the noisy accelerometer signals at low frequency inthese tests are expected. Unlike the accelerometer, the proximitors only perform well at frequencies below 50 Hz. From these results, it is confirmed that the rotation is negligible during the measurements, with all roation being less than 4×10^{-6} radians.

The R_c and L_c measurements were also performed on the UT drive plate No. 9 at The University of Texas at Austin. Results are shown in Figures 6.7 and 6.8 for R_{ref} of 24 and 100 ohms. The variation of R_c and L_c with frequency is very similar to the results observed for the USU drive plate. The overall average value of R_c is 44.7 ohms and L_c is 0.02375 H.

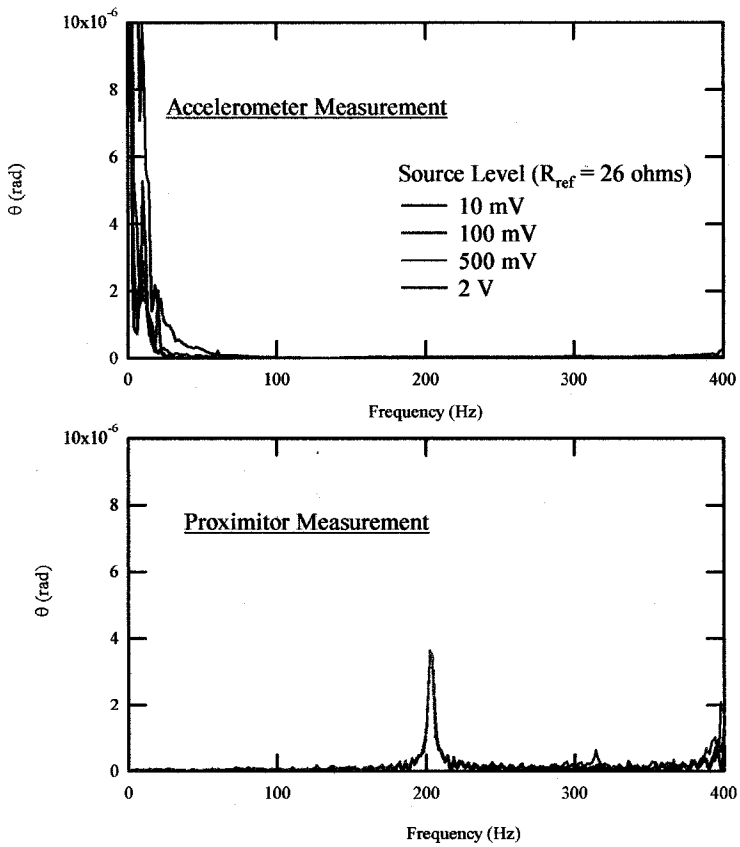

Figure 6.6 Rotations measured during R_c and L_c measurement on the USU drive plate

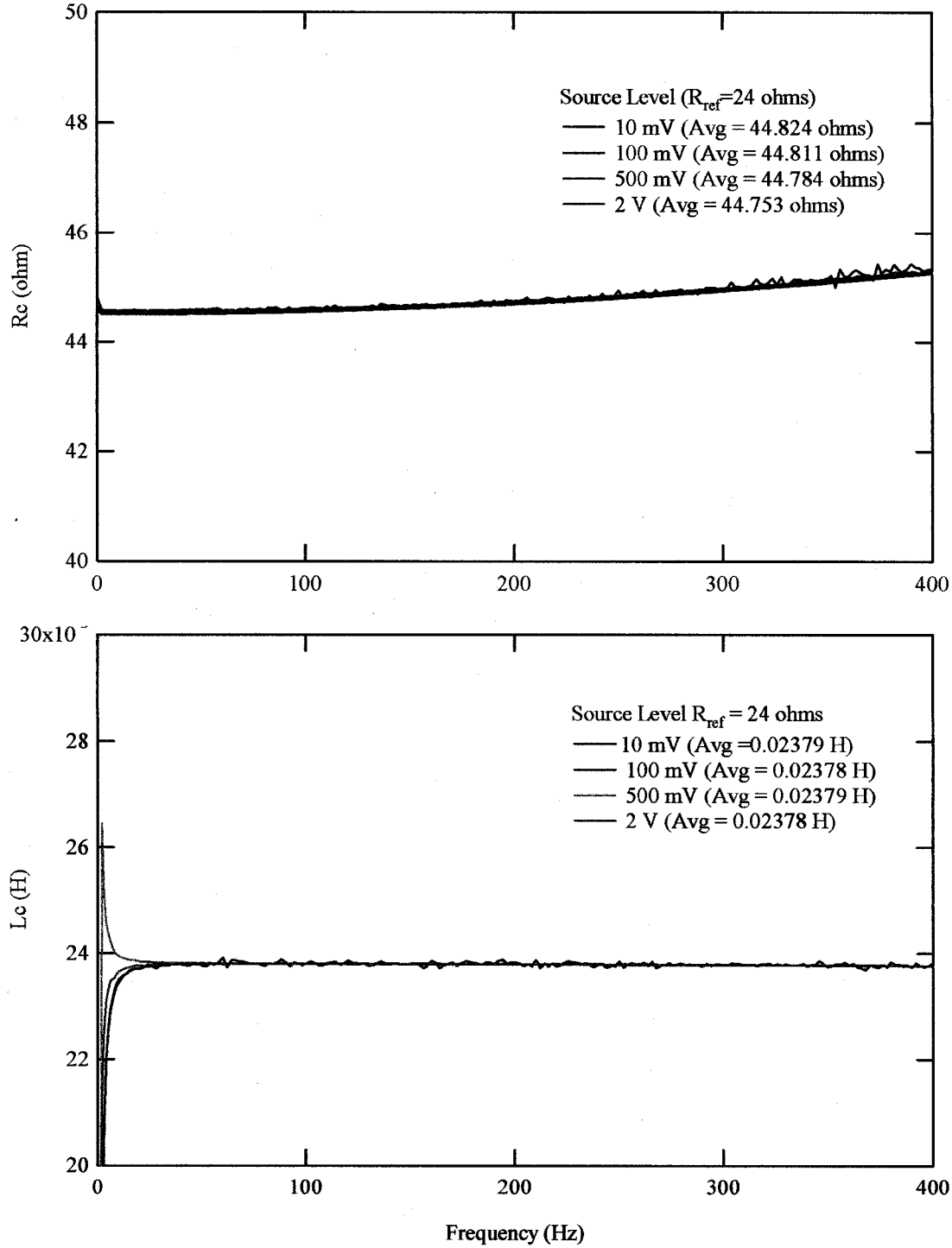

Figure 6.7 Coil resistance and inductance for R_{ref} of 24 ohms at different source voltage levels for the UT drive plate No. 9

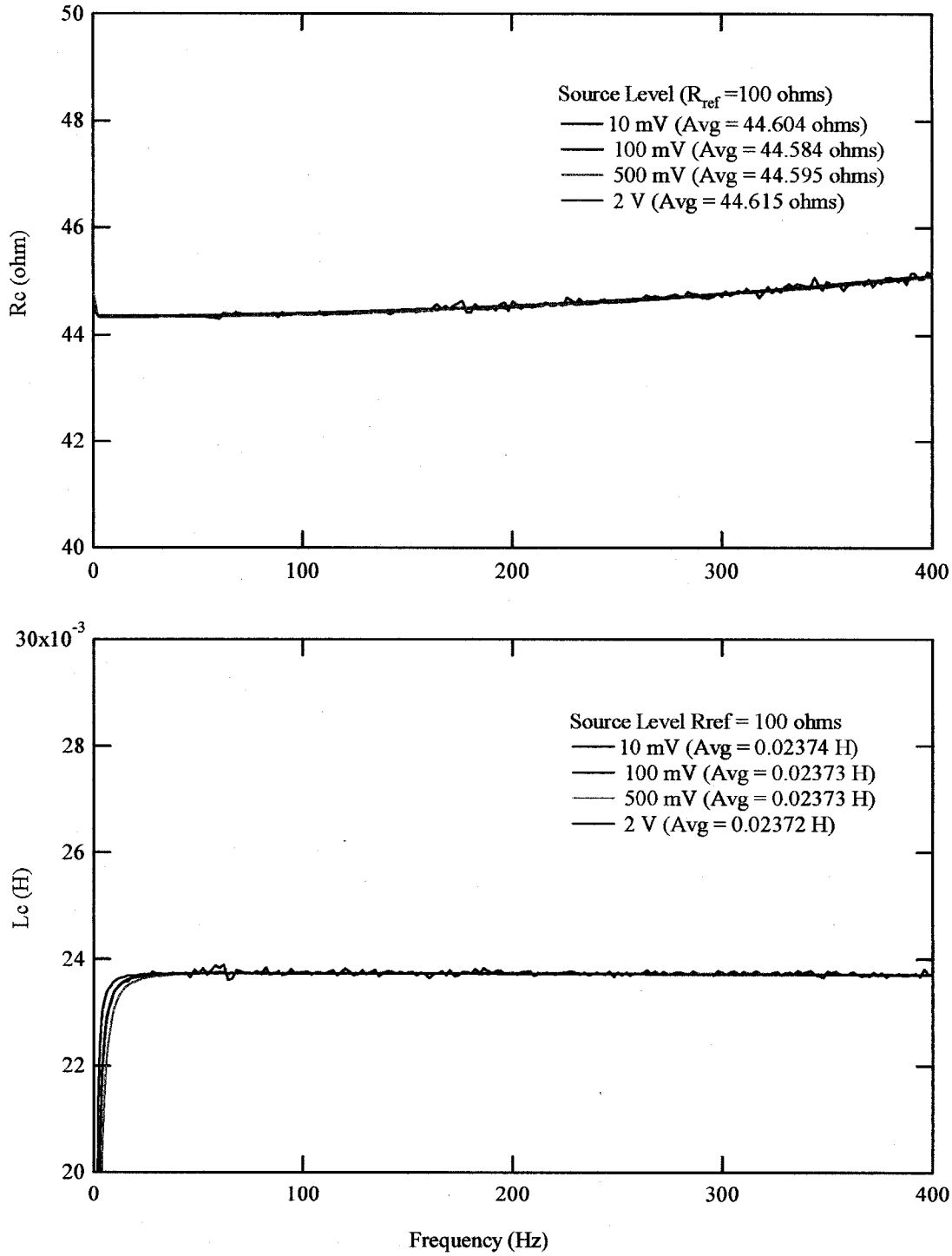

Figure 6.8 Coil resistance and inductance for R_{ref} of 100 ohms at different source voltage levels for the UT drive plate No. 9

6.2.2 *Torque-current Factor*

The torque-current factor (k_i) is used for calculating torque in RC/TS tests. The factor is also one of the parameters in the electromagnetic model used to predict the equipment generated damping from the back emf effect. As explained in the previous chapter, torque generated in the RC/TS drive system is proportional to the applied current, thus the factor k_i can be expressed as:

$$k_i = \frac{T}{i}, \tag{6.6}$$

where k_i = torque-current factor (lb-ft/A),

T = torque generated to the drive plate, and

i = current in the drive coil circuit.

Determination of the factor, k_i requires the measurement of torque and current. In this study current was measured directly using a current proportional signal from the power amplifier. Torque was determined using two different methods. First, by performing the torsional shear tests using calibration specimens with known torsional stiffnesses. Second, by measuring torque directly using a torque sensor. Details of these two methods are presented below.

In the first method, torsional shear tests were performed on each calibration specimen, each having different stiffness. The rotational stiffness, K_θ, of each specimen was calculated along with the polar moment of inertia of the drive plate presented in Chapter 4. Average values of K_θ for each specimen are used for this measurement and are presented in Table 4.4.

Torsional shear tests were performed on the calibration specimens at frequencies of 0.01, 0.05, 0.1, 0.5, and 1 Hz. Current and rotation were measured during the tests. In addition, the applied voltage was also measured to determine the torque-voltage factor, k_v. Torque was calculated using:

$$T = K_\theta \theta, \tag{6.7}$$

where K_θ = rotational stiffness of calibrated specimen (lb-ft/rad), and

θ = rotation.

Plots of torque versus current and torque versus voltage are shown in Figure 6.9. Because material damping of calibration specimens is very small, the hysteresis behavior is negligible. A linear relationship between torque and current, and torque and voltage was observed. Factors k_i and k_v are determined from slope of the plots in Figure 6.9. The k_i and k_v values obtained from the torsional shear test on each calibrated specimen at different frequencies are tabulated in Table 6.1.

Results for each specimen show consistency in the values of k_i and k_v obtained from the tests at different frequency. Slight differences exist in the results between the specimens. As explained earlier, the torque calculated in this test is based on the torsional stiffness of the specimen, which was estimated during the drive plate calibration. Errors in the value of K_θ will result in errors in calculations of torque. Despite this, the variation of k_i and k_v is very small. The overall average results of this test are k_i = 0.3172 lb-ft/A, and k_v = 0.007075 lb-ft/V.

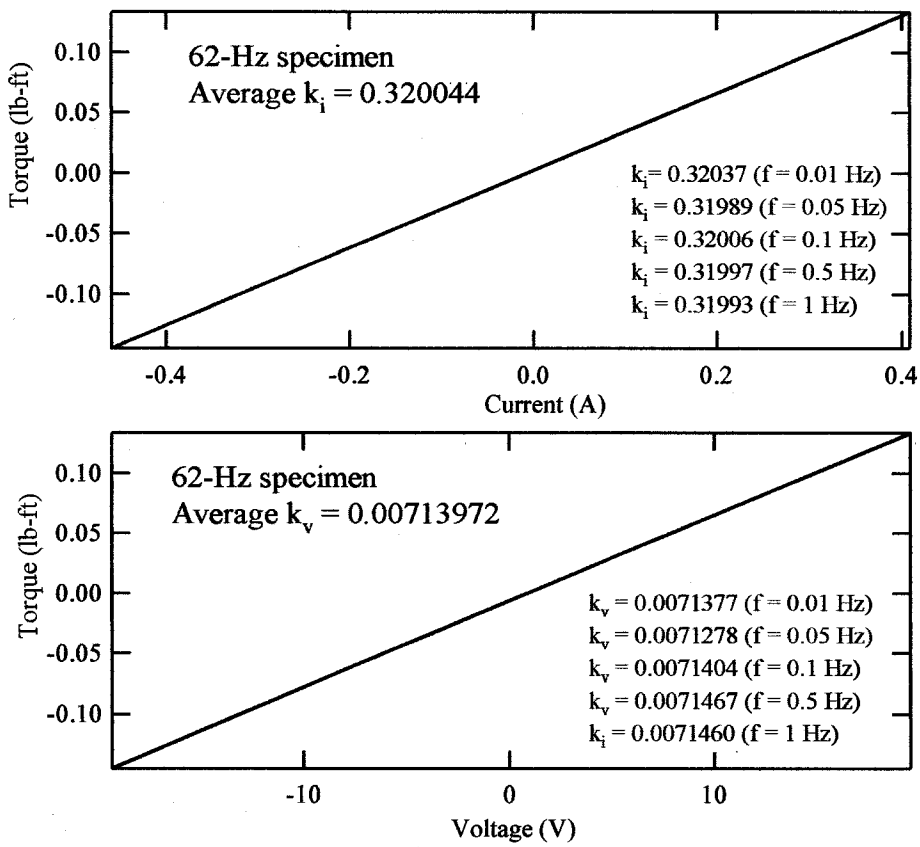

Figure 6.9 Torsional shear test results on 62-Hz calibration specimen

Table 6.1 Factors k_i and k_v Determined from Torsional Shear Tests on Calibration Specimens

Frequency (Hz)	14-Hz Specimen		62-Hz Specimen		128-Hz Specimen		188-Hz Specimen	
	k_i (lb-ft/A)	k_v (lb-ft/V)	k_i (lb-ft/A)	k_v (lb-ft/V)	k_i (lb-ft/A)	k_v (lb-ft/V)	k_i (lb-ft/A)	k_v (lb-ft/V)
0.01	0.30480	0.0068502	0.32037	0.0071377	0.32474	0.0072577	0.31993	0.0070971
0.05	0.30476	0.0068519	0.31989	0.0071278	0.32210	0.0071593	0.32121	0.0071249
0.10	0.30478	0.0068517	0.32006	0.0071404	0.32168	0.0071565	0.32043	0.0071105
0.50	0.30507	0.0068595	0.31997	0.0071467	0.32112	0.0071576	0.3213	0.0071344
1.00	0.30623	0.0068676	0.31993	0.0071460	0.32318	0.0072039	0.32106	0.0071241
Average	0.30513	0.0068546	0.32037	0.0071397	0.32256	0.0071870	0.32079	0.0071182

The second method to determine k_i value is to measure torque directly using a torque sensor. The torque sensor used in this study was a Futek model T5100. It has capacity to measure torque up to 160 in-oz (0.83 ft-lb). The calibration factor of the torque sensor is 462.8 lb-ft/V per excitation voltage. When performing this measurement, the torque sensor was mounted rigidly to the top of the aluminum column designed and custom built to fit the torque sensor and drive plate of RC/TS equipment. The calibration factor of the torque sensor provided by manufacturer was used to determine torque. The factor k_i was then obtained from the ratio of torque and applied current.

The variation of k_i versus frequency was not measurable using the torque sensor because the resonant frequency of the combined torque sensor-aluminum column-drive plate system was found at a frequency at about 30 Hz. Thus, the torque measurement with frequency encounters significant dynamic effects. As a result, the test was only performed under static conditions. Figure 6.10 shows the k_i value at different source levels plotted versus time. The average value of k_i from these tests is 0.31795 (lb-ft/A).

The values of factor k_i from both methods are very close. However, the frequency effect on the factor k_i is uncertain. As explained in Chapter 5, the factor k_i is related to the magnetic field of a magnet. The possibility of magnetic field varying with frequency is discussed in next section. Despite this, the variation of k_i with frequency that could theoretically occur does not cause a significant effect on the predicting equipment generated damping. This is discussed in Chapter 7. For this study, a value k_i equal to 0.318 is used for calculating torque and as a model parameter, which is assumed to be constant at all frequencies.

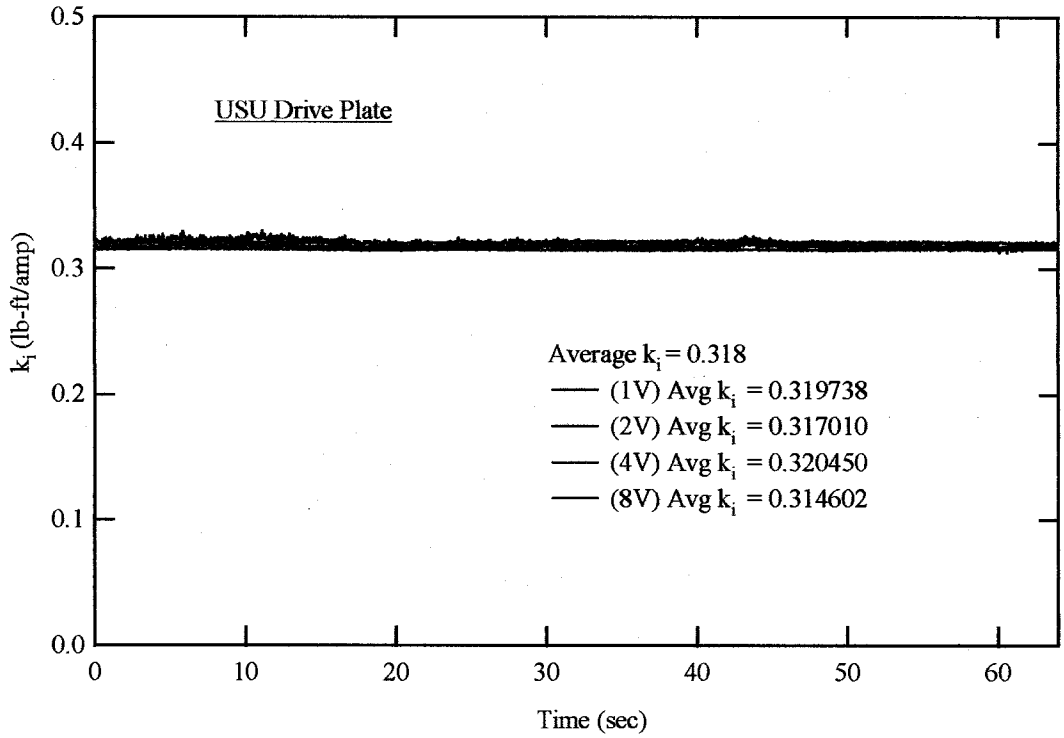

Figure 6.10 Static test results for k_i measurements of the USU drive plate

The torque sensor was used to measure the factor k_i for the UT drive plate. Results are plotted in Figure 6.11. An average k_i value of 0.657 lb-ft/A was measured. The k_i of UT drive plate is about twice the value measured for the USU drive plate. The difference in k_i values results from the different types of magnets in the drive plate. Referring to Equation 5.10, the value of k_i is proportional to the numbers of loops in the coil and the strength of magnetic field of the magnet. The magnets used in the USU drive plate are made from Alnico 5 and the magnets used in the UT drive plate No. 9 are maded from Alnico 8. The Alnico 8 magnet generates higher magnetic field than the Alnico 5 hence, the higher value of k_i for the UT drive plate.

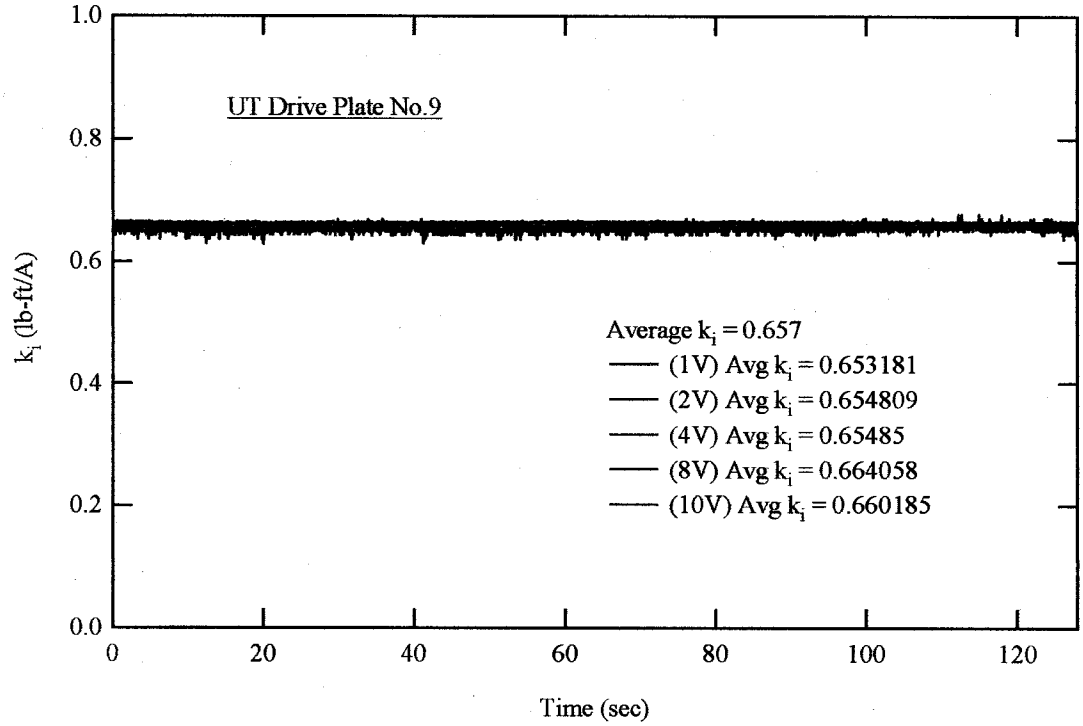

Figure 6.11 Static test results for k_i measurements of the UT drive plate No. 9

6.2.3 Back Emf – rotational Velocity Factor

As described in Chapter 5, the back electromotive force (back emf), ε_{emf}, is created from the movement of the magnet through coil. The back emf-rotational velocity factor, k_B is obtained from rearranging Equation 5.13 to gives:

$$k_B = \frac{\varepsilon_{emf}}{\partial\theta/\partial t}, \tag{6.8}$$

where $\frac{\partial\theta}{\partial t}$ = rotational velocity.

To measure the value of k_B, the drive coils were rewired and separated into two groups. Each group has two pairs of coils located opposite each other. One group was

used as the drive coils and the other was used as the response coils. Configuration of the drive coils and response coils and magnet for k_B measurement are shown in Figure 6.12.

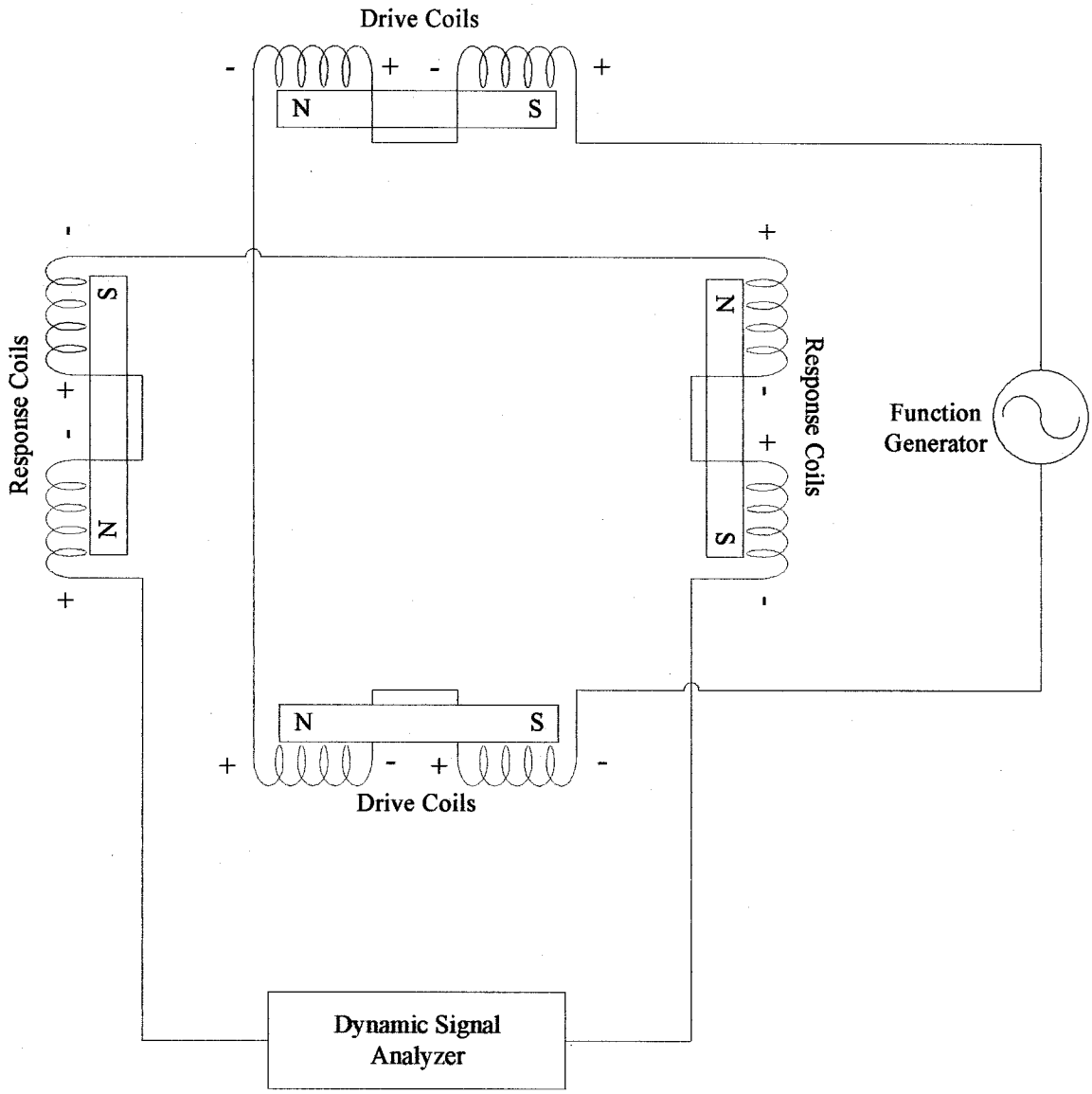

Figure 6.12 Configuration of coils and magnets for k_B measurement

The tests were performed using the calibration specimens. Electrical circuits of the drive and response coils are presented in Figure 6.13. Sinusoidal voltage with constant amplitude was applied to the drive coils over a frequency range of 0-400 Hz, creating the movement of the drive magnets and the magnets in the response coils. The back emf voltage occurring from movement of the magnets in the response coils and the drive plate rotation was measured. The value of k_B that represents all four coils is simply calculated from:

$$k_B = 2\frac{V_{out}}{\partial\theta/\partial t} = 2\frac{V_{out}}{\theta j\omega}, \tag{6.9}$$

where V_{out} = voltage potential across the response coils.

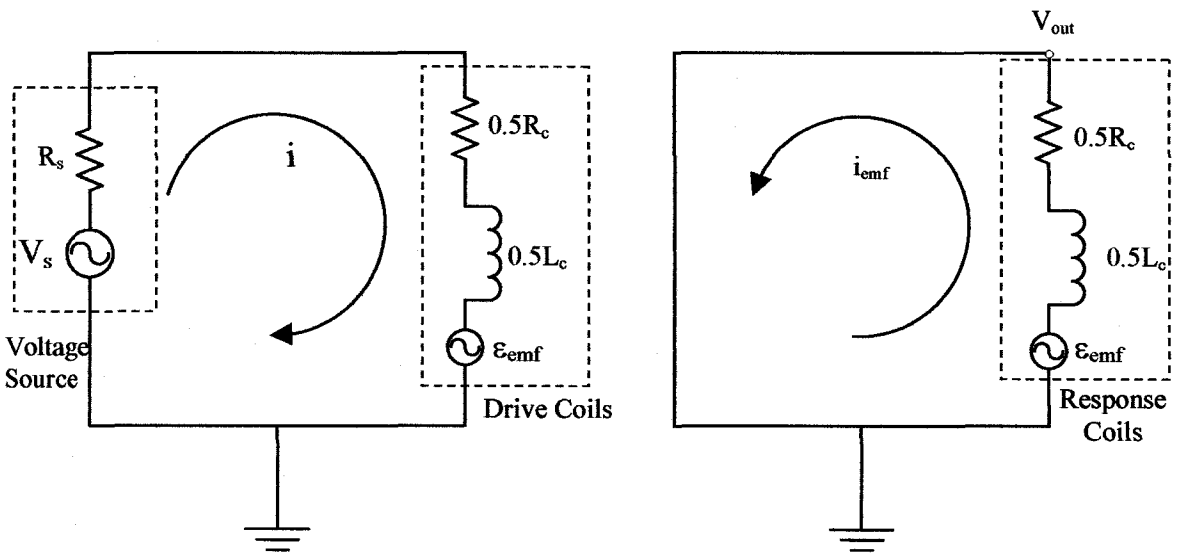

a) Drive coils b) Response coils

Figure 6.13 Electrical circuit setup for k_B measurement

In this study, an effect of crosstalk voltage was discovered during k_B measurement. The crosstalk effect occurs due to the voltage coupling between the response coils and the drive coils. The crosstalk tends to interfere with the measured V_{out} in the response coils. When the crosstalk is combined with the measured V_{out}, the calculated value of k_B becomes unrealistic. As shown in Figure 6.14, the crosstalk effect was investigated by an evaluation of the phase shift between the measured rotation and the V_{out}. According to Faraday's law, the back emf is proportional to the velocity or in this case, the rotation. This means that there should be no phase different between the back emf and rotation velocity. The phase shift of 180 degree observed in Figure 6.14a is clearly the effect of the crosstalk. If the crosstalk is not taken into account in this measurement, the value of k_B would be as shown in Figure 6.14b, with negative value of k_B at frequencies below the phase shift occurs. The physical meaning of the negative k_B is that the back emf turns the magnet and coil into a self-perpetuated motor driving itself, a physically impossible condition.

The crosstalk effect has to be taken into account for the k_B measurement. The simplest approach is to measured the crosstalk voltage and subtract it out from the measured V_{out}. The crosstalk voltage needs to be measured independently without the back emf effect. To accomplish this, the crosstalk measurement was performed using the rigid aluminum specimen. As explained earlier, the rigid specimen was used so that the back emf effect can be neglected. The cross talk test was performed using the same circuit as the k_B measurement, and V_{out} was measured and considered as the crosstalk voltage, V_c, as shown in Figure 6.15.

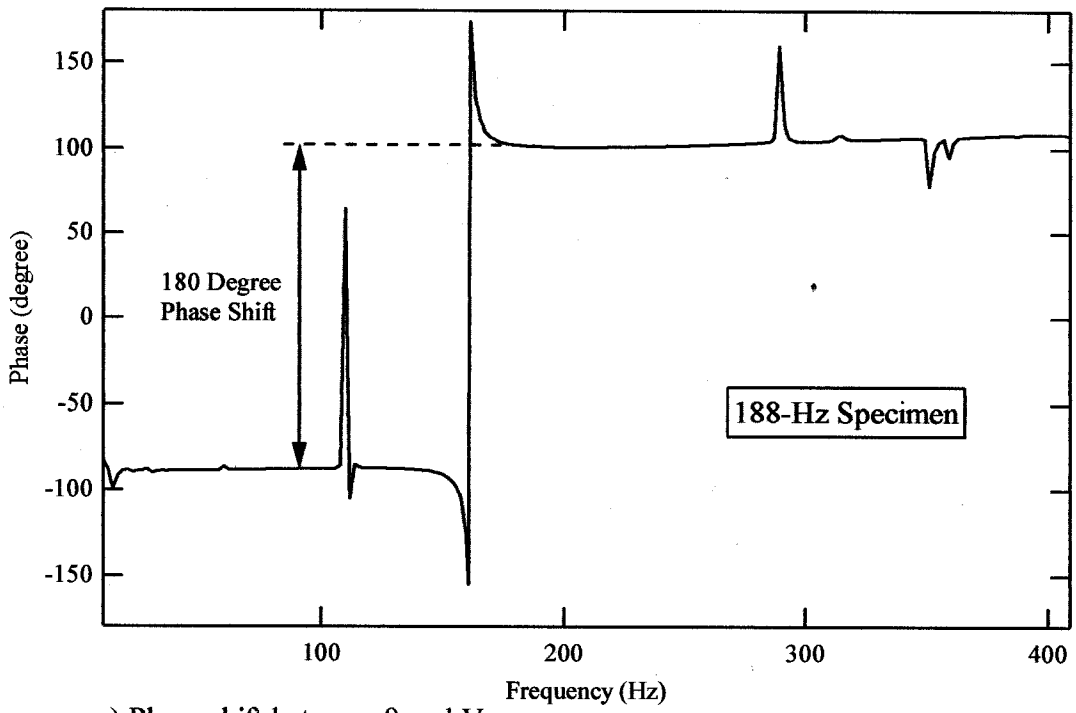

a) Phase shift between θ and V_{out}

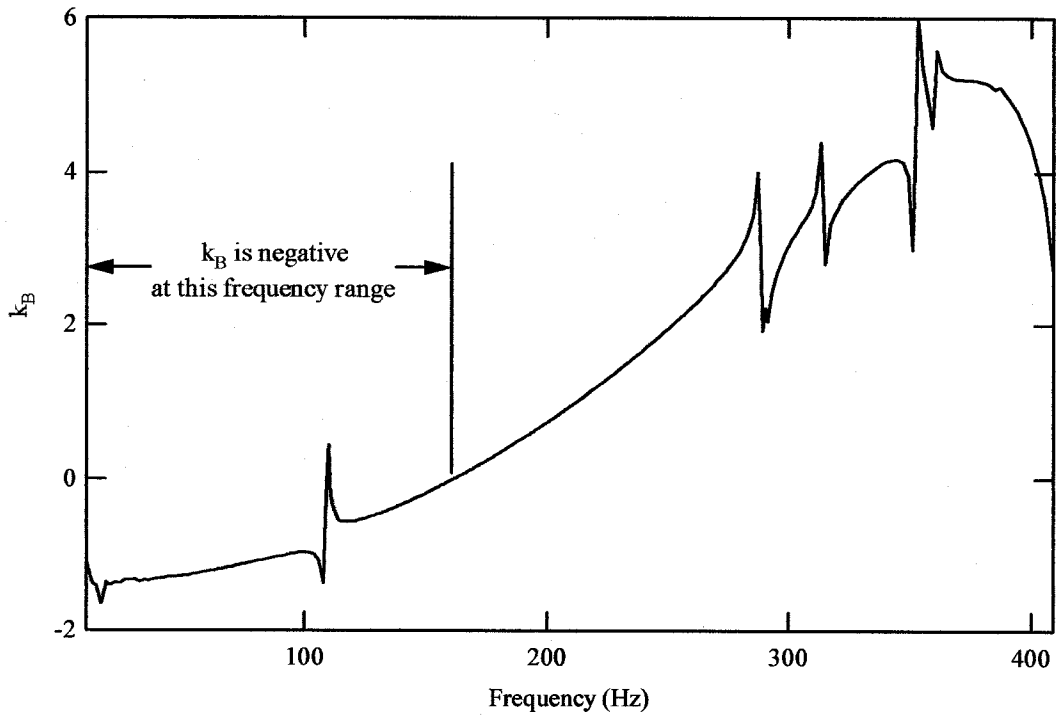

b) Measured k_B with crosstalk effect

Figure 6.14 Crosstalk effect on k_B measurement

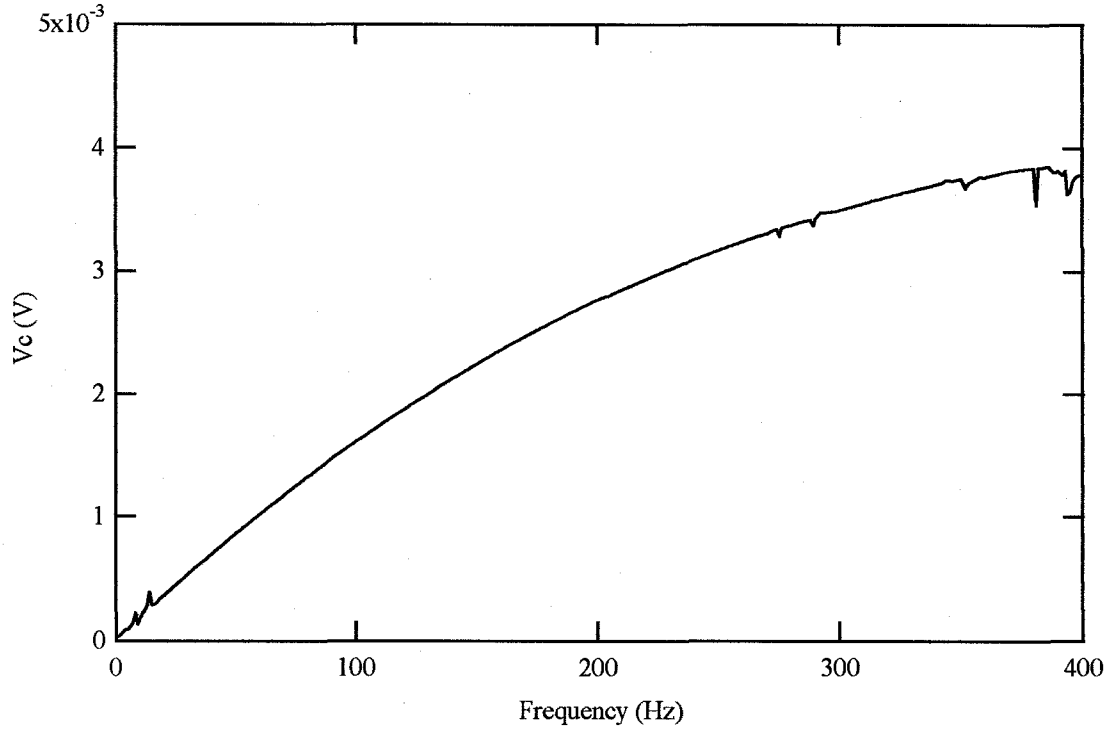

Figure 6.15 Variation of crosstalk voltage with frequency

The results shown in Figure 6.15 show that the crosstalk voltage developed during the measurement. The crosstalk increases up to about 4 mV as the frequency increases to 400 Hz. To account for the effect of crosstalk voltage, the behavior of crosstalk was investigated. Results from crosstalk measurement showed that the crosstalk was observed to be a function of the rate of change of current, $\partial i/\partial t$ which can be expressed as:

$$V_c = k_c \frac{\partial i}{\partial t} = k_c ij\omega . \qquad (6.10)$$

The constant k_c is called the crosstalk factor. The value of k_c is a complex number that consists of two parts; real and imaginary. The plot of k_c value versus frequency is

shown in Figure 6.16. There is a slightly variation in the real part of k_c with frequency and the imaginary part k_c is very small, thus it was neglected. Therefore, a k_c value of $-3.6x10^{-5}$ (V/A/s) is used for this study.

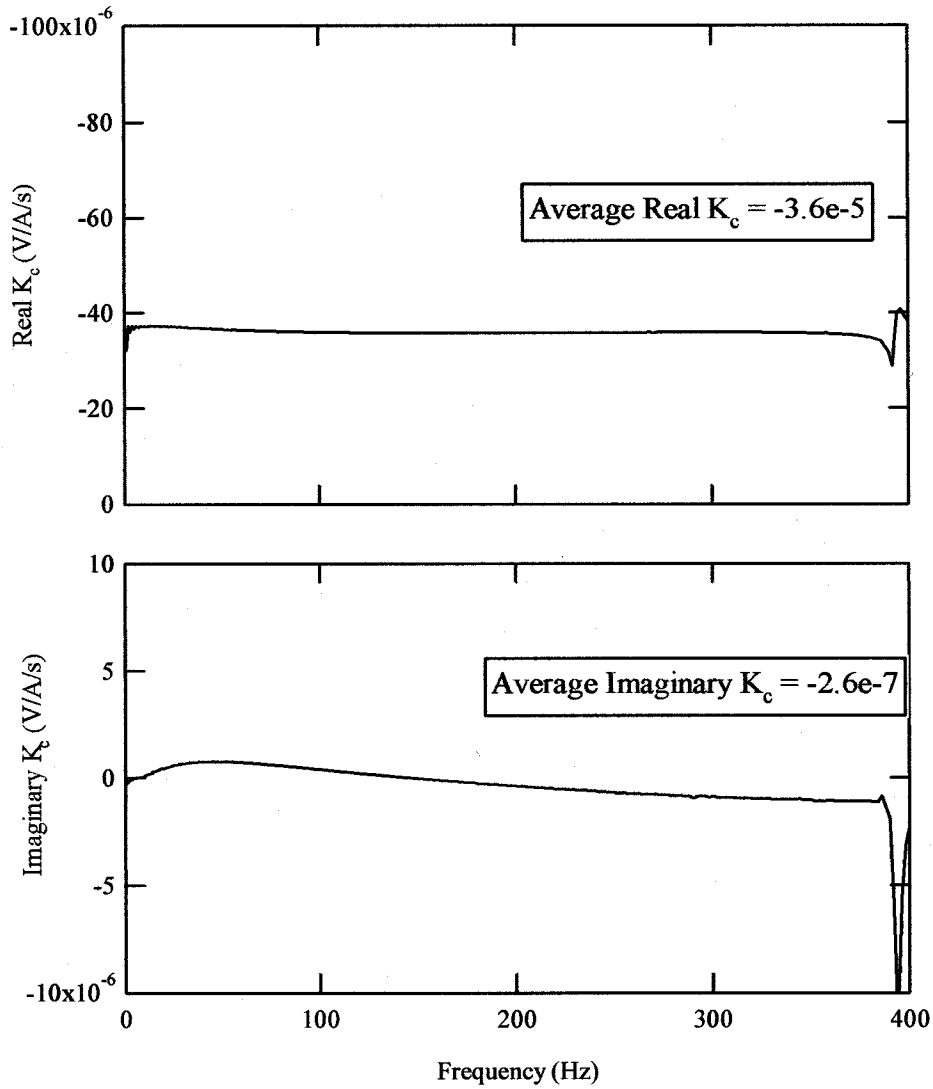

Figure 6.16 Variation of the crosstalk factor with frequency

The effect of crosstalk is taken into account by applying the crosstalk factor into the measured current when performing the k_B measurement. As a result, Equation 6.9 becomes:

$$k_B = 2\frac{V_{out} + k_c ij\omega}{\theta j\omega}. \qquad (6.11)$$

It is noted that the value of k_B calculated from Equation 6.11 is also a complex number. As explained earlier, the back emf is proportional to the velocity of the magnet. After correcting the crosstalk voltage, the back emf voltage should be in phase with the rotational velocity hence the real part k_B is a constant and the imaginary part is equal to zero.

Results of k_B measurement of the USU drive plate showing plots of the k_B value varying with frequency for four calibrated specimen are presented in Figure 6.17. It is observed the overall value of k_B is much smaller after being corrected for the crosstalk voltage and no negative values of k_B were measured. There is an increase of the real part k_B with frequency especially at frequency above 200 Hz. The same variation but less significant is also observed for the imaginary part k_B. The value of imaginary part k_B is very small and is neglected. Test results from different specimens are identical except for the outlying results from the specimen A with the resonant frequency of 14 Hz. This specimen is very soft and rocking motion may affect the test result. Curve fitting was performed for the average, upper and lower bound for the value of k_B varying with frequency, the curve fitting equations are presented in Figure 6.17.

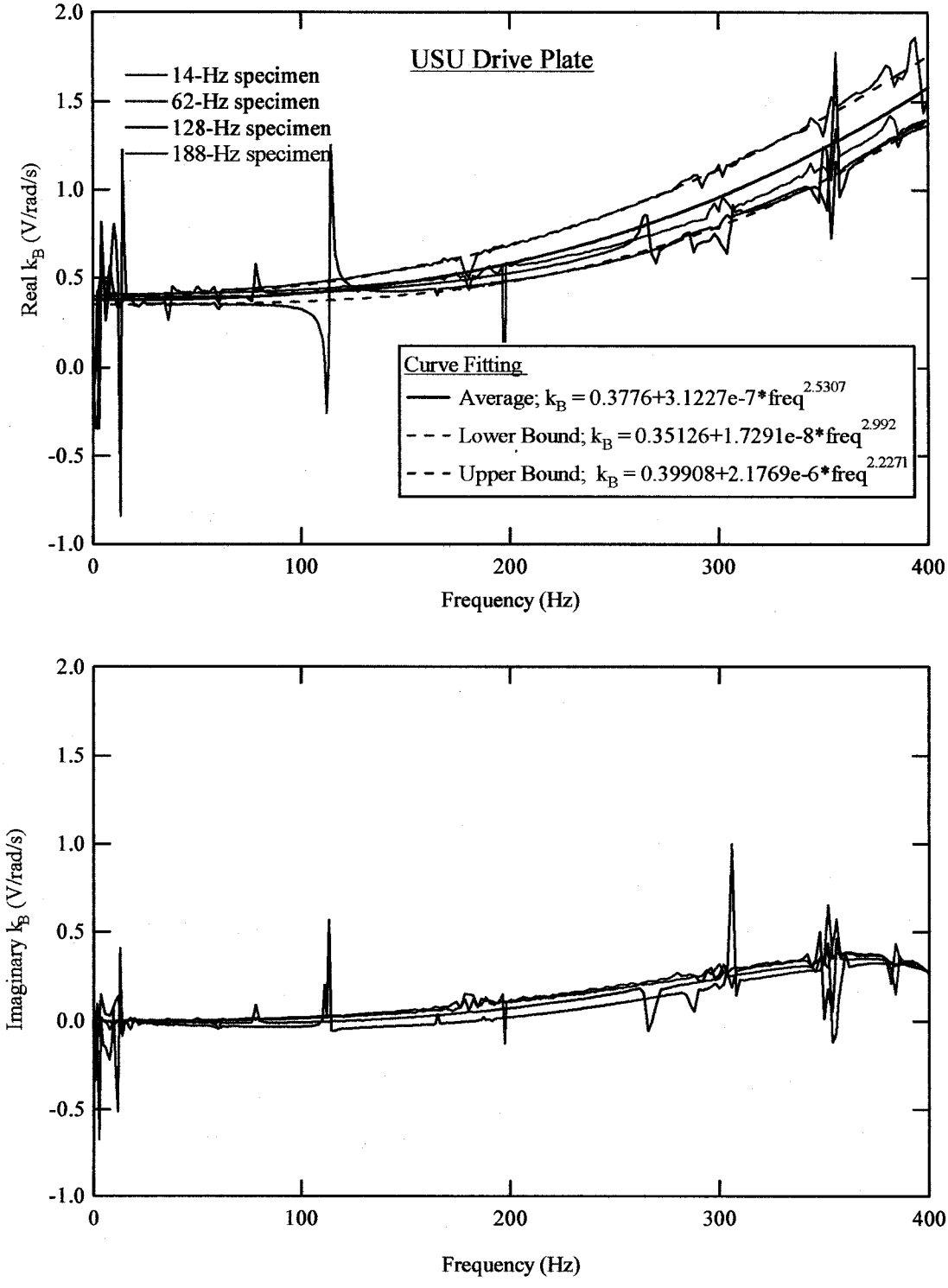

Figure 6.17 Variation of k_B with frequency for the USU drive plate

The same k_B measurement method was performed to measure the factor, k_B for the UT drive plate. Results for real part and imaginary part of k_B are plotted with frequency in Figure 6.18. The increasing trend was also observed for the UT drive plate. There is a less significant effect of the calibrated specimen on the k_B measurement, therefore, the curve fitting was performed on the average real part k_B. The curve fitting equation is presented in Figure 6.18. To compare this result with the result for the USU drive plate the curve fitting functions for both drive plates are plotted as shown in Figure 6.19. The factor k_B of the UT drive plate are found to be almost twice times of the factor k_B for the USU drive plate at low frequencies. The increasing rate of k_B values for the UT drive plate was lower than for the USU drive plate.

Referring to Equation 5.18, the value of k_B is a function of numbers of loops in the coils and magnetic field of the magnet. As discussed in previous section, different types of magnet were used for the UT drive plate and the USU drive plates. The stronger magnet is used for the UT drive plate. Therefore, a higher value of k_B for the UT drive plate is expected.

There is no clear explanation for the variation of k_B versus frequency. One possibility is that the magnetic field may vary with frequency. The change of magnetic field with frequency is not yet fully understood and requires further study. For the USU drive plate, the curve fitting equation for the average k_B is used and the difference between values of the upper and lower bound k_B is considered as an uncertainty. The uncertainty in k_B value of the USU drive plate is evaluated and discussed in Chapter 7. For the UT drive plate, the average curve fitting equation is used to represent the value of k_B with frequency.

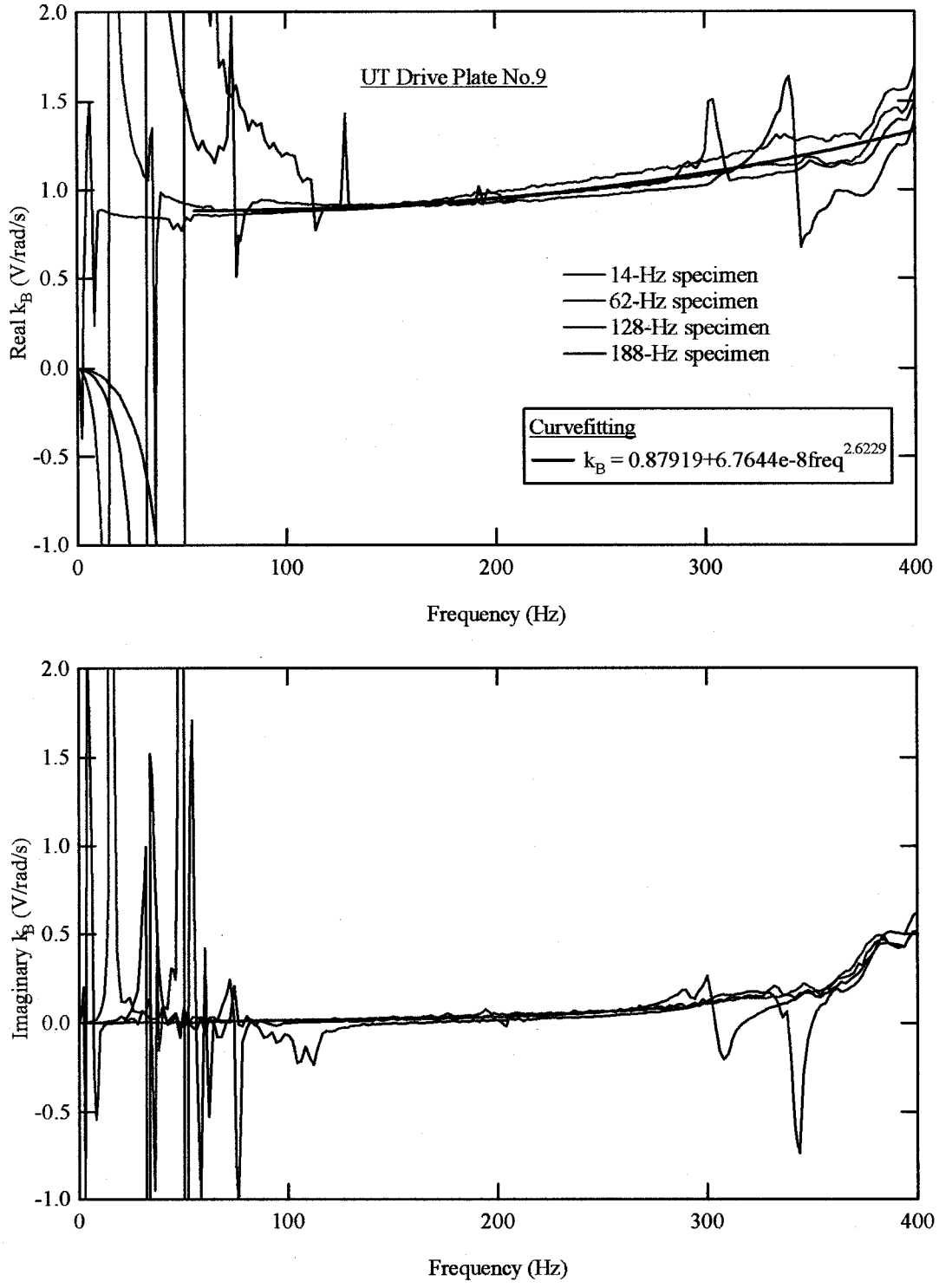

Figure 6.18 Variation of k_B with frequency for UT drive plate No. 9

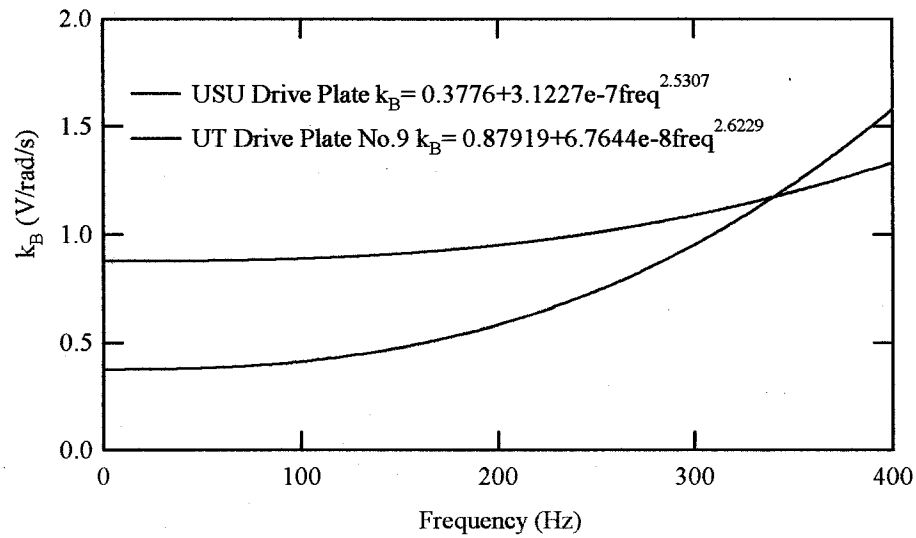

Figure 6.19 Comparison of k_B values for the USU drive plate and the UT drive plate

6.3 DRIVE PLATE EFFICIENCY

In this section, the strength of magnetic field, B, of the magnet for the USU and UT drive plate was measured. The value of B can be used to determine theoretical k_i and k_B for ideal coils and magnets. The calculated value of k_i and k_B were then compared with the measured value and efficiency of the drive plate can be evaluated.

Strength of magnetic field of each magnet was measured using a Gauss meter. The meter used was a DC Gauss meter Model DCM Serial 1487 manufactured by AlphaLab, Inc. Strength of magnetic field generated by all four magnets for the USU drive plate and UT drive plate No. 9 was measured. The measurement was performed at multiple positions on the cross sections of the north and south poles of the magnet. The values of B at different position varied slightly, however, the average B value for north and south pole of each magnet is differed by less than 10%. Therefore, an average B of all four magnets was used to represent the magnetic field of the drive plate. For the USU

drive plate, the average B was equal to 733 Gauss. For the UT drive plate No. 9, the average B was equal to 1463 Gauss. The B value for the UT drive plate No. 9 was about twice the value for the USU drive plate. This as expected due to the different magnet material used for each drive plate (Alnico 5 for the USU drive plate and Alnico 8 for the UT drive plate). These values were used for calculating the theoretical k_i and k_B for an ideal coil and magnet for each drive plate.

To calculate the theoretical value of k_i and k_B, Equation 5.13 and 5.18 are also presented in this chapter as shown below:

$$k_i = N_x N_y l_c B d, \tag{6.12}$$

and

$$k_B = \frac{2}{d}\frac{B A_c N_x N_y}{y}, \tag{6.13}$$

where B = magnetic field of the magnet,

N_x = number of loops in the coil in x-z plane,

N_y = number of loops in the coil in y-z plane,

L_c = circumference length of the coil loop,

A_c = cross section area of the coil loop in x-z plane,

y = width of coil loop in y direction, and

d = moment arm of the drive plate.

The cross section area and coil in x-z plane and y-z plane and the dimensions of coil are presented in Figures 6.20 and 6.21 for the USU and UT drive plate. Average circumference length of the coil loop and cross section area in x-z plane were determined. The number of loops in the coil in x and y direction were counted. The calculation of

theoretical of k_i and k_B was then performed based on this information and results are tabulated in Tables 6.2 and 6.3. It is important to note that unit of B is in Gauss and voltage is also in Joule/Coulomb, which are the SI unit, therefore in calculation, the unit conversion must be considered.

The theoretical value of k_i and k_B were calculated and compared with the measured value obtained in previous sections as shown in Table 6.2 and 6.3. The theoretical k_i values are equals to 0.426 and 0.828 for the USU and the UT drive plate. And, the theoretical k_B values are equals to 1.178 and 2.290 for the USU and the UT drive plate. The different between the theoretical and experimental value can be considered as an efficiency of the drive plate. The efficiency represents how well the drive plate performs in comparison with the theoretical prediction. The k_i, efficiency represents how much torque can be generated in an ideal coil and magnet compared to with the actual case, therefore, the k_i, efficiency represents torque efficiency of the drive plate. The torque efficiencies of 75% and 80% were obtained for the USU drive plate and the UT drive plates, respectively, as shown in Table 6.2.

For the case of k_B, the efficiency represents back emf efficiency of the drive plate. In this case, the measured value of k_B increases as the frequency increases. For this study, the k_B values in frequency range of 0-200 Hz is considered because the resonant frequencies of most soil type fall in this range. Therefore, a back emf efficiency was calculated for frequency range of 0-200 Hz as shown in Table 6.3. The back emf efficiency of 32-50% was obtained for the USU drive plate and 38-42% was obtained for the UT drive plate.

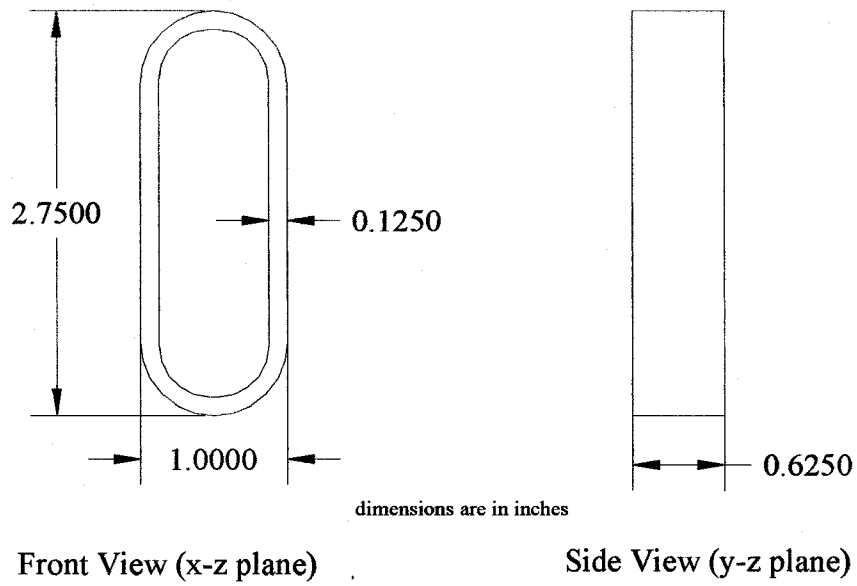

Figure 6.20 Cross sections of coil for the USU drive plate

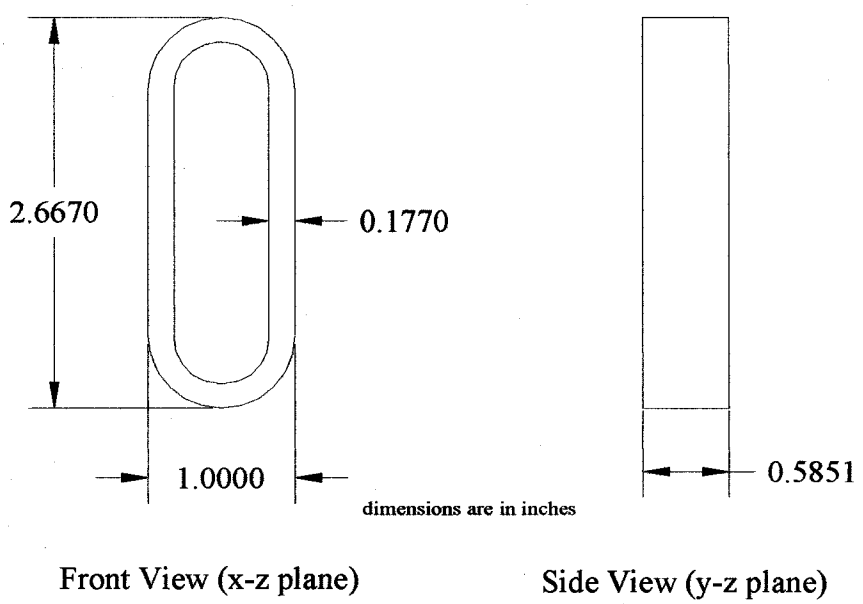

Figure 6.21 Cross sections of coil for the UT drive plate No. 9

Table 6.2 Calculation of Torque Efficiency

Drive Plate	l_c (in)	N_x (turns)	N_y (turns)	B (Gauss)	k_i (lb-ft/A)		
					Ideal k_i	Measured k_i	Efficiency (%)
USU	6.270	10	30	733	0.426	0.318	74.56
UT No. 9	5.949	8	38	1463	0.818	0.657	80.28

Table 6.3 Calculation of Back Emf Efficiency

Drive Plate	A_c (in^2)	y (in)	N_x (turns)	N_y (turns)	B (Gauss)	k_B (V/rad/s)		
						Ideal k_B	Mesured k_B[1]	Efficiency (%)
USU	2.153	0.625	10	30	733	1.178	0.378-0.585	32.06-49.73
UT No. 9	1.938	0.585	8	38	1463	2.290	0.879-0.953	38.39-41.59

Note: 1. The k_B values for frequency range of 0-200 Hz.

The efficiency for k_B is much lower than for the case of k_i because the calculation for k_B is based on the assumption that the magnetic field is uniform over the cross sectional area of the coil loop. If the torque efficiency is used as the ground truth, the actual cross section area with a uniform magnetic field is only about 50% of total area as the back emf efficiency is about 50% less than the torque efficiency.

6.4 SUMMARY

In this chapter, the measurements of parameters of the proposed electromagnetic model are presented. The experiment methods were developed to determine the variation of the parameters with frequency.

The coil resistance, R_c shows a slight variation with frequency. This is very small variation and can be neglected. The average coil resistance for all 8 coils is 45.6 ohms for the USU drive plate.

The coil inductance, L_c is constant for the frequency range of 0 to 400 Hz. A value of 0.0256 H was measured for the USU drive plate.

The torque-current factor, k_i measured from both low frequency and static condition are in agreement. Both methods of measurement are unable to evaluate the variation of k_i with frequency. In this study, the factor k_i is assumed to be a constant and equal to 0.318 lb-ft/A for the USU drive plate.

The crosstalk effect was found in the back emf-rotational velocity, k_B measurement. The crosstalk needs to be taken into account to determine the k_B values. The factor k_B increases from about 0.4 up to 1.4 V/rad/s for frequencies from 0 to 400 Hz. The uncertainty of k_B values measured from different calibrated specimen is shown in Figure 6.22. The curvefitting equation for the average k_B is used and the uncertainty is evaluated in Chapter 7.

The theoretical value of k_B and k_i can be predicted using the equations derived in Chapter 5. The theoretical k_i values are equals to 0.426 and 0.828 for the USU and the UT drive plate. And, the theoretical k_B values are equals to 1.178 and 2.290 for the USU and the UT drive plate. The torque and back emf efficiency represents the different between the measured and theoretical value of k_i and k_B. The torque effieciency for both drive plate was in the range of 75-80%. And, the back emf efficiency for both drive plate was in the range of 32-50%. The lower back emf efficiency is due to the lack of a section uniform magnetic field in the coil cross section.

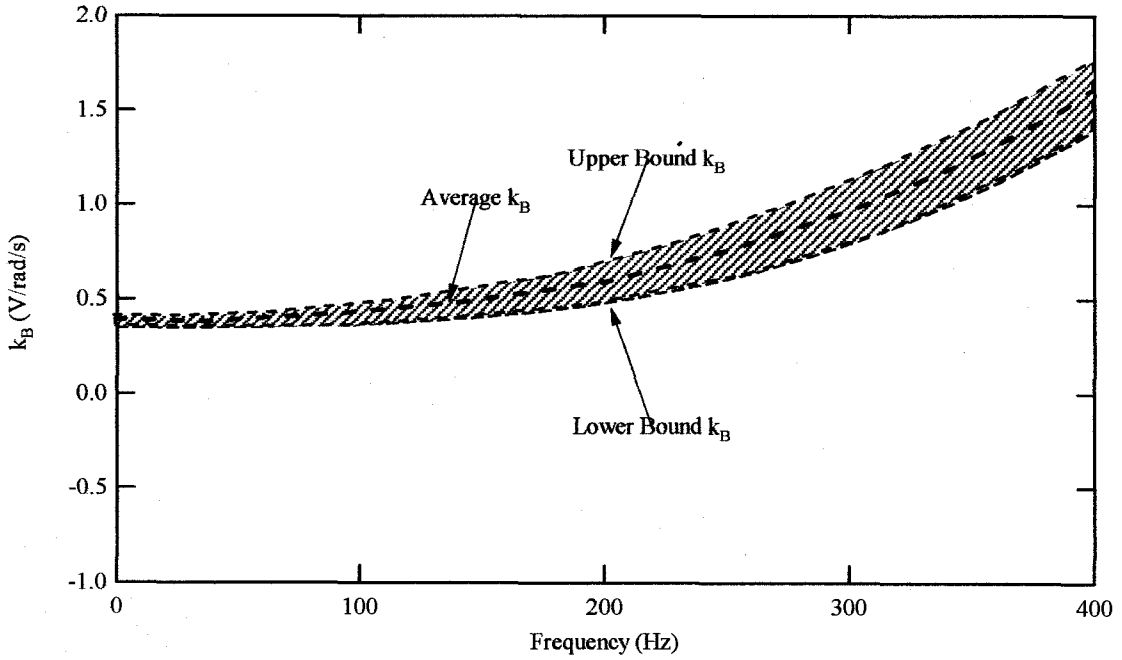

Figure 6.22 Uncertainty for the k_B measurement of the USU drive plate

CHAPTER 7

VERIFICATION OF ELECTROMAGNETIC MODEL

7.1 INTRODUCTION

In this chapter, measured equipment generated damping is compared to the predicted equipment generated damping using the electromagnetic model developed in Chapter 5. The model parameters used for these predictions were described in Chapter 6. The uncertainty in predicting equipment generated damping from the model parameters is evaluated. The model predictions for the USU drive plate are compared with the UT drive plate. Procedures to apply the electromagnetic model to RC and TS testing are presented. An explanation of discrepancies in the literature between predictions of the equipment generated damping in RC and TS test is presented.

7.2 MEASURMENT OF BACK EMF EFFECT

The electromagnetic model derived in Chapter 5, predicts that the back emf effects the stiffness and the damping of the system. The back emf effect tends to increase the measured resonant frequency and damping in the RC test and causes an error in torque measurement in the TS test. The effect of back emf on the TS test was found to be very small and negligible. This is discussed later in this chapter. This study primarily focuses on the back emf effect in the RC test. To verify the electromagnetic model prediction developed in this study, the back emf effects on the resonant frequency and damping need to be quantified.

The first step in quantifying the effects of back emf on resonant frequency and damping is to measure those properties without the back emf effect. One method that can

be used to eliminate the back emf effect is to perform the RC test with an open drive circuit. This is the same approach that was employed in Chapter 4. The drive plate calibration was performed on the calibration specimens with free vibration and an open drive circuit. The resonant frequency and material damping of each calibration specimen is reported in Table 4.4. These results are repeated in Tables 7.1-7.4 to show the resonant frequency and damping can be effect. A slight effect of added mass on material damping can be observed in Tables 7.1-7.4. Adding mass tends to slightly decrease the material damping of the calibration specimens. However, the damping values of the calibration specimens are very small, about 0.02%.

Once the stiffness and material damping of the calibration specimen was determined, the effects of back emf were measured. Typical RC tests using a closed drive circuit were performed by applying a constant force vibration over a band of frequency spanning the resonant frequency. The vibration response of the specimen at first mode resonance was evaluated. Because this experiment was performed with a closed drive circuit, the back emf effect was included. These tests were performed on each calibration specimen with added masses in the same manner as the drive plate calibration.

Table 7.1 Summary of Back Emf Effect for 14-Hz Specimen

K_θ = 17.942 lb-ft/rad						
Test	Without Back Emf		With Back Emf		Δf_m (Hz)	D_{eq} (%)
	f_m (Hz)	D (%)	f'_m (Hz)	D' (%)		
No Added Mass	14.314	0.020	14.321	0.739	0.0075	0.719
Mass No.1	13.603	0.013	14.608	0.686	0.0055	0.673
Mass No.2	12.988	0.020	12.993	0.653	0.0050	0.633
Mass No.3	12.463	0.011	12.468	0.612	0.0050	0.600

Table 7.2 Summary of Back Emf Effect for 62-Hz Specimen

K_θ = 343.80 lb-ft/rad						
Test	Without Back Emf		With Back Emf		Δf_m (Hz)	D_{eq} (%)
	f_m (Hz)	D (%)	f'_m (Hz)	D′ (%)		
No Added Mass	61.861	0.020	61.887	0.176	0.0262	0.158
Mass No.1	58.902	0.013	58.928	0.169	0.0263	0.160
Mass No.2	56.317	0.020	56.337	0.163	0.0205	0.155
Mass No.3	54.064	0.011	54.083	0.163	0.0188	0.150

Table 7.3 Summary of Back Emf Effect for 128-Hz Specimen

K_θ = 1560.60 lb-ft/rad						
Test	Without Back Emf		With Back Emf		Δf_m (Hz)	D_{eq} (%)
	f_m (Hz)	D (%)	f'_m (Hz)	D′ (%)		
No Added Mass	128.418	0.010	128.474	0.083	0.0558	0.073
Mass No.1	122.718	0.008	122.758	0.074	0.0400	0.066
Mass No.2	117.564	0.007	117.604	0.072	0.0400	0.065
Mass No.3	113.029	0.007	113.069	0.069	0.0400	0.062

Table 7.4 Summary of Back Emf Effect for 188-Hz Specimen

K_θ = 3768.53 lb-ft/rad						
Test	Without Back Emf		With Back Emf		Δf_m (Hz)	D_{eq} (%)
	f_m (Hz)	D (%)	f'_m (Hz)	D′ (%)		
No Added Mass	188.079	0.023	188.133	0.060	0.0534	0.038
Mass No.1	180.775	0.019	180.816	0.052	0.0415	0.034
Mass No.2	173.917	0.017	173.959	0.050	0.0422	0.033
Mass No.3	167.797	0.015	167.838	0.051	0.0406	0.036

Figure 7.1 shows the comparison between the response curves from tests with and without back emf effects on the 62 Hz calibration specimen. The response curve with the back emf effect clearly shows a much broaden shape hence higher damping. The resonant frequency for the test including the back emf is also slightly higher than the test without the back emf. Similar effects were observed for all of the other calibration specimens with and without added mass. Results of all the these tests are tabulated in Table 7.1-7.4. Note that symbol f'_m and D' represent the measured resonant frequency and damping that included the back emf effect.

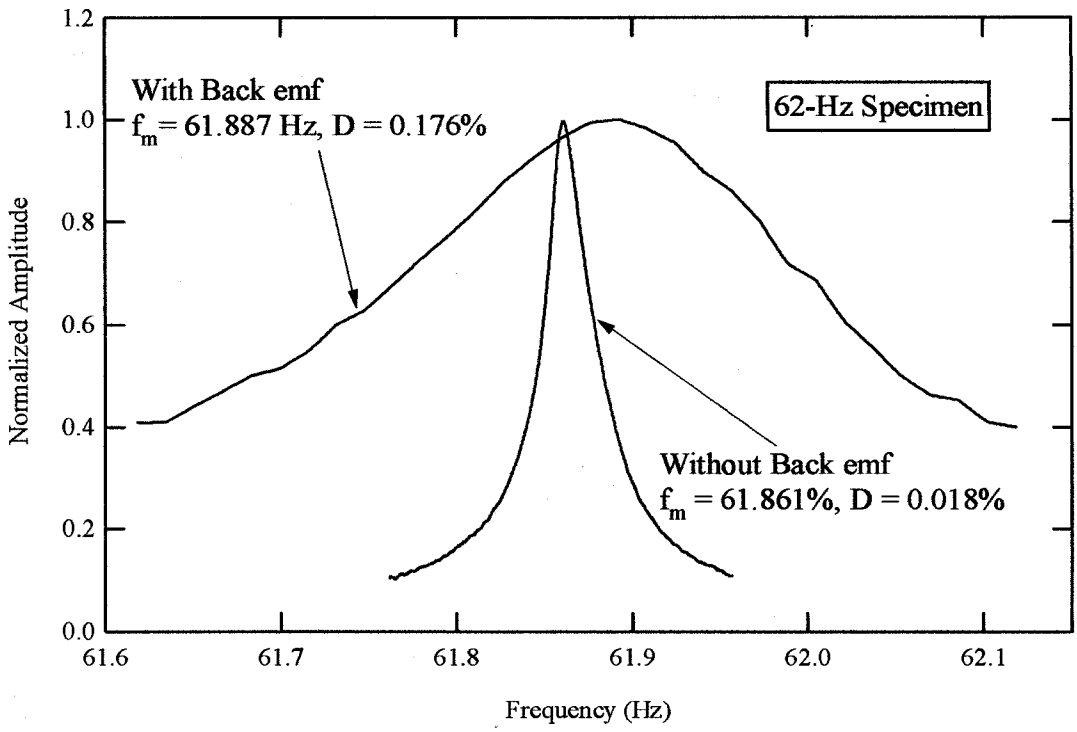

Figure 7.1 Typical back emf effect on the response curve in RC test

The increase of resonant frequency, Δf_m and the equipment generated damping, D_{eq}, are obtained from the difference between the resonant frequency and damping with and without back emf effect. The Δf_m represents the additional stiffness created from the effect of the back emf. This increase in stiffness is very small, less than 0.05%. The D_{eq} decreases as the resonant frequency increases. The increase of stiffness and damping are observed for all specimens. The variation of the Δf_m and the D_{eq} with resonant frequency are plotted in Figure 7.2.

The back emf effect on resonant frequency and damping of the UT drive plate were also evaluated. Similar tests were performed using the same calibration specimens and the values of Δf_m and the D_{eq} were determined. Figure 7.3 presents the plots of Δf_m and the D_{eq} with resonant frequency for both the USU drive plate and UT drive plate No. 9. In addition, the D_{eq} of UT drive plate No.4 measured by Hwang (1977) is also included in Figure 7.3. As shown in Figure 7.3, values of D_{eq} for UT drive plate No.4 measured Hwang are very similar to those measured on drive plate No. 9 in this study. The Δf_m of the UT drive plate shows an increasing trend except for the one data point at about 14 Hz. The values of Δf_m and D_{eq} for the UT drive plates are much higher than the values observed for the USU drive plate. The higher values are explained by the different magnet material thus the different value of k_i and k_B, as presented in Chapter 6.

In the electromagnetic model, the effect of back emf is presented in terms of k_{eq} and c_{eq}. The term k_{eq} and c_{eq} represents the equipment spring constant and equipment viscous damping coefficient due to the back emf. The measured k_{eq} and c_{eq} can be

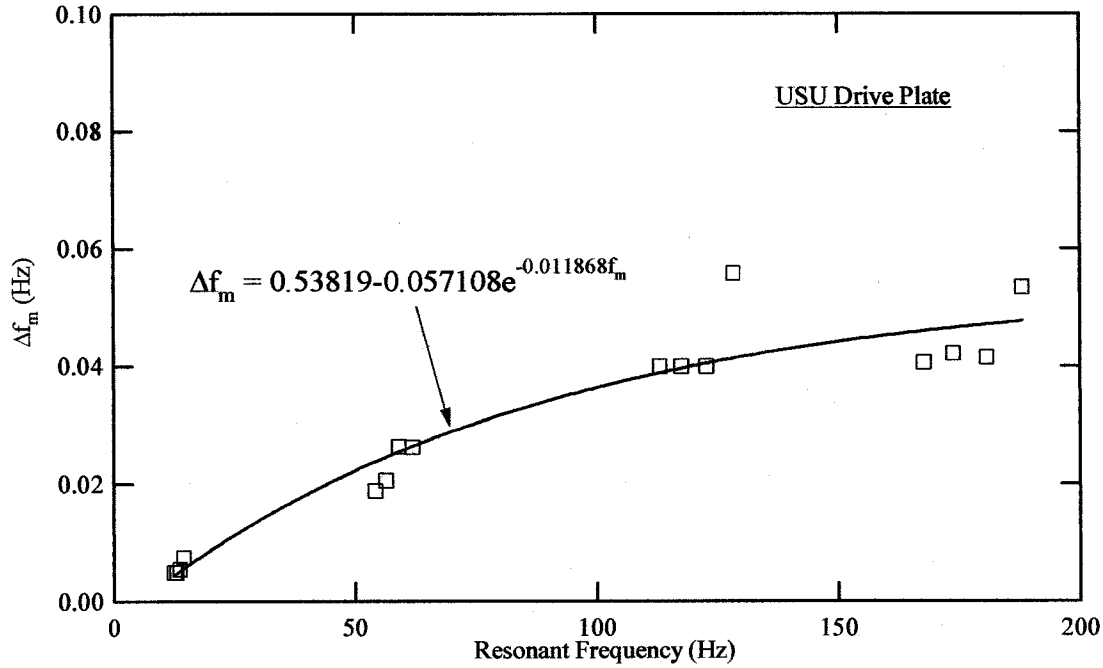

a) Change in resonant frequency, Δf_m, from back emf effect

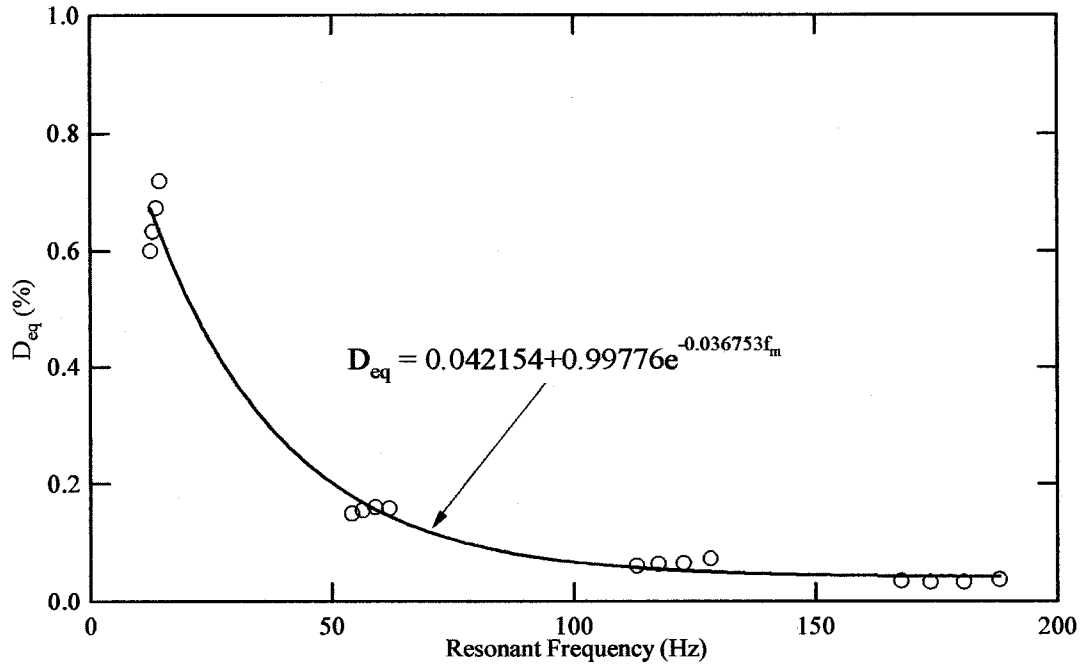

b) Equipment generated damping, D_{eq}, from back emf effect

Figure 7.2 Effect of back emf on the USU drive plate

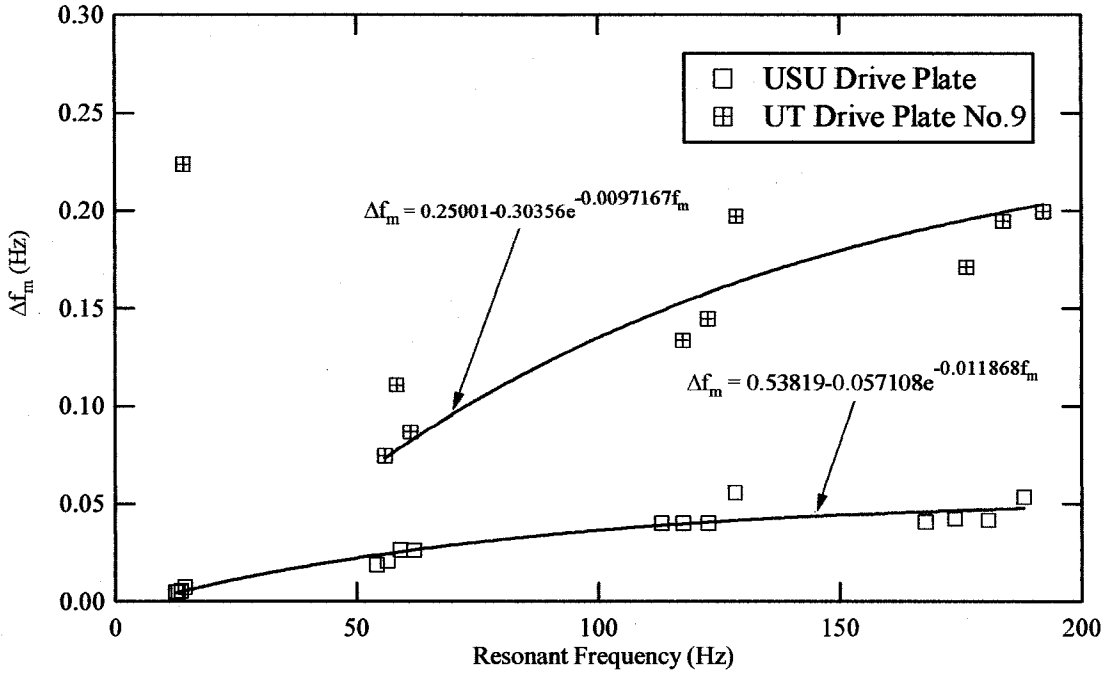

a) Change in resonant frequency, Δf_m, from back emf effect

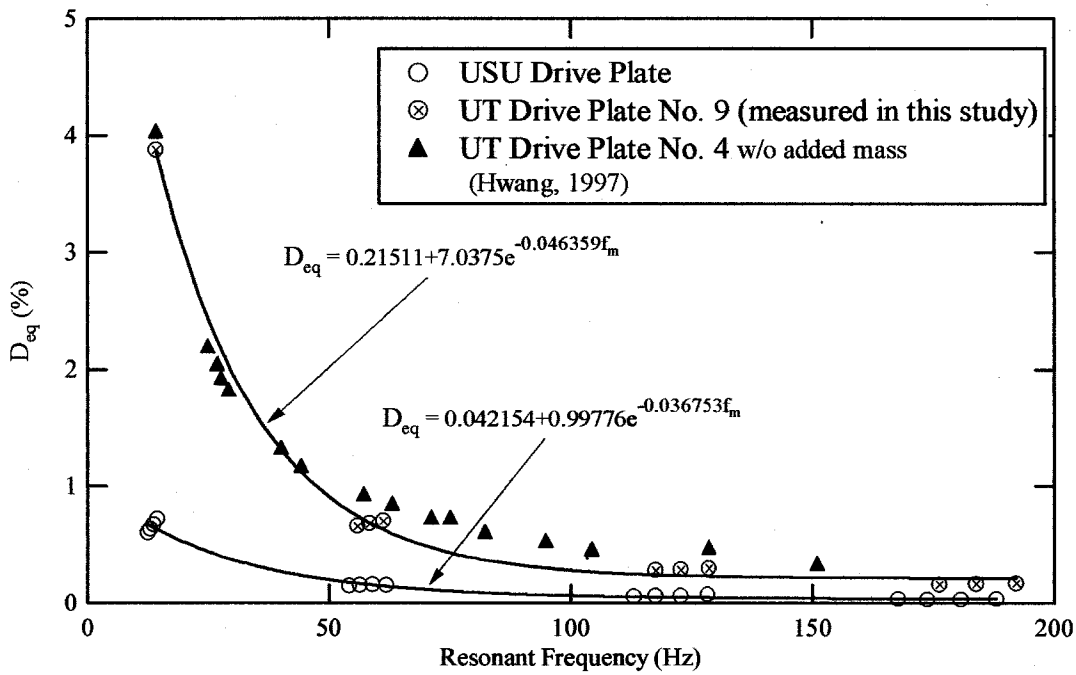

b) Equipment generated damping, D_{eq}, from back emf effect

Figure 7.3 Comparison of back emf effect for the USU drive plate and the UT drive plate

evaluated from the increases of resonant frequency and equipment generated damping, D_{eq} presented in Tables 7.1-7.4. The measured k_{eq} and c_{eq} are calculated from equations shown below:

$$k_{eq} = \left(\frac{2\pi f_m'}{\sqrt{1-2D'^2}} \right)^2 \Sigma J - K_\theta \text{, and} \tag{7.1}$$

$$c_{eq} = D_{eq} \left[4\pi \Sigma J \frac{f_m'}{\sqrt{1-2D'^2}} \right], \tag{7.2}$$

where K_θ = torsional spring stiffness of calibration specimen

ΣJ = total mass polar moment of inertia of the system.

The measured values of k_{eq} and c_{eq} calculated using Equations 7.1 and 7.2 for the USU and the UT drive plates are compared with the predicted values of k_{eq} and c_{eq} in next section.

7.3 ELECTROMAGNETIC MODEL

7.3.1 Model Prediction

The predictions were made of the equipment spring stiffness, k_{eq}, and equipment viscous damping coefficient, c_{eq}, due to the back emf using the electromagnetic model developed in this study. The terms k_{eq} and c_{eq} are parameters in the transfer function for a voltage measurement derived in Chapter 5. This transfer function is:

$$H_v = \frac{\dfrac{k_i}{R_c + j\omega L_c}}{\left[(k + k_{eq}) + j\omega(c + c_{eq}) - \omega^2 J \right]}, \tag{7.3}$$

$$k_{eq} = \frac{\omega^2 k_i k_B L_c}{R_c^2 + \omega^2 L_c^2}, \tag{7.4}$$

$$c_{eq} = \frac{k_i k_B R_c}{R_c^2 + \omega^2 L_c^2}, \tag{7.5}$$

where $\omega = 2\pi f$.

Four model parameters; R_c, L_c, k_i, and k_B can be used to predict the values of k_{eq} and c_{eq}. These parameters were measured using procedures described in Chapter 6. Results of the measurements of model parameters are summarized in Table 7.5 for the USU drive plate. Using these parameters, and Equations 7.4 and 7.5, values of k_{eq} and c_{eq} can be calculated for the back emf effect at any loading frequency.

Model parameters were measured at frequencies up to 400 Hz, however, verification of k_{eq} and c_{eq} is limited for frequencies below 200 Hz. This limitation is due to the lack of the measured values of k_{eq} and c_{eq} at frequency higher than 188 Hz. Predicting of the back emf effect for frequency above 200 Hz requires further study.

Table 7.5 Measured Model Parameters for the USU Drive Plate

Parameter	Unit	Variation with Frequency	Measured Value
Coil Resistance, R_c	ohm	Constant	45.6
Coil Inductance, L_c	henry	Constant	0.0256
Torque-current Factor, k_i	lb-ft/A	Uncertain	0.318
Back emf-rotataional velocity Factor, k_B	V/rad/s	Increasing	Upper Bound $k_B = 0.39908+2.1769e\text{-}6f^{2.2271}$
			Average $k_B = 0.3776+3.1227e\text{-}7f^{2.5307}$
			Lower Bound $k_B = 0.35126+1.7291e\text{-}8f^{2.992}$

Figure 7.4 shows the comparison of measured and predicted values of k_{eq} and c_{eq}. The upper and lower bounds in the prediction represent the uncertainty in the measurement of k_B. The measured and predicted values of k_{eq} increase with frequency in similar fashion. However, the model prediction underestimates the value of k_{eq} at frequency between 60 and 130 Hz. This discrepancy is of little concern because the effect of back emf on resonant frequency is very small, less than 0.05%. The measured values of c_{eq} scattered and reasonably constant over the frequency range of 0-130 Hz, with a slight decrease at higher frequency. The prediction shows slightly underestimates c_{eq} for frequencies below 60 Hz.

There are two possible explanations for the underprediction of c_{eq} values using the electromagnetic model. First, the model was developed based on the assumption that the equipment generated damping is solely the product of the back emf effect. In actual system, additional energy losses can be created from other sources. Typically, these additional energy losses only have a very small effect on damping, thus it can be neglected. Second, the variation of k_i with frequency is uncertain. As discussed in Chapter 6, the measurement method used for measuring the factor k_i was unable to obtain the variation of k_i with frequency and the parameter was assumed to be a constant with frequency. To evaluate a possible variation of k_i with frequency, Equation 7.5 was used to back calculate possible values of k_i. These values are plotted in Figure 7.5. This figure shows that a slight variation in k_i values will improve the agreement between the measured and predicted c_{eq}.

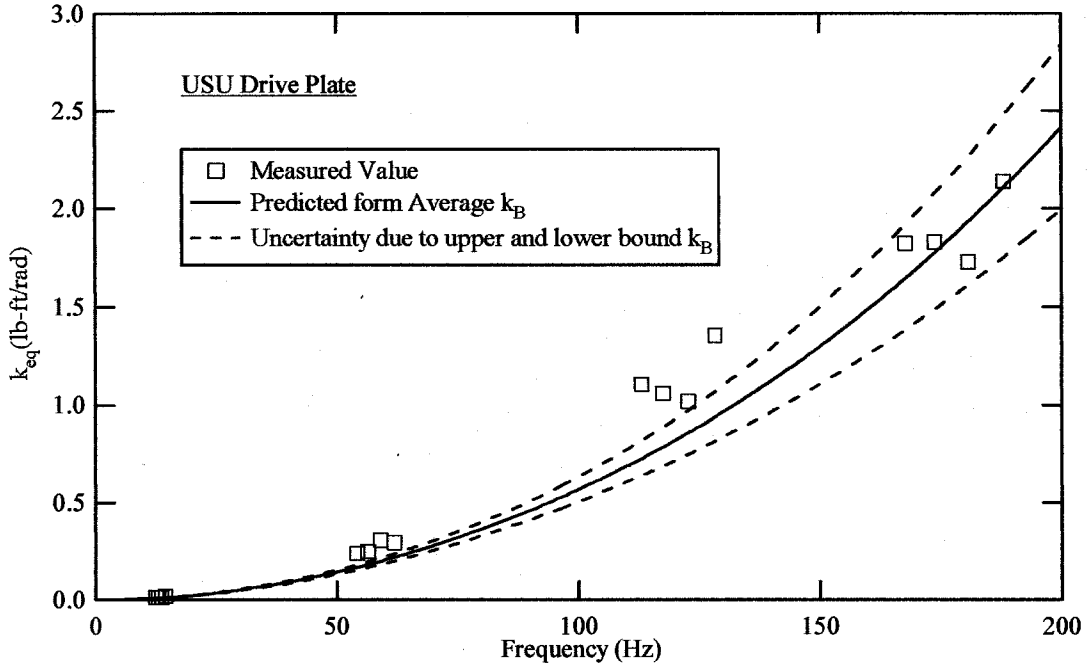

a) Measured and predicted value of k_{eq}

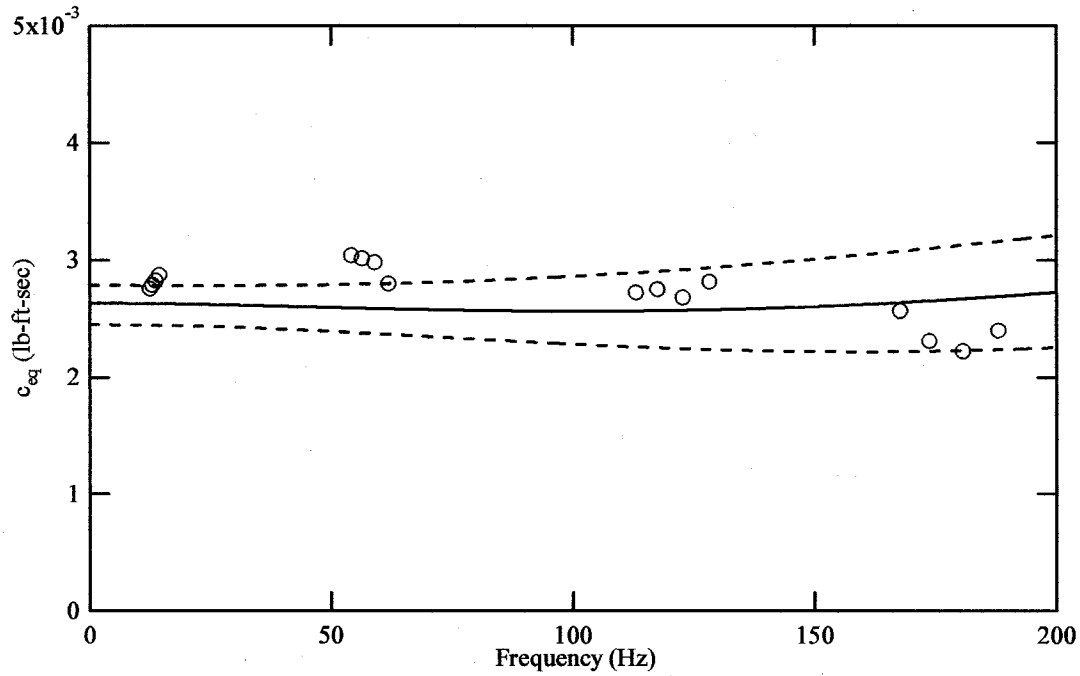

b) Measured and predicted value of c_{eq}

Figure 7.4 Comparison of the measured and predicted values of k_{eq} and c_{eq} for the USU drive plate

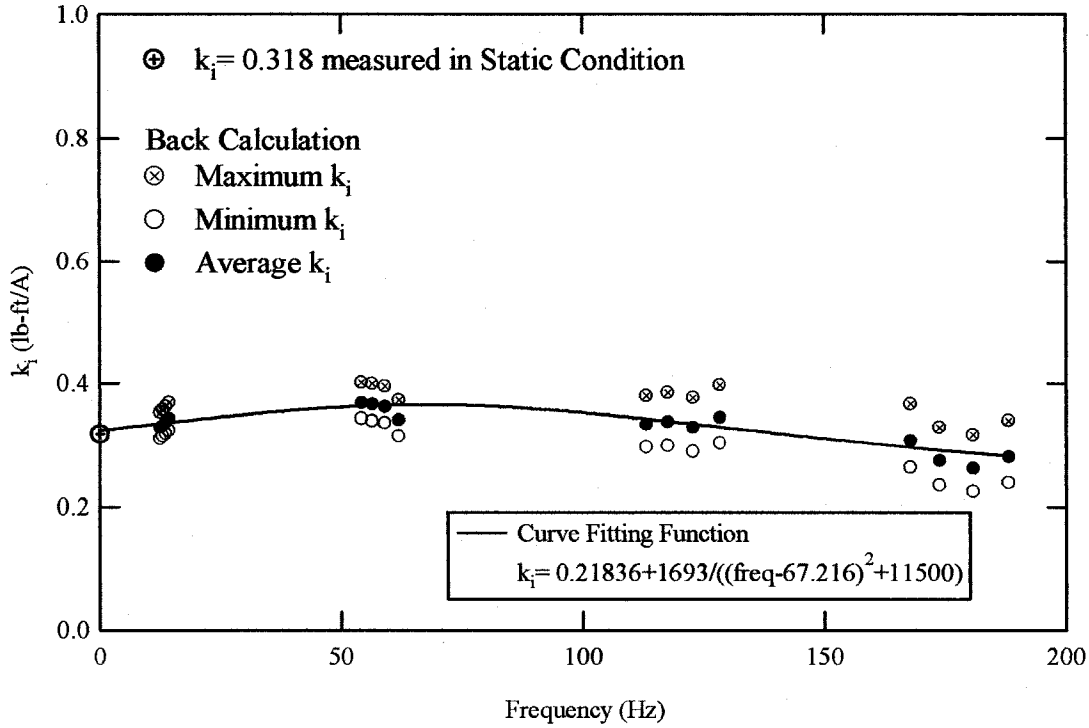

Figure 7.5 Back calculated k_i from measured c_{eq} using the electromagnetic model

A summary of the model parameter for the UT drive plate is presented in Table 7.6. The comparison of the measured and predicted k_{eq} and c_{eq} of the UT drive plate is also plotted in Figure 7.6. For this drive plate, c_{eq} was again slightly underpredicted at low frequencies. The model performs very well at higher frequencies in predicting both k_{eq} and c_{eq}. The error in predicting c_{eq} values at low frequency for the UT drive plate may come from the sources as discussed earlier.

7.3.2 Model Verification

The electromagnetic model is verified by comparing the model prediction of Δf_m and D_{eq} with the measured values. The primary focus of this study is the prediction of D_{eq} because the Δf_m is very small and can be neglected. The measured values of Δf_m and

Table 7.6 Measured Model Parameters for the UT Drive Plate

Parameter	Unit	Variation with Frequency	Measured Value
Coil Resistance, R_c	ohm	Constant	44.7
Coil Inductance, L_c	henry	Constant	0.02375
Torque-current Factor, k_i	lb-ft/A	Uncertain	0.657
Back emf-rotataional velocity Factor, k_B	V/rad/s	Increasing	$k_B = 0.87919+6.7644e\text{-}8f^{2.6929}$

D_{eq} were presented earlier in this chapter. The predicted Δf_m and D_{eq} are determined from the predicted values of k_{eq} and c_{eq} presented earlier. The predicted values of Δf_m and D_{eq} can be determined from Equations 5.34 and 5.35 which are also presented below:

$$\Delta f_m = \frac{1}{2\pi}\left[\sqrt{\frac{K_\theta + k_{eq}}{\Sigma J}}\sqrt{1-2(D+D_{eq})^2} - \sqrt{\frac{K_\theta}{\Sigma J}}\sqrt{1-2D^2}\right], \text{ and} \tag{7.6}$$

$$D_{eq} = \frac{c_{eq}}{c_c}. \tag{7.7}$$

In this case, the torsional stiffness and damping of calibration specimen and polar moment of inertia of the system are known therefore, the Δf_m and D_{eq} can be evaluated with frequency from Equations 7.6 and 7.7.

Figure 7.7 shows the measured and predicted effects of back emf on Δf_m and D_{eq} with resonant frequency for each calibration specimen, with and without the added mass for the USU drive plate. The values presented in Figure 7.7 are the average predicted value and the error bars represent the uncertainty in the model prediction.

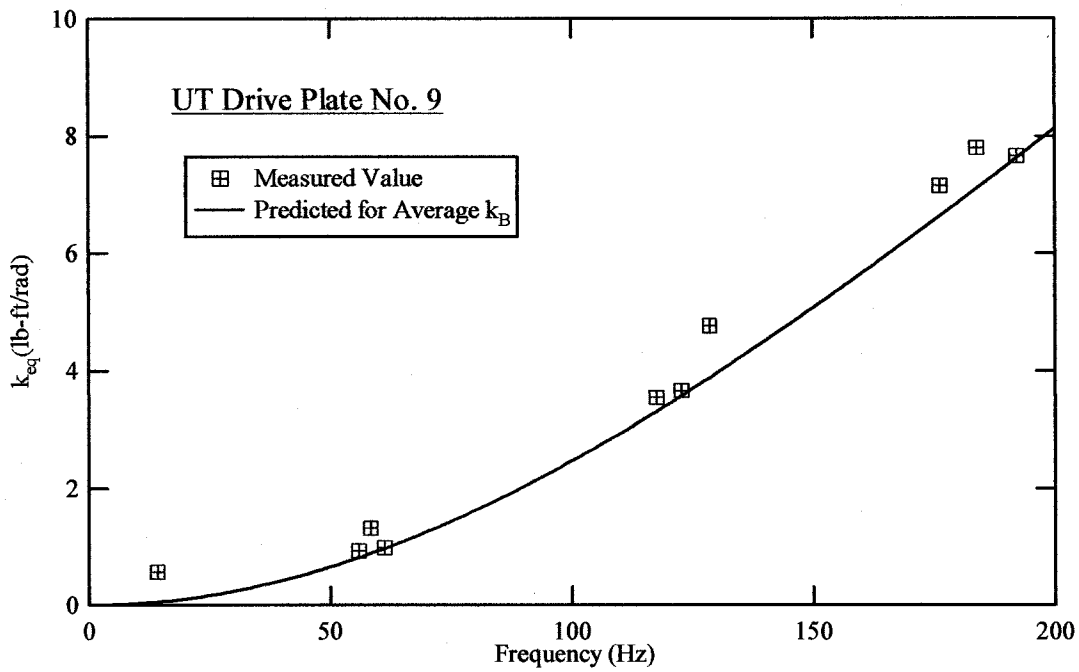

a) Measured and predicted value of k_{eq}

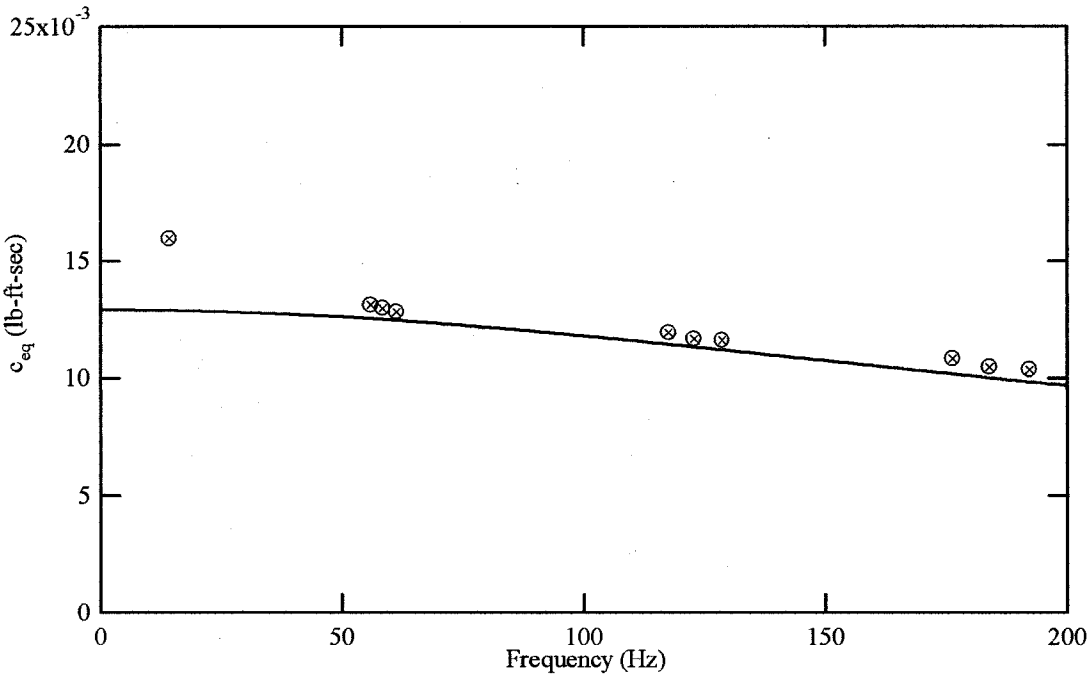

b) Measured and predicted value of c_{eq}

Figure 7.6 Comparison of the measured and predicted values of k_{eq} and c_{eq} for the UT drive plate No. 9

An exponential function was fitted to the measured and predicted values. Predictions of Δf_m are not especially good, however, this is of little concern because Δf_m is very small. The model accurately predicts D_{eq}. It slightly underestimates the values of D_{eq} for resonant frequencies between 14 and 62 Hz, and overestimates D_{eq} for resonant frequencies between 128 and 188 Hz. However, these errors are inconsequential.

The model performs very well in predicting the Δf_m and D_{eq} for the UT drive plate as shown in Figure 7.8. In these tests, large amounts of ambient noise corrupted low-frequency measurements. If the Δf_m measurement at 14 Hz is ignored, the model predicting Δf_m performs better for the UT drive plate than the USU drive plate. The model underpredicts the D_{eq} at 14 Hz by about 0.7%, however, the matches between measured and predicted values is very good for the higher frequencies. One possible explanation for the better performance of the model for the UT drive plate is that back emf effects are larger for the UT drive plate, so small errors and inconsistencies in the model have less effect.

7.3.3 Model Application for RC and TS Test

As explained in Chapter 5, different methods should be used to account for the back emf effect in RC and TS tests. The electromagnetic model prediction presented earlier was verified for the RC test. The model can also be used for the TS test. In this section, an example of the application of electromagnetic model to account for the back emf effect in RC and TS is presented.

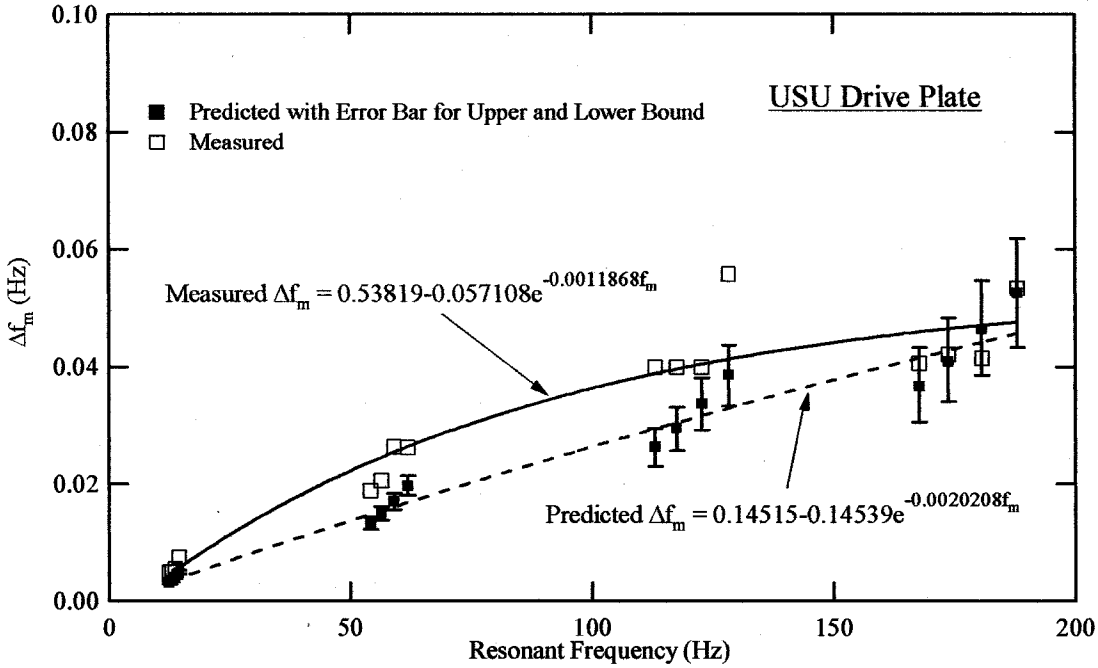

a) Measured and predicted value of Δf_m

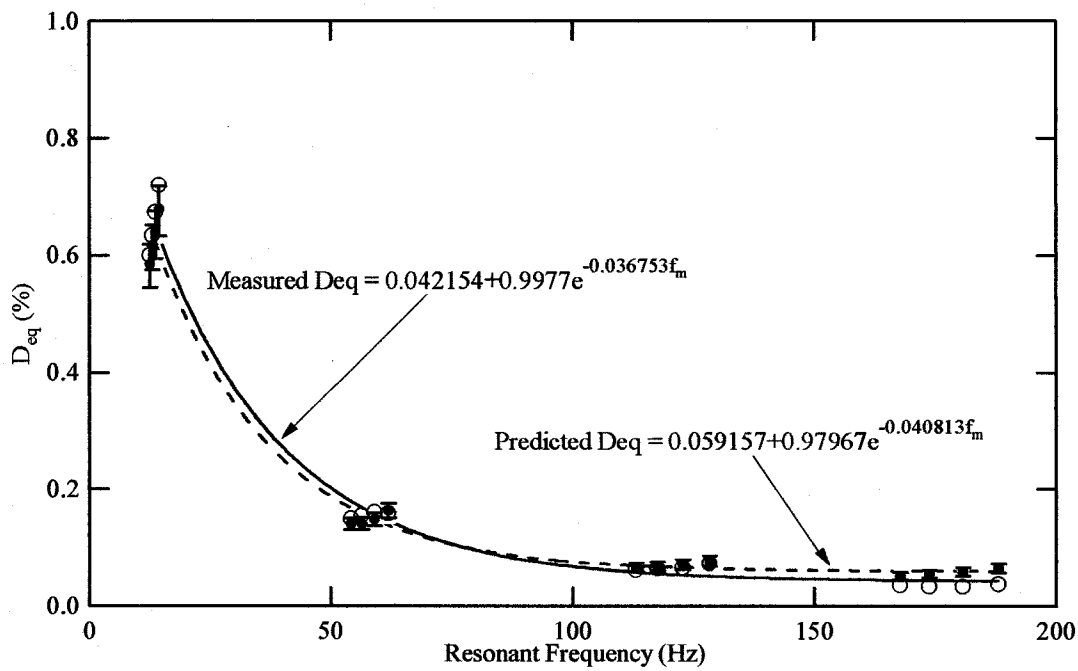

b) Measured and predicted value of D_{eq}

Figure 7.7 Electromagnetic model prediction of Δf_m and D_{eq} for the USU drive plate

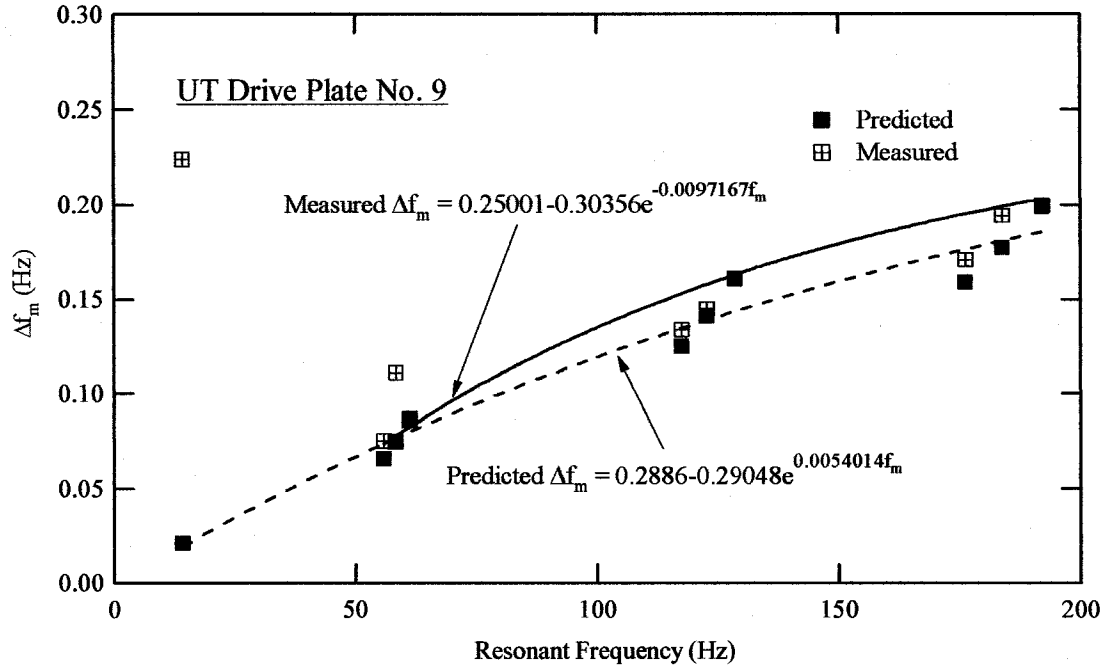

a) Measured and predicted value of Δf_m

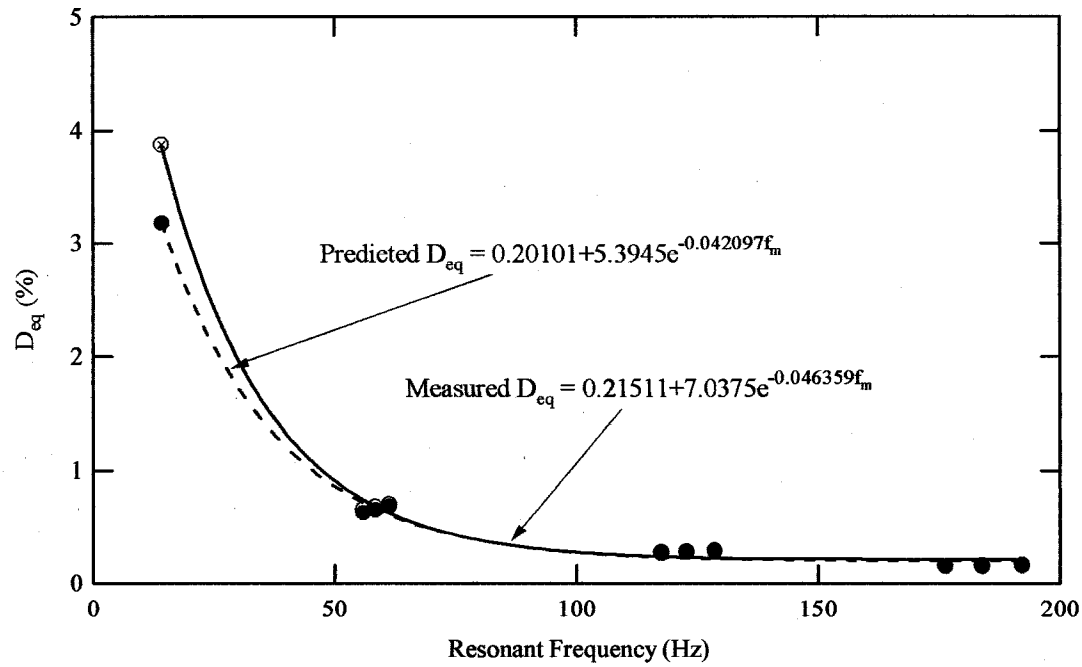

b) Measured and predicted value of D_{eq}

Figure 7.8 Electromagnetic model prediction of Δf_m and D_{eq} for the UT drive plate No. 9

For the RC test, the increasing of resonant frequency due to the back emf effect is very small and can be neglected. The electromagnetic model is mainly employed for predicting the back emf effect on damping measurements. As explained earlier, the model presents the back emf effects on damping in term of c_{eq}. The value of c_{eq} can be predicted by using measured model parameters and Equation 7.5. The equipment generated damping due to the back emf effect, D_{eq}, is evaluated from a ratio of c_{eq} and critical damping coefficient, c_c, presented earlier in Equation 7.7. c_c is a function of resonant frequency, f_m, and total mass polar moment of inertia of the system, ΣJ, as presented below:

$$c_c = 4\pi f_n \Sigma J, \tag{7.8}$$

where $f_n = \dfrac{f_m}{\sqrt{1-2D^2}}$.

Equation 7.8 implies that the D_{eq} is not only a function of resonant frequency but also a function of ΣJ. Therefore, the different damping corrections should be applied for different sized specimens, and different drive plates and top platens. Equipment generated damping can be calculated by determining c_{eq} from the electromagnetic model, c_c from the resonant frequency of the specimen and moment of inertia of the drive plate and top platen. Measured damping, D' can be corrected using:

$$\text{Corrected } D = D' - D_{eq} \tag{7.9}$$

In addition, the model can be used to predict the response curve that included the back emf effect. Equations 7.3-7.5 are used to generate a transfer function for a voltage measurement in RC tests. The response curve is a plot of this transfer function versus

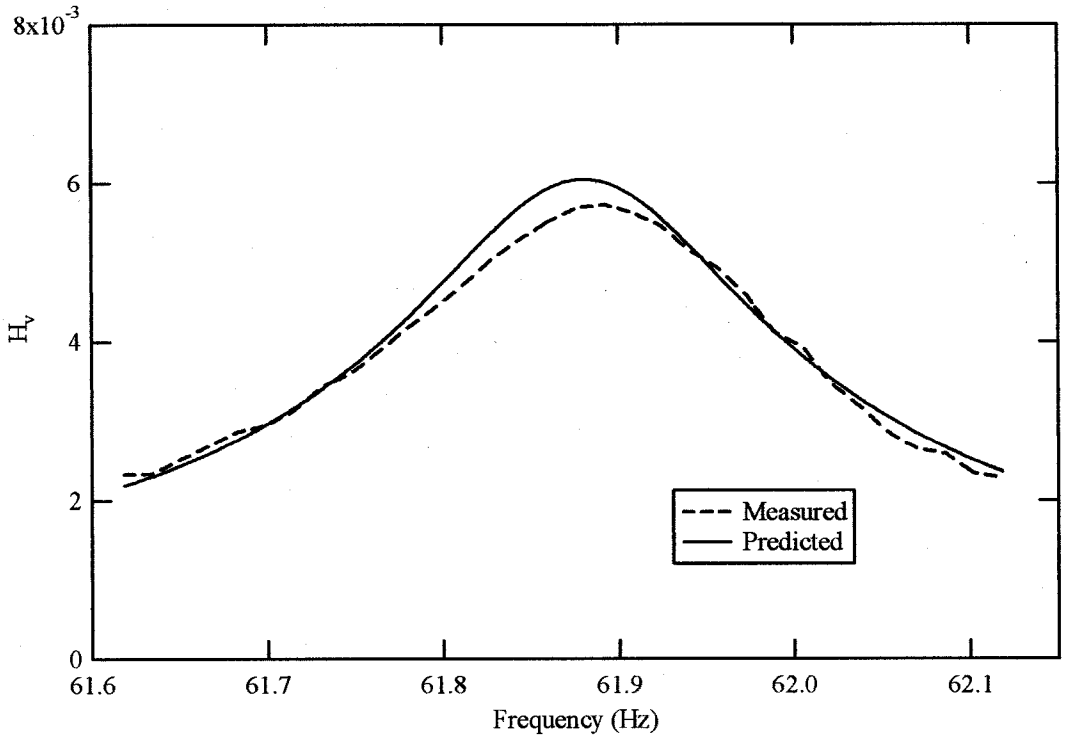

Figure 7.9 Predicting response curve for RC test using the electromagnetic model

frequency. Figure 7.9 shows an example of model prediction of response curve for the RC test on the 62 Hz calibration specimen.

For the TS test, loading frequency is much lower than in the RC test, hence, the rotational velocity of the magnet is much lower. As described in Chapter 5, torque created in the RC/TS drive system is partially transmitted to the dashpot, thus the actual torque applied to the drive plate needs to be corrected. The measured torque can be corrected by using Equation 5.36, which is repeated here:

$$T_c = T_m - (k_{eq}\theta + c_{eq}s\theta) = k_\theta\theta + c_\theta s\theta + Js^2\theta\,, \tag{7.10}$$

where T_c = corrected torque due to the back emf,

T_m = measured torque,

θ = rotational angle,

k_θ = torsional spring stiffness of soil specimen,

c_θ = torsional coefficient of viscosity of soil specimen,

J = mass polar moment of inertia of the system, and

$s = j\omega$ ($\omega = 2\pi f$).

Because the loading frequency is very low in the TS test, the c_{eq} has a very small effect to the applied torque. Figure 7.10 shows the measured and corrected torque calculated from Equation 7.10 for a TS test on soil specimen at 0.333 Hz. Both curves are virtually identical, therefore the stiffness and damping calculated from these torques are exactly the same. As a result, the effect of back emf in the TS test is very small and can be neglected.

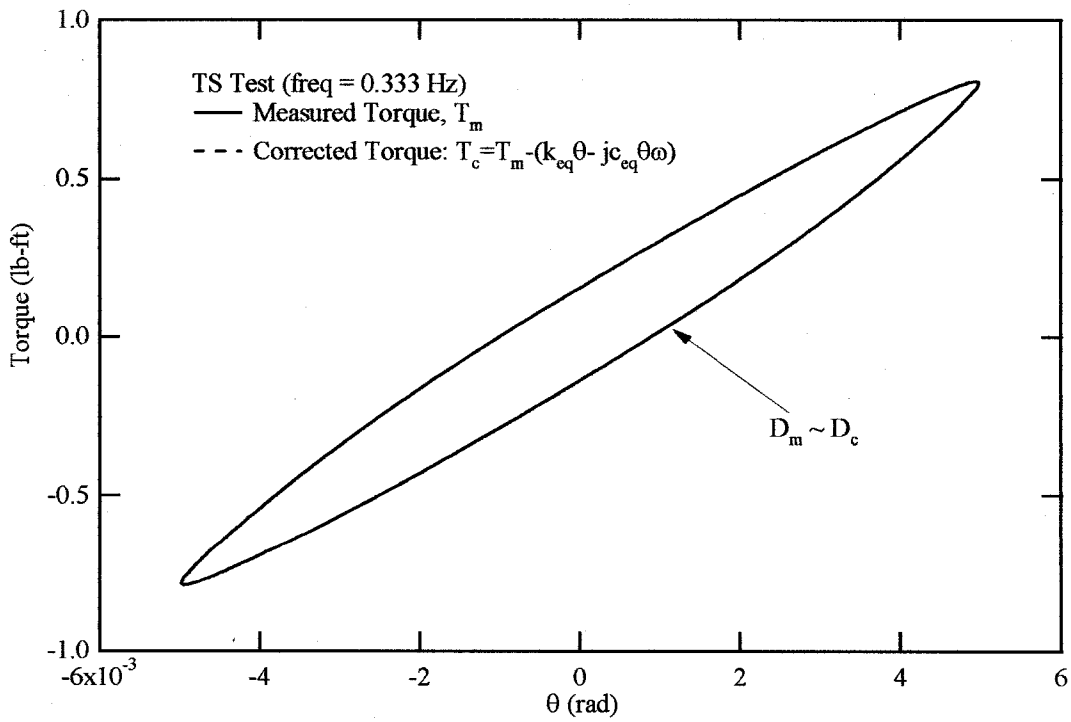

Figure 7.10 Effect of back emf on TS test

7.3.4 Model Limitations

The model proposed for this study is limited to predict D_{eq} at frequencies less than 200 Hz. The uncertainties in the model parameters seem to have a very small effect in predicting D_{eq}. The model performs very well in predicting D_{eq} for this range of frequency. It should be noted that although the model is limited for frequencies less than 200 Hz, the values of D_{eq} above 200 Hz are very small and most likely can be neglected.

7.4 DISCUSSION ON DISCREPANCIES IN EQUIMENT GENERATED DAMPING IN RC/TS TESTS

The measured D_{eq} reported by Hwang (1997) decreases with increasing resonant frequency in RC tests. This same trend was observed in this study. However, in TS test, Hwang (1997) reported an increasing of D_{eq} with loading frequency. This discrepancy is investigated in this section.

In the TS test, the hysteresis loop is created from the plot of torque versus rotational angle. The damping is determined from area of hysteresis loop which is directly related to the phase difference between the torque and rotation. As explained in Chapter 5, torque created in the RC/TS drive system is proportional to the current and torque should be calculated from the current signal using the torque-current factor, k_i. However, voltage measurements are more commonly used for determine torque in TS testing. To investigate the effect of using voltage rather than current in torque calculations, the correlation between current (i) and voltage (V) is shown below:

$$i = \frac{V}{(R_c + j\omega L_c)}. \tag{7.11}$$

Equation 7.11 implies that the voltage and current signals are not in phase with each other due to the coil inductance. This phase shift tends to increases as the frequency increases as shown in Figure 7.11. As a result, an addition of apparent damping is created when the voltage is used for calculating torque. Figure 7.12 illustrates the area of hysteresis loops due to the phase shift between the voltage and current. The increasing of loop area represents the error in measuring damping as the frequency increases when voltage is measured instead of current. Therefore, the phase shift of voltage and current is a source of error in measuring damping. If voltage is measured, a correction for phase shift is required when calculating torque.

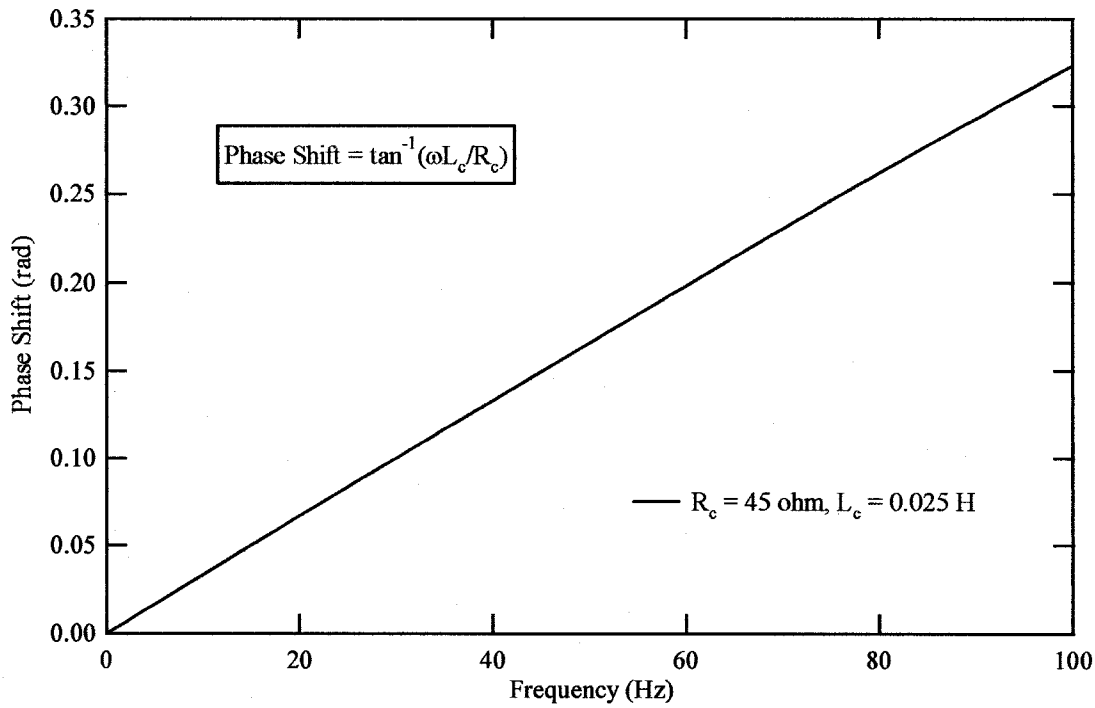

Figure 7.11 Phase shift between voltage and current in RC/TS equipment

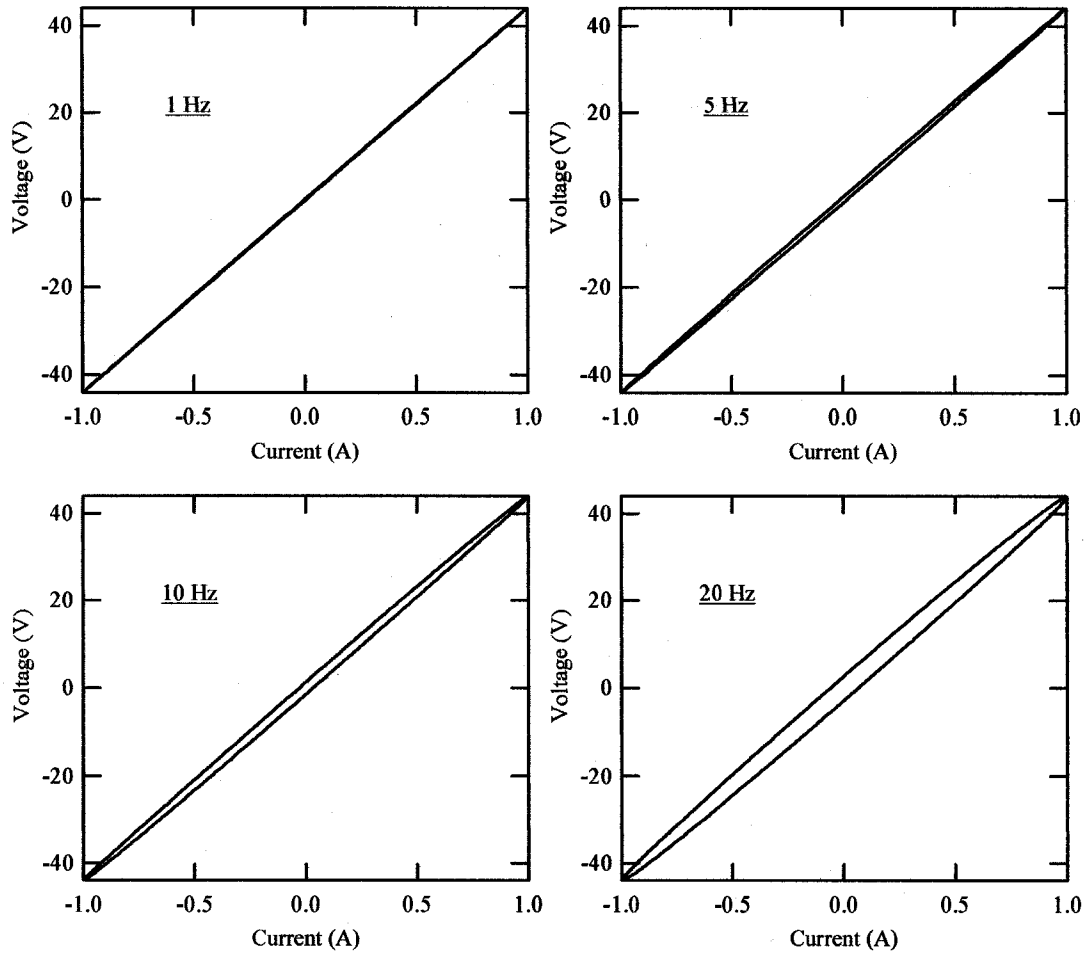

Figure 7.12 Variation of additional damping due to voltage measurement for torque

This discussion explains the discrepancy of the increasing of equipment generated damping with frequency in the TS test as oppose to the resonant column test reported by Hwang (1997). The damping from the voltage and current phase shift for each frequency is calculated from the loop presented in Figure 7.12 and compared with the assumed equipment generated damping measured by torsional shear test using voltage for calculating torque as shown in Figure 7.13. The phase shift damping matches very well

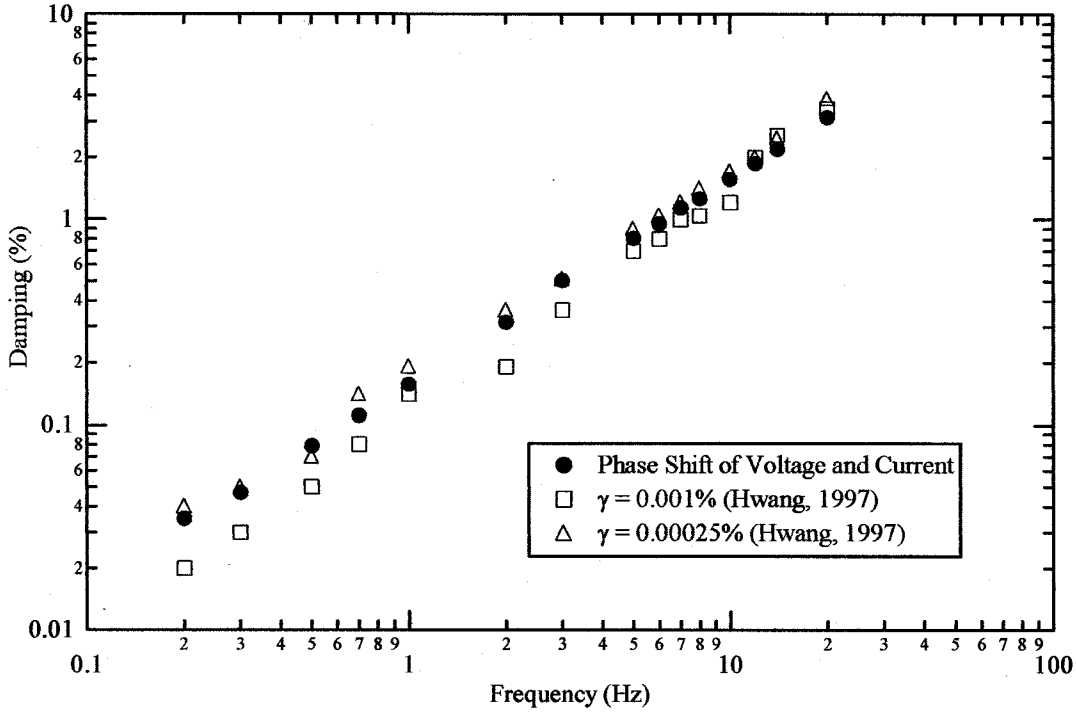

Figure 7.13 Comparison of damping from a phase shift and measured equipment generated damping for TS test by Hwang (1997)

with the Hwang's experimental data. As a result, the damping reported by Hwang is the damping created from using torque calculated by voltage without a phase shift correction. The actual equipment generated damping created from the back emf is negligible in TS test.

CHAPTER 8

ACCOUNTING FOR NONUNIFORM SRESS-STRAIN IN RC/TS TESTS

8.1 INTRODUCTION

Nonuniform stress-strain effects occurring over the radius of soil specimen are one of the weaknesses in the RC/TS testing. An equivalent radius approach proposed by Chen and Stokoe (1979) has been used to account for this effect. As discussed in Chapter 2, the equivalent radius approach uses an equivalent radius to calculate stress and strain when analyzing RC/TS test results. In this study, a method called the stress integration approach was developed to account for the effect of nonuniform stress-strain more precisely. The stress integration approach utilizes three assumed soil stress-strain models to develop representative stress-strain relationships for soils in RC/TS testing.

This chapter presents the development of the stress integration approach. Procedures used for each assumed stress-strain soil model are described. Limitations of the equivalent radius approach are discussed. Finally, the equivalent radius approach was modified using the stress integration method to improve damping measurements.

8.2 STRESS-STRAIN DISTRIBUTION IN SOIL FOR RC/TS TESTING

A soil specimen subjected to torsional loading in a RC/TS test is analyzed as a cylindrical bar twisted by torque, T, acting at the end of the bar as shown in Figure 8.1. Circular cross sections of the bar are identical at every cross section and subjected to the same internal torque, T. Torque on a right-circular cylinder causes as condition of pure

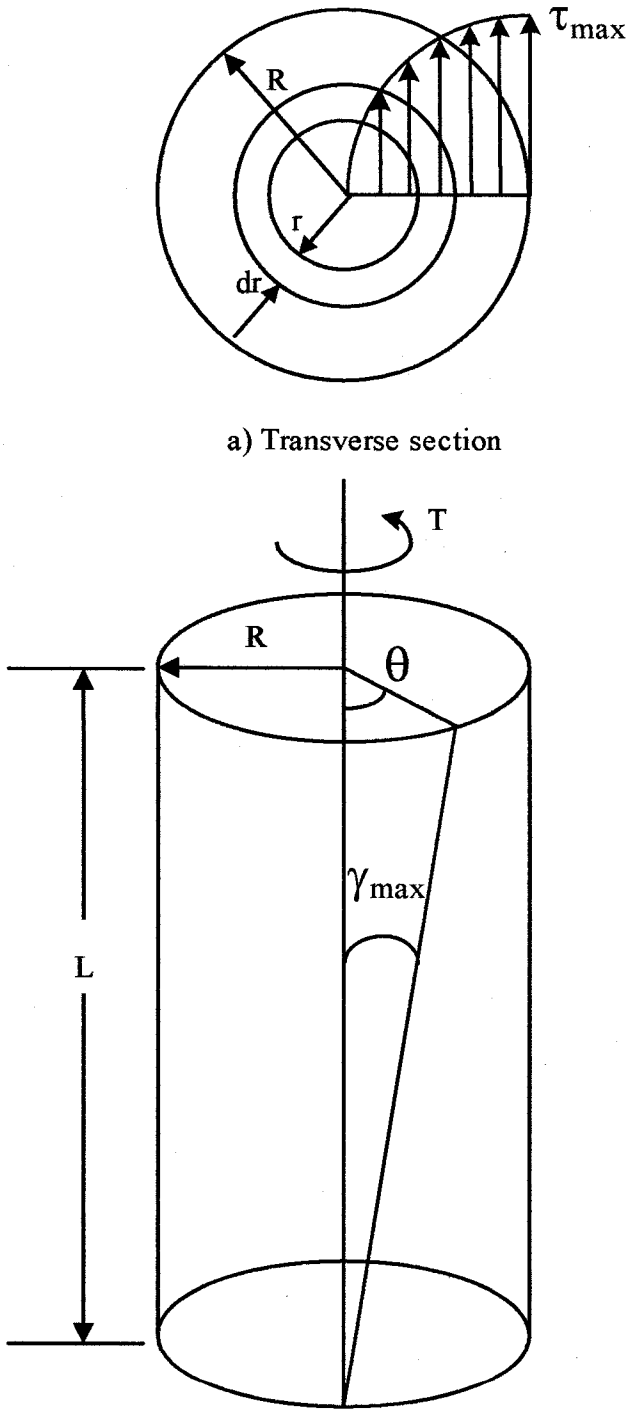

Figure 8.1 Distribution of shearing stress in soil column for RC/TS test

shear. This means that every cross section remains planar and circular and all radii remain straight. Shear strain at the outer surface or maximum shear strain, γ_{max} can be expressed as:

$$\gamma_{max} = \frac{\theta R}{L}, \tag{8.1}$$

where θ = rotational angle,

R = radius of the bar, and

L = length of the bar.

Because the radii in the cross sections of the bar remain straight and undistorted during twisting, the shear strain within the interior of the bar is given by:

$$\gamma = \frac{\theta r}{L} = \frac{r}{R}\gamma_{max}, \tag{8.2}$$

where r = interior radius of the bar.

Equations 8.1 and 8.2 are the equations for the torsional deformations of circular bars that are based upon the geometry of the deformed bar, therefore they are valid for any material whether it behaves linearly or nonlinearly. The rotation, θ, along a longitudinal section of the soil column in a RC/TS tests varies linearly because of its uniform cylindrical shape. However, the distribution of shear stress over the radius of soil specimen is non-uniform as shown in Figure 8.1a, due to nonlinear behavior of soil at medium to high strain levels. This nonuniform stress strain distribution must be taken into account when analyzing RC/TS tests.

8.3 STRESS INTEGRATION APPROACH

The stress integration approach is a new, more general approach to account for nonuniform stress-strain than the conventional equivalent radius approach (Chen and Stokoe 1979). The equivalent radius approach applies an equivalent radius ratio to calculate stress and strain corresponding to the measured torque (T) and rotation (θ) in RC/TS tests. The nouniform stress-strain can be accounted for more precisely by integrating the stress over the radius of soil specimen to obtain a T-θ relationship.

The stress integration approached developed in this study can be derived using basic equations of mechanics. The approach starts by relating the shear stress acting on a circular cross section to the applied torque, T, using the equation:

$$T = \int_A dM = \int \tau r dA = \int_0^R 2\pi r^2 \tau dr , \tag{8.3}$$

where M = resultant moment over the entire cross section area,

A = cross section area, and

τ = shear stress.

If the stress-strain relationship is known, then for any given value of θ, the shear stress at any point in the specimen can be determined. This requires using Equation 8.2 to calculate the shear strain and calculating the corresponding shear stress from the known stress-strain relationship. Thus, the distribution of shear stress and strain over the entire cross section of the soil can be evaluated. Since the shear strain varies linearly with the radius, the distribution of the shear stresses has the same shape as the stress-strain relation. Torque then can be obtained from the integral is Equation 8.3.

There are three procedures that must be performed in order to apply the stress integration approach to RC/TS testing. First, an experimental T-θ relationship must be measured. Second, an assumed soil stress-strain model is applied to Equation 8.3 and a theoretical T-θ relationship is developed using either closed form integration or numerical integration. And third, curve fitting techniques are then used to match the theoretical T-θ relationship with the measured T-θ relationship to obtain the best fit model parameters. These model parameters are then used to develop the stress-strain relationship for soil.

8.3.1 Measurement of T-θ Relationship in RC/TS Testing

In RC testing, a resonant frequency of the system and a corresponding peak rotation at resonance are measured. If the mass polar moment of inertia of the specimen and drive plate are known, the resonant frequency of the system can be related to the shear wave velocity, v_s of the soil specimen obtained by using the βtanβ method, as presented in Chapter 3. An equivalent linear elastic shear modulus or an effective shear modulus, G_{eff}, is calculated from:

$$G_{eff} = \rho v_s^2, \tag{8.4}$$

where ρ = mass density of soil specimen.

By linearizing the problem, G_{eff} and peak rotation at resonance, θ, can be related to an applied torque, T, using the equation:

$$T = \frac{G_{eff} I_p \theta}{L}, \tag{8.5}$$

where I_p = area polar moment of inertia, and

L = length of specimen.

Equation 8.6 is used to generate measured T-θ relationship in RC testing.

In the TS testing, the T-θ relationship is measured directly and a hysteresis loop is developed in the T-θ plane. The measured T-θ relationship in TS testing is generated from the maximum T and θ in each loading level.

8.3.2 Development of Theoretical T-θ Relationship

The three soil stress-strain models used in this study were the hyperbolic model, the modified hyperbolic model, and the Ramberg-Osgood model. Each model is evaluated corresponding to theoretical T-θ relationship using either closed form or numerical integration. Closed form integration was used for the hyperbolic model and the numerical integration was used for the modified hyperbolic model and the Ramberg-Osgood model. Procedures for the closed form integration and numerical integration are presented in the following sections.

8.3.2.1 Closed Formed Integration. For the hyperbolic model, a closed form solution is used to develop the theoretical T-θ relationships. The hyperbolic stress-strain relationship can be expressed as:

$$\tau = \frac{G_{max}\gamma}{1+\frac{\gamma}{\gamma_r}}, \tag{8.6}$$

where G_{max} = small strain shear modulus, and

γ_r = reference strain.

For a cylindrical specimen in torsion, the shear strain at any point within the interior of soil specimen is defined in Equation 8.2, therefore, shear stress can be related to the interior radius as follow:

$$\tau = \frac{G_{max}\theta\frac{r}{L}}{1+\frac{1}{\gamma_r}\theta\frac{r}{L}}. \tag{8.7}$$

Substituting Equation 8.7 into Equation 8.3 gives:

$$T = \int_0^R 2\pi r^2 \frac{G_{max}\theta\frac{r}{L}}{1+\frac{1}{\gamma_r}\theta\frac{r}{L}}dr. \tag{8.8}$$

By integrating Equation 8.8, the following equation for a T-θ relationship for the hyperbolic model is obtained:

$$T = \frac{1}{3}\pi G_{max}\gamma_r R\left[2R^2 - 3R(\frac{\gamma_r L}{\theta}) + 6(\frac{\gamma_r L}{\theta})^2\right] + 2\pi G_{max}\gamma_r^4(\frac{L}{\theta})^3\left[\ln(\gamma_r) - \ln(\gamma_r + \frac{\theta R}{L})\right]. \tag{8.9}$$

A flow chart showing the stress integration approach using the hyperbolic model is presented in Figure 8.2. A measured T-θ relationship from a RC/TS test is shown in Figure 8.2a. First, the model parameters G_{max} and γ_r are assumed, and a theoretical T-θ relationship is calculated using Equation 8.9. The theoretical T-θ curve is plotted with the measured T-θ curve as Figure 8.2b. Curve fitting techniques are then used to match the theoretical and measured T-θ curves by adjusting values of G_{max} and γ_r iteratively. The best fit parameters are used to develop the stress-strain relationship presented in Figure 8.2c.

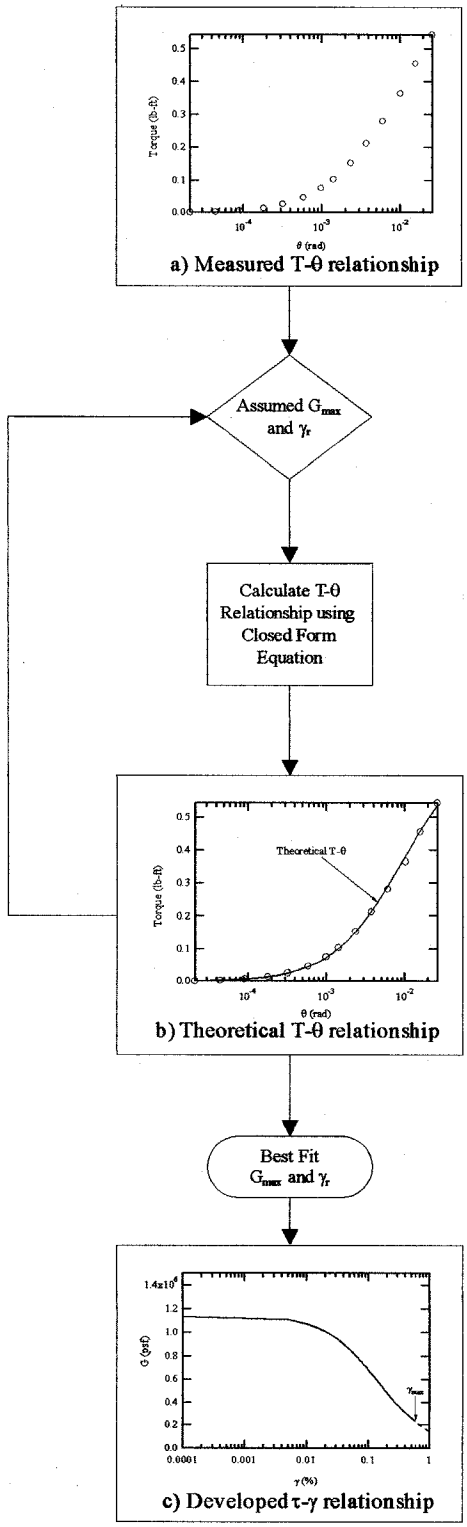

Figure 8.2 Flow chart showing the stress integration approach using the hyperbolic model

8.3.2.2 Numerical Integration. Numerical integrations are used to develop the theoretical T-θ relationships for both the modified hyperbolic model and Ramberg-Osgood model. The model parameters for the modified hyperbolic model are: G_{max}, γ_r, and a. The modified hyperbolic stress-strain relationship can be expressed as:

$$\tau = \frac{G_{max}\gamma}{1+\left(\frac{\gamma}{\gamma_r}\right)^a}. \tag{8.10}$$

And, the model parameter for the Ramberg-Osgood model are: G_{max}, γ_r, α, and b. The Ramberg-Osgood stress-strain relationship can be expressed as:

$$\gamma = \frac{\tau}{G_{max}}\left[1+\alpha\left|\frac{\tau}{G_{max}\gamma_r}\right|^{b-1}\right]. \tag{8.11}$$

Equation 8.10 and 8.11 cannot be integrated like the two parameter hyperbolic model. Therefore, a numerical integration is used for these models. Two different methods for numerical integration can be used.

The first method involves integration relative to strain. From Equation 8.2, the interior radius, r, relative to strain, γ, is:

$$r = \frac{L}{\theta}\gamma. \tag{8.12}$$

The differential of strain, $d\gamma$, can be related to the differential of radius, dr, using Equation 8.12 as follows:

$$dr = \frac{L}{\theta}d\gamma. \tag{8.13}$$

Equations 8.12 and 8.13 are substituted into Equation 8.3, and changing the upper limit of integration to γ_{max} to correspond with the new independent variable, γ, gives:

$$T = 2\pi\left(\frac{L}{\theta}\right)^3 \int_0^{\gamma_{max}} \tau(\gamma)\gamma^2 d\gamma, \tag{8.14}$$

where $\tau(\gamma) = \tau$-γ relationship.

Figure 8.3 presents a flow chart illustrating the stress integration approach using integration relative to strain, γ, for the modified hyperbolic model. A measured T-θ relationship from a RC/TS test is shown in Figure 8.3a. The stress-strain relationship described by the modified hyperbolic model is substituted in Equation 8.14 to obtain:

$$T = 2\pi\left(\frac{L}{\theta}\right)^3 \int_0^{\gamma_{max}} \left(\frac{G_{max}\gamma}{1+\left(\frac{\gamma}{\gamma_r}\right)^a}\right)\gamma^2 d\gamma \tag{8.15}$$

Torque is determined by numerically integrating the stress-strain relationship as shown in Figure 8.3b. The resulting theoretical T-θ relationship is shown in Figure 8.3c. Curve fitting is then performed to determine the best fit model parameters.

The second method involves integrating with respect to radius, r. Figure 8.4 presents a flow chart illustrating the stress integration approach using integration relative to radius, r, for the Ramberg-Osgood model. A measured T-θ relationship from a RC/TS test is shown in Figure 8.4a. The Ramberg-Osgood model presents γ as a function of shear stress, τ. For a given rotation, θ, there is a one-to-one correspondence between γ and r, shown in Equation 8.12. In the case of Ramberg-Osgood model, the radius, r, can then be expressed as:

$$r = \frac{L}{\theta}\frac{\tau}{G_{max}}\left[1+\alpha\left|\frac{\tau}{G_{max}\gamma_r}\right|^{b-1}\right] \tag{8.16}$$

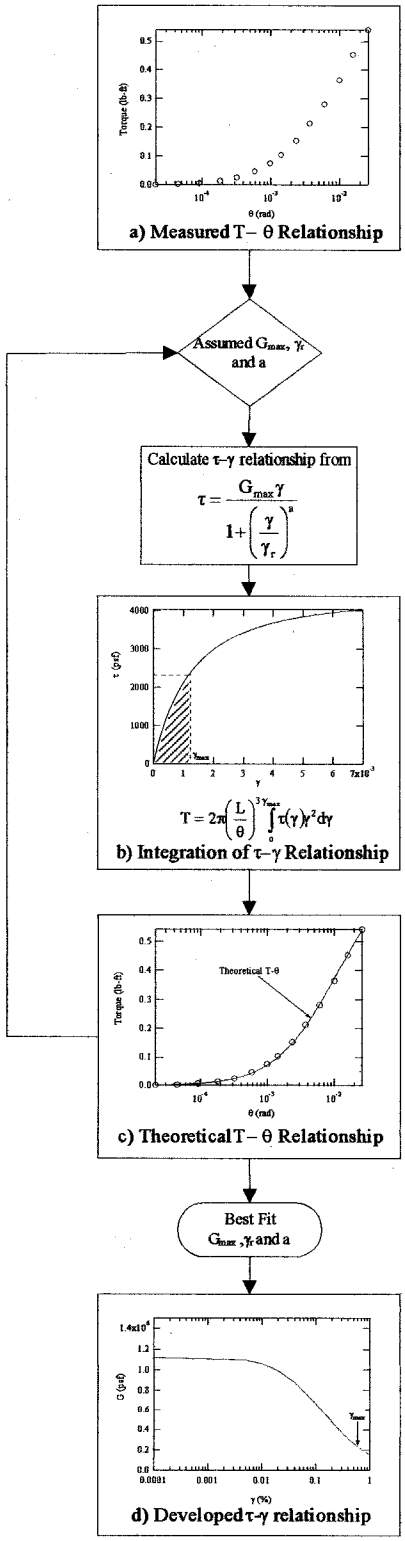

Figure 8.3 Flow chart showing the stress integration approach for the modified hyperbolic model using integration relative to strain

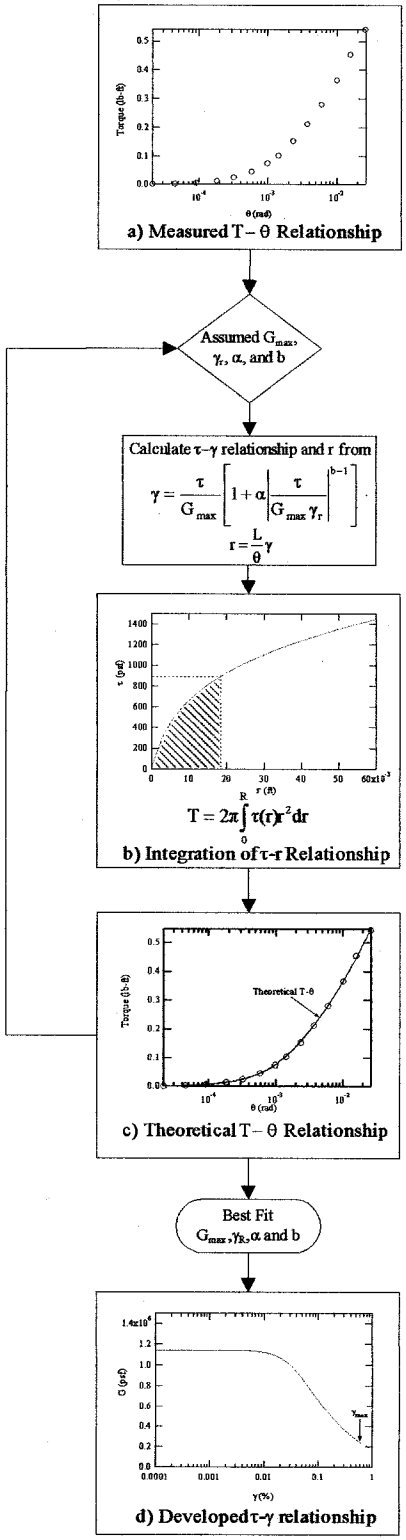

Figure 8.4 Flow chart showing the stress integration approach for the Ramberg-Osgood model using integration relative to radius

A plot of shear stress, τ, and radius, r, can be generated using Equation 8.16. Torque is determined by numerically integrating the τ–r relationship using:

$$T = 2\pi \int_0^R \tau(r) r^2 dr , \qquad (8.17)$$

where $\tau(r)$ = τ-r relationship.

Figure 8.4b presents the integration of the τ–r relationship. The resulting theoretical T-θ relationship is shown in Figure 8.4c. Curve fitting is then performed to determine the best fit model parameters.

8.3.3 Curve Fitting Technique

Curve fitting techniques were performed using an assumed stress-strain soil model following the procedure illustrated in Figures 8.2-8.4. The program Igor Pro 4.01 was used to perform the curve fitting. The details on curve fitting techniques used in Igor are presented in this section.

In curve fitting, the theoretical T-θ relationship calculated from the assumed soil stress-strain model is fit to the measured T-θ relationship by adjusting values of the model parameters. For the hyperbolic model, the curve fitting function is a closed form solution. For the modified hyperbolic model and the Ramberg-Osgood model, the curve fitting function requires numerical integration. The Igor curve fitting program searches for the values of model parameter that best match the experimental data. The "best"values of the model parameters are the ones that minimize the value of chi-square. chi-square is defined as:

$$\text{chi} - \text{square} = \sum \left(\frac{y - y_i}{\sigma_i} \right)^2 , \tag{8.18}$$

where y = fitted value for a given point,

y_i = original data value for the point, and

σ_i = standard deviation of each data value

Igor uses the Lavenberg-Marquardt algorithm to search for the minimum value of chi-square using nonlinear, least square curve fitting. The search starts from a supplied initial guesses of the model parameters. The initial guesses must be provided manually and the curve fitting algorithm searches for the best fit starting from these initial guesses. As the fit proceeds and better values are found the chi-square value decreases. The fit is finished where the difference between experimental data and fitted data are minimum. If the initial guess is poor, the fit may conclude with an unsatisfactory result. This can be observed visually. The initial guesses must be adjusted until the fit achieves the lowest chi-square value.

The chi-square factor is an indicator of the quality of the fit. However, judgment must be exercised in evaluating the quality of the fit. In some cases, two models may return similar values of chi-square, however, one model may match the experimental data very well at low to medium strain levels and the other may match better at high strains. In this case, neither of the models are good for predicting the soil behavior over the entire range of strains and special considerations must be taken.

8.4 EVALUATION OF THE EQUVALENT RADIUS APPROACH FOR PREDICTING STRESS-STRAIN RELATIONSHIP FOR SOIL

The equivalent radius approach is based on the assumption that the representative stress and strain in soil specimen in torsion occurs at a radius called the equivalent radius, r_{eq}. To apply the equivalent radius approach, an equivalent radius ratio, R_{eq}, which defined as the ratio of the equivalent radius and the outside radius of soil specimen is used to calculate the stress and strain. According to Chen and Stokoe (1979), R_{eq} value varies from 0.82 for strains below 10^{-3} % to 0.79 for strains at 10^{-1} % for a solid specimen. Shear strain is calculated from:

$$\gamma = R_{eq} \times \gamma_{max} . \tag{8.19}$$

Shear stress, τ, is calculated using:

$$\tau = R_{eq} \times \tau_{max} , \tag{8.20}$$

where τ_{max} = maximum shear stress for a linear elastic specimen:

$$\tau_{max} = \frac{TR}{I_p} . \tag{8.21}$$

To evaluate the equivalent radius approach, theoretical stress-strain curves were developed using three soil models. The thress models are the hyperbolic model, the modified hyperbolic model and the Ramberg-Osgood model. The model parameters assumed for each soil model and the stress-strain curves are presented in Figure 8.5.

From the theoretical soil models presented in Figure 8.5, the T-θ relationships were determined. The closed form solution was used calculate the theoretical T-θ relationship for the hyperbolic model. Numerical integration was use to calculate the

theoretical T-θ relationships for the modified hyberbolic model and Ramberg-Osgood model. The theoretical T-θ relationships for each soil model are presented in Figure 8.6.

Once the theoretical T-θ relationships were developed, the equivalent radius approach was then applied to determine the stress-strain relationship using Equations 8.19 and 8.20. The stress-strain relationship from equivalent radius approach was then compared with the actual stress-strain relationship to evaluate how well the equivalent radius approach predicts the stress-strain relationships. Those curves are presented in Figure 8.7. Results are plotted in terms of dimensionless or normalized stress and strain so that the results are independent of model parameter: G_{max} and γ_r. Shear stress was normalized by τ_f, where τ_f is defined as:

$$\tau_f = G_{max}\gamma_r . \tag{8.22}$$

And, shear strain was normalized by γ_r.

Figure 8.7 shows that the equivalent radius approach slightly overestimates shear stress, τ, at high strain levels for all three soil models. This overestimation indicates the equivalent radius approach has limitations when performing RC/TS tests at high strains. At strains below 0.1% the equivalent radius approach is satisfactory.

The equivalent radius approach was developed based upon moduli calculations. This approach does not necessarily apply equally well for damping measurements. The following section presents an approach used for damping measurements.

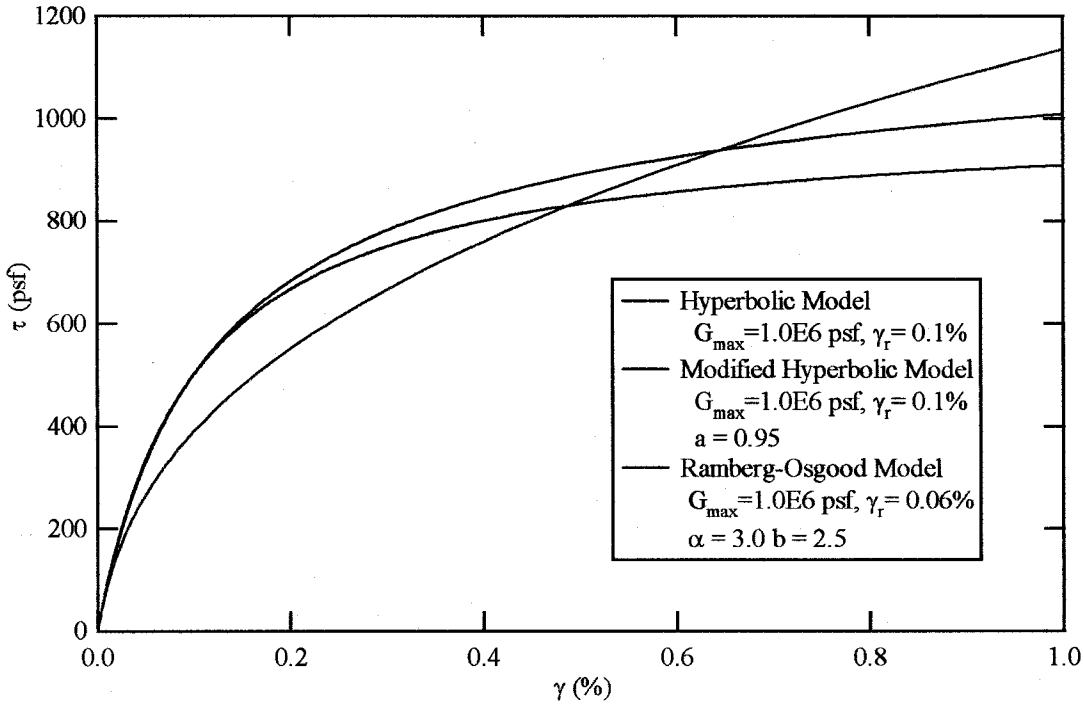

Figure. 8.5 Three soil models used for evaluation of equivalent radius approach

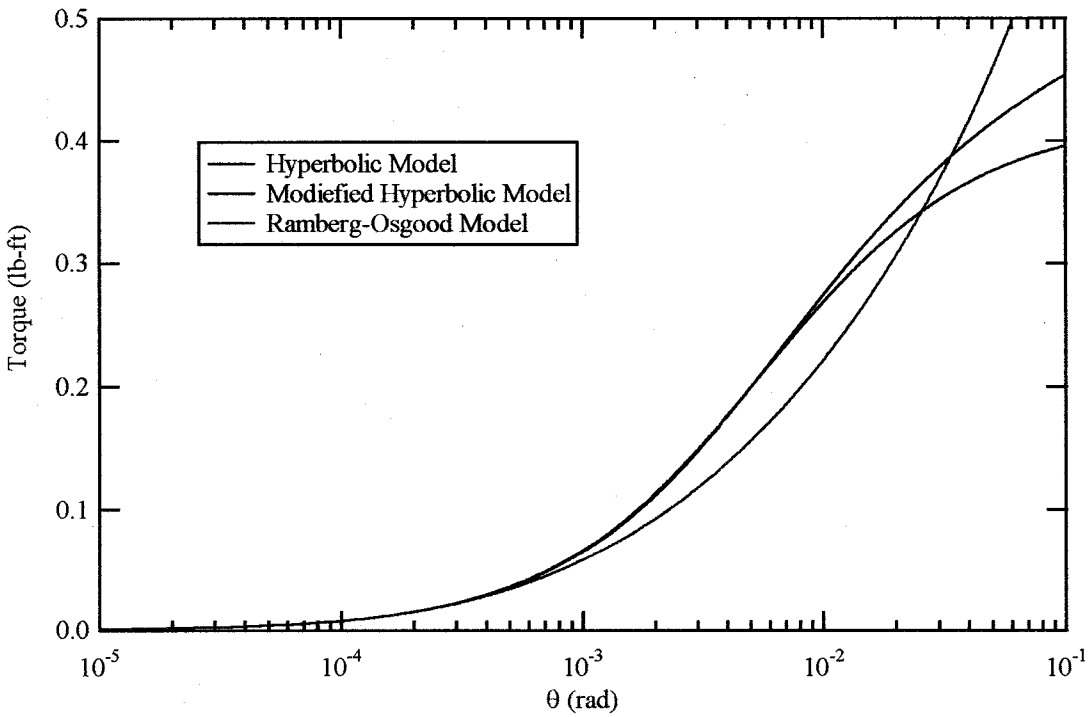

Figure 8.6 Theoretical T-θ relationship of the soil models presented in Figure 8.5

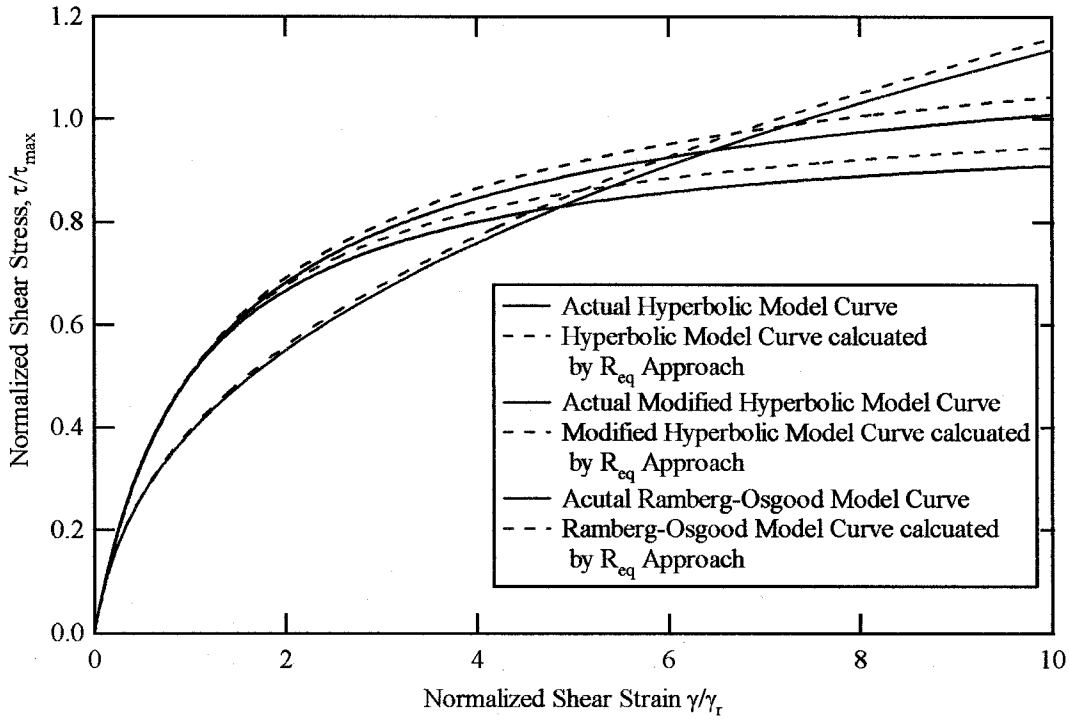

Figure 8.7 Comparison of actual stress-strain curves and the stress-strain curves using the equivalent radius approach

8.5 ACCOUNTING FOR NON-UNIFORM STRES-STRAIN IN DAMPING

The nonuniform stress-strain effect on soil specimens in torsion must be taken into account when developing damping curve in RC/TS testing. In this study, the equivalent radius approach was modified to determine the strain corresponding to a measured damping value more precisely. Values of R_{eq} based on both shear modulus and damping are determined separately. These results are compared and normalized curves are presented.

8.5.1 *Procedure to Determine $(R_{eq})_G$ Based upon Shear Modulus*

Figure 8.8 illustrates a procedure to evaluate the $(R_{eq})_G$ based on shear modulus. The hyperbolic model was used to develop a stress-strain relationship for a theoretical soil. This stress-strain relationship was then used to generated modulus reduction (G versus γ) curve shown in Figure 8.8a. The stress-strain for the theoretical soil was used to calculate a T-θ relationship using Equation 8.9. With this T-θ relationship, the effective shear modulus, G_{eff} can be calculated using Equation 8.5. The G_{eff} versus θ curve is shown in Figure 8.8b. For a given, γ_1, the corresponding value, G_1, can be obtained from Figure 8.8a. A value θ_1 that is associated with the G_{eff} value equal to G_1 is identified in Figure 8.8b. Then using the following equation, a value of $(R_{eq})_{G1}$ is found for θ_1 and γ_1 as shown in Figure 8.8c.

$$R_{eq} = \frac{1}{R}\frac{\gamma L}{\theta}. \tag{8.23}$$

8.5.2 *Procedure to Determine $(R_{eq})_D$ Based upon Damping*

Figure 8.9 illustrates a procedure to evaluate $(R_{eq})_G$ based on damping. Again, the hyperbolic model was used to develop a stress-strain relationship for a theoretical soil. As described in Chapter 3, hysteretic damping of soil can be obtained from the characteristics of the hysteresis loop. Assuming the theoretical soil behaves according to Masing rules, the damping can be determined from:

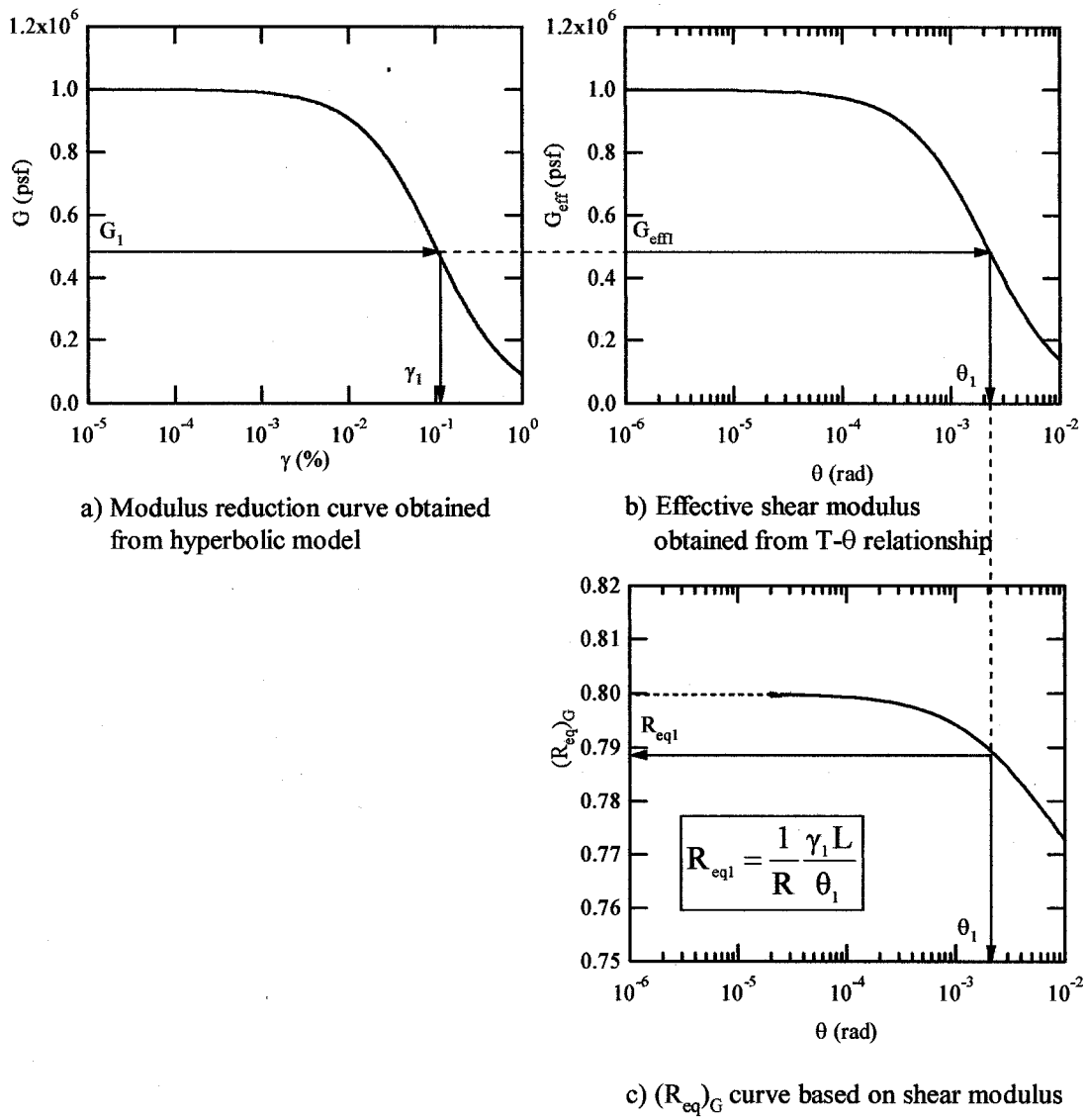

Figure 8.8 Determination of R_{eq} based on shear modulus

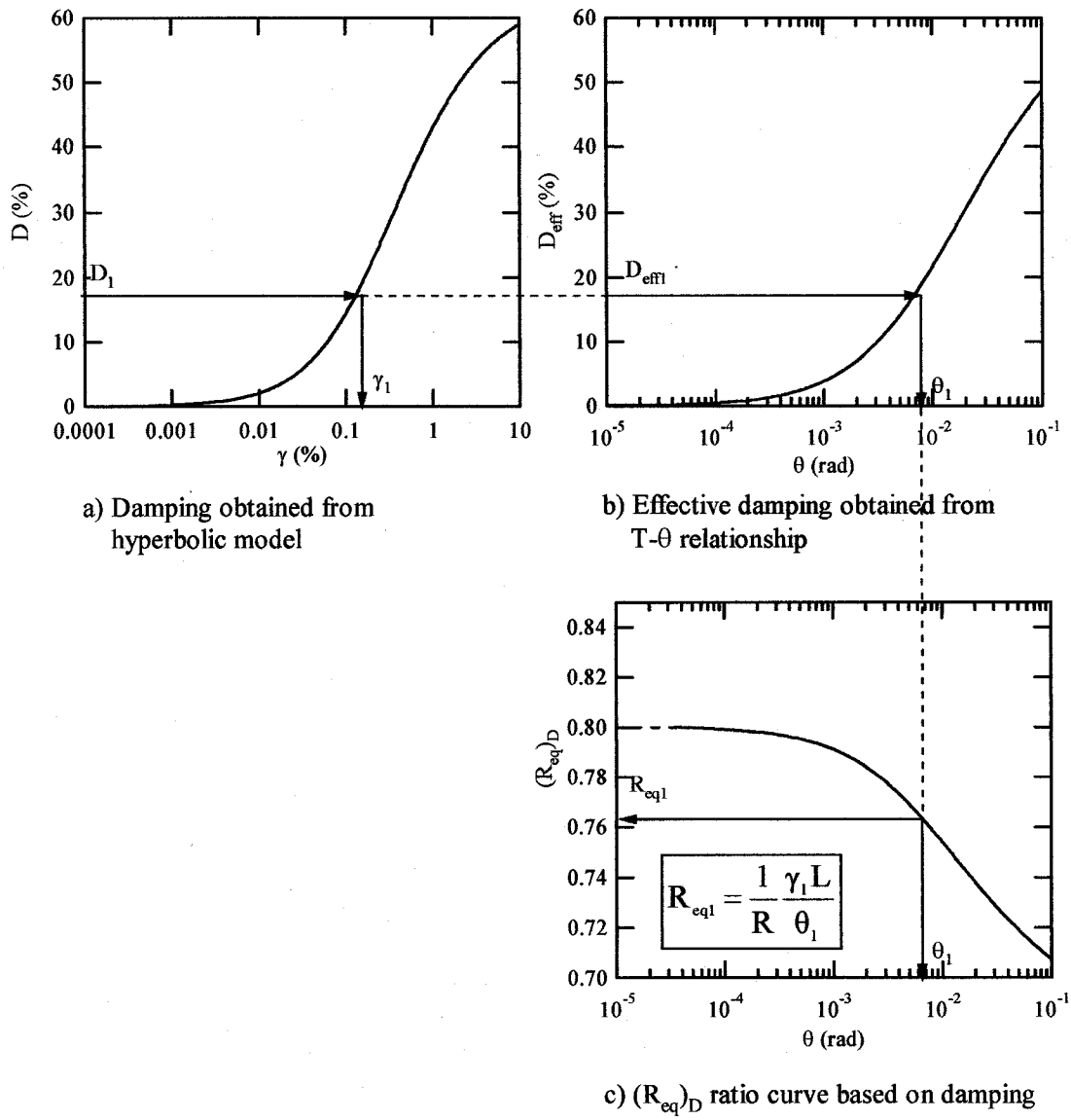

Figure 8.9 Determination of R_{eq} based on damping

$$D = \frac{2}{\pi}\left[\frac{2\int_0^{\gamma}\tau(\gamma)d\gamma}{\gamma\tau(\gamma)} - 1\right]. \tag{8.24}$$

Equation 8.24 was used to develop the D-γ curve can be generated as shown in Figure 8.9a. The stress-strain relationship for the theoretical soil was then used to calculate T- θ relationship using Equation 8.9. This T-θ relationship was then integrated using:

$$D_{eff} = \frac{2}{\pi}\left[\frac{2\int_0^{\theta}T(\theta)d\theta}{\theta T(\theta)} - 1\right]. \tag{8.25}$$

With this T-θ relationship, the effective shear modulus, D_{eff} can be calculated using Equation 8.25. The D_{eff} versus θ curve is shown in Figure 8.9b. For a given, γ_1, the corresponding value, D_1, can be obtained from Figure 8.9a. A value θ_1 that is associated with the D_{eff} value equal to D_1 is identified in Figure 8.9b. Then using Equation 8.23, a value of $(R_{eq})_{D1}$ is found for θ_1 and γ_1 as shown in Figure 8.9c.

8.5.3 Instability in Closed Form Solution

Instability of the closed form solution for the T-θ relationship was observed at low values of θ. This occurred when shear modulus was in the linear range where G_{eff} was equal to G_{max} as shown in Figure. 8.10. The instability of the closed form solution results in unrealistic values of the calculated G_{eff} where G_{eff} becomes larger than G_{max} which is theoretically impossible. Consequently, an error can be created in the evaluation

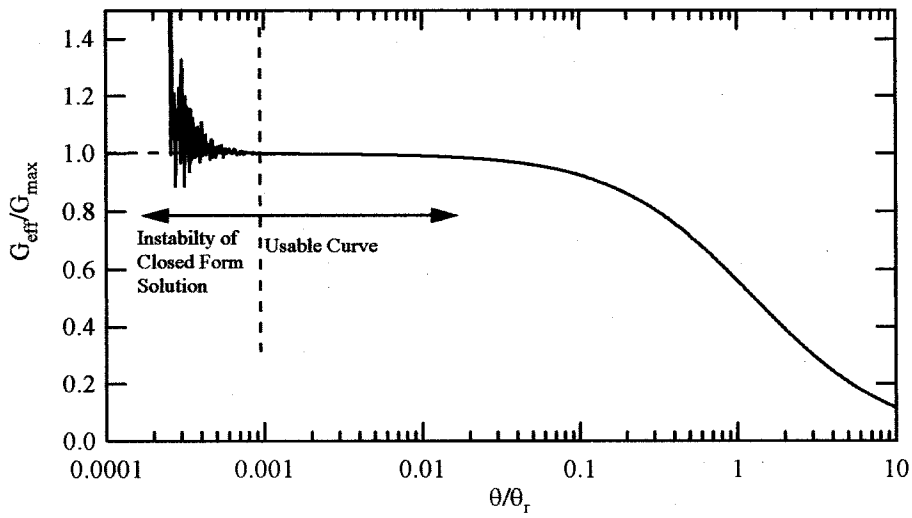

Figure 8.10 Instability of the closed form solution

of R_{eq} ratio due to this instability. As shown in Figure 8.10, the instability occurs when value of G_{eff}/G_{max} is approximately one. For these low strains, the value of R_{eq} is independent of strain level. In this study, R_{eq} was analyzed only in the range of usable curve data. R_{eq} was assumed to be constant for strains in the linear range.

8.5.4 Evaluation of Effects of Soil Nonlinearity on R_{eq}

Effect of soil nonlinearity on R_{eq} based on both G and D was investigated. Three hyperbolic soil models were used. These soil models have reference strains, γ_r, of 0.01%, 0.1%, and 1%, and have same value of G_{max}, 1.0E6 lb/ft^2. The modulus reduction curves and damping curves for all soil models are presented in Figure 8.11a and Figure 8.12a, respectively. The R_{eq} ratio curves based on G and D for these soil models were developed following the procedure shown in Figures 8.8 and 8.9.

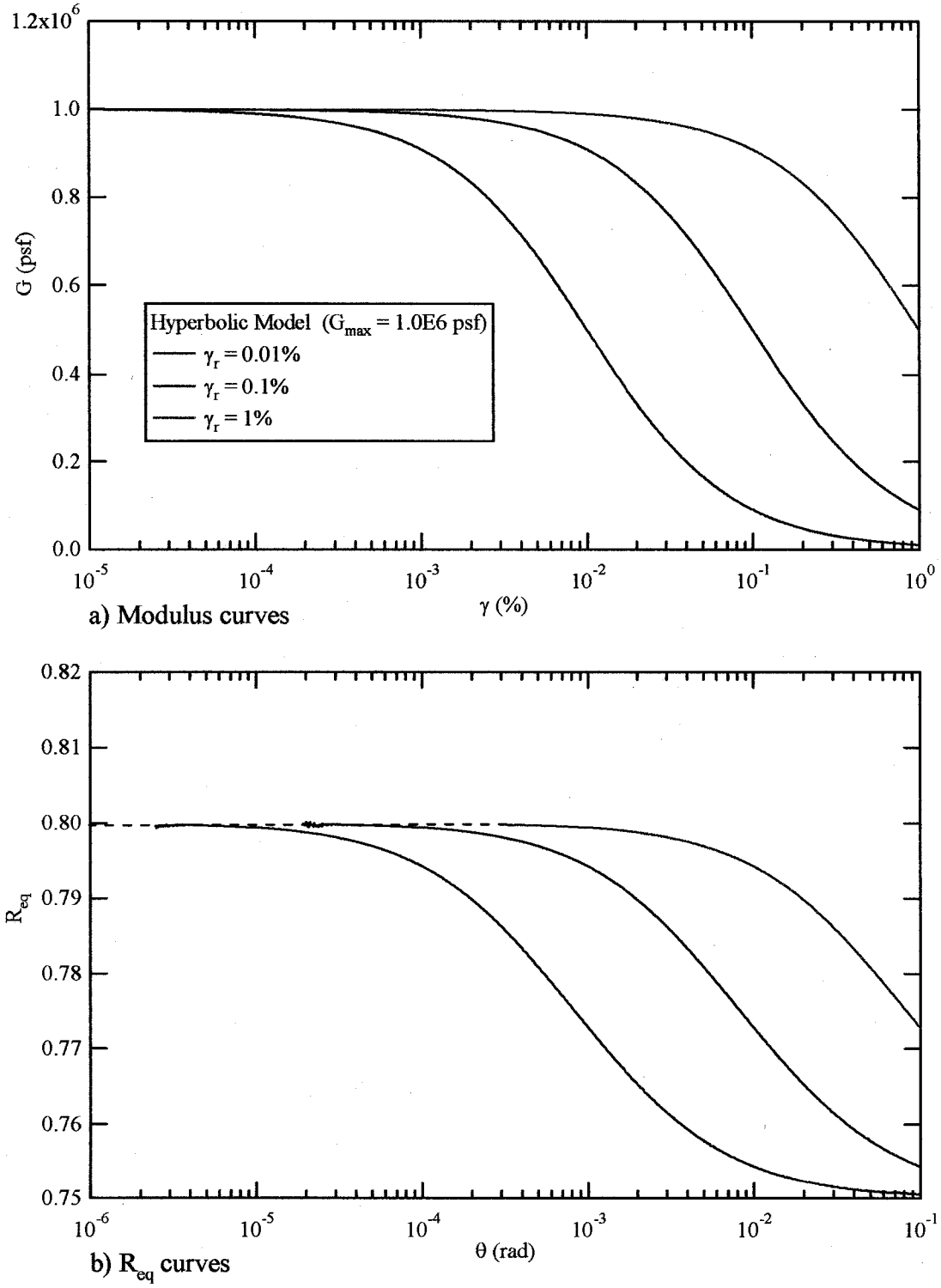

Figure 8.11 Modulus curve and their associated R_{eq} curves based on G with different soil models

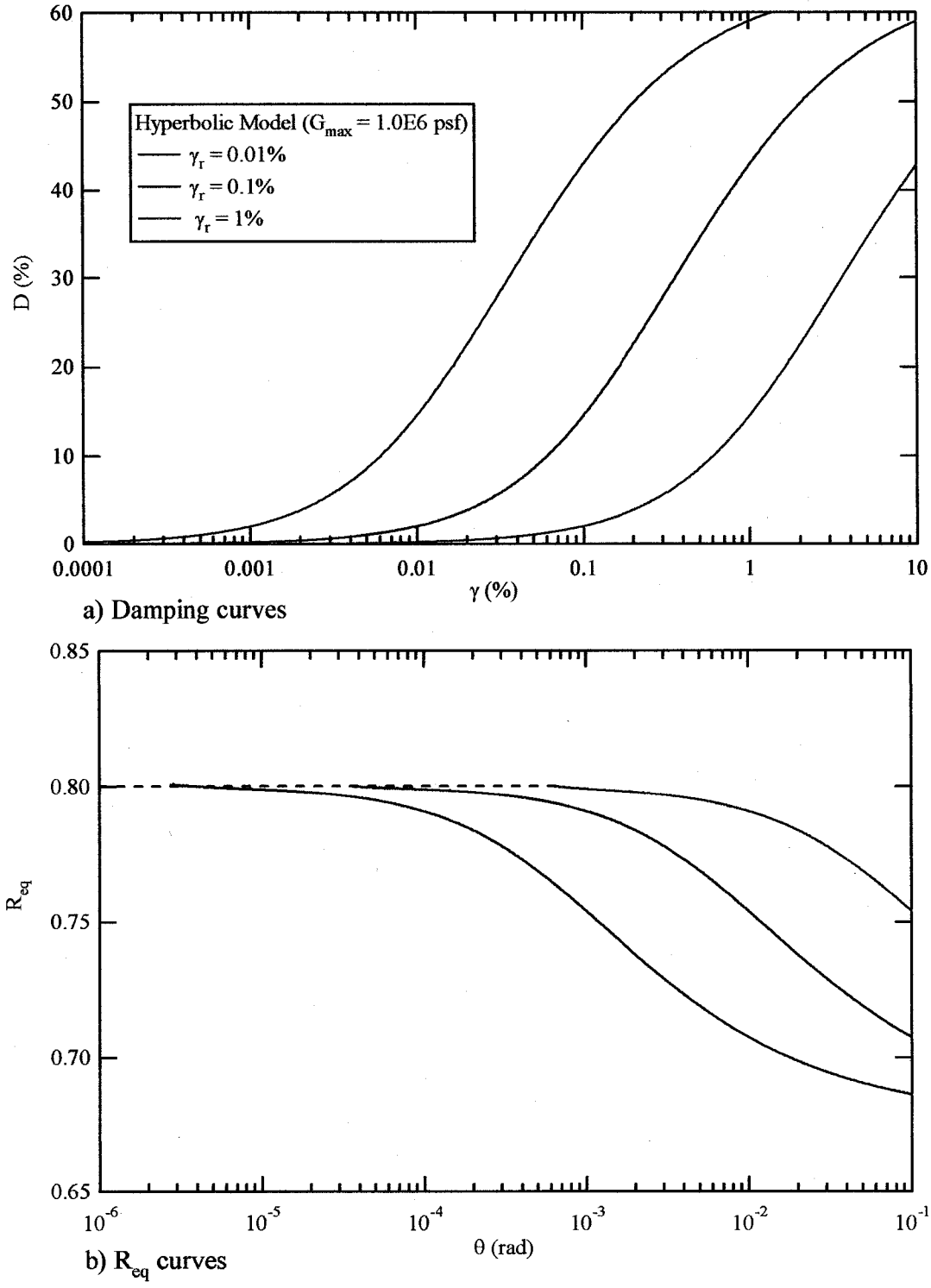

Figure 8.12 Damping curve and their associated R_{eq} curves based on D with different soil models

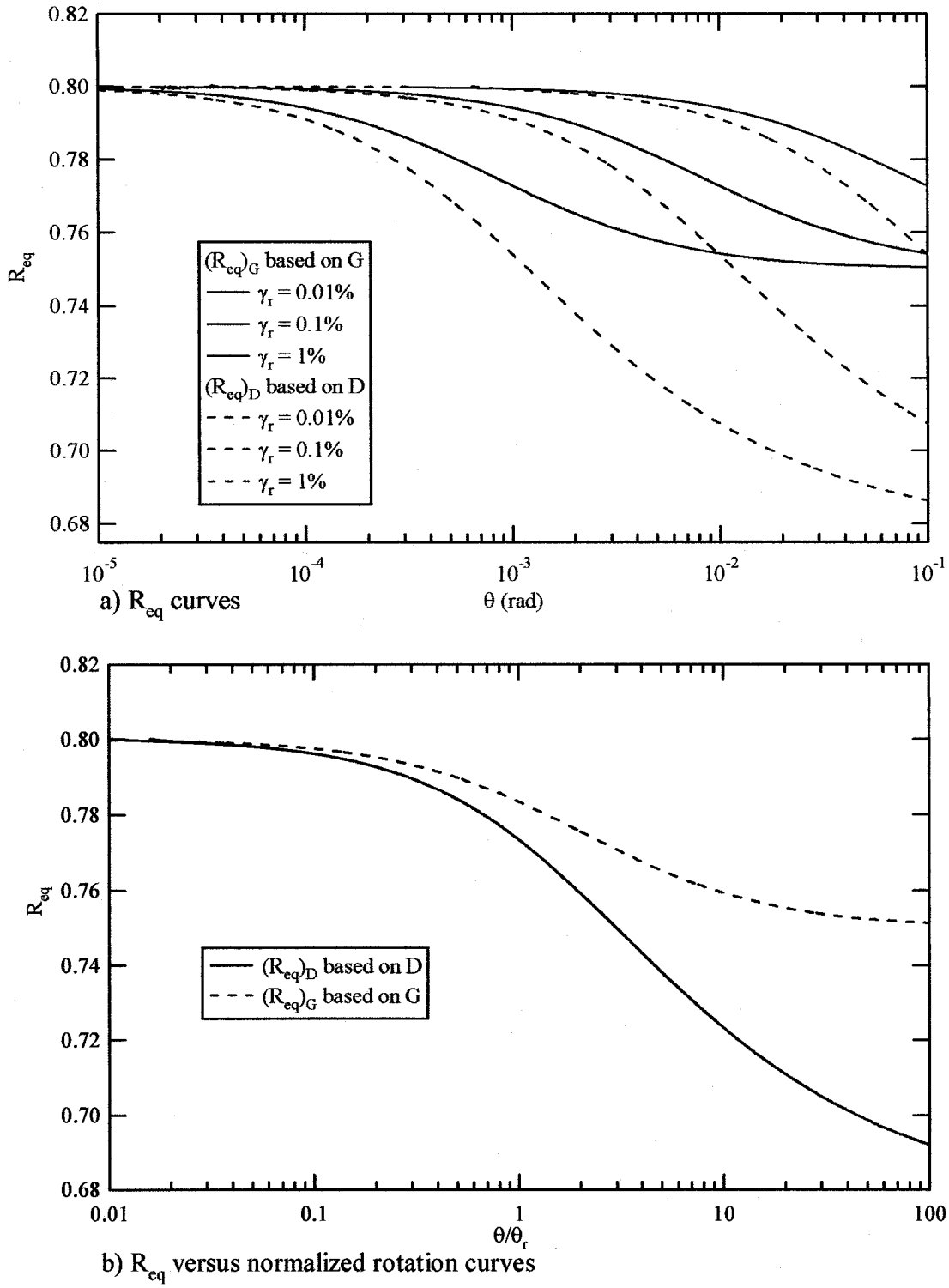

Figure. 8.13 R_{eq} curves based on both G and D

$(R_{eq})_G$ curves based on G are presented in Figure 8.11b. All $(R_{eq})_G$ curves converge to a value of about 0.8 in their linear range. As the strain and rotation increase, values of $(R_{eq})_G$ decrease. The points where these curves decrease associated with the value of γ_r.

$(R_{eq})_D$ curves based on G are presented in Figure 8.12b. Again, all $(R_{eq})_D$ curves converge to a value of about 0.8 in their linear range. The curves also fall off similarly to the $(R_{eq})_G$ curves but decrease to lower values.

It is more useful to present the results of R_{eq} in terms of normalized rotation, θ/θ_r, so that results are independent of the soil nonlinearity. The reference rotation, θ_r, is defined as:

$$\theta_r = \frac{\gamma_r L}{R}. \tag{8.26}$$

All R_{eq} curves based upon G and D, are plotted versus the θ/θ_r, and the results are presented in Figure 8.13b. Now all of the $(R_{eq})_G$ curves based on G plot on top of each other, and all of the $(R_{eq})_D$ curves based upon D plot on top of each other. All curves converge to a value of about 0.8 at low strains. At high strains, the $(R_{eq})_D$ curves are significantly lower than the $(R_{eq})_G$ curves. This suggests that using the same R_{eq} values for both G and D is not appropriate.

Figure 8.14 presents a comparison of R_{eq} values generated in this study with the R_{eq} values suggested by Chen and Stokoe (1979). Three weaknesses with the approach suggested by Chen and Stokoe (1979) are observed in Figure 8.14. First, the soil

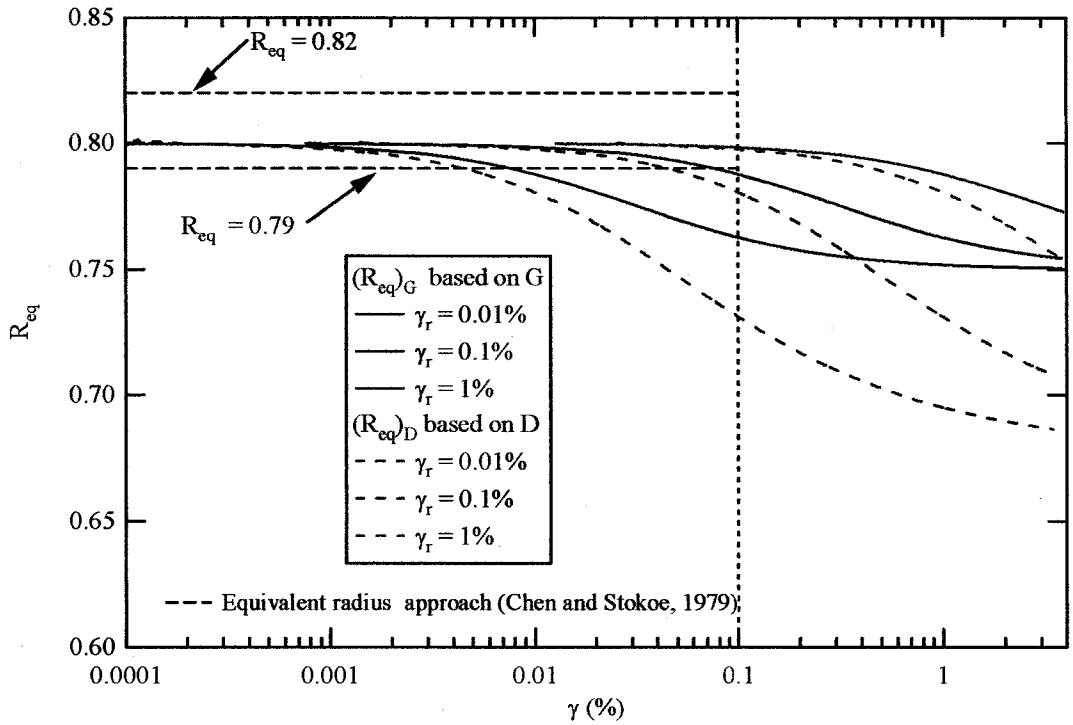

Figure 8.14 Comparison of R_{eq} values from this study and Chen and Stokoe (1979)

nonlinearity is not taken into account. Second, a single value of R_{eq} does not accurately represented the actual R_{eq} for a wide range of strains. Third, values of $(R_{eq})_D$ based upon damping are significantly lower than the values of $(R_{eq})_G$ based upon G at high strains.

8.5.5 Using Modified Equivalent Radius Approach to Generate Damping Curves

Figure 8.13b can be used to develop damping curves from RC/TS tests. To do this, reference strain, γ_r, must first be determined. This value would typically be identified during curve fitting to generate modulus reduction curves. Using the γ_r, reference rotation, θ_r, can be calculated using Equation 8.26. For every rotation measured in RC/TS testing, a value of $(R_{eq})_D$ can be obtained from Figure 8.13b. Strains

for each rotation can be determined using Equation 8.18. In the TS testing, the damping associated with that strain can be obtained from the properties of the T-θ hysteresis loop. In the RC testing, the damping associated with the calculated strain can be determined from either the half power bandwidth method or free vibration decay method.

8.5.6 Limitations of Modified Equivalent Radius Approach

Three limitations in using hysteretic damping to describe the material damping for soil are recognized. First, the hysteretic damping is zero at very small strains because the area of hysteresis loop becomes zero in the linear range. Actual material damping of soil has never becomes zero due to damping from other mechanisms. Second, the hysteretic damping overestimates the damping for soil at high strains. The hysteretic damping increases up to a maximum value of 63.7 % at strain levels above 50%, which does not happen in the real soil behavior. Third, the hysteresis loop is governed by the Masing behavior which does not accurately describe the behavior of soil. These limitations require further study.

CHAPTER 9

RC/TS TESTING OF BONNEVILLE CLAY

9.1 INTRODUCTION

RC/TS testing was performed on Bonneville clay to develop modulus reduction curves and damping curves. Previous to this study, no measurements have been made of modulus reduction and damping in Bonneville clay. In this testing, the electromagnetic model was used to correct for equipment generated damping and the stress integration approach was used to calculate stresses and strains. This chapter is separated into four sections. Each section is described below.

The first section presents a description of soil specimens used in this study. Soil description includes sample depth and location, physical properties, and soil classification.

The second section presents the RC/TS testing procedures. These procedures include the specimen preparation and RC and TS testing sequences.

The third section presents the RC/TS analysis procedures. These procedures include correction for equipment generated damping, and application of the stress integration approach to develop modulus reduction and damping curves.

And the fourth section presents a discussion of the factors affecting the modulus reduction and damping curves for Bonneville clay. These factors are plasticity index, confining pressure, and a cyclic degradation. The modulus reduction and damping of Bonneville clay are compared with generic modulus reduction and damping curves.

These comparisons show that Bonneville clay behaves more linear than generic curves predict. At the end of this section, conclusions drawn from the test results are presented.

9.2 SOIL SPECIMENS

Bonneville clay is very soft lacustrine silty-clay deposited in Ancient Lake Bonneville. It underlies the shores of both the Great Salt Lake and Utah Lake as well as the large portions of Salt Lake Valley and adjacent valleys. Seven samples of Bonneville clay were tested in this study. They were obtained from four different sites distributed across the Wasatch front. Three samples were collected at a site near the Provo River in Utah County. One sample was from a site at Nibley in Cache County. One sample was from a site in Logan in Cache County. And, two samples were collected from a site near the Salt Lake City Airport in Salt Lake County. Locations of each site are presented in Table 9.1.

Table 9.1 Sample Sites Location

Site No.	County	Address
1	Utah	Geneva Rd. Bridge over Provo River, Provo, UT
2	Cache	2835 S 1000 W Nibley, UT
3	Cache	USU Drainage Farm Site Logan, UT
4	Salt Lake	BYU Research Site North West of Salt Lake City International Airport, Salt Lake City, UT

Undisturbed samples were recovered from the sites using thin-walled Shelby tubes. Radiographic (X-ray) images were made of all samples prior to opening sample tubes to assess the sample quality and to select portions of the sample for testing. Atterberg limits and hydrometer tests were performed on each sample to determine the soil classification and index properties of soil specimen. Other physical properties of the soil specimen were also determined prior to the RC/TS testing. The physical properties and unified soil classification are presented in Table 9.2.

All of the soil specimens in this study are fine-grained soils with, the percent passing the No. 200 sieve all greater than 85%. The index properties of each soil specimen are plotted on the plasticity chart as shown in Figure 9.1. Specimens from the site near the Provo River, PRV37 and PRV67, are low to medium plasticity silty clay (CL), except for one sample, PRV93, from the depth of 93 ft which was clayey silt with very fine sands (ML). A specimen from shallow depth, SLC14, from a site near the Salt Lake City airport is a low to medium plasticity clay (CL) and a specimen from a deeper depth, SLC35, was low plasticity silty sand (ML). Soil specimens from Nibley, NBL24, and Logan, LGN14, are high plasticity clay (CH).

9.3 RC/TS TESTING PROCEDURE

9.3.1 Specimen Preparation

The X-ray images of the sample tube were visually examined to select the best quality portions of the samples. Once a sample portion was chosen, each end of the selected portion was cut using a tube cutter. The side of the tube was then cut vertically

Table 9.2 Physical Properties of Soil Specimens

Sample ID	Site No.	Depth (ft)	Unified Soil Classification	Liquid Limit	Plasticity Index	% Passing No.200 Sieve	% Clay Size Particle < 0.002 mm	Water Content (%)	Unit Weight (pcf)	Void Ratio	Degree of Saturation (%)
PRV37	1	37	CL	43	20	99.46	16.81	30.61	113.86	0.981	85.77
PRV67	1	67	CL	33	11	85.84	8.42	22.40	123.13	0.661	89.83
PRV93	1	93	ML	41	10	97.60	16.10	41.64	115.09	1.052	99.85
NBL24	2	24	CH	63	34	99.32	24.03	53.83	106.53	1.483	99.78
LGN14	3	14	CH	65	34	98.82	19.92	60.90	101.80	1.744	91.54
SLC14	4	14	CL	42	17	98.98	9.06	41.07	114.57	1.043	99.91
SLC35	4	35	ML	27	2	89.94	7.00	22.26	117.15	0.735	76.48

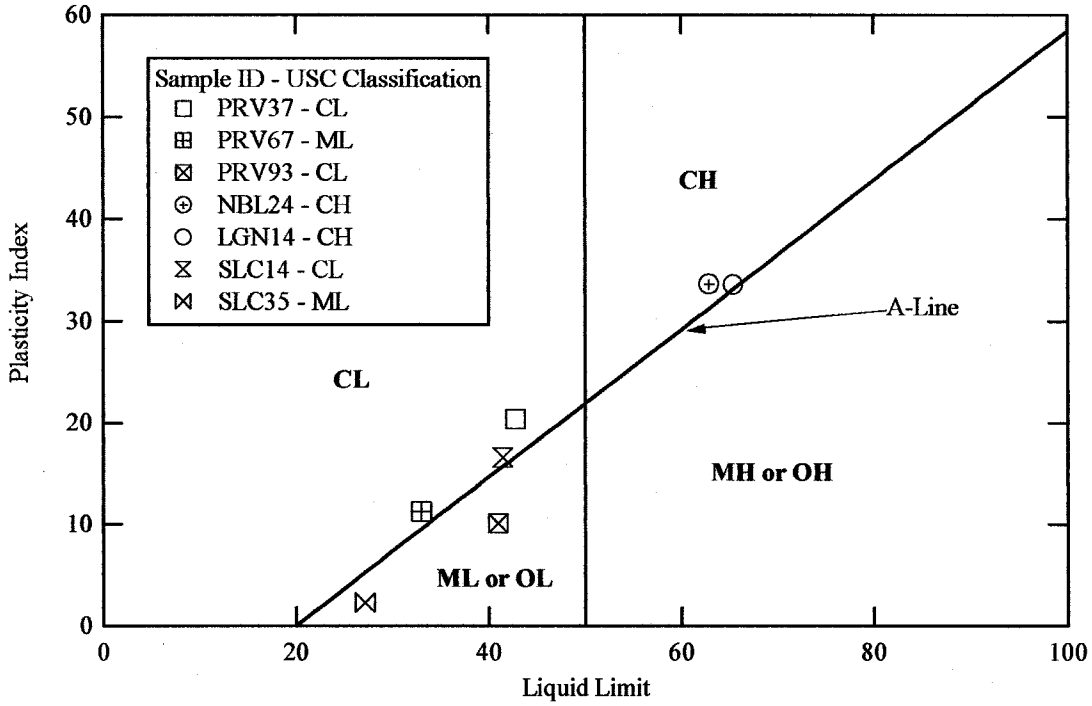

Figure 9.1 Unified soil classification of Bonneville clay specimens tested in this study

using a band saw. In most case, the tube sprung open after cutting, and the soil was easily removed. When the tube did not spring open, the opposite side of the tube was cut to remove soil with minimal disturbance.

Soil specimens were carefully hand-trimmed to a diameter of approximately 1.4 inches and a height of about 3.0 inches using a trimming device and wire saw. Water content was determined using the trimmings. The trimmed specimen was weighed and dimensions were measured before placing the specimen on the base pedestal of the RC/TS equipment.

Next, two small circular pieces of filter paper were placed over the drainage holes on the base pedestal. The base pedestal was then secured to the base plate with four

screws. The specimen was then set on the base platen and the top cap was gently placed on top of specimen. Two layers of latex membrane were then placed over the soil specimen and each layer of membrane was sealed separately with O-rings on the top cap and the base pedestal. A silicon oil bath was then placed around the specimen to minimize the diffusion of air through the membrane.

At this point the drive plate was attached to the top platen and the cell was positioned around the specimen and drive plate. The confining pressure was then applied and soil specimen was allowed to consolidate. When the specimen reached the end of primary consolidation, RC/TS testing was performed.

9.3.2 RC/TS Testing Sequence

A series of RC and TS tests were performed on soil specimens at each confining pressure. In this study, soil specimens were consolidated to the estimated mean in situ effective confining pressure (σ'_m) and two additional higher pressures at levels of $2\sigma'_m$ and $4\sigma'_m$. The RC and TS test are separated into two categories; low-amplitude tests and high-amplitude tests. The low-amplitude tests are tests at strains at which the soil specimen behaves linearly. The high amplitude tests are tests at strains where the soil acts nonlinearly. This nonlinearity can be identified from a decrease in resonant frequency in the RC test. Typically, the strain of a high-amplitude test is above 10^{-3}%.

In this study, the TS testing was performed using loading frequency of 0.333 Hz for 5 cycles. The TS testing sequence is presented in Figure 9.2. For each confining pressure the TS tests were always performed first because the soil specimen was

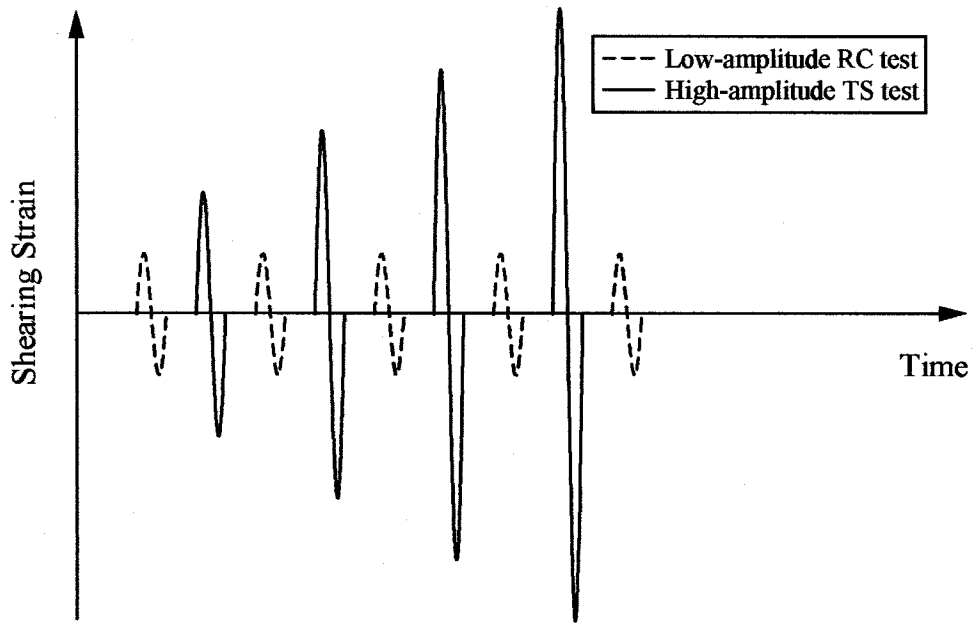

Figure 9.2 Testing sequence for the TS test

subjected to fewer cycles than in the RC test. However, low-amplitude RC tests were always performed before any high-amplitude TS tests to monitor any change in the small strain shear modulus (G_{max}) of the soil specimen. If the G_{max} changed significantly, the testing was paused until soil specimen returned to the original G_{max}.

After finishing the last high-amplitude TS test, a low amplitude RC test was performed. The RC test sequence is presented in Figure 9.3. Since the soil was subjected to high strain during high-amplitude TS test, a significant decrease in the value of G_{max} was always observed after the last high-amplitude TS test. A series of low-amplitude RC test were then performed over period of time to monitor the increase in G_{max} of the soil specimen. Once the value of G_{max} was recovered to its original value (typically after at

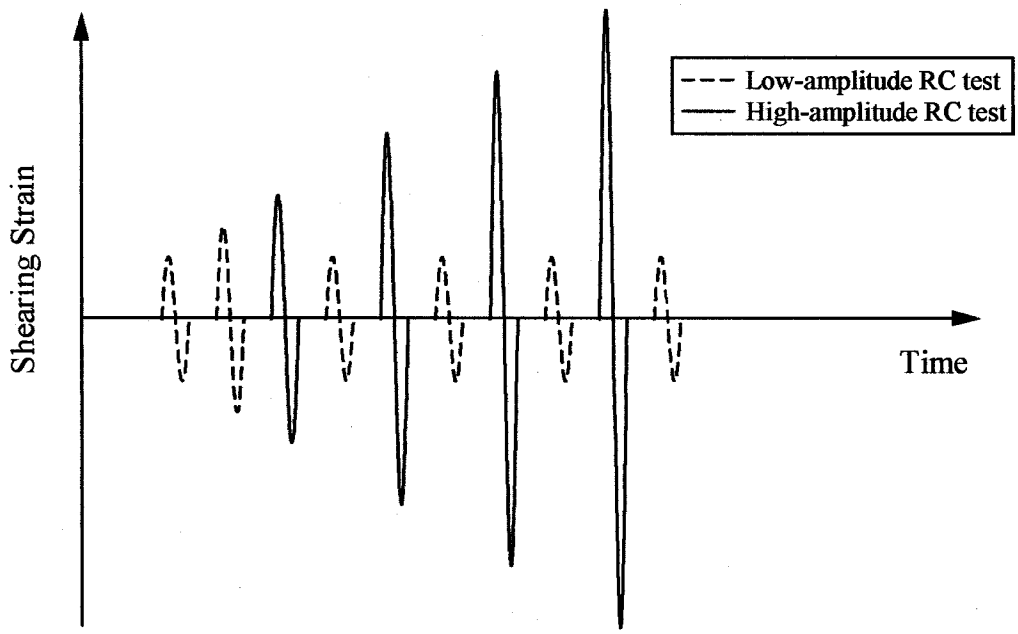

Figure 9.3 Testing sequence for the RC test

least 4 hours), the series of high strain amplitude RC tests were performed. The RC testing sequence was similar, to the TS sequence, with low amplitude RC tests performed before any high amplitude RC test. If the value of G_{max} did not return to the original value after a reasonably period of time, the change in the value of G_{max} was then recorded and the next high amplitude test was performed.

For both RC and TS tests the shear strains from less than10^{-4} to more than 10^{-1}% were applied to the soil, depending upon the soil specimen stiffness. When the high amplitude RC testing was completed the confining pressure was increased to the next level, the specimen was allowed to consolidated and the RC and TS testing sequence was repeated.

9.4 RC/TS ANALYSIS PROCEDURE

9.4.1 Correction for Equipment Generated Damping

The electromagnetic model presented in this study was used to predict the equipment generated damping, D_{eq}, generated in the RC/TS drive system due to the back emf effect. As presented in Chapter 7, the back emf effect is modeled as an additional spring and an additional dashpot creating additional stiffness and viscosity in the system. The additional stiffness, called the equipment generated spring stiffness, k_{eq}, is considered to be very small and can be neglected. The additional equipment generated viscous damping coefficient, c_{eq}, was used to calculate D_{eq}. The c_{eq} value can be predicted using Equation 5.31, and the model parameters; L_c, R_c, k_i, k_B. For the RC test, the value of D_{eq} is calculated from:

$$D_{eq} = \frac{c_{eq}}{c_c}. \tag{9.1}$$

As discussed in Chapter 7, the value of c_{eq} is reasonably constant over the a frequency range of 0-130 Hz, with a slight decrease at higher frequencies. The critical damping, c_c is a function of resonant frequency and the polar moment of inertia of the drive plate, J_o and top cap, J_t. Consequently, the variation of predicted D_{eq} with resonant frequency mostly depends upon variation in critical damping, c_c. In this study, a variation of J_o with frequency was observed due to the non-rigid body motion of the drive plate, as presented in Chapter 4. This J_o variation was taken into account when calculating c_c. Decreasing values of D_{eq} with increasing resonant frequency was observed, as presented in Chapter 7.

In a series of RC test, the resonant frequency, f_m at each stage of the test was used to determine the frequency dependent parameters, k_B and J_o. Values of c_{eq} and c_c were then calculated using:

$$c_{eq} = \frac{k_i k_B R_c}{R_c^2 + \omega^2 L_c^2}, \text{ and} \tag{9.2}$$

$$c_c = 4\pi \Sigma J f_n \tag{9.3}$$

where $f_n = \frac{f_m}{\sqrt{1-2D^2}}$, and

ΣJ = total mass polar moment of inertia of the added mass (J_o+J_t).

The model parameters, k_i, R_c and L_c have constant values of 0.318 lb-ft/rad, 45.6 ohms, and 0.0256 H, respectively. Values of k_B and J_o vary with frequency. An example of the calculations for correcting D on specimen LGN14 is presented in Table 9.3.

Increasing strain amplitude in RC tests results in decreasing resonant frequencies as can be seen in Table 9.3. The D_{eq} generated in the RC/TS drive system is inversely proportional to the resonant frequency, so as the strain amplitude increases, the D_{eq} also increases. Figure 9.4 shows a plot of the predicted D_{eq} versus strain for the RC test of specimen LGN14. This soil specimen is very soft with low-strain resonant frequency of about 12 Hz, and a low-strain material damping of about 2%. As shown in Table 9.3 and Figure 9.4, the calculated D_{eq} ranges from about 0.8% at low-strain amplitudes up to as high as 1.3% for high-strain amplitudes. The value of D_{eq} is almost 40% of the actual material damping at low-strains. As a result, correcting for the equipment generated damping, D_{eq}, is critical when performing low-strain RC test on low-resonant frequency soils.

Table 9.3 Example of Calculations to Correct D for Equipment Generated Damping, D_{eq}, for RC Test of Soil Specimen LGN14 from Logan, Utah

Resonant Frequency, f_m (Hz)	Shear Strain, γ (%)	Measured D (%)	J_o[1] (lb-ft-sec^2)	k_B[2] (V/rad/s)	Predicted c_{eq} (lb-ft-sec)	Calculated c_c (lb-ft-sec)	Predicted D_{eq} (%)	Corrected D (%)
11.96	1.286e-3	3.061	2.102e-3	0.3778	2.630e-3	3.178e-1	0.827	2.234
11.95	2.608e-3	3.012	2.102e-3	0.3778	2.630e-3	3.176e-1	0.828	2.184
11.88	4.962e-3	3.191	2.102e-3	0.3778	2.630e-3	3.157e-1	0.833	2.358
10.80	1.100e-2	4.503	2.102e-3	0.3777	2.630e-3	2.873e-1	0.915	3.588
10.26	1.868e-2	7.112	2.102e-3	0.3777	2.631e-3	2.737e-1	0.961	6.151
9.24	3.341e-2	10.307	2.101e-3	0.3777	2.631e-3	2.479e-1	1.061	9.246
8.24	4.494e-2	15.855	2.101e-3	0.3777	2.631e-3	2.244e-1	1.172	14.683
7.54	5.408e-2	20.595	2.101e-3	0.3777	2.632e-3	2.092e-1	1.258	19.337

Note: 1. $J_o = 0.0021013+4.673e\text{-}10freq^{2.6798}$
2. $k_B = 0.3776+3.1227e\text{-}7freq^{2.5307}$

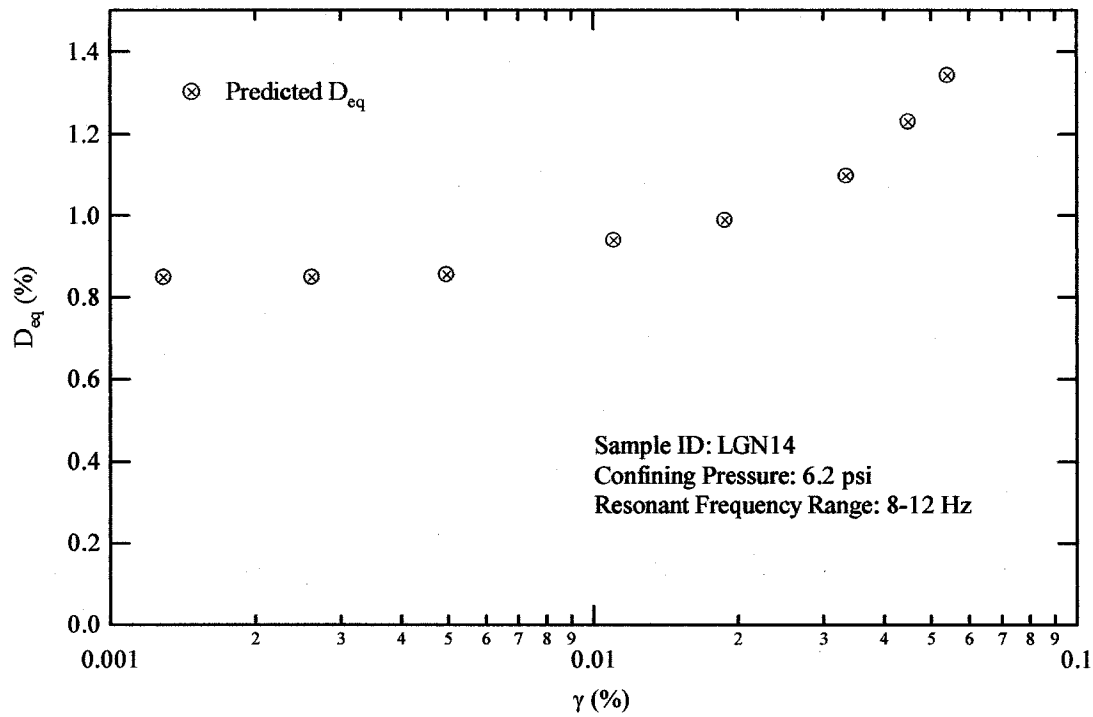

Figure 9.4 Predicted D_{eq} for a series of RC test on soil specimen LGN14

Figure 9.5 shows the plot of measured D and corrected D versus strain amplitude for specimen LGN4 at confining pressure of 6.2 psi. The damping was corrected by subtracting the predicted D_{eq} from the measured D. This procedure was used to account for the equipment generated damping for all of the RC tests throughout this study.

9.4.2 Application of Stress Integration Approach

The stress integration approach developed in this study was applied to all of the RC/TS tests on Bonneville clay. This approach was developed to account for the nonuniform stresses and strains occurring over the radius of the soil specimen. The basic concept of this approach is to find a τ–γ relationship described by an assumed soil model that results in a theoretical T-θ relationships that corresponds to the measured T-θ relationship using curve fitting techniques. Details of this approach are presented in Chapter 8.

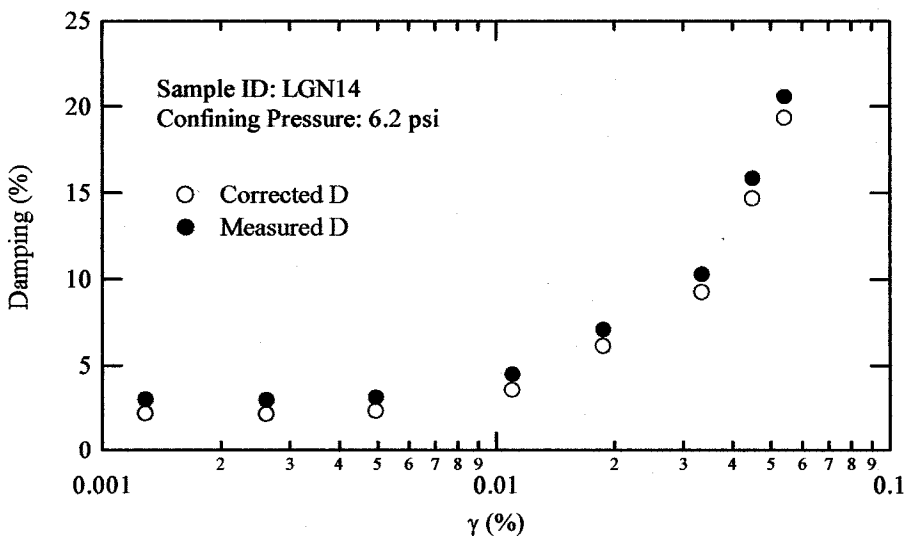

Figure 9.5 Measured and corrected damping for a series of RC test on soil specimen LGN14 obtained from Logan, Utah at a depth of 14 feet

The stress integration approach was used to develop modulus reduction curves and damping curves using the following procedure. (1) Perform curve fitting on the measured T- θ relation using either the closed form solution or numerical integration of each soil models following procedures presented in Chapter 8. (2) Select the best soil model that provides the best fit to the experimental data. (3) Develop the modulus reduction curves based on the selected soil model and the model parameters. (4) Determine values of R_{eq} based on the hyperbolic model parameters over the range of rotations generating in testing. (5) Develop the damping curve by calculating the shear strain associated with each value of θ using the appropriate R_{eq} value.

9.4.2.1 Curve Fitting for T-θ Relationships and Model Selection. The measured T-θ relationship from RC and TS test on seven soil samples at different confining pressures are presented in Figures 9.6-9.18. Curve fitting was performed on each measured T-θ relationship using three soil models; the hyperbolic, the modified hyperbolic, and the Ramberg-Osgood. The closed form solution was used to predict the T-θ relationship for the hyperbolic model while the numerical integration was used to predict the T-θ relationship for the modified hyperbolic and the Ramberg-Osgood models.

The small strain shear modulus, G_{max} was evaluated from low-strain RC/TS tests. The G_{max} value for each test was known, therefore it was constrained during the curve fitting. The best fit T-θ relationships using the three soil models are also plotted in Figures 9.6-9.18. The model parameters and chi-square values determined from the

curve fitting are presented in Table 9.4. The shaded fields in Table 9.4 are the model parameter providing the best fit.

In Figures 9.6-9.18, the measured and calculated values of T are plotted versus log θ so the curve fitting can be evaluated over a wide range of strains. The values of G_{max} were constrained, therefore the curve fitting T-θ relationships always converge at low strains. All of the assumed soil models perform very well in the linear range verifying that the value G_{max} used for curve fitting is close to the actual value of G_{max}. At high strains, the stress integration approach performs effectively when the data points of the T-θ relationship are separated by small gaps. This can be observed by comparing the curve fitting results between specimen PRV93, in Figure 9.9, were the data points are separated by small gaps and specimen NBL24, Figures 9.11a and 9.11b, the data points are separated by large gaps. In Figures 9.11a and 9.11b, the modified hyperbolic model and Ramberg-Osgood performed equally well in fitting the last two points at high strains. However, in the region with no data points, the match is poor. The spacing between data points is a concern when applying the stress integration approach.

Once the curve fitting was performed for each assumed soil model, the best fit model was selected to represent the τ–γ relationship for the soil. As discussed in Chapter 8, chi-square is one indicator of how well the curve fitting matched the data. However, the chi-square value was always considered along with visual justification. The chi-square should be used alone only in the cases where all of assumed models match the measured T-θ relationship such that the differences cannot be distinguished visually. In

this study, the best fit soil model was selected for each test individually after careful consideration.

The modified hyperbolic model fit was the most commonly selected model for predicting the τ–γ relationships for Bonneville clay in this study. The Ramberg-Osgood model generally fit the T-θ relationship at high strains better than the other two models. However, the Ramberg-Osgood model fit the data poorly at strain levels close to the elastic threshold strain, γ_e^t. The hyperbolic model fit the T–θ relationship well at low to medium strain levels but typically fit the data poorly at high strain levels.

9.4.2.2 Development of Modulus Reduction Curve. The modulus reduction curve (G versus log γ), and normalized modulus reduction curve (G/G_{max} versus log γ) were developed from the τ–γ relationship that provided the best fit to the measured T-θ data. The modulus reduction curve and normalized modulus reduction curve are generated as continuous functions. They can be generated for over any range of strains. However, it is only rational to develop the curve for strain levels in the range where the T-θ relationship was measured. In this study, the modulus reduction curve was generated for each RC and TS test for the range of strain levels up to the strain level performed in each test which was corresponded to the maximum measured rotation, θ_{max} measured for each test. The equivalent radius approach was used to determine maximum measured strain, γ_{max}, corresponded to that value of θ_{max}. The γ_{max}, of each test is calculated from:

$$\gamma_{max} = R_{eq} \frac{\theta_{max} R}{L} \tag{9.4}$$

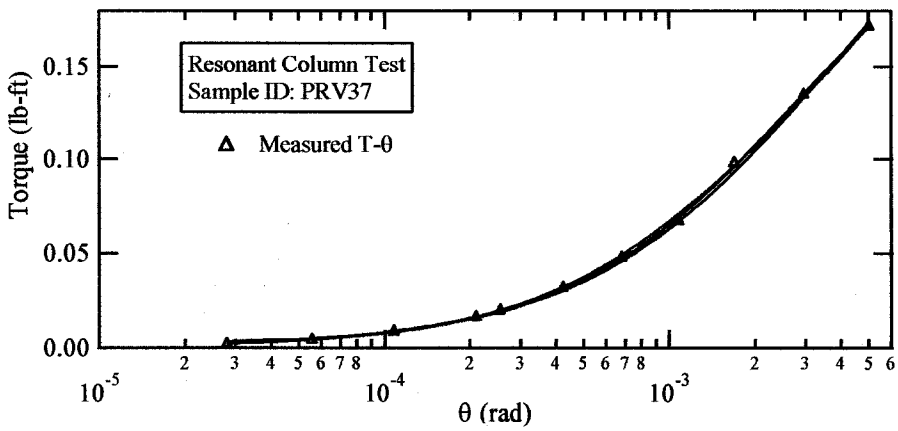

a) Confining pressure of 12.4 psi

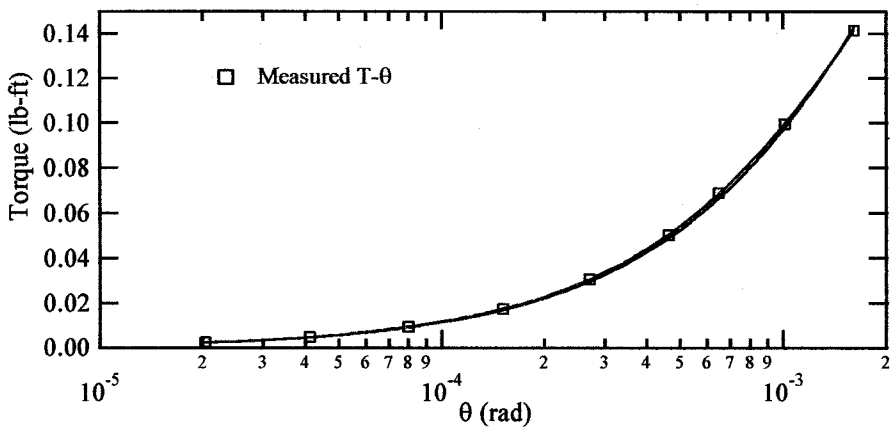

b) Confining pressure of 24.8 psi

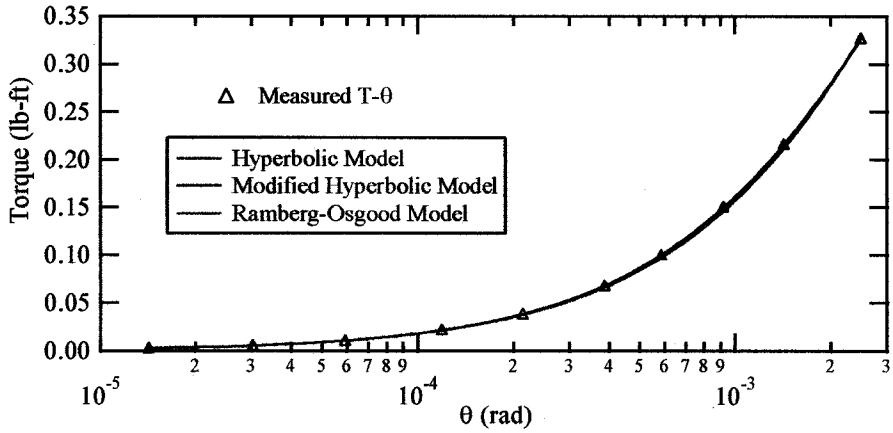

c) Confining pressure of 49.6 psi

Figure 9.6 Curve fitting T-θ relationships for the RC test on soil specimen PRV37 obtained near the Provo River at a depth of 37 ft

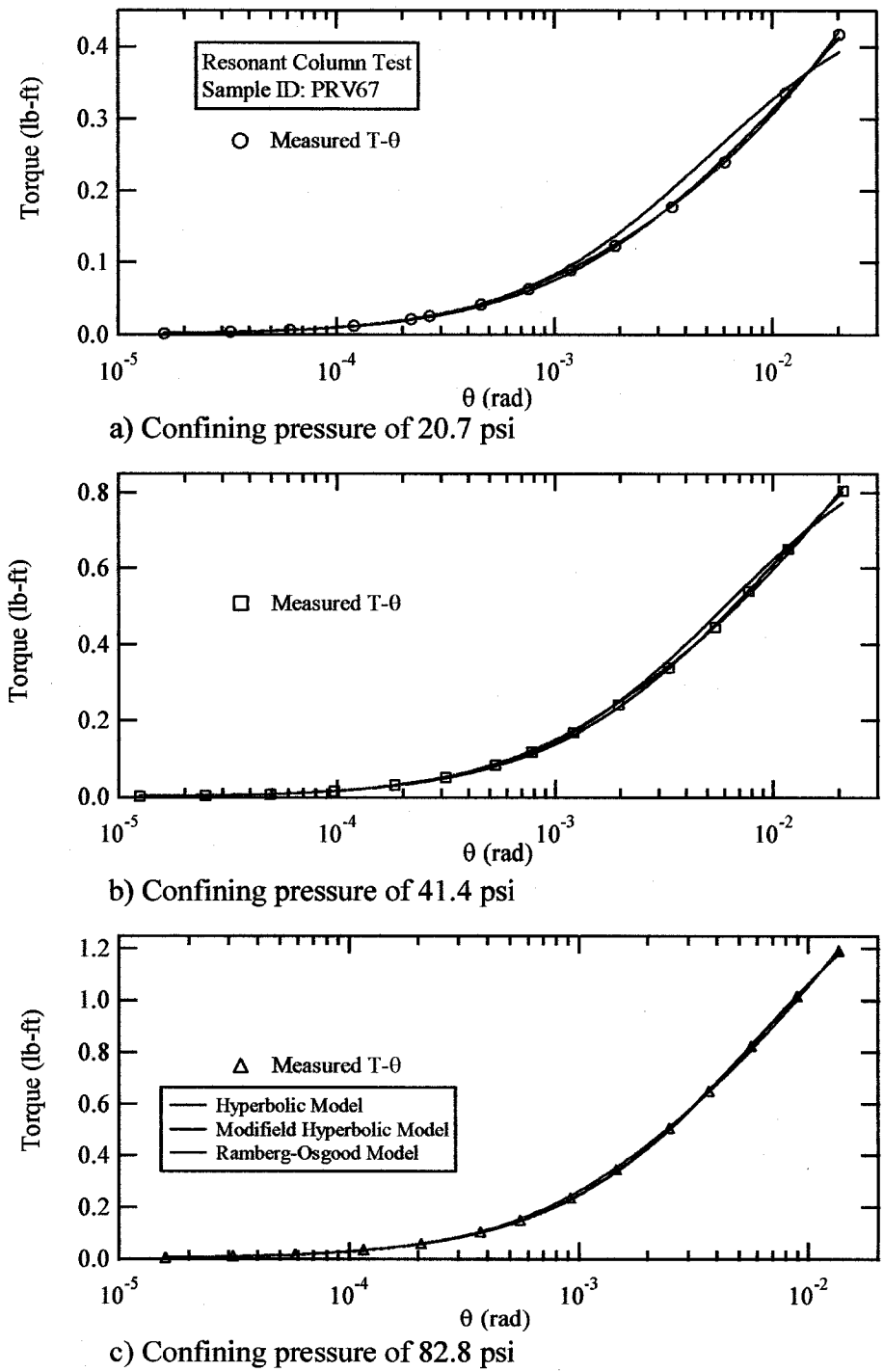

Figure 9.7 Curve fitting for T-θ relationship for the RC tests on soil specimen PRV67 obtained near the Provo River at a depth of 67 ft

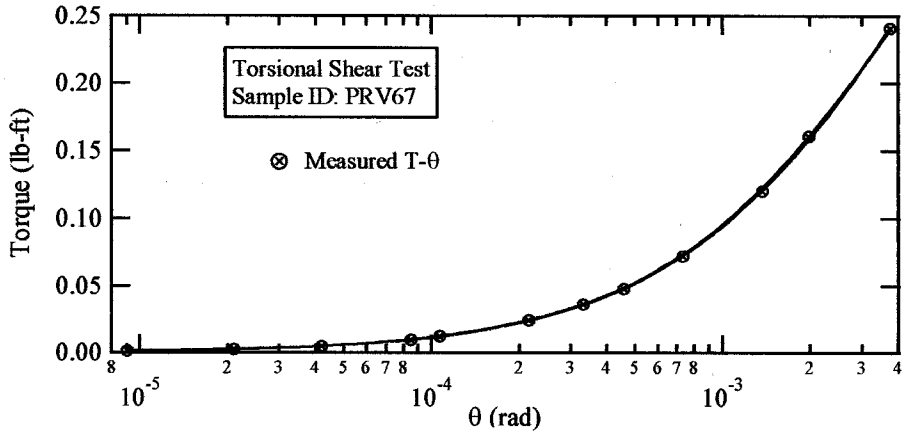

a) Confining pressure of 20.7 psi

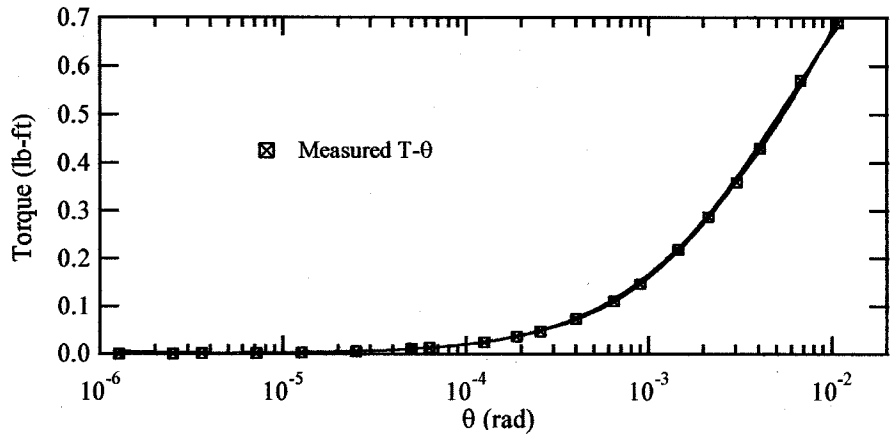

b) Confining pressure of 41.4 psi

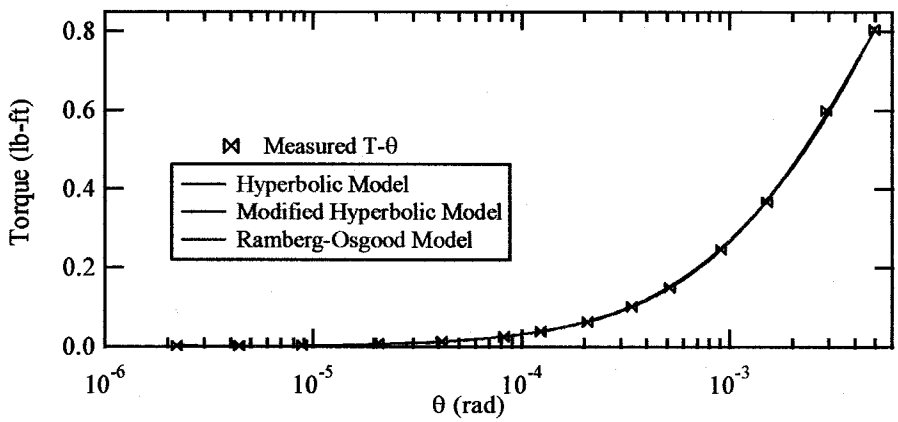

c) Confining pressure of 82.8 psi

Figure 9.8 Curve fitting for T-θ relationship for the TS tests on soil specimen PRV67 obtained near the Provo River at a depth of 67 ft

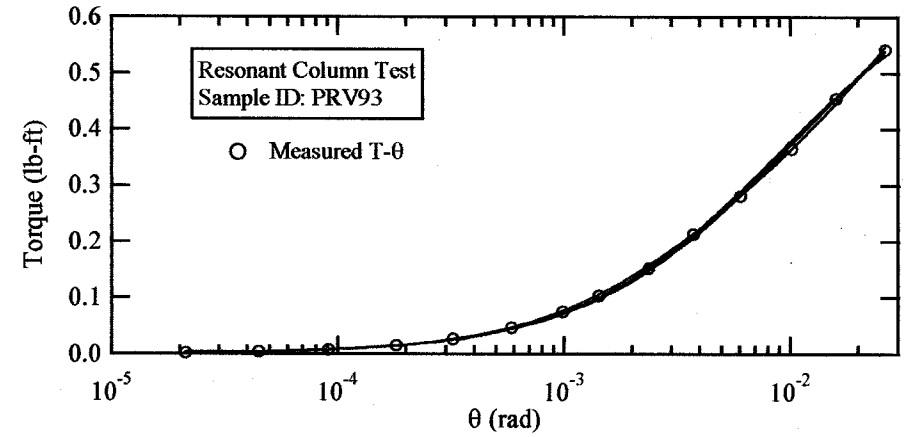

a) Confining pressure of 28 psi

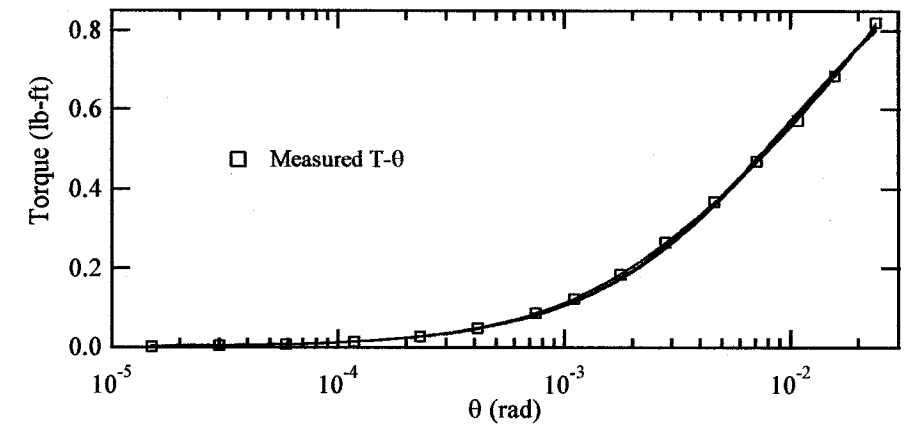

b) Confining pressure of 56 psi

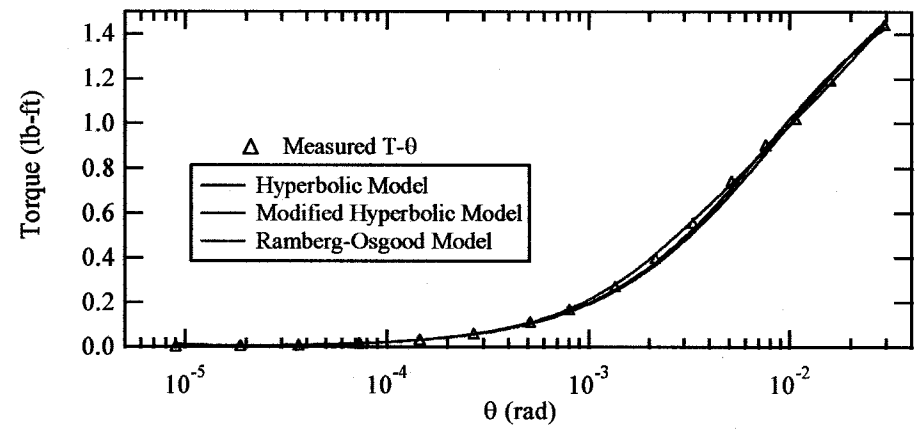

c) Confining pressure of 112 psi

Figure 9.9 Curve fitting for T-θ relationship for the RC tests on soil specimen PRV93 obtained near the Provo River at a depth of 93 ft

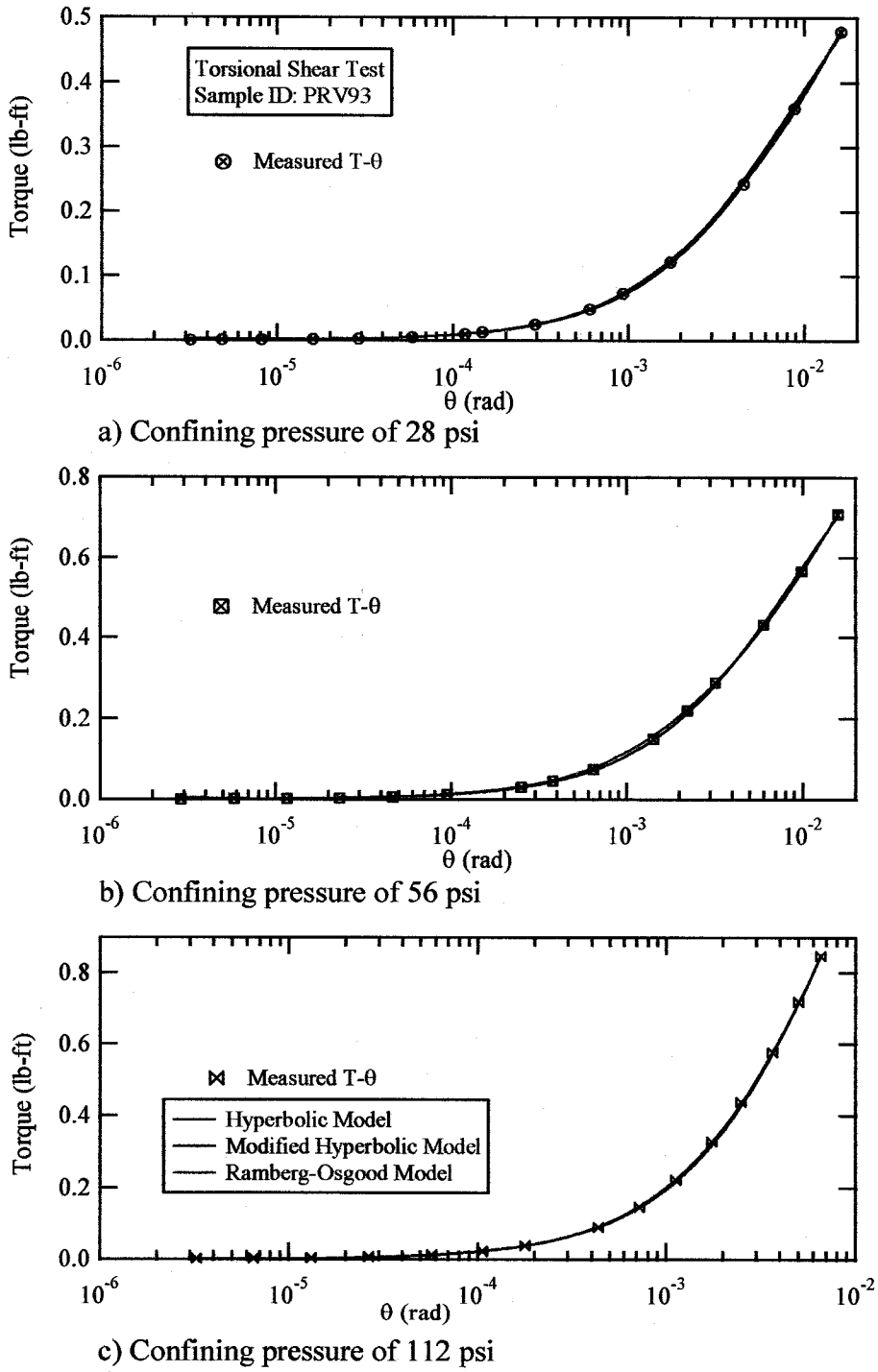

Figure 9.10 Curve fitting for T-θ relationship for the TS tests on soil specimen PRV93 obtained near the Provo River at a depth of 93 ft

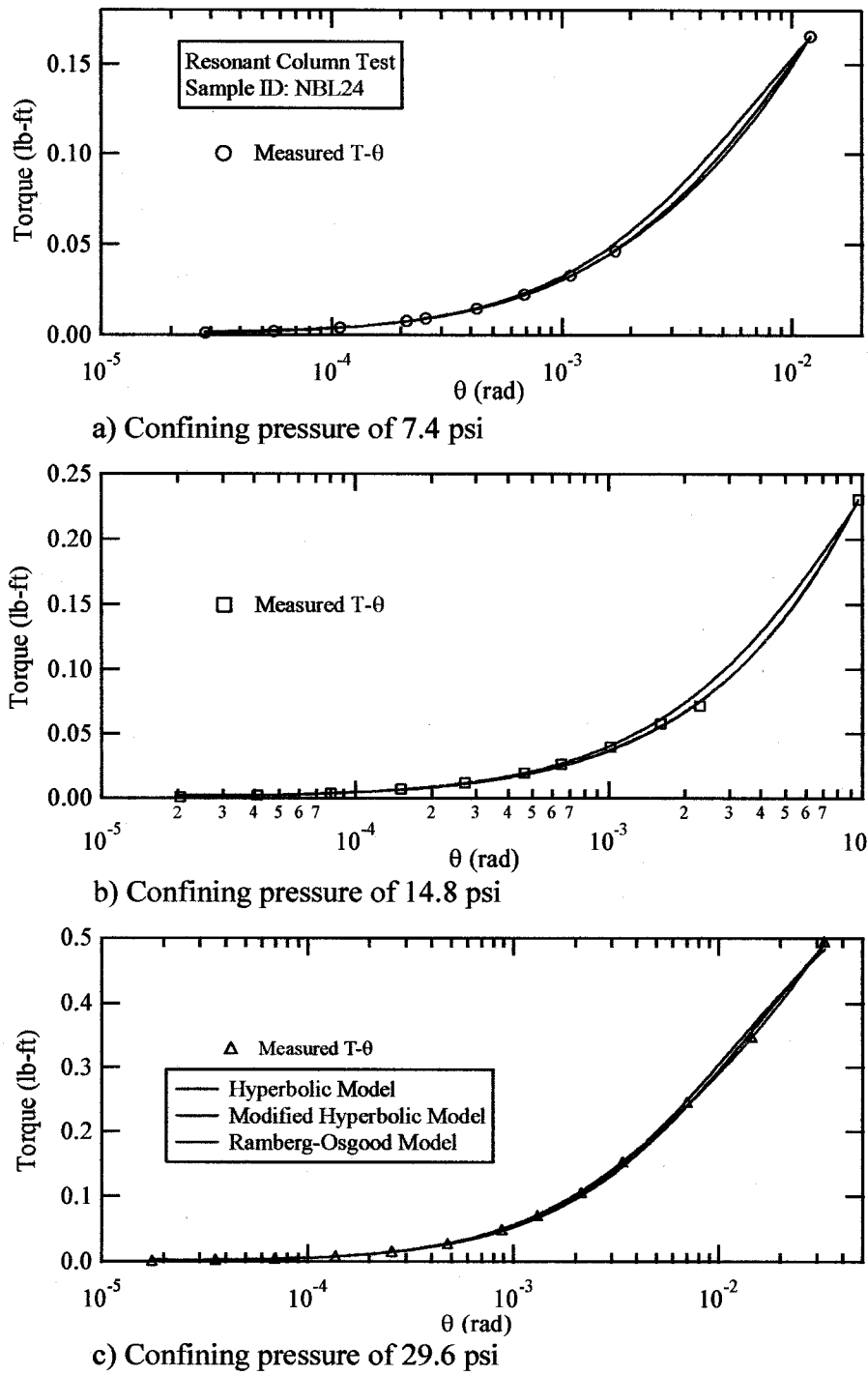

Figure 9.11 Curve fitting for T-θ relationship for the RC test on soil specimen NBL24 obtained from Nibley at a depth of 24 ft

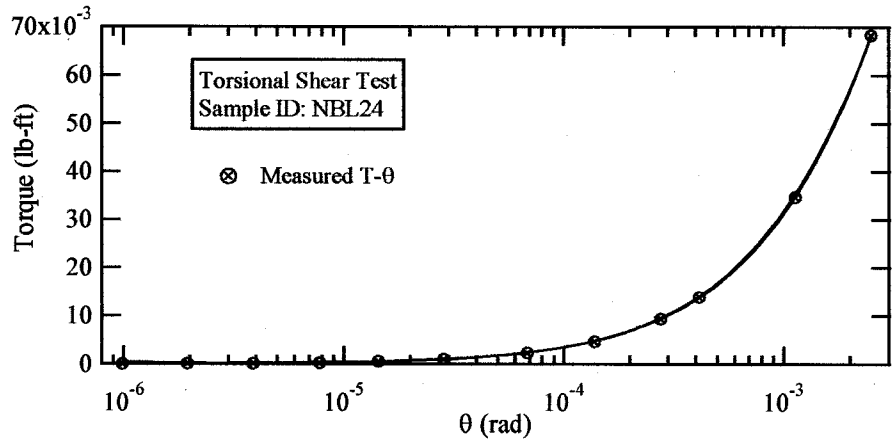

a) Confining pressure of 7.4 psi

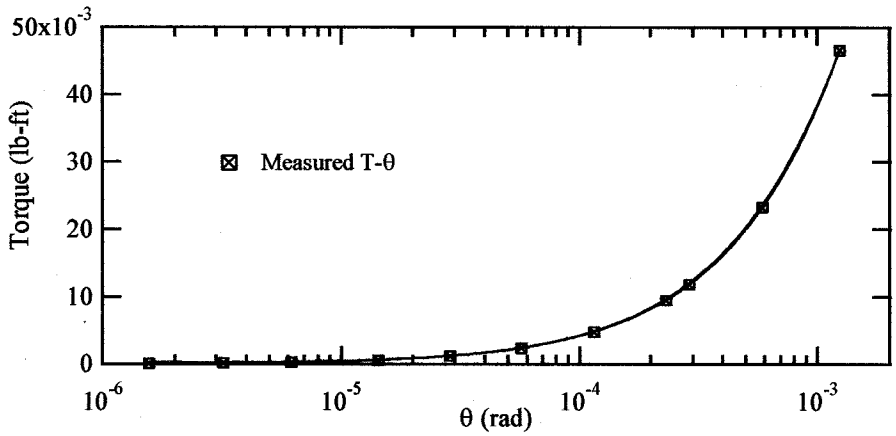

b) Confining pressure of 14.8 psi

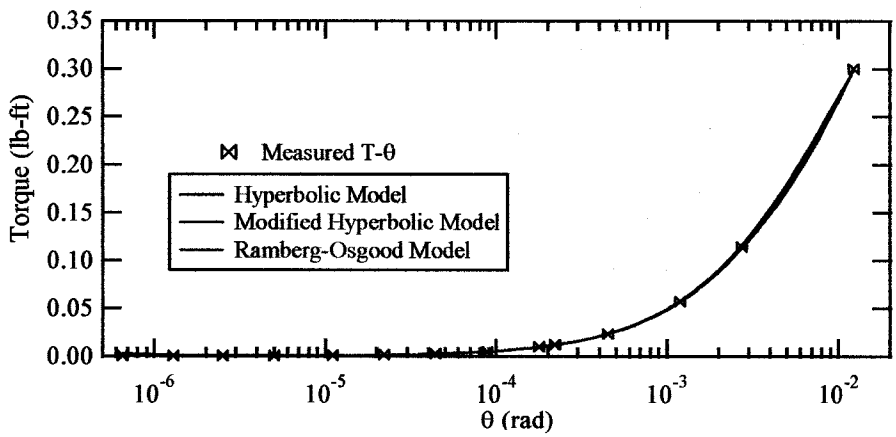

c) Confining pressure of 29.6 psi

Figure 9.12 Curve fitting for T-θ relationship for the TS tests on soil specimen NBL24 obtained from Nibley at a depth of 24 ft

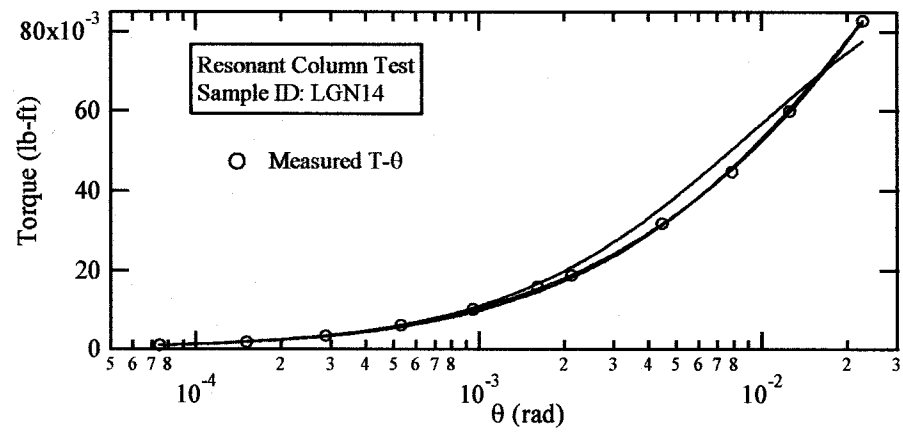

a) Confining pressure of 6.2 psi

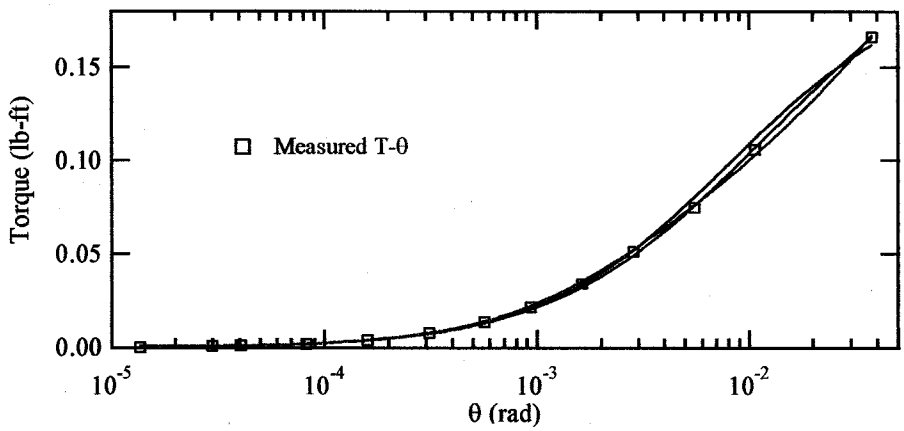

b) Confining pressure of 12.4 psi

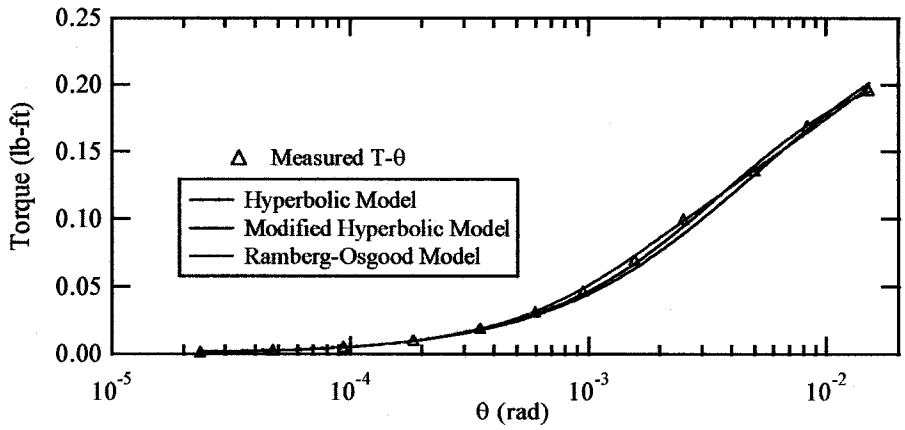

c) Confining pressure of 24.8 psi

Figure 9.13 Curve fitting for T-θ relationship for the RC tests on soil specimen LGN14 obtained from Logan at a depth of 14 ft

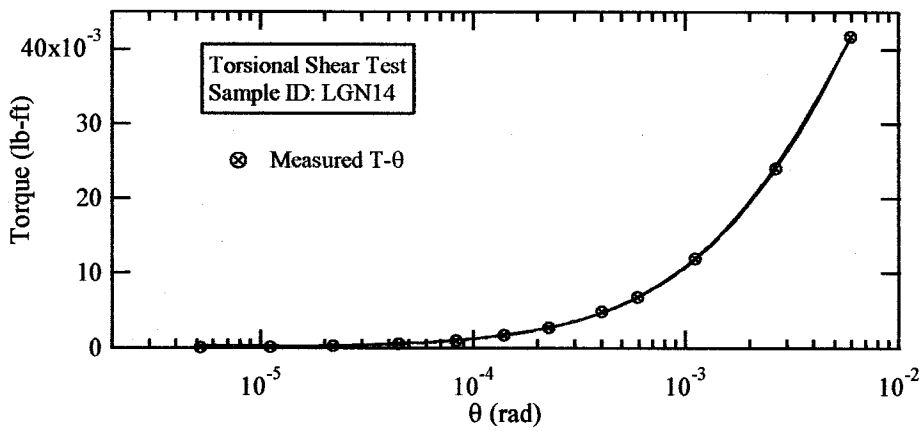

a) Confining pressure of 6.2 psi

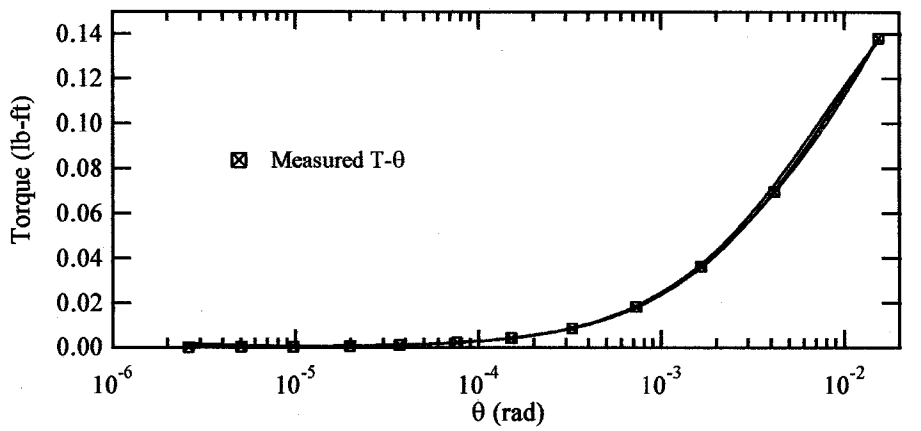

a) Confining pressure of 6.2 psi

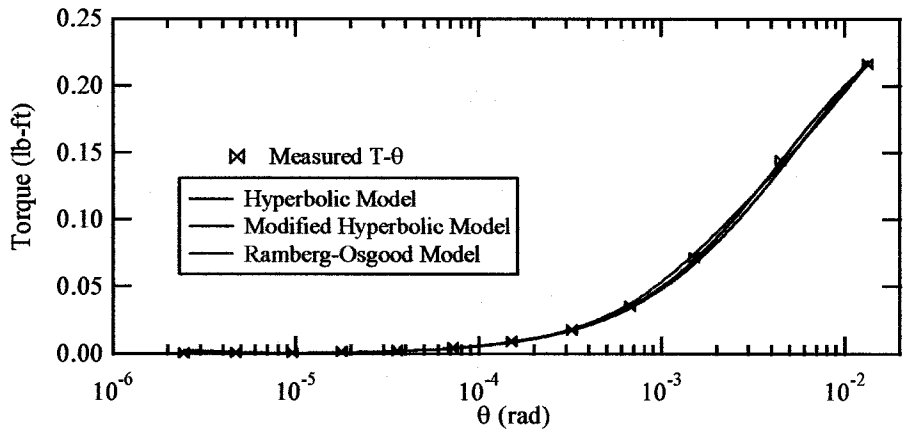

a) Confining pressure of 6.2 psi

Figure 9.14 Curve fitting for T-θ relationship for the TS tests on soil specimen LGN14 obtained from Logan at a depth of 14 ft

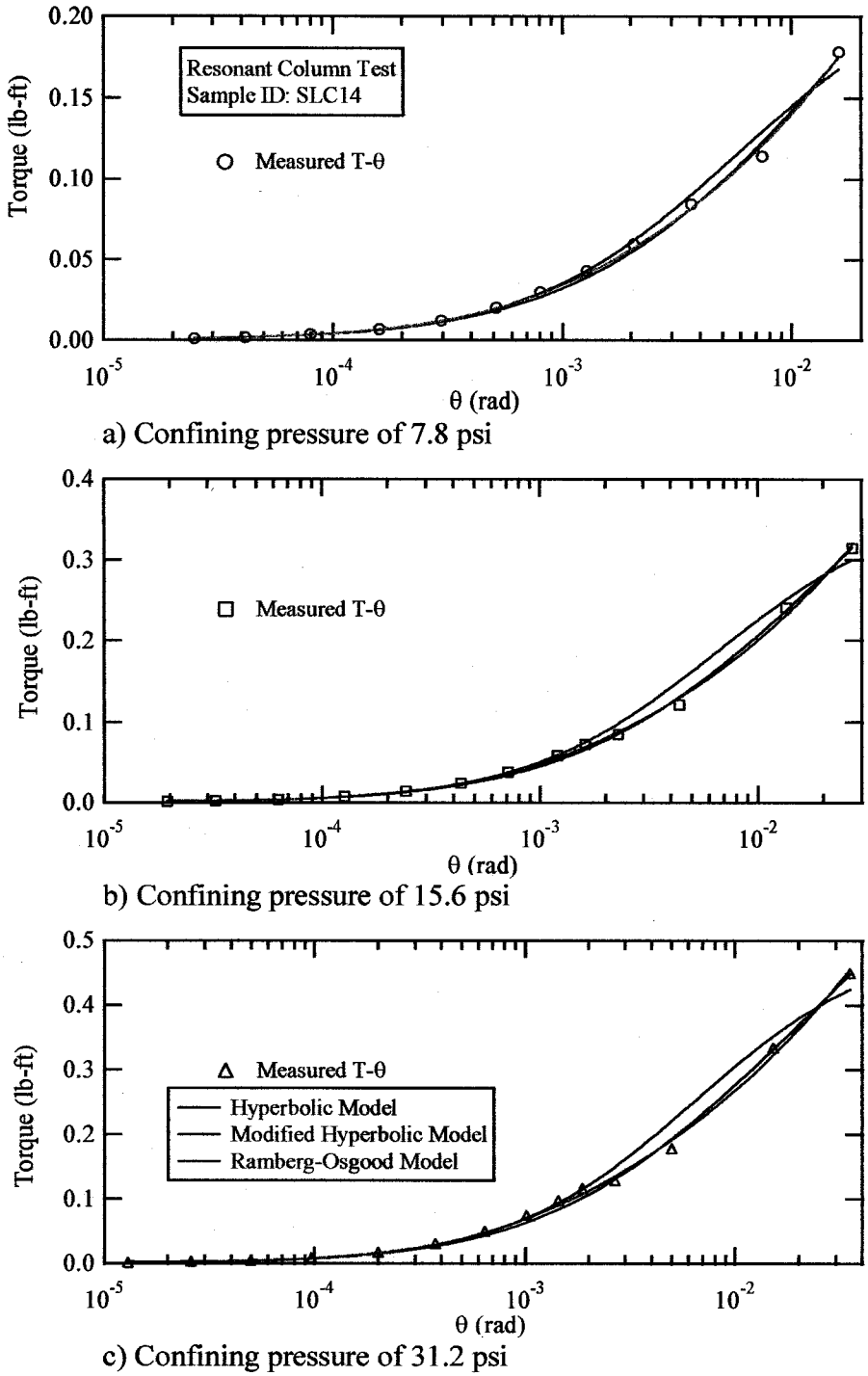

Figure 9.15 Curve fitting for T-θ relationship for the RC tests on soil specimen SLC14 obtained near Salt Lake City Airport at a depth of 14 ft

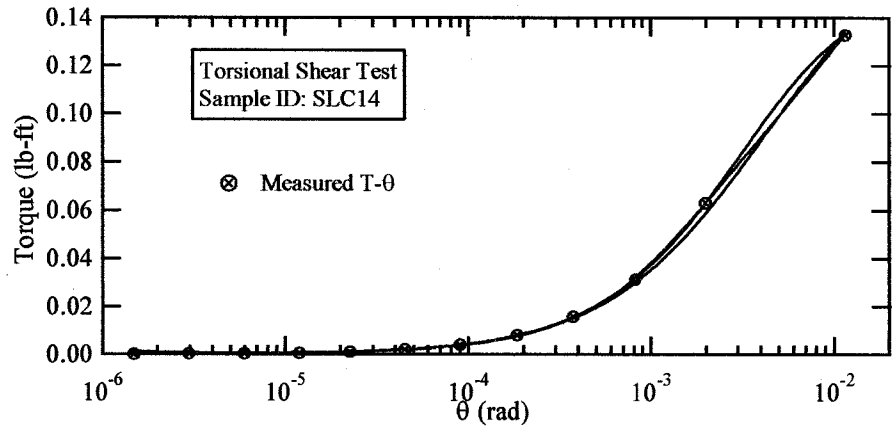

a) Confining pressure of 7.8 psi

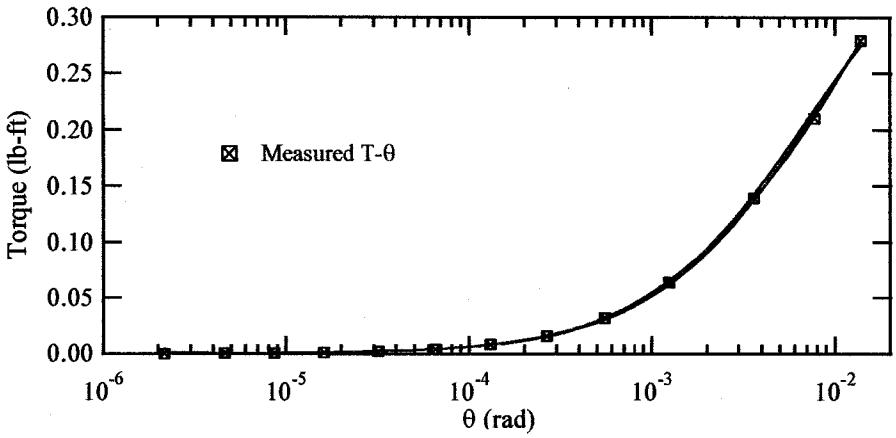

c) Confining pressure of 15.6 psi

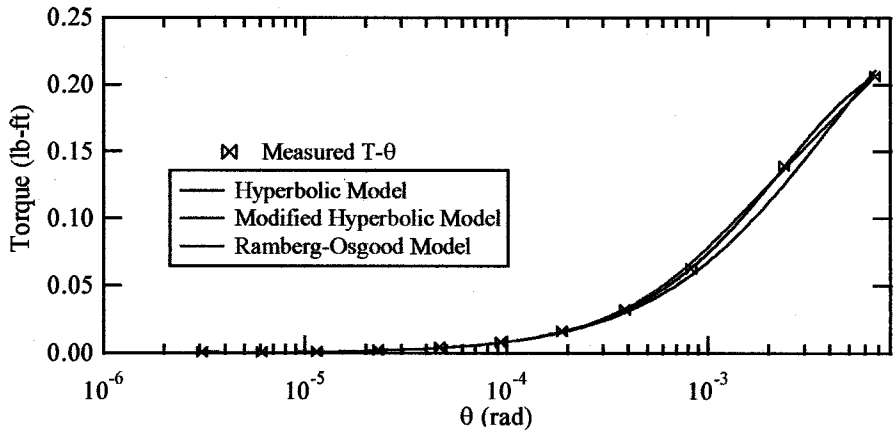

c) Confining pressure of 31.2 psi

Figure 9.16 Curve fitting for T-θ relationship for the TS tests on soil specimen SLC14 obtained near Salt Lake City Airport at a depth of 14 ft

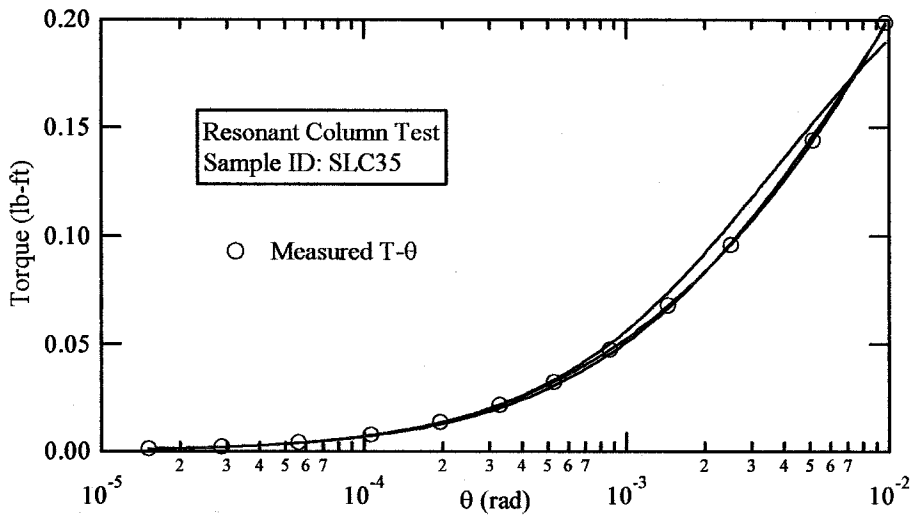

a) Confining pressure of 13.2 psi

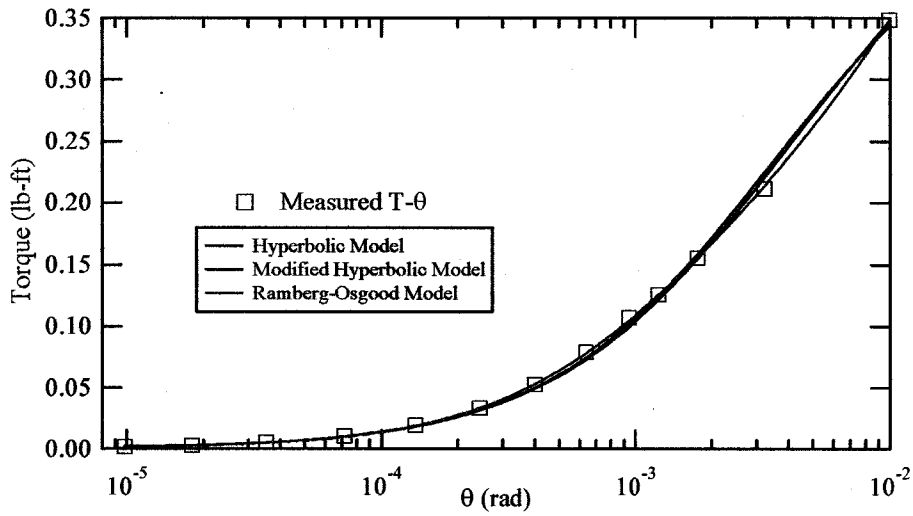

b) Confining pressure of 26.4 psi

Figure 9.17 Curve fitting for T-θ relationship for the RC tests on soil specimen SLC14 obtained near Salt Lake City Airport at a depth of 35 ft

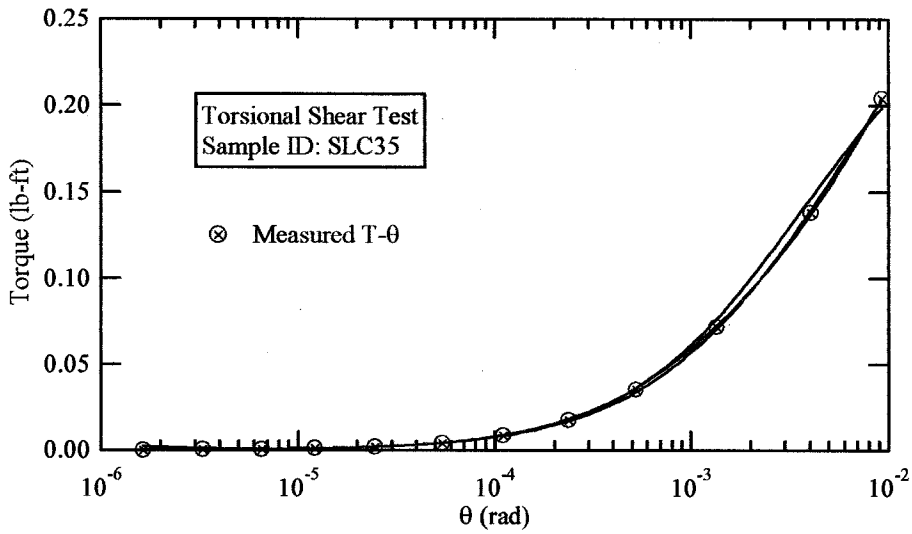

a) Confining pressure of 13.2 psi

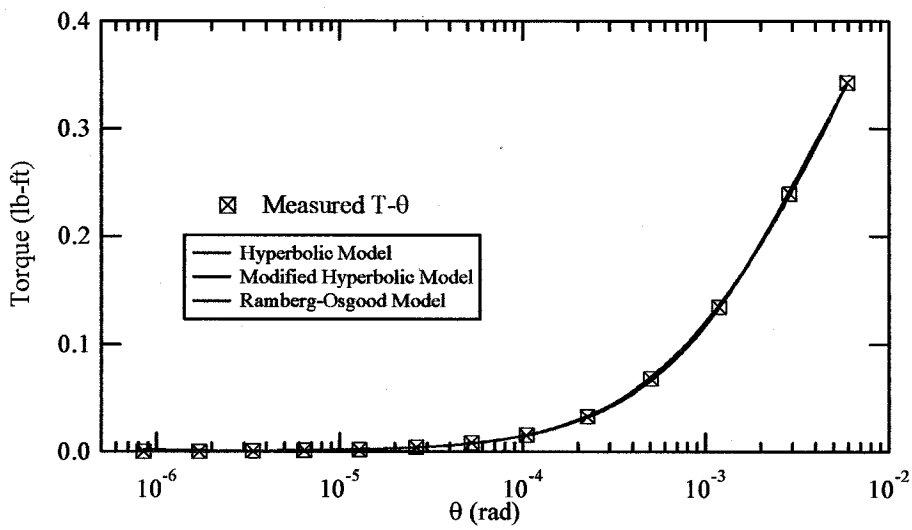

b) Confining pressure of 26.4 psi

Figure 9.18 Curve fitting for T-θ relationship for the TS tests on soil specimen SLC14 obtained near Salt Lake City Airport at a depth of 35 ft

Table 9.3 Curve Fitting Results from RC/TS tests on Bonneville Clay

Sample ID	Test	Confining Pressure (psi)	G_{max} (psf)	Hyperbolic Model		Modified Hyperbolic Model			Ramberg-Osgood Model			
				γ_r (%)	chi-square	γ_r (%)	a	chi-square	γ_r (%)	α	b	chi-square
PRV37	RC[1]	12.4	9.854e5	0.0682	3.755e-5	0.0686	1.1247	1.125e-5	0.0517	2.5892	3.1565	2.294e-5
		24.8	1.417e6	0.1003	1.391e-5	0.0711	1.2718	1.746e-7	0.0845	1.8386	2.8475	1.594e-7
		49.6	2.237e6	0.12024	4.311e-5	0.0975	1.2199	3.707e-8	0.0751	1.5531	2.6576	9.285e-7
PRV67	RC	20.7	1.360e6	0.0826	2.358e-5	0.0646	0.8156	1.140e-4	0.0911	5.7177	2.6408	1.115e-4
		41.4	2.369e6	0.09883	2.827e-3	0.0884	0.8848	1.703e-4	0.0943	1.5387	2.9293	4.389e-4
		82.8	4.120e6	0.1002	2.218e-4	0.0991	0.9804	1.359e-4	0.0881	3.5389	3.0348	7.820e-4
	TS	20.7	1.576e6	0.0787	1.507e-5	0.0813	0.9247	4.777e-6	0.0672	1.8889	2.3368	1.213e-5
		41.4	2.700e6	0.0890	3.909e-4	0.0837	0.9332	7.048e-5	0.0810	1.2712	2.7652	3.230e-4
		82.8	4.512e6	0.0901	1.390e-3	0.0903	0.9822	1.463e-4	0.1260	4.3452	2.4520	3.903e-4
PRV93	RC	28	1.143e6	0.1468	4.158e-4	0.1405	0.9461	1.977e-4	0.1206	3.3366	3.0810	1.245e-4
		56	1.730e6	0.1626	1.117e-3	0.1589	0.9612	9.534e-4	0.1164	1.0101	3.0471	3.234e-5
		112	3.406e6	0.1496	6.555e-3	0.1575	1.0676	3.758e-3	0.0725	0.8989	3.9020	1.383e-3
	TS	28	1.191e6	0.1447	1.274e-4	0.1397	0.9245	2.171e-6	0.0917	1.7197	2.7414	5.821e-5
		56	1.750e6	0.1621	1.251e-4	0.1618	0.9957	1.455e-4	0.1130	1.2465	2.6823	1.884e-4
		112	3.388e6	0.1750	1.910e-4	0.1665	1.0905	6.015e-5	0.0520	0.4246	2.6025	7.282e-5
NBL24	RC	7.4	4.985e5	0.1233	2.251e-5	0.1105	0.8179	1.334e-6	0.0860	1.9180	2.2430	1.188e-7
		14.8	6.012e5	0.2041	1.432e-4	0.2338	0.6307	2.804e-5	0.1652	1.1277	1.8279	2.231e-5
		29.6	8.053e5	0.1907	4.766e-4	0.1784	0.9231	2.215e-4	0.0983	1.3168	2.9929	4.862e-5
	TS	7.4	4.790e5	0.1454	4.439e-7	0.1903	0.8268	1.334e-7	0.1387	1.1602	1.9624	1.534e-7
		14.8	5.920e5	0.1607	1.627e-7	0.3564	0.7183	6.790e-8	0.1667	0.5338	1.6435	4.149e-8
		29.6	7.500e6	0.1736	1.1207e-5	0.1708	0.9196	7.085e-5	0.0089	1.1244	2.4910	2.154e-6
LGN14	RC	6.2	1.900e5	0.1499	8.807e-6	0.1190	0.7200	4.263e-6	0.1660	3.7006	2.2539	8.051e-7
		12.4	4.130e5	0.1309	9.038e-5	0.1160	0.9101	1.354e-5	0.2011	3.0293	3.2337	1.498e-5
		24.8	8.810e5	0.0845	2.055e-4	0.0924	1.1340	5.800e-5	0.0583	2.4987	4.1770	5.050e-5
	TS	6.2	2.050e5	0.1148	1.463e-6	0.1206	0.8130	1.491e-7	0.1895	3.6054	2.1361	2.504e-7
		12.4	4.530e5	0.1251	1.127e-5	0.1176	0.9104	3.888e-6	0.2278	2.8652	2.6826	1.305e-6
		24.8	9.350e5	0.0909	4.658e-5	0.0973	1.0986	8.159e-6	0.0682	2.9783	3.7016	3.390e-5

Table 9.3 (continued)

Sample Location	Test	Confining Pressure (psi)	G_{max} (psf)	Hyperbolic Model		Modified Hyperbolic Model			Ramberg-Osgood Model			
				γ_r (%)	chi-square	γ_r (%)	a	chi-square	γ_r (%)	α	b	chi-square
SLC14	RC	7.8	5.918e5	0.0876	3.832e-4	0.0719	0.8014	1.328e-4	0.0644	2.5520	2.5660	6.295e-5
		15.6	8.200e5	0.1045	1.335e-3	0.0169	0.7898	1.992e-4	0.0765	3.0820	2.5711	1.919e-4
		31.2	1.175e6	0.1000	3.349e-4	0.0741	0.8210	7.909e-4	0.0356	0.9476	2.8067	4.986e-4
	TS	7.8	6.213e5	0.0680	2.297e-5	0.0767	1.1452	1.852e-6	0.0278	3.0341	4.0786	1.094e-6
		15.6	8.628e5	0.1094	8.992e-5	0.1037	0.9067	2.957e-5	0.0723	1.9080	2.7680	5.563e-6
		31.2	1.232e6	0.0649	2.192e-4	0.0720	1.3202	2.105e-6	0.0437	2.4400	4.3630	2.997e-5
SLC35	RC	13.2	6.897e5	0.0769	3.027e-4	0.0640	0.7958	1.695e-5	0.0670	2.4297	2.4638	6.825e-8
		26.4	1.370e6	0.0696	2.830e-4	0.0669	0.9522	2.185e-4	0.0438	2.0074	3.0837	1.312e-5
	TS	13.2	7.568e5	0.0737	1.233e-4	0.0640	0.8463	1.189e-5	0.0528	2.4193	2.6647	2.577e-6
		26.4	1.480e6	0.0787	9.096e-6	0.0783	0.9819	1.086e-5	0.0486	1.6063	2.8360	1.232e-5

Note: 1. Due to the technical program, the TS test was not performed on this sample
2. Shaded fields represent the best fit soil model

The parameter γ_r from the hyperbolic model was used to obtain a normalized rotation (θ_{max}/θ_r). Thus, the value of R_{eq} is obtained from the normalized R_{eq} curve based on shear modulus developed in this study presented in Figure 8.13b. The modulus reduction curve at strains above γ_{max} is uncertain.

The modulus reduction curve and normalized modulus reduction curve from RC and TS tests on each soil specimen are presented in Figures 9.19-9.25. The modulus reduction curves are plotted versus strain level up to the maximum measured strain. The curve was then extended to higher strains using the dashed lines.

The results from RC and TS test were compared for all soil specimens except for specimen PRV37. On this sample, only the RC test was performed. It should be noted that the shear moduli obtained in the TS test, were evaluated from the first cycle of the hysteresis loop. For all of the specimens except for specimen NBL24, the shear modulus from TS test is higher than the shear modulus from the RC test. The two differences between the RC and TS tests are the frequency and the number of loading cycles. The TS tests were performed at a frequency of 0.333 Hz for five cycles while the RC test was performed at resonant frequency with a high number of cycles. In general, the stiffness of a cohesive soil increases as the frequency increases. On the other hand, stiffness decreases as the number of cycles increases (Kim 1991). The lower values of shear modulus in RC test maybe explained by the effects of cyclic degradation outweighing the frequency effects.

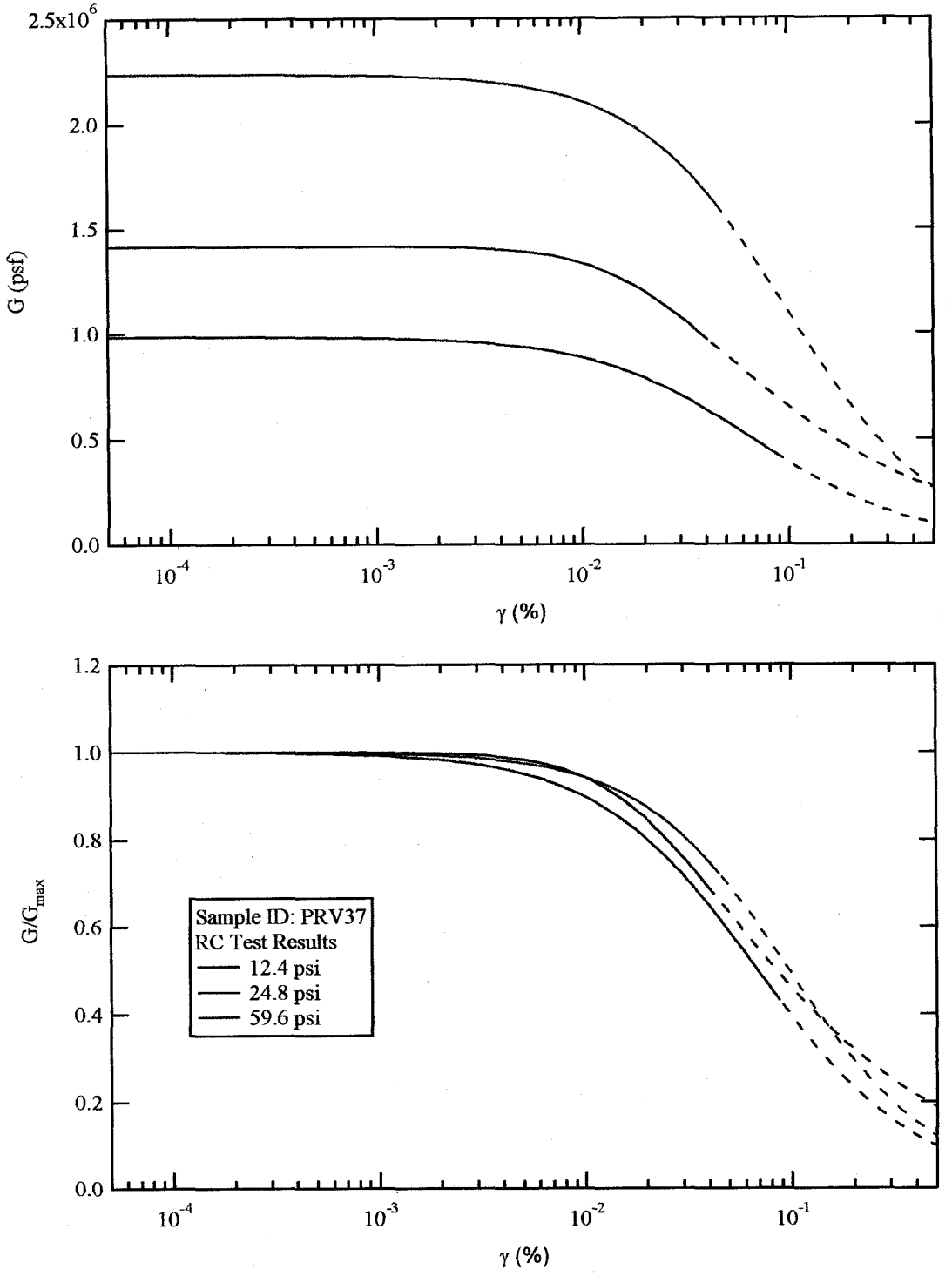

Figure 9.19 Modulus reduction curves and normalized modulus reduction curves measured at various confining pressures for soil specimen PRV37 near the Provo River at a depth of 37 ft

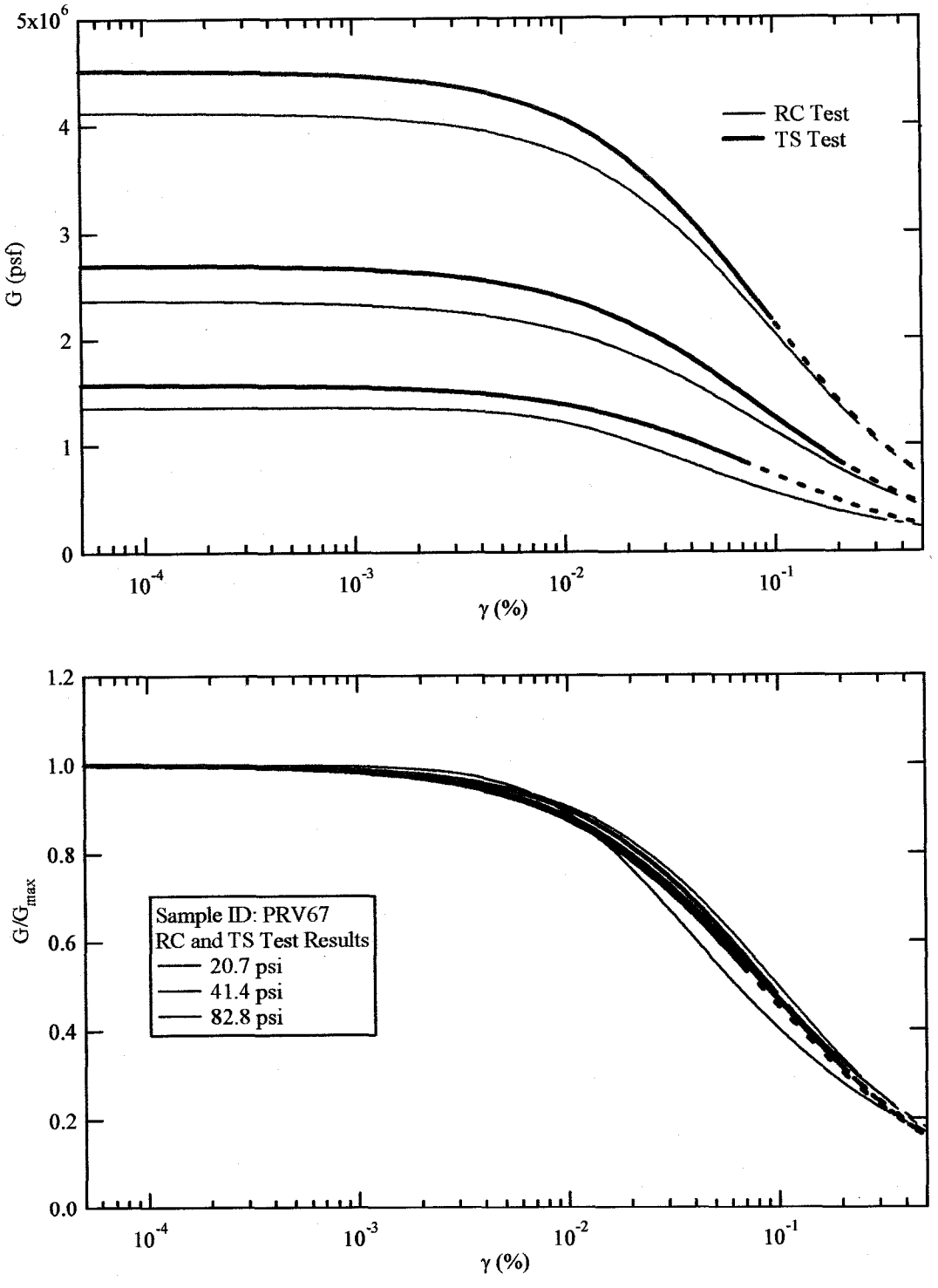

Figure 9.20 Modulus reduction curves and normalized modulus reduction curves measured at various confining pressures for soil specimen PRV67 near the Provo River at a depth of 67 ft

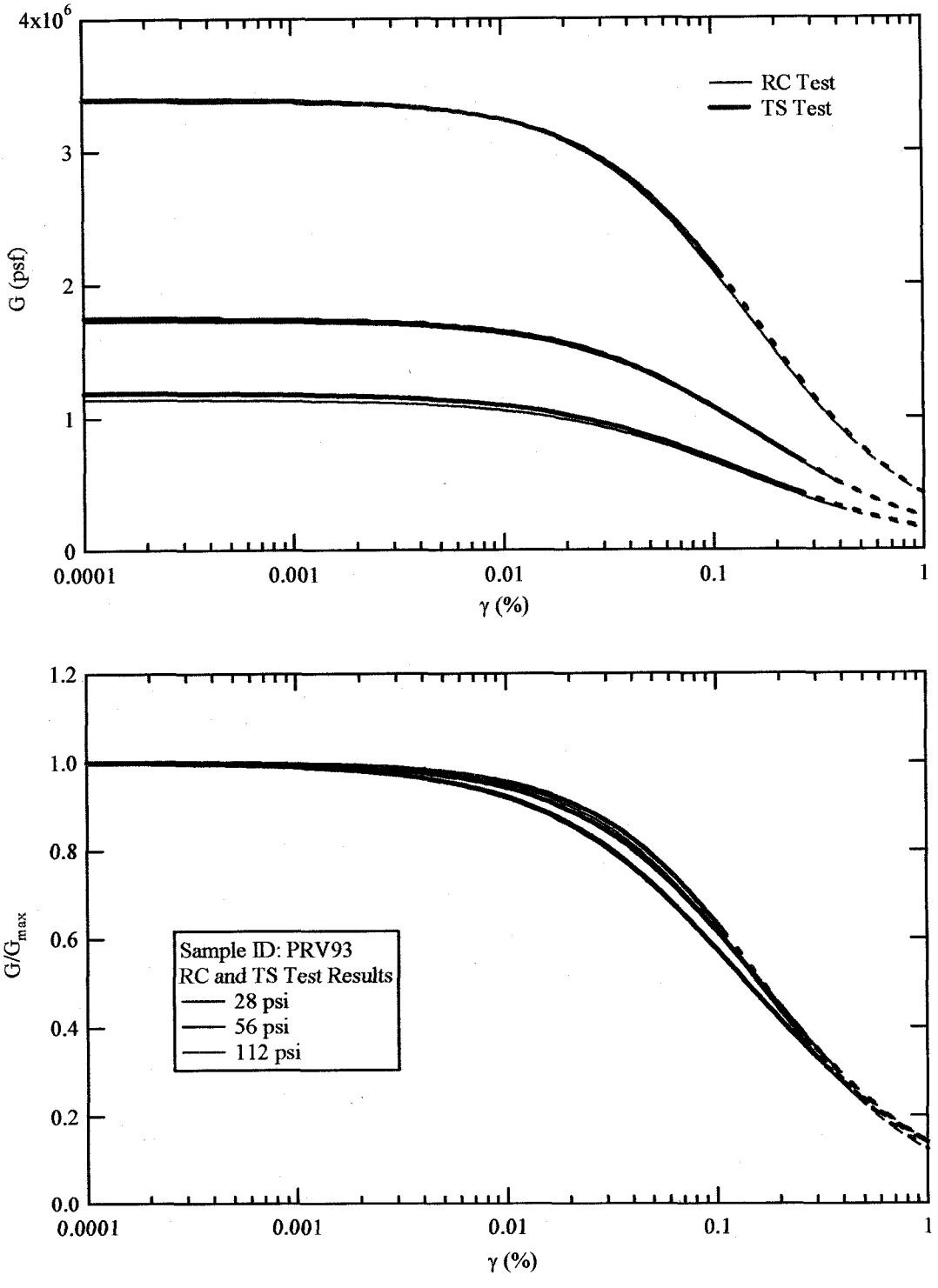

Figure 9.21 Modulus reduction curves and normalized modulus reduction curves measured at various confining pressures for soil specimen PRV93 near the Provo River at a depth of 93 ft

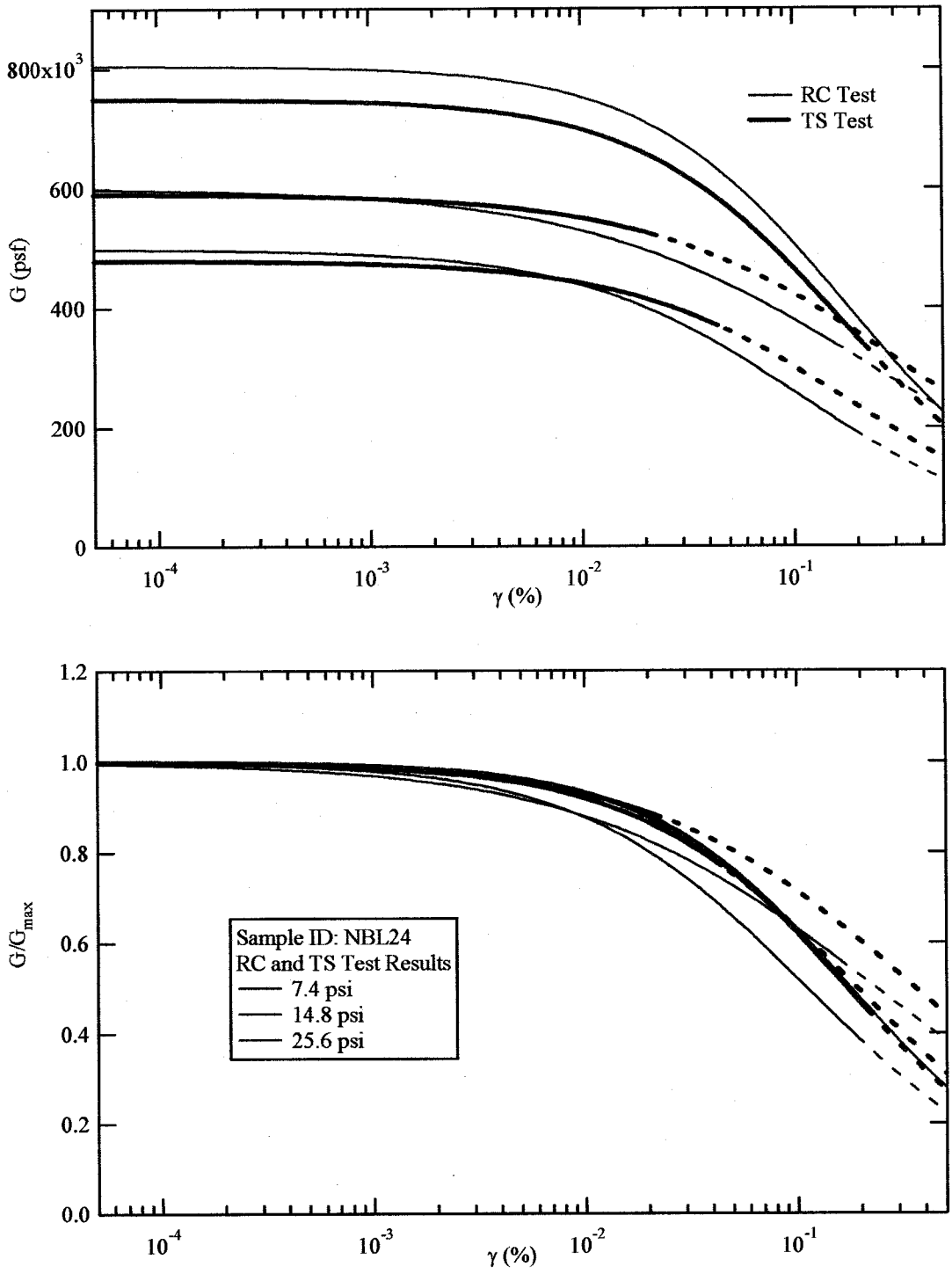

Figure 9.22 Modulus reduction curves and normalized modulus reduction curves measured at various confining pressures for soil specimen NBL24 at Nibley at a depth of 24 ft

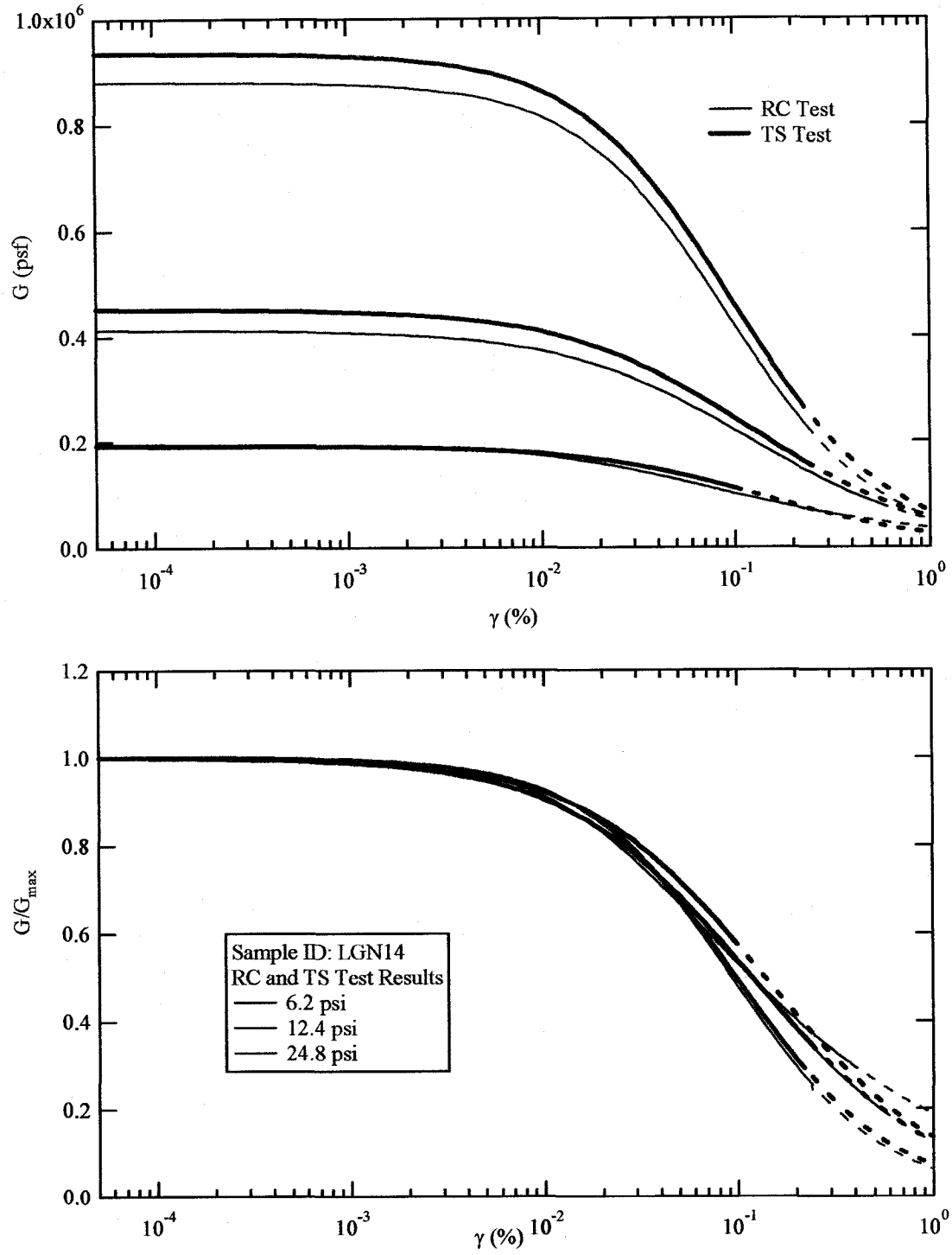

Figure 9.23 Modulus reduction curves and normalized modulus reduction curves measured at various confining pressures for soil specimen LGN14 at Logan at a depth of 14 ft

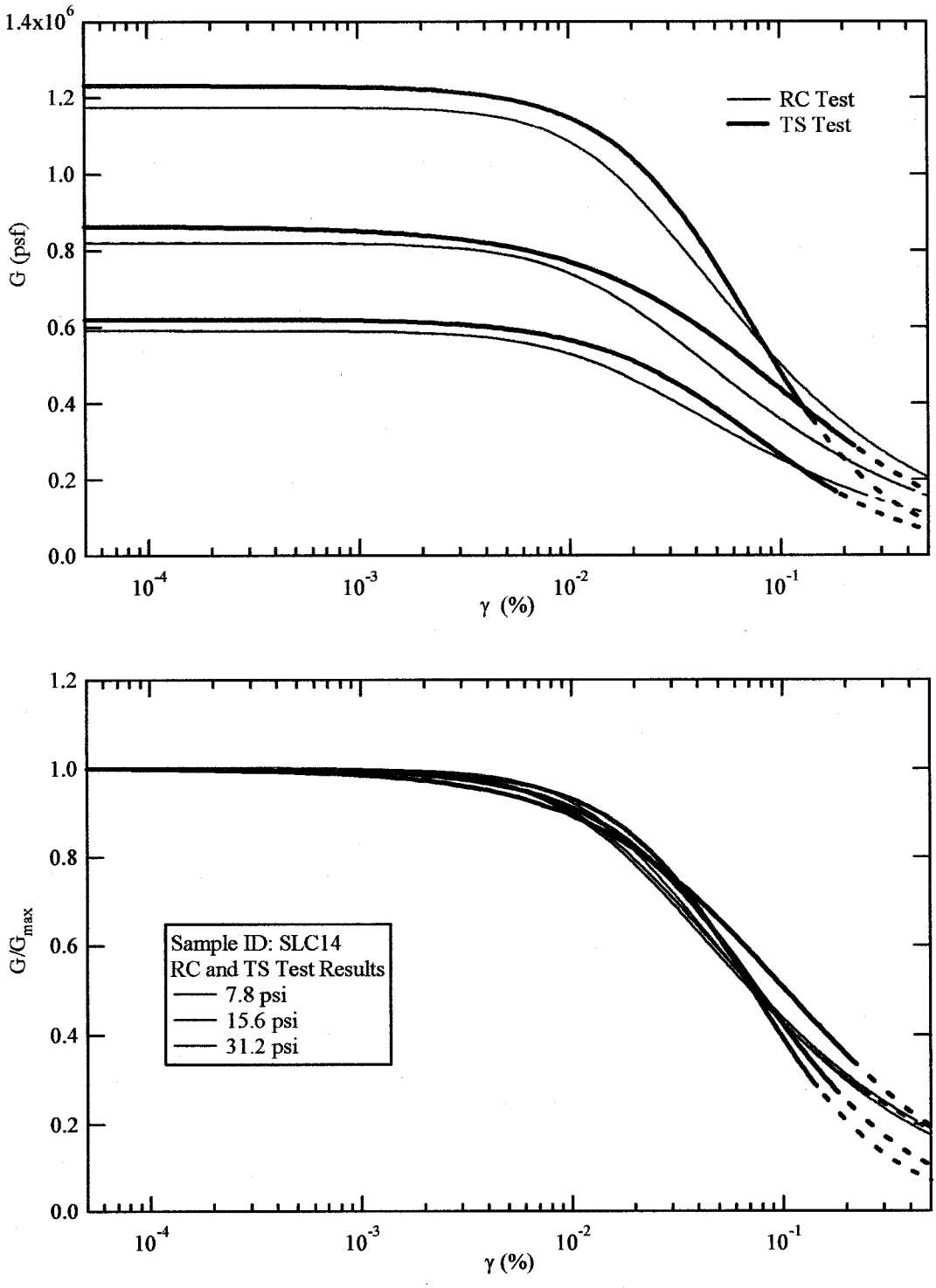

Figure 9.24 Modulus reduction curves and normalized modulus reduction curves measured at various confining pressures for soil specimen SLC14 near Salt Lake City Airport at a depth of 14 ft

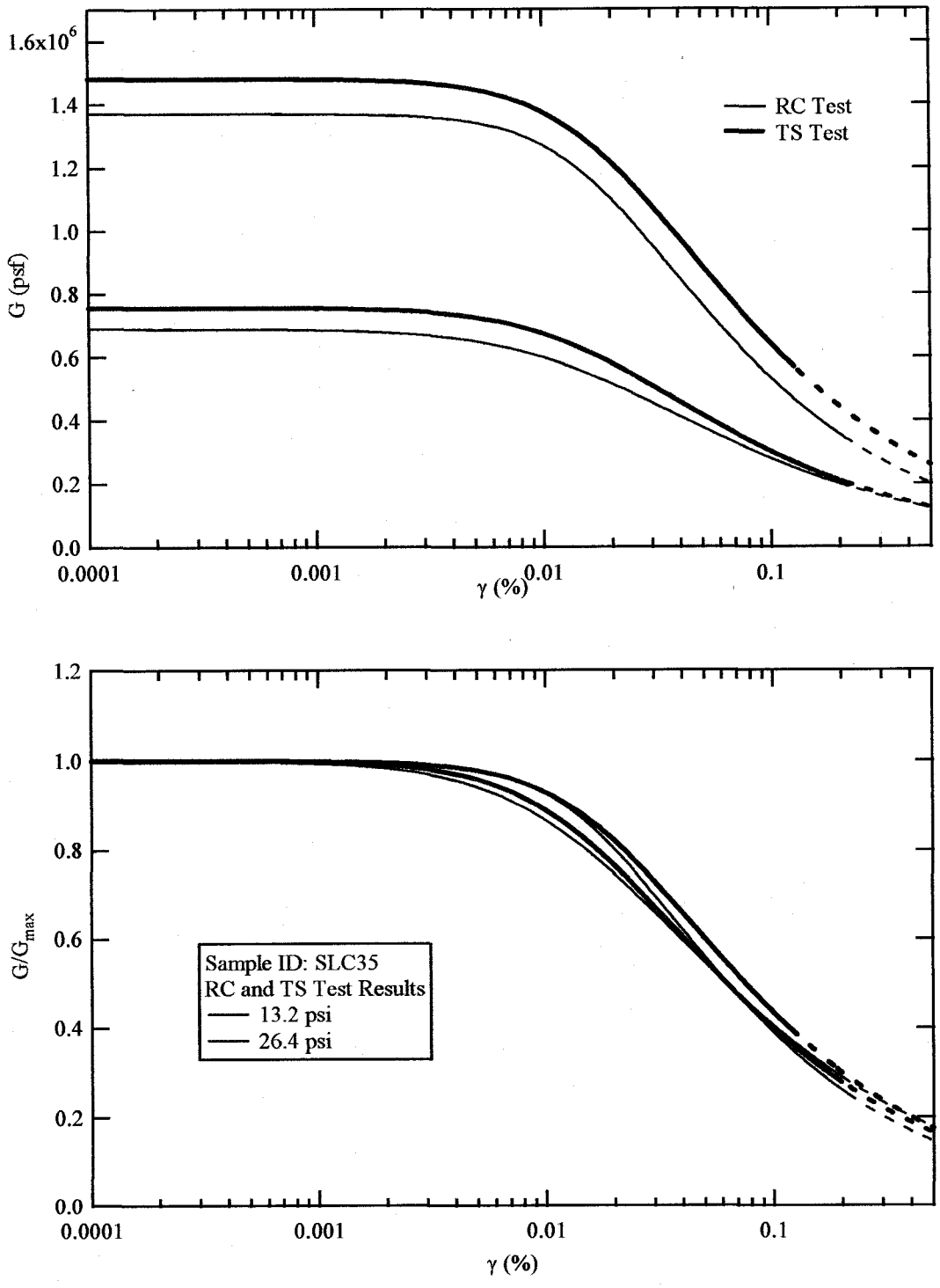

Figure 9.25 Modulus reduction curves and normalized modulus reduction curves measured at various confining pressures for soil specimen SLC35 near Salt Lake City Airport at a depth of 35 ft

The effect of confining pressure can be investigated using the normalized modulus reduction curves. In Figures 9.19-9.25, the normalized modulus reduction curves show small effects of confining pressure with the curves falling in a very narrow band especially below the threshold strain γ_c^t.

9.4.2.3 Development of Damping Curve. Material damping of the soil was determined using the half power bandwidth method and the free vibration decay method for the RC tests, and hysteretic damping for TS tests. The damping, D, was measured with an associated θ for each method. To develop damping curves, the modified R_{eq} approach presented in Chapter 8 was used. The R_{eq} for damping can be obtained for any given θ using the curve presented in Figure 8.13b, if the hyperbolic reference strain, γ_r is known.

Procedures for developing damping curves are as follows. (1) Determine the value of γ_r from hyperbolic model using the stress integration approach. (2) Calculate normalized quantity θ/θ_r where θ_r is calculated from Equation 8.26. (3) Determine the value of R_{eq} from Figure 8.13b. (4) Calculate γ for a given θ using the R_{eq} value. Figure 9.26 shows an example of the R_{eq} values used to develop the damping curve for the TS test on sample PRV93.

In this study, the half power bandwidth method was used in the RC test for determining damping of soil in its linear range (D_{min}). The free vibration decay method was used to determine the damping at high strains in the RC tests. Free vibration decay tests were only performed on soil specimens obtained from Logan and near Salt Lake City Airport. Figures 9.27-9.29 shows the material damping curves for specimens from

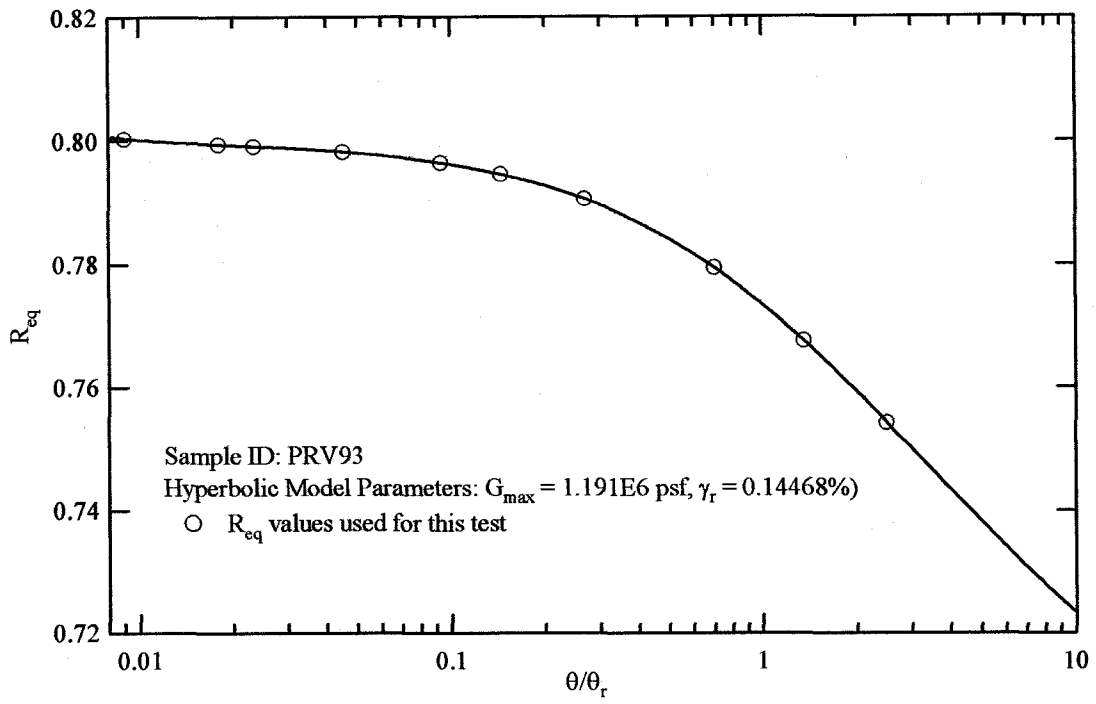

Figure 9.26 Example for the evaluation of R_{eq} values for generating material damping curves for specimen PRV93

Provo and Nibley. The high strain damping of specimens from Provo and Nibley were obtained only from the TS test. The damping for specimen PRV37 is not presented because the TS test was not performed on this specimen.

Figures 9.30-9.32 shows a comparison of material damping from RC and TS tests for specimens obtained from Logan and near the Salt Lake City Airport. The D_{min} obtained from RC and TS tests match well. However, the high strain damping measured in RC tests is higher than the damping measured in the TS tests. Typically, material damping for cohesive soil is independent of number of cycles but is significantly effect by the frequency (Kim, 1991). The RC and TS tests are performed at different

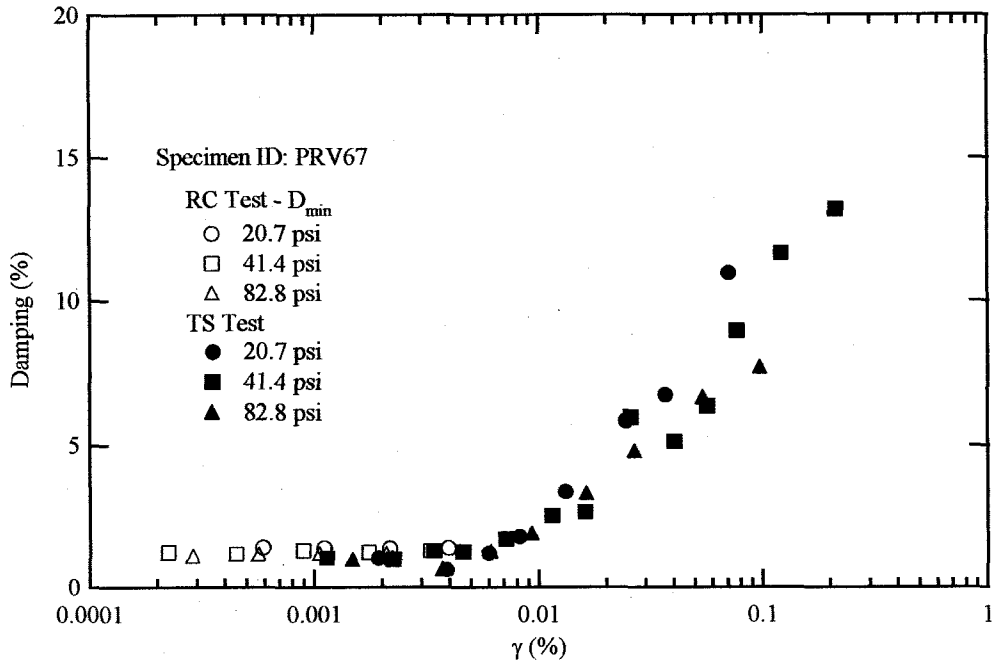

Figure 9.27 Damping curves measured on soil specimen PRV67 obtained near the Provo River at a depth of 67 ft

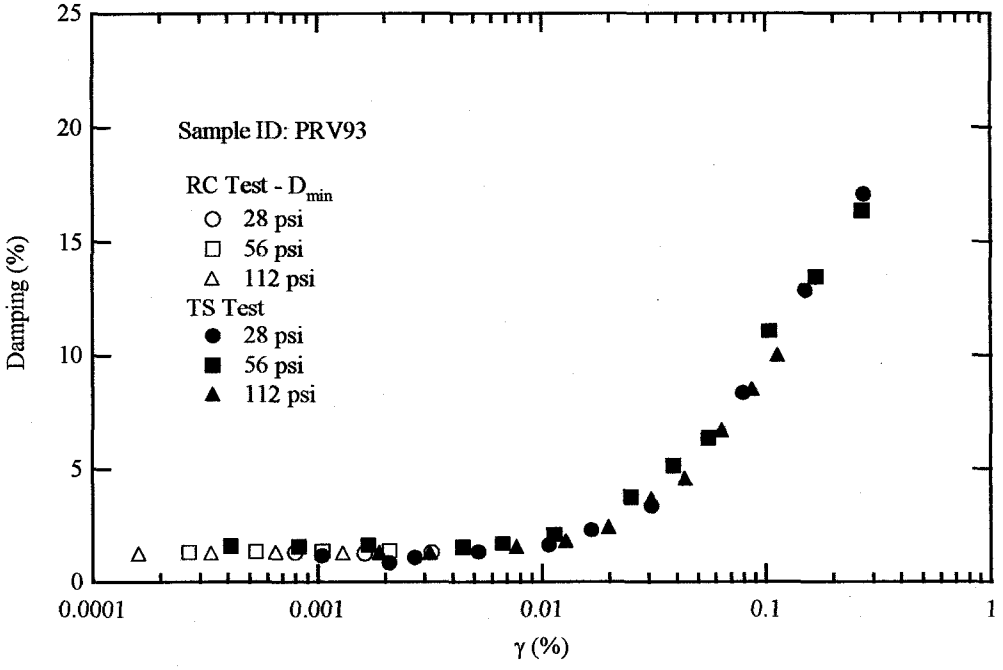

Figure 9.28 Damping curves measured on soil specimen PRV93 obtained near the Provo River at a depth of 93 ft

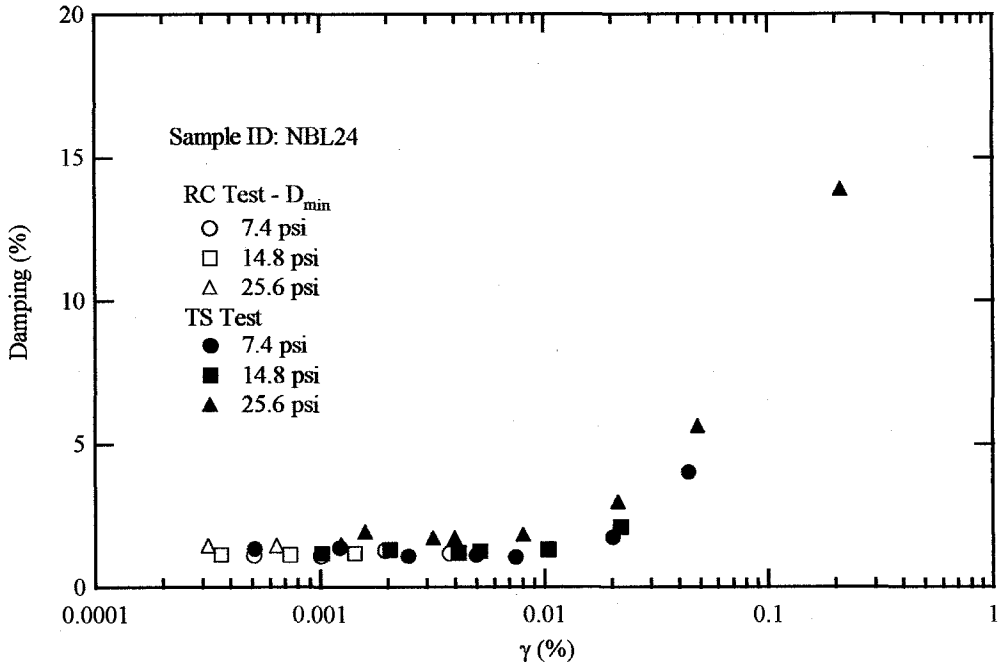

Figure 9.29 Damping curves measured on soil specimen NBL24 obtained from Nibley at a depth of 24 ft

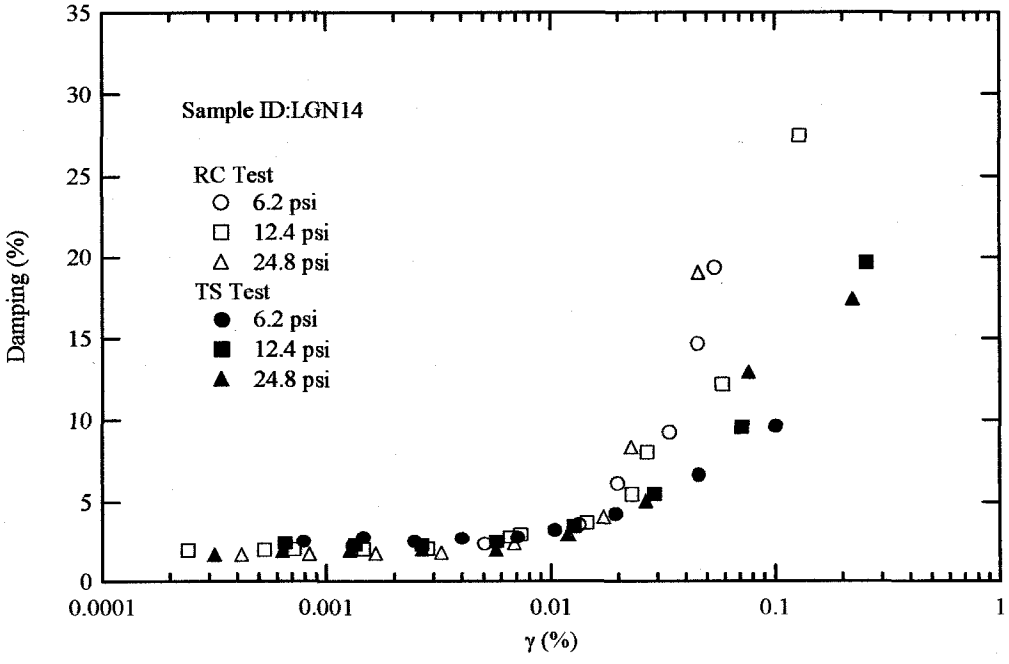

Figure 9.30 Damping curves measured on soil specimen LGN14 obtained from Logan at a depth of 14 ft

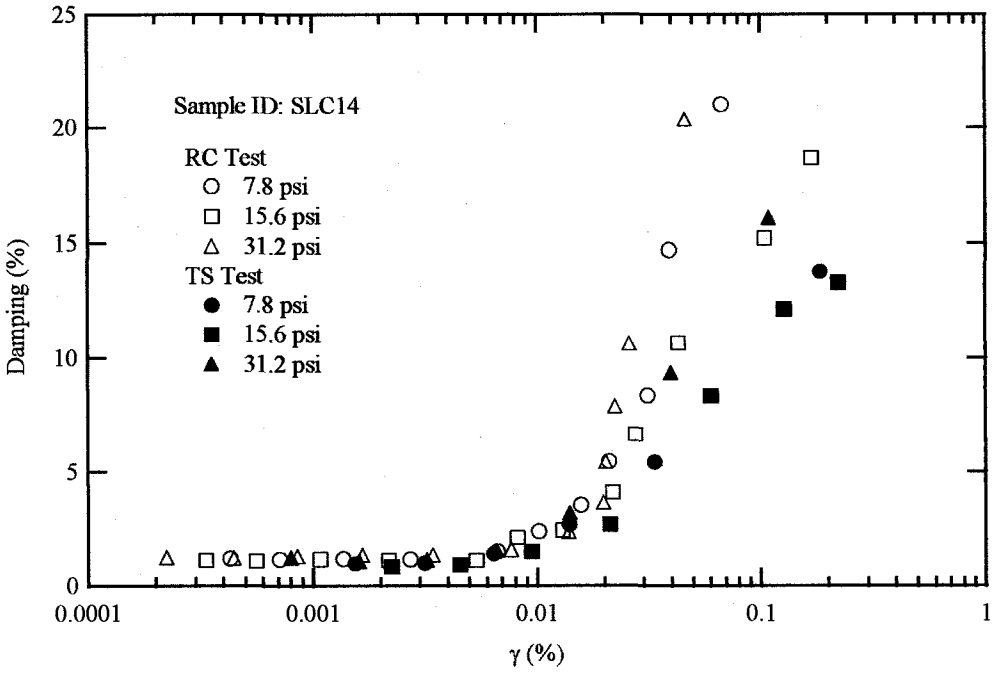

Figure 9.31 Damping curves measured on soil specimen SLC14 obtained near Salt Lake City Airport at a depth of 14 ft

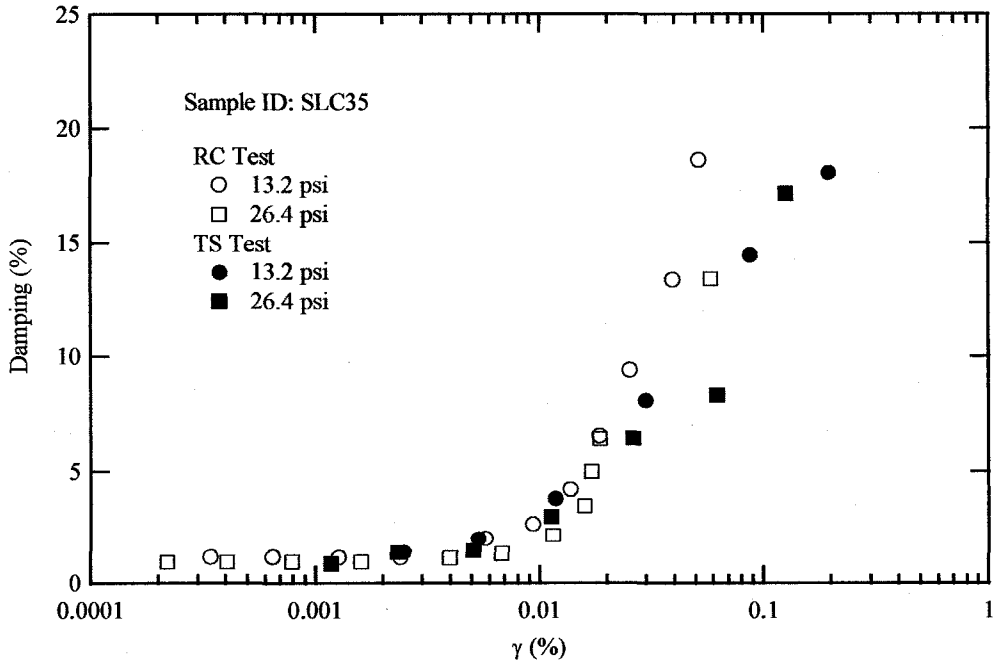

Figure 9.32 Damping curves measured on soil specimen SLC35 obtained near Salt Lake City Airport at a depth of 35 ft

frequencies. In the RC test, damping is measured at resonant frequency (above 10 Hz for this study) while the damping in the TS tests was measured at 0.333 Hz for this study.

Typically, the damping curve is not presented in terms of a normalized quantity. The effect of confining pressure can be observed from the typical damping curves as shown in Figures 9.27-9.32. In general, the damping value decreases as the confining pressure increases. In this study, the confining pressure has a very small effect on the damping of Bonneville clay. In most cases, the damping values measured at different confining pressures at the same strain level are similar. An example of this is specimen PRV93 presented in Figure 9.28.

9.4.3 Conclusions

An improvement was achieved in obtaining the accurate material damping of Bonneville clay using the electromagnetic model. The model was used to correct for equipment generated damping, D_{eq}, due to the back emf effect. The back emf effect is critical when performing low-strain RC test on low-resonant frequency material.

The stress integration approach performs effectively when there are small gaps between the data points of the measured T-θ relationship. The modified hyperbolic model was most commonly the best model used for developing stress-strain relationships of Bonneville clay. The Ramberg-Osgood model provided best fit of the T-θ relationship at high strains and poorly fit of the T-θ relationship at low strains. The hyperbolic model fit the T-θ relationship well at low to medium strains by typically fit the data poorly at high strains.

9.5 DISCUSSION ON FACTORS AFFECTING MODULUS REDUCTION AND DAMPING CURVES

This section contains a discussion of the effects of plasticity index and confining pressure on the normalized modulus reduction and damping curves. The normalized modulus reduction curves and damping curves are compared with generic curves used in practice for a given plasticity index and confining pressure. In addition, effect of cyclic degradation on Bonneville clay is also discussed.

9.5.1 Plasticity Index Effect

An important soil property affecting the nonlinear stress-strain behavior of clay is plasticity index (PI). The seven Bonnville clay specimens used in this study have PI's ranging from 2 to 34 as shown in Table 9.2. The effect of PI can be evaluated using normalized modulus reduction curves for all soil specimens at their in situ mean effective confining pressure presented in Figure 9.33.

The normalized modulus reduction curves presented in Figure 9.33 were determined from RC and TS tests. Soil specimens used in this study can be divided into four groups: samples with PI's of 34, samples with PI's of 17-20, samples with PI's of 10-11, and samples with PI's of 2. In general, soil behaves more linearly (the elastic threshold strain, γ_e^t, increases) as the PI increases. This general trend of PI with soil linearity is not clearly observed in the RC test results. For the TS test results, the samples with PI of 34 behave more linear than the samples with PI's of 10-17. An outlier was observed in sample with a PI of 11 that behaves as linearly as the samples with a PI of 34.

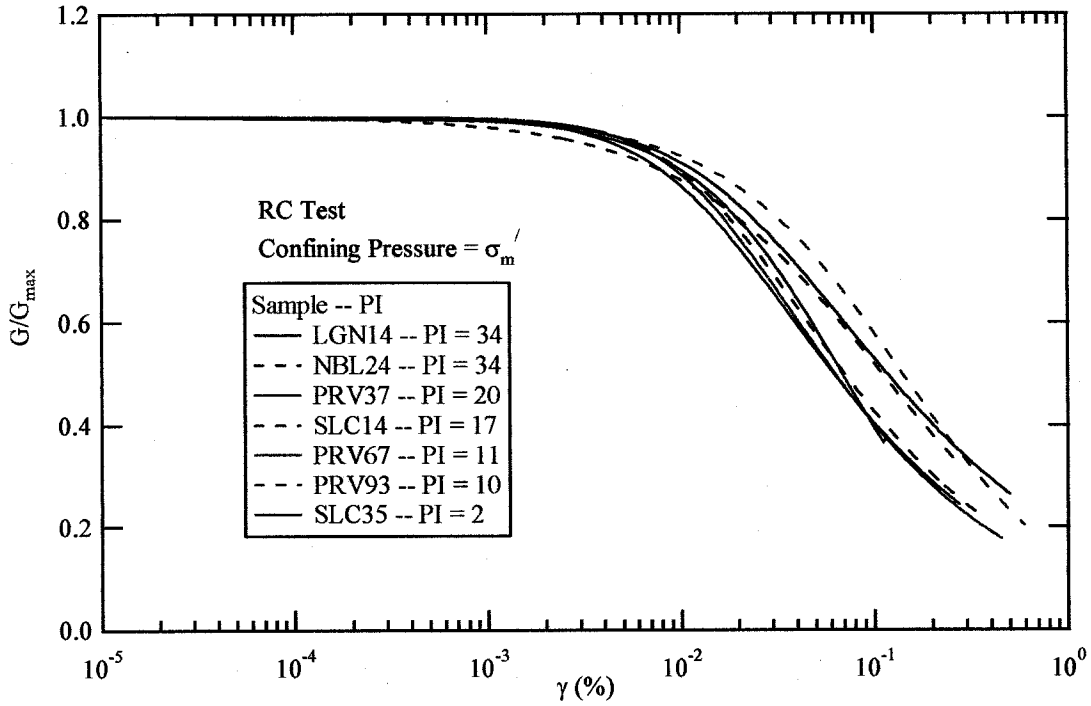

a) RC test results

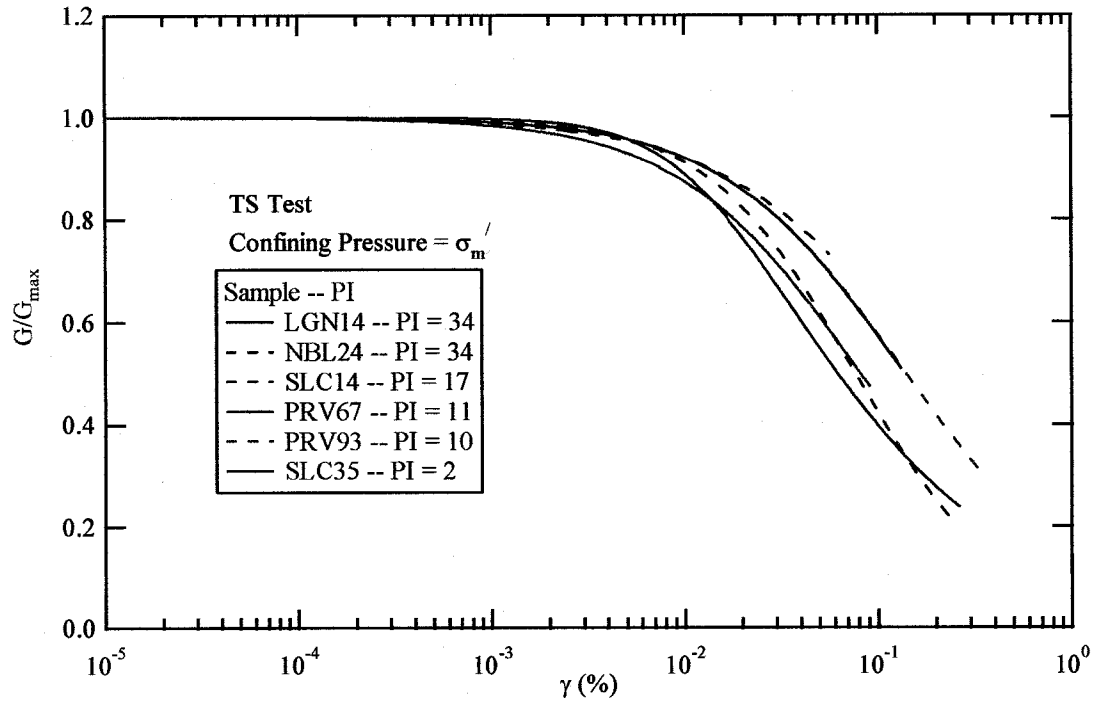

b) TS test results

Figure 9.33 Variation of normalized modulus reduction curves with PI for RC and TS tests on Bonneville clay

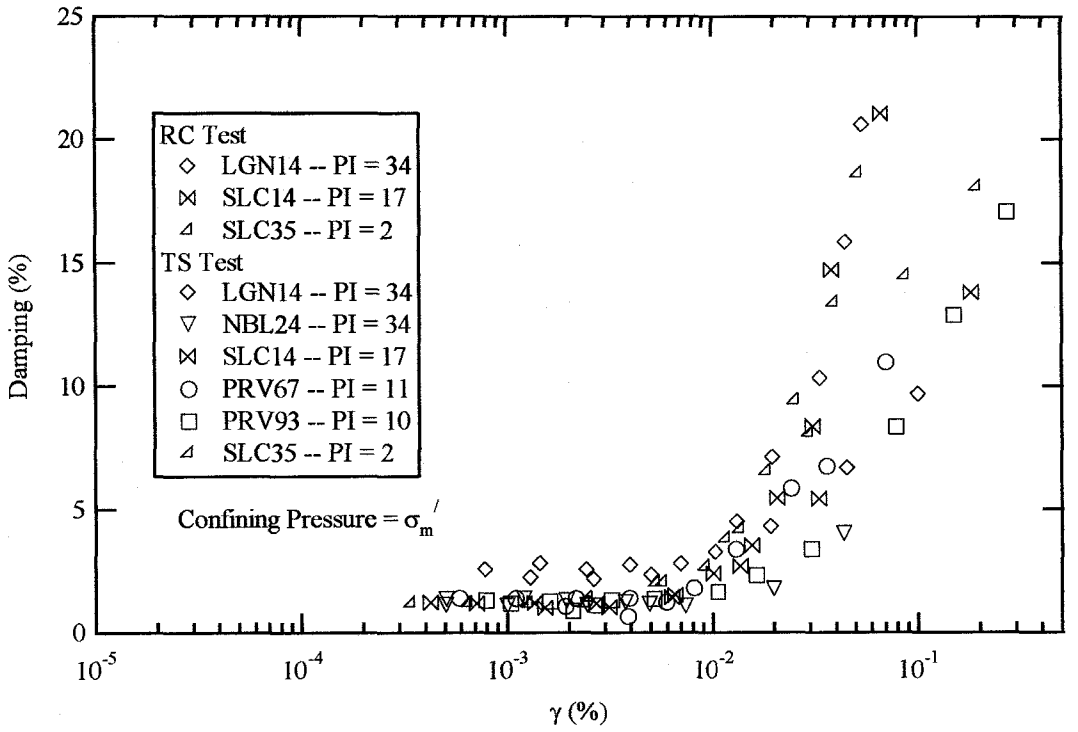

Figure 9.34 Variation of damping with PI for RC and TS tests on Bonneville clay

The sample with a PI of 2 was expected to behave the most nonlinearly but, the results show that this sample behaves similarly to the samples with PI's of 10-20. This might be because this sample has the interbeded layers of silt and clay. The clay layers may have more effect on damping than the silt layers.

The variation of damping with PI for the Bonneville clay tested in this study is presented in Figure 9.34. In general, the damping decreases as PI increases. The measured damping in TS test on specimen SLC35 with PI of 2 has the highest damping value. In the TS tests, the damping in specimens LGN14 and NBL24 with PI's of 34 show the lowest values of damping. Therefore, the damping behavior of Bonneville clay is typical of cohesive soils.

Empirical curves used to estimate modulus reduction and damping curves based upon PI where compared with the results from RC and TS tests on Bonneville clay. The empirical curves used are curves by Sun et al. (1988), Vucetic and Dobry (1991), and Darendeli (2001).

Sun et al. (1988) proposed empirical modulus reduction and damping curves for clays with different ranges of PI's. Figure 9.35 and 9.36 show the comparison for the curves measured in this study and the curves proposed by Sun et al. (1988). In Figure 9.35, three empirical curves are plotted for PI ranges of 5-10, 10-20, and 20-40. Bonneville clay specimens with PI's of 2-20 plot close to the Sun et al (1988) curve for a PI range of 10-20. The modulus reduction curves for samples with PI of 34 are in reasonably agreement with the Sun et al curve for a PI range of 20-40. The empirical curve for a PI range of 5-10 underestimates the measured modulus for the soil specimen with a PI of 2.

Sun et al. (1988) proposed the empirical damping curves with no correlation to PI as shown in Figure 9.36. The damping curve of Bonneville clay from TS tests plot close to the average curve at medium strains and close to the upper bound at high strains. While the small strain damping curve plots closer to the lower bound curve. However, these empirical damping curves span such a wide band that they are of little practical value.

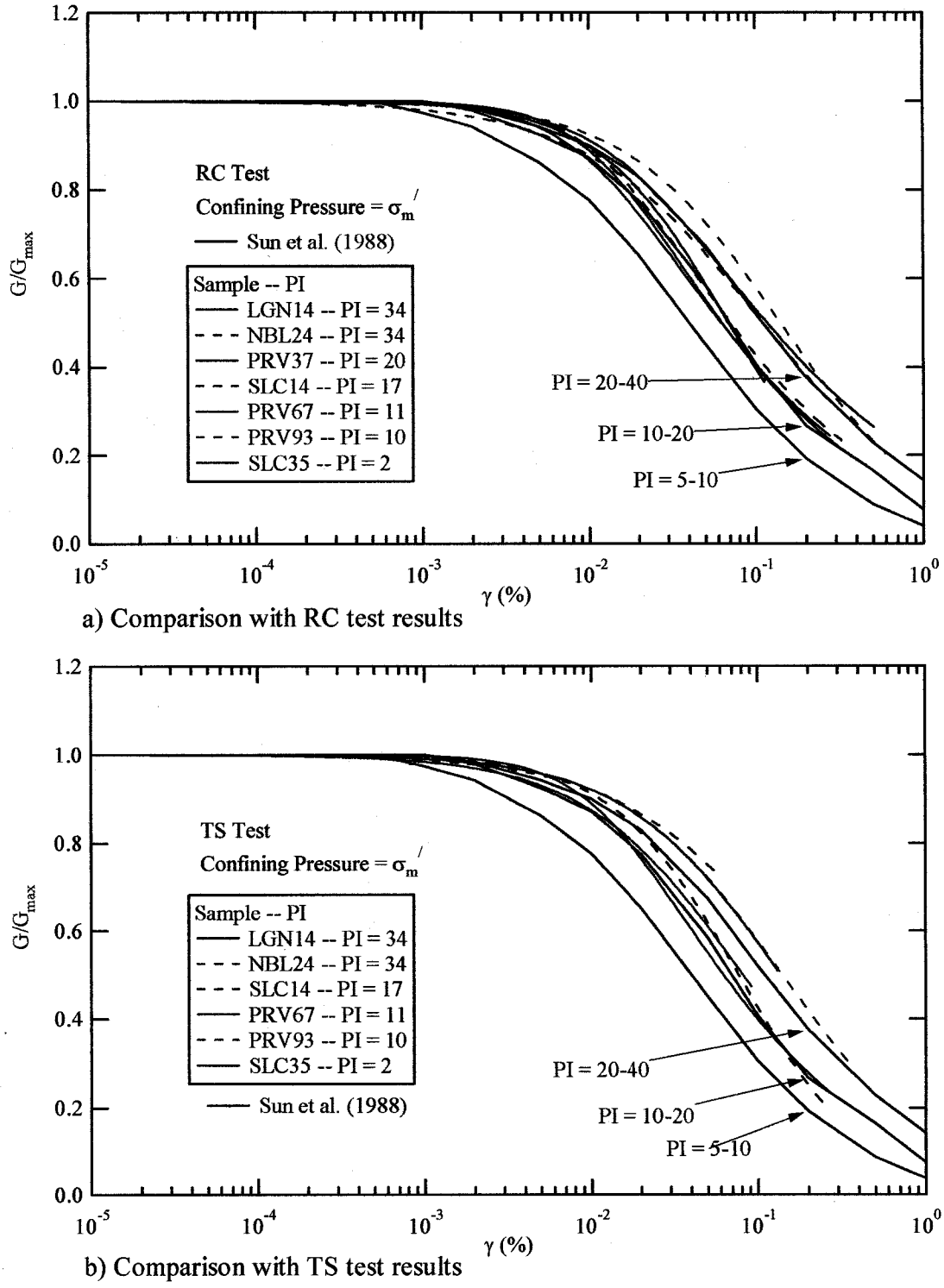

Figure 9.35 Comparison of normalized modulus reduction curves of Bonneville clay with empirical curves proposed by Sun et al. (1988)

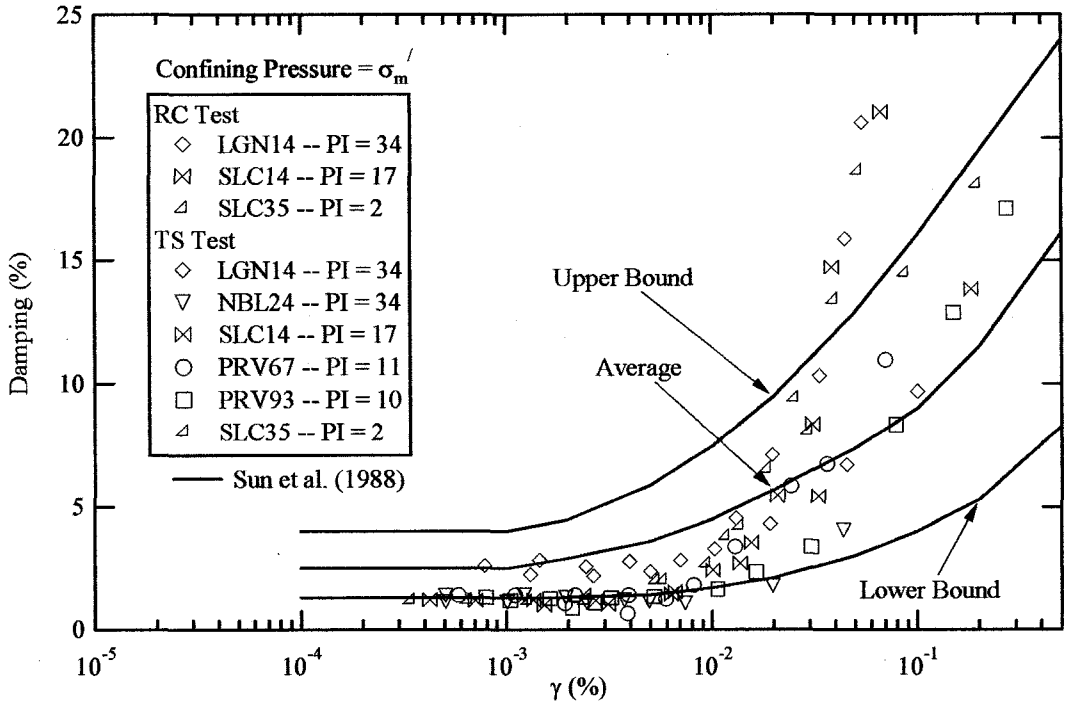

Figure 9.36 Comparison of damping curves of Bonneville clay with empirical curves proposed by Sun et al. (1988)

Comparisons of modulus reduction curves and damping curves to the empirical curves proposed by Vucetic and Dobry (1991) are presented in Figures 9.37-9.38. The Vucetic and Dobry (1991) curves for PI of 2, 10, 20, and 34 were generated by interpolation from their original proposed curves presented in Chapter 2. In Figure 9.37, the Vucetic and Dobry (1991) modulus reduction curve for PI of 34 shows good agreement with the curves of Bonneville clays with the same PI value. The Vucetic and Dobry (1991) curves for PI of 2 and 10 exhibit more nonlinearity than the actual behavior of Bonneville clay at the same values of PI.

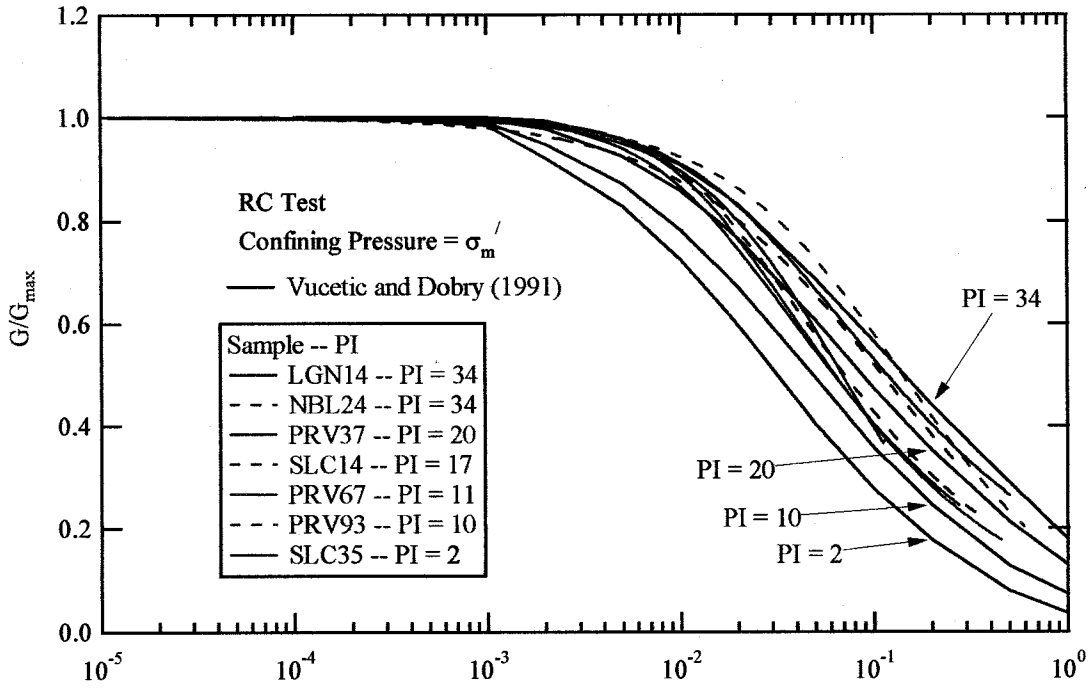

a) Comparison with RC test results

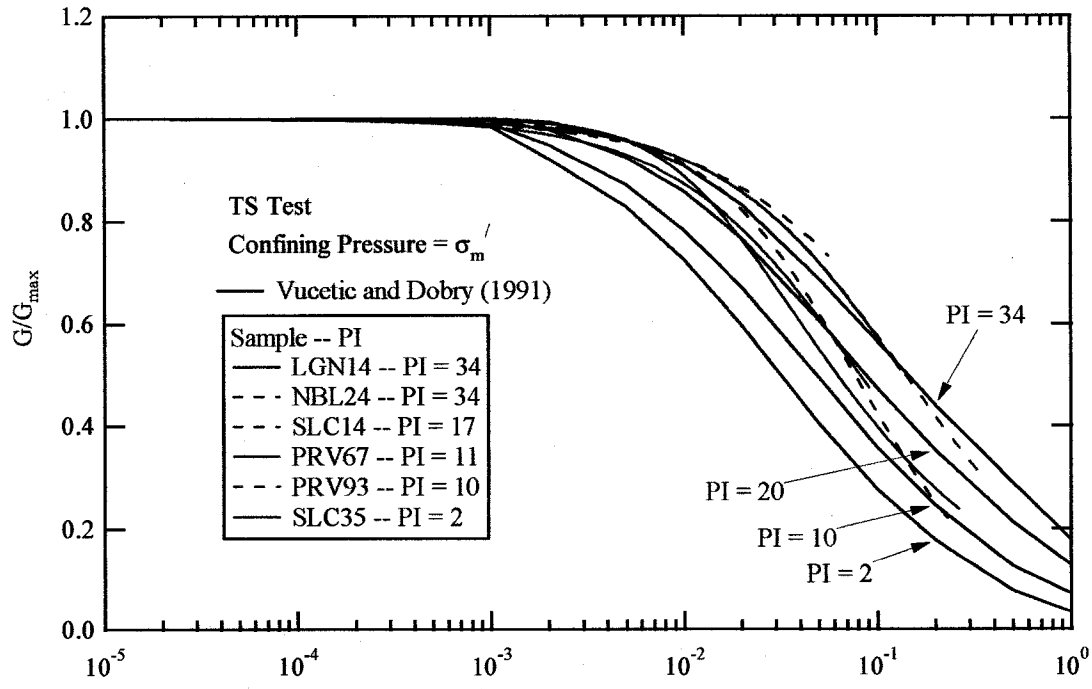

b) Comparison with TS test results

Figure 9.37 Comparison of normalized modulus reduction curves of Bonneville clay with empirical curves proposed by Vucetic and Dobry (1991)

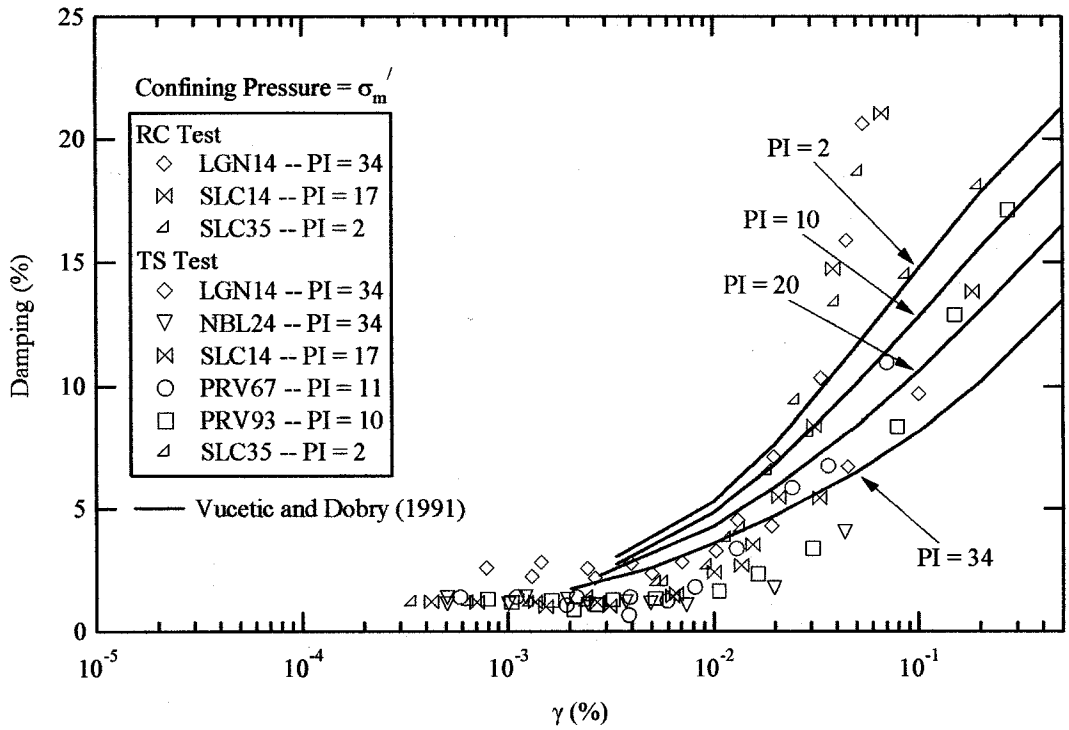

Figure 9.38 Comparison of damping curves for Bonneville clay with empirical curves proposed by Vucetic and Dobry (1991)

Damping curves proposed by Vucetic and Dobry (1991) show higher values of damping at medium strain levels (10^{-3}-10^{-2}%) than the damping curves for Bonneville clay presented in Figure 9.38. The Vucetic and Dobry (1991) damping curves also show a more pronounced effect of PI than was measured on the Bonneville clay. The Vucetic and Dobry (1991) damping curves have been left undefined at low strains. At high strains, the Vucetic and Dobry (1991) damping curves underestimates the Bonneville clay damping curves. The measured damping for the soil sample with a PI of 2 matches well with the Vucetic and Dobry (1991) curve for a PI of 2 at strains above 0.1%.

Darendeli (2001) proposed a model to predict the modulus reduction curves and damping curves accounting for the effect of PI, confining pressure, OCR, frequency (freq), and number of cycles (N). The modulus reduction curves and damping curves were generated using the proposed model by Darendeli (2001) for PI values of 2, 10, 20, and 34 with an OCR = 1, σ_m' = 1 atm, freq = 0.333 Hz, and N = 5 cycles. The Darendeli (2001) curves were compared with Bonneville clay curves in Figures 9.39-9.40. The Darendeli (2001) modulus reduction curves show a smaller PI effect than the other empirical curves. In Figure 9.39, all of the Darendeli (2001) curves for different PI plot below the curve for Bonneville clay. This indicates that Bonneville clay behaves more linearly than predicted by the Darendeli (2001). It is interesting to note that the width of the band for effect of PI value of of 2 up to 34 predicted by Darendeli (2001) is close to the bandwidth of the measured curves.

Damping curves proposed by Darendeli (2001) are compared to the measured damping in Figure 9.40. Again, the damping curves proposed by Darendeli (2001) shows narrow band of PI effect. Damping from RC test was higher than that predicted damping by Darendeli (2001). However, the damping from TS tests matches the Darendel (2001) damping curve at high strains. The Darendeli (2001) damping curve slightly overestimates the damping at medium strains. This is consistent with the more linear behavior of Bonneville clay. The Darrendeli (2001) damping curve for a PI of 2 underpredicts the damping of the Bonneville clay at high strains.

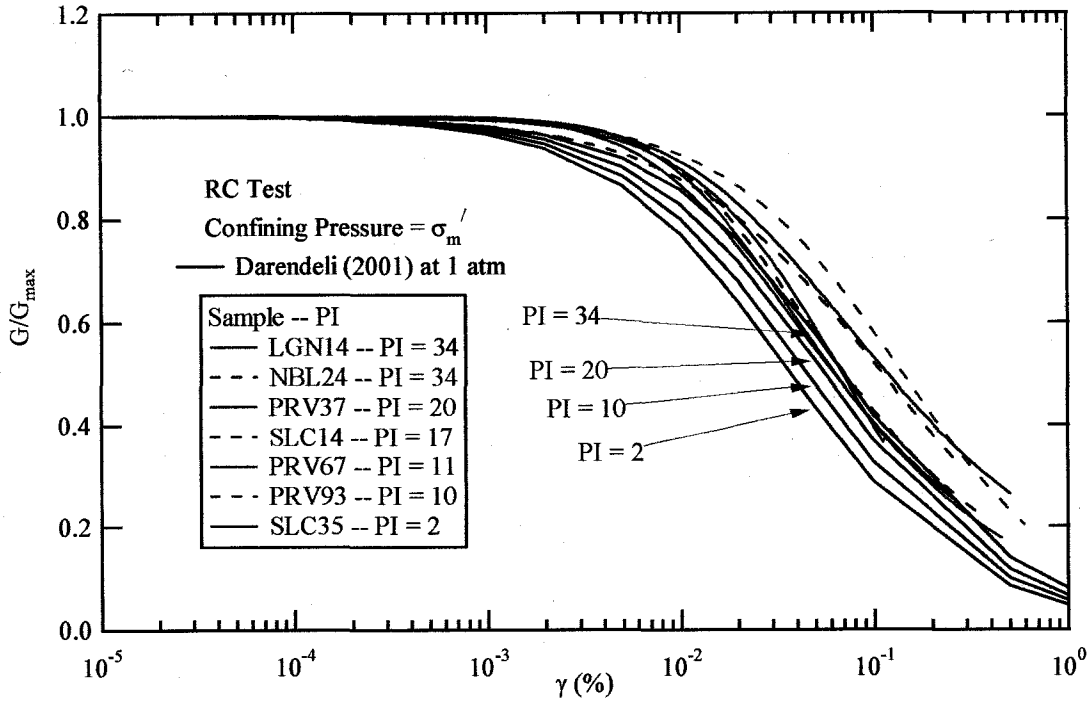

a) Comparison with RC test results

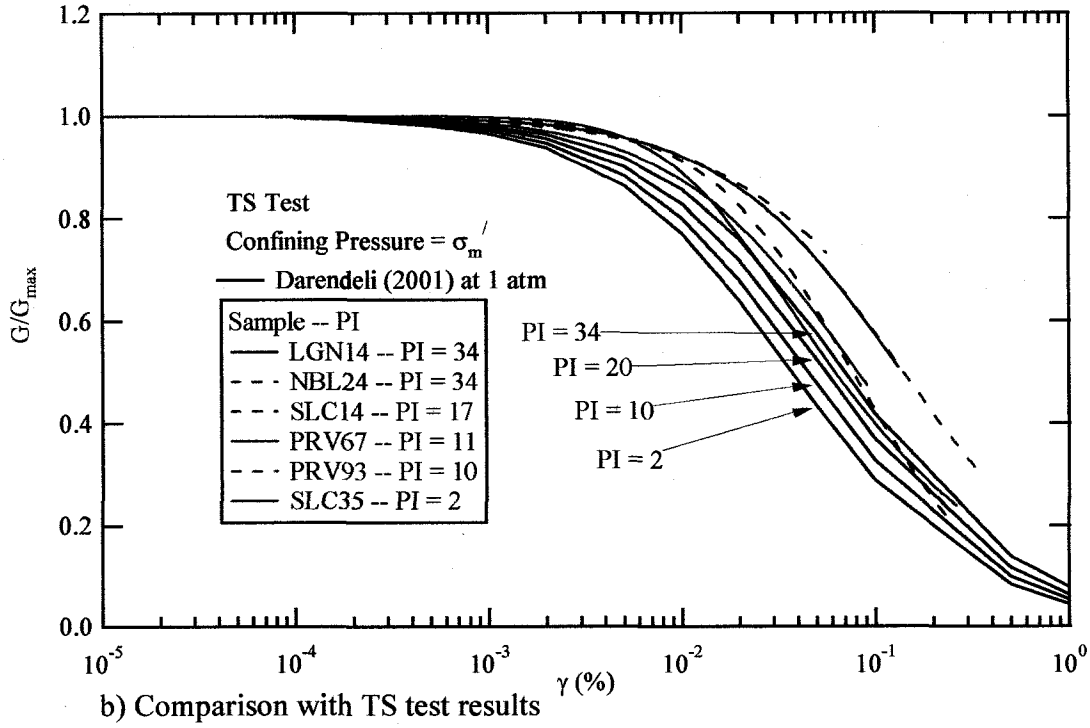

b) Comparison with TS test results

Figure 9.39 Comparison of normalized modulus reduction curves of Bonneville clay with empirical curves proposed by Darendeli (2001)

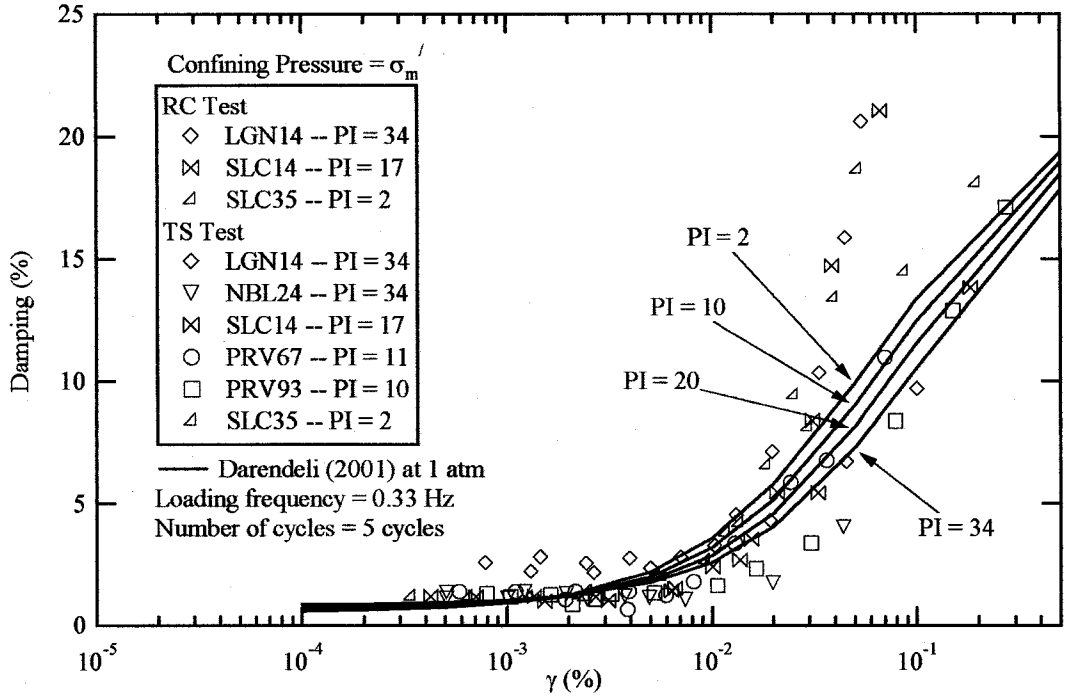

Figure 9.40 Comparison of damping curves for Bonneville clay with empirical curves proposed by Darendeli (2001)

Another model to predict the modulus reduction curves and damping proposed by Ishibashi and Zhang (1993). Ishibashi and Zhang (1993) developed a set of equations to generate the modulus reduction and damping curves for a given values of PI and σ_m'. However, the equations proposed by Ishibashi and Zhang (1993) shows unrealistic modulus reduction and damping curves at high strain levels for the range of PI between 10-40. A discussion about Ishibashi and Zhang (1993) curves is presented in Chapter 2. In this study, comparisons are not made between Bonneville clay Ishibashi and Zhang (1993).

9.5.2 Confining Pressure Effect

In this section, the effects of confining pressure on the modulus reduction curves and damping curves for Bonneville clay is compared with the empirical curves developed by Darendeli (2001). The empirical curves are compared with the results from TS tests on soil specimen PRV93. Three different confining pressures were applied to this specimens during testing. The sample PRV93 was confined at mean effective stresses of 28, 56, and 112 psi. The modulus reduction and damping curves of the specimen PRV93 are presented in Figures 9.21 and 9.28, respectively.

The normalized reduction and damping curves for sample PRV93 are compared with the Darendeli (2001) empirical curves presented in Figure 9.41. The normalized reduction curve becomes more linear as the confining pressure increases. Damping curves of specimen PRV93 shows a very small effect of the confining pressure.

The Darendeli (2001) curves in Figure 9.41 were regenerated for the same confining pressure at which each specimen was subjected to in the RC and TS tests. In Figure 9.41, the measured normalized modulus reduction curve for sample PRV93 plots above the predicted curves. Less effect of confining pressure is seen in the normalized reduction curves of PRV93 than that predicted by the Darendeli (2001). For damping, the Darendeli (2001) curve plots above the measured curve at medium strains. With the normalized modulus reduction curve, the effect of confining pressure in damping for PRV93 is less than that predicted by Darendeli (2001).

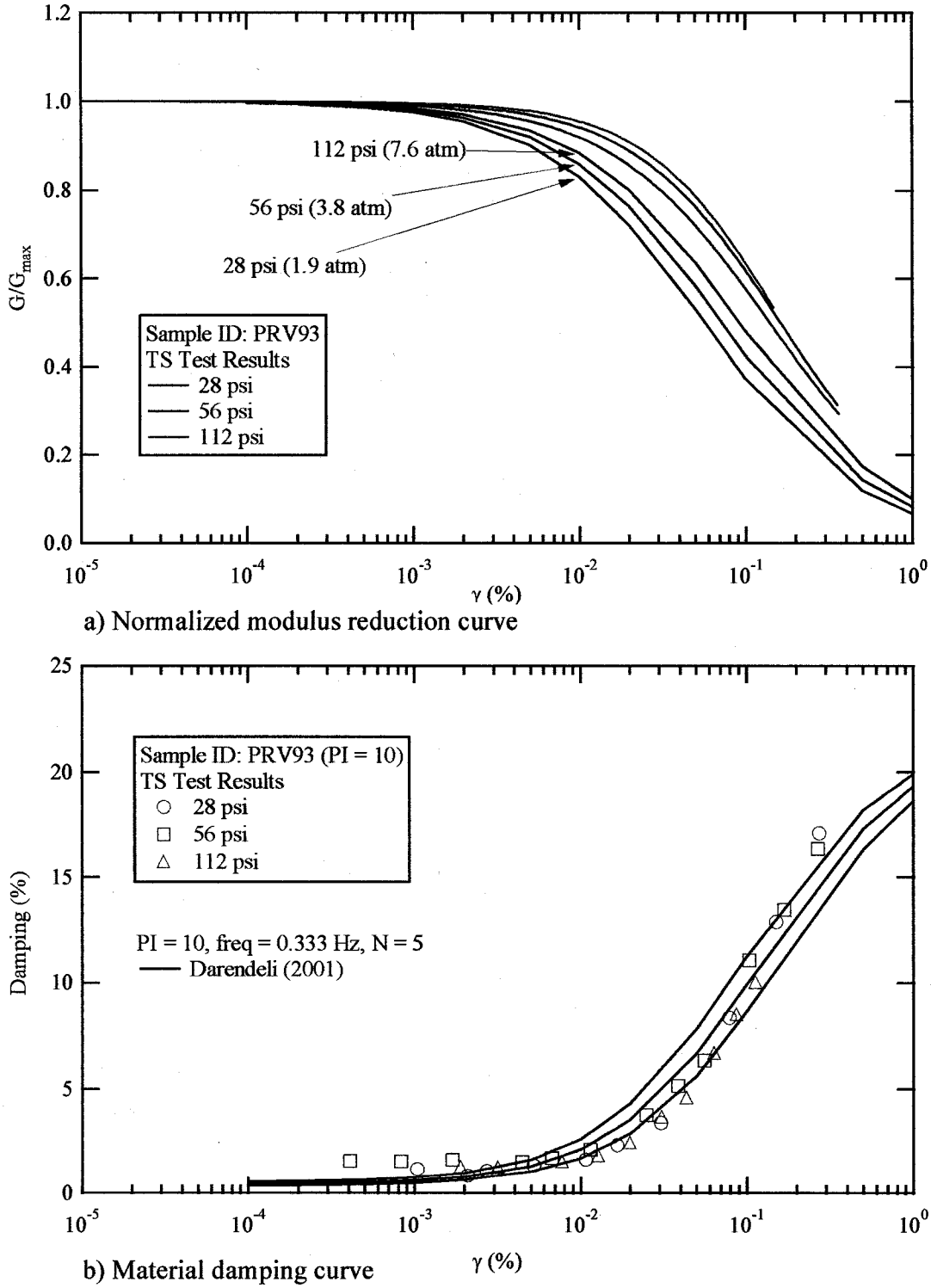

Figure 9.41 Comparison of confining pressure effects from TS tests on specimen PRV93 and curves proposed by Darendeli (2001)

9.5.3 Cyclic Degradation

At high strain levels, the stiffness of soil is reduced due to cyclic degradation. This is observed as the slope of hysteresis loop begins to flatter with increasing number of cycles. This means that the secant shear modulus decreases as the numbers of cycle increases.

The shear modulus and damping in this study was determined using the first loading cycle. However, the cyclic degradation of Bonneville clay was observed for most of the soil specimens at high strain levels. Figure 9.42 shows an example of cyclic degradation for sample PRV67 test at a confining pressure of 42 psi for strain level of 0.06-0.22%. These hysteresis loops are plotted relative to T-θ measured directly from TS tests. These was little cyclic degradation in tests performed at strains of 0.06% and 0.08% as shown in Figures 9.42a and 9.42b. However, increasing degradation occurred at strains of 0.12% and 0.22% as shown in Figures 9.42c and 9.42d.

To quantify the effect of cyclic degradation, the slope of the T-θ relation for each cycle was determined. The stress integration approach was then applied to determine the modulus for each cycle. For this specimen PRV67, the modified hyperbolic model was used to describe the τ–γ relationship. The normalized reduction curves for specimen PRV67 for each cycle are presented in Figure 9.43. Model parameters for the modified hyperbolic model for each cycle are in Figure 9.43. The value of γ_r decreases as the number of cycle increases which is expected because of the decreasing shear modulus. The change of parameter, a, does not show a consistent trend in this case however, the value of the first cycle was observed to be the lowest.

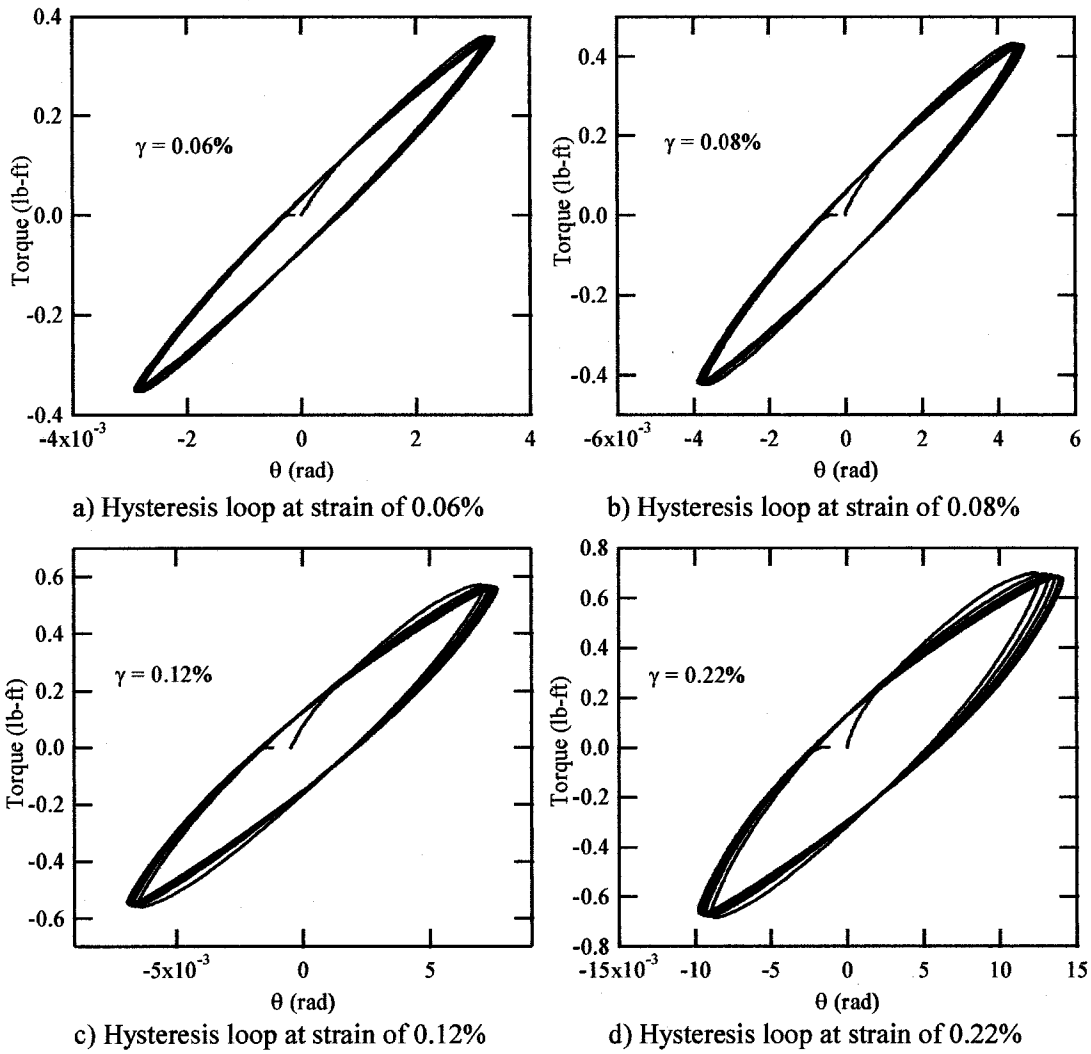

Figure 9.42 Hysteresis loops of five cycles of loading on soil specimen PRV67 obtained near the Provo River at a depth of 67 ft tested at a confining pressure of 42 psi

From Figure 9.43, two threshold strains were determined. These are the elastic threshold strain, γ_t^e and the cyclic threshold strain, γ_t^c. The γ_t^e is defined earlier as the strain level where shear modulus begins to be affected by strain amplitude. The γ_t^c is

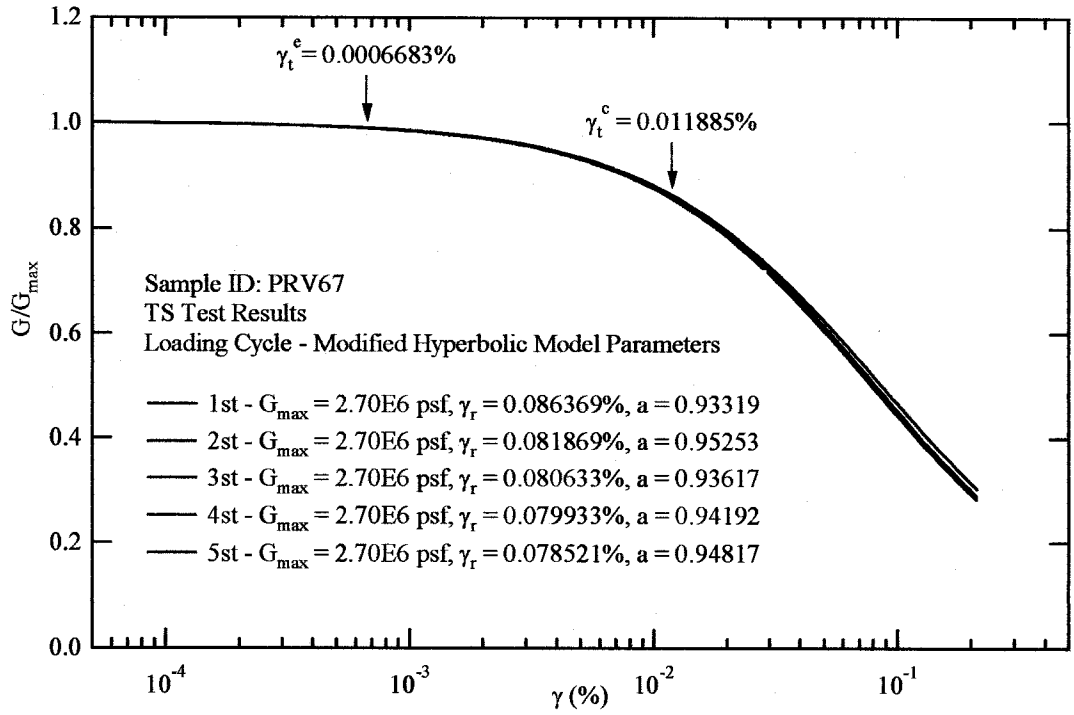

Figure 9.43 Variation of normalized modulus reduction curves with number of cycles for specimen PRV67

defined as the strain level at which the shear modulus begins to be affected by the number of loading cycles. As shown in Figure 9.43, the γ_t^e was selected at strains where the shear modulus was equal to 0.98 of G_{max} and the γ_t^c was defined at strain levels at which the difference between the shear modulus of first and fifth cycle is equal to 2% (Kim 1991). For this sample, the γ_t^e and γ_t^c were equal to 0.0006683% and 0.029853%. The different in shear modulus at first and fifth cycles was up to 8% at a strain of 0.22%.

The effect of cyclic degradation on damping was also investigated. The damping was determined from hysteresis loops presented in Figure 9.42 for each cycle of TS loading. The variation in damping with strain level for each cycles is presented in Figure

9.44. The damping for each cycle is identical for all loading cycle at strains below the cyclic threshold, γ_t^c. At strain above γ_t^c, the first cycle of loadings exhibited lower damping than subsequent cycles. These are consistent with typical cohesive soils reported by Kim (1991).

Because the number of cycles in this study was limited to five cycles, more study would be required to further investigate the effect of cyclic degradation. Kim (1991) investigated cyclic degradation using up to one hundred cycles and his results show a more pronounced reduction of shear modulus with large number of cycles.

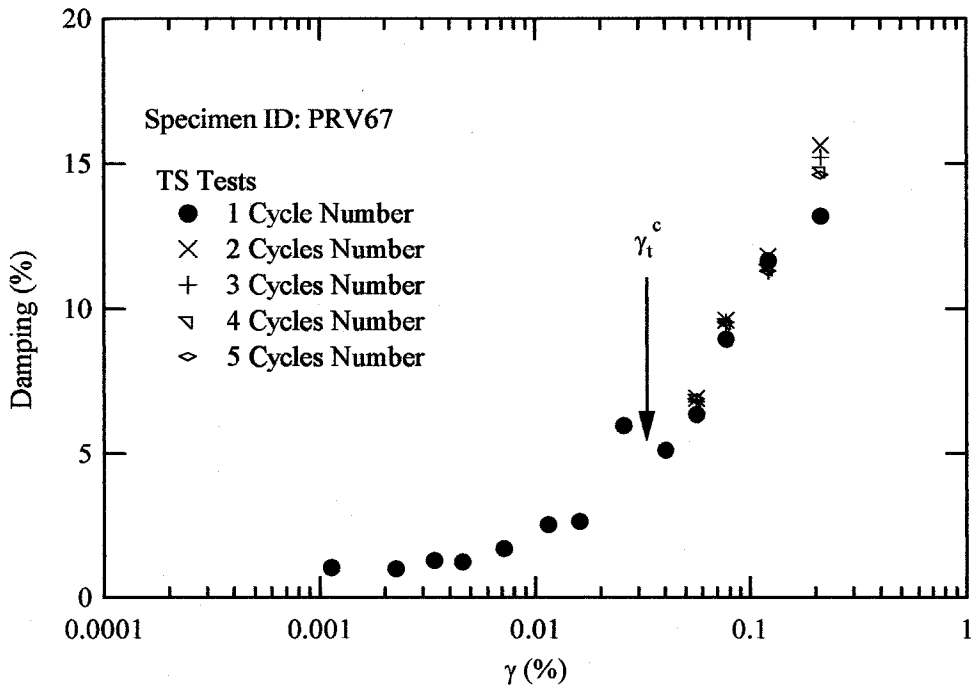

Figure 9.44 Variation of damping for different numbers of loading cycle

9.5.4 Conclusions

The overall behavior of Bonneville clay was found to behave more linearly than was predicted by the empirical curves for behavior of typical clay at the same values of PI. Less confining pressure effect was also observed for Bonneville clay. The empirical curves proposed by Darendeli (2001) provide the best match with the behavior of Bonneville clay. Cyclic degradation of Bonneville clay requires more study.

The more linear behavior of the Bonneville clay may be explained by geologic age effect. Bonneville clay is a relatively young soil, deposited 12,000-20,000 years ago during the Quaternary period. Zhang et al. (2004) compared modulus reduction curves from three groups of soils: Quaternary, Tertiary and older, and residua/saprolite. They found that Quaternary soils exhibit more linearity than soils of the other two groups. They also observed that most of the soils used to develop the Darendeli (2001) model are Tertiary soils. Accordingly, Zhang et al. (2004) showed a better agreement between the Darendeli (2001) model and Tertiary age soils than the Darendeli (2001) model and Quaternary soils.

CHAPTER 10

SUMMARY, CONCLUSIONS AND RECOMMENDATIONS

10.1 BACKGROUND

A goal of this study was to achieve the accurate measurement of nonlinear stress-strain behavior for soil using the combined resonant column and torsional shear (RC/TS) testing device. Two weaknesses of the RC/TS tests are the back electromotive force (back emf) created in the coil and magnet drive system of the RC/TS apparatus and nonuniform stress-strain occurring over the radius of the soil specimen in the RC/TS test. This study focused on developing methods to deal with these problems more precisely. The methods developed in this study are the use of electromagnetic model to describe and predict the back emf effect, and the stress integration approach to account for the nonuniform stress-strain in the soil specimen.

The electromagnetic model was developed by combining the electrical, magnetic, and mechanical properties of the RC/TS apparatus. The electrical part of model describes the current flowing in the drive coil circuit. The magnetic part of the model describes the development of torque and back emf in the coil-magnet system. The mechanical part of the model describes the RC/TS drive system and soil specimen as a single-degree-of-freedom oscillater. All independent measurement was made of each model parameters. Each model parameter was measured as a function of frequency, when possible, to identify and account for the frequency dependent parameters. The model was verified by comparing open and closed circuit measurements. And procedures were developed to apply the electromagnetic model to both the RC and TS tests.

Previous studies have developed an suggested the use of equivalent radius approach to account for the nonuniform stress-strain in soil in the RC/TS tests (Chen and Stokoe 1979). The equivalent radius approach proposed utilizes an equivalent radius ratio to calculate the stress and strain from the torque and rotation measured in RC/TS testing. This approach is adequate for the tests at low to medium strains however, it becomes less accurate for the tests at high strains. The stress integration approach was developed in this study to more precisely account for nonuniform stress-strain at any strain level. The stress integration approach is applied by integration using three different soil stress-strain models and to calculate a theoretical torque and rotation relationship. Curve fitting techniques are then applied to match the measured torque and rotation relationship with the theoretical torque and rotation relationship. The stress-strain model providing the best fit to the measured data is used to characterize the soil specimens. The stress integration approach was also used to account for nonuinform stress-strain in damping.

10.2 SUMMARY AND CONCLUSIONS

10.2.1 Polar Moment of Inertia of RC/TS Drive Plate

The polar moment of inertia of the drive plate was calibrated in this study. Calibration specimens with different resonant frequency were used to investigate the moment of inertia of the drive plate at frequencies up to 200 Hz. An open circuit test was used to eliminate the back emf effect in the drive plate calibraiton. The drive plate calibration was performed on the USU drive plate and the UT drive plate No. 9 and results were compared.

A frequency effect on the polar moment of inertia of the drive plate was observed. Results showed that the polar moment of inertia of the USU drive plate increases 28% as the frequency increases from 14 to 188 Hz. This frequency effect in polar moment of inertia causes an error in shear wave velocity for up to 12% if not account for. The frequency effect on the polar moment of inertia of the UT drive plate was much smaller. The increasing polar moment of inertia of the drive plate with frequency is explained by non-rigid body motion of the drive plate. The non-rigid body motion of the drive plate was verified using a finite element model of the drive plate.

The finite element analysis showed that stiffness of the connection of the drive plate and magnet plays an important role in frequency effect on polar moment of inertia. Different drive plates behave differently if they utilize different types of connections. Investigation of the polar moment of inertia of the drive plate with frequency should be performed to characterize any effect. To obtain high accuracy RC measurements, the shear wave velocity, the frequency effect on the polar moment of inertia of the drive plate must be taken into account.

10.2.2 Electromagnetic Model

10.2.2.1 Torque and Back Emf in the Drive System. The application of the principles of electromagnetism was used to describe the torque generated in RC/TS drive system and the back emf effect created due to the motion of magnets through the coils. In this study, the theoretical equations were developed to predict the electromagnetic properties of an ideal coil and magnet system. These are:

$$k_i = Nl_c Bd, \tag{10.1}$$

$$k_B = \frac{2}{d}\frac{BA_cN}{y}. \tag{10.2}$$

where B = strength of magnetic field of the permanent magnet,

N = total number of loops in the coil

l_c = circumference length of coil loop,

A_c = cross section area of coil loop,

y = width of coil loop in longitudinal section, and

d = moment arm of the drive plate.

10.2.2.2 Tranfer Function. The electromagnetic model was developed by combining the electrical, magnetic, and mechanical properties of to the RC/TS apparatus. The transfer function for voltage to rotation in the RC/TS tests is:

$$H_v = \frac{\theta}{V_a} = \frac{\frac{k_i}{R_c + j\omega L_c}}{\left[(k_\theta + k_{eq}) + j\omega(c_\theta + c_{eq}) - \omega^2 J\right]}, \tag{10.3}$$

$$k_{eq} = \frac{\omega^2 k_i k_B L_c}{R_c^2 + \omega^2 L_c^2}, \text{ and} \tag{10.4}$$

$$c_{eq} = \frac{k_i k_B R_c}{R_c^2 + \omega^2 L_c^2}. \tag{10.5}$$

where H_v = transfer function for voltage to rotation,

θ = rotation,

V_a = measured voltage output from voltage source,

k_θ = torsional spring stiffness,

c_θ = torisonal viscous damping coefficient,

J = polar moment of inertia of the system,

k_{eq} = equipment spring stiffness,

c_{eq} = equipment viscous damping coefficient,

R_c = coil resistance,

L_c = coil inductance,

k_i = torque-current factor,

k_B = back emf-rotational velocity factor, and

ω = angular velocity ($\omega = 2\pi f$).

This model describes where the back emf effect in terms of an equipment spring stiffness, k_{eq}, and an equipment viscous damping coefficient, c_{eq}.

10.2.2.3 Model Parameters. There are four model parameters in the model presented in Equations 10.3-10.4. These are the coil resistance, R_c, the coil inductance, L_c, the torque-current factor, k_i, and the back emf-rotational velocity, k_B. Independent measurements were made of the model parameters for the USU drive plate and the UT drive plate No.9. Where possible, the variation of each model parameter with frequency was evaluated.

For the USU drive plate, a slight variation in R_c and L_c with frequency was measured, however, this variation is small and can be neglected. The value of k_i was measured in statically condition and compared with the back-calculated k_i at higher frequency and it was found to be nearly constant at all frequencies. A crosstalk effect was observed during the measurement of k_B. The cross talk interfered with the measurement of k_B and resulted in unrealistic k_B values. A measurement of crosstalk voltage was performed and the calculation of k_B values was corrected to account for the crosstalk effect. An increasing of k_B with frequency was measured. Additionally, there

was some scatter in the values measured with different calibration specimens. k_B was characterized using an average value and upper and lower bounds. This uncertainty was found to have a minor effect on RC/TS results.

For the UT drive plate No. 9, the variation of R_c and L_c with frequency showed trends similar to the USU drive plate. The measured value of k_i was about twice the value measured for the USU drive plate. The value of k_B was also about twice as high as the value for the USU drive plate with less variation with frequency than the USU drive plate. The higher values of k_i and k_B can be explained by stronger magnets used in the UT drive plate.

Efficiency of torque and back emf was determined from the theoretical and measured k_i and k_B. The torque efficiency was found to be about 75-80% for both USU and UT drive plate. And, the back emf efficiency was about 32-50% for both drive plate. The lower back emf efficiency is due to the nonuniform magnetic field in the coil cross section.

Based on the equations derived from the theoretical value of k_i and k_B, the capacity of the RC/TS drive system in generating torque can be improved by using the higher numbers of loops in the coil or stronger magnet. However, more back emf effects result from these modifications.

10.2.2.4 Model Verification. In RC test, the increasing of resonant frequency, Δf_m, and the equipment generated damping, D_{eq}, due to the back emf effect was quantified. The k_{eq} and c_{eq} were predicted using the measured model parameters and the predicted value of Δf_m and D_{eq} were calculated. Open and closed circuit measurements

were performed on calibration specimens in the RC/TS apparatus to determine experimental values of Δf_m and D_{eq}.

The experimental values of Δf_m and D_{eq} was used to calculate the measured k_{eq} and c_{eq}. The measured and predicted k_{eq} increase with frequency in similar fashion. The model underprediction of k_{eq} value at frequency between 60-130 Hz for the USU is of little concern because the effect of back emf on resonant frequency is very small and can be neglected. The slight decreasing value of the measured c_{eq} with frequency was observed for the USU and UT drive. The measured value of c_{eq} scattered and reasonably constant over the frequency range of 0-130 Hz. The predicted c_{eq} value shows slightly underestimates the measured c_{eq} at higher frequency. This underprediction is explained by other sources of energy loss and the uncertainty in frequency effet on k_i value.

10.2.2.5 Model Application. In RC test, the back emf effect on resonant frequency is very small and can be neglected. Effect of back emf on damping must be taken into account. The electromagnetic model with measured model parameters can be used to predict c_{eq} and the equipment generated damping, D_{eq}. The model predicts D_{eq} as a function of resonant frequency and mass polar moment of inertia of the system. Therefore, the prediction of D_{eq} can be performed for the RC testing on soil specimen that setup using any type of top platen. The D_{eq} is then corrected with the measured damping.

In TS test, the electromagnetic model verified that the effect of back emf on the torque measurement is very small and can be neglected. The discrepancy of equipment-generated damping in RC and TS test from previous work (Hwang 1997) was verified by the effect of phase shift between the voltage and current.

10.2.2.6 Model Limitation. The electromagnetic model prediction of D_{eq} is limited for up to 200 Hz, however the D_{eq} is very small above this frequency range. Therefore, the D_{eq} at frequency above 200 Hz can be negligible.

10.2.2.7 Advantages of Electromagnetic Model. Three advantages of the electromagnetic model are summarized. First, the model successfully describes the behavior of back emf generated in the RC/TS equipment. Second, the model is applied for both the RC and TS tests. Third, the model can be applied for any typical RC/TS apparatus.

10.2.3 Stress Integration Approach

The stress integration approach is a new, more general approach to account for nonuniform stress-strain effect in RC/TS testing. The stress integration approach is applied by integration using three different soil stress-strain models to calculate a theoretical torque and rotation relationship. The stress-strain model providing the best fit of the theoretical torque and rotation relationship to the measured torque and rotation relationship is used to develop the stress-strain relationship of the soil specimen. The Three assumed model used for this approach are the hyperbolic model, the modified hyperbolic model, and Ramberg-Osgood model. The stress integration approach use either closed form integration or numerical integration to develop a theoretical torque and rotation relationship. The closed form integration was applied for the hyperbolic model and the closed form equation is:

$$T = \frac{1}{3}\pi G_{max}\gamma_r R\left[2R^2 - 3R\left(\frac{\gamma_r L}{\theta}\right) + 6\left(\frac{\gamma_r L}{\theta}\right)^2\right] + 2\pi G_{max}\gamma_r^4\left(\frac{L}{\theta}\right)^3\left[\ln(\gamma_r) - \ln\left(\gamma_r + \frac{\theta R}{L}\right)\right]. \quad (10.6)$$

Numerical integration was applied for the modified hyperbolic model and Ramberg-Osgood model.

The nonuniform stress-strain in damping is taken into account by using a modified equivalent radius approach. The conventional equivalent radius approach was modified to determine the strain corresponding to a measured damping value more precisely. Values of R_{eq} defined as ratio of the equivalent radius and the outside radius of soil specimen, were evaluated based on shear modulus and damping are determined separately. Results from this study are the plots of the R_{eq} versus normalized rotation curve for shear modulus and damping shown in Figure 10.1. These R_{eq} versus normalized rotation curves account for the soil nonlinearity. All curves converge to a value of about 0.8 at low strains. At high strains, the R_{eq} curves based on damping are significantly lower than the R_{eq} curves based on shear modulus. Figure 10.1 suggests that using the same R_{eq} values for both shear modulus and damping is not appropriate.

Advantages of using the stress integration approach are summarized as follows:

1. The conventional equivalent radius approach uses single values of R_{eq} for ranges of strain to calculate stress and strain. The actual R_{eq} decreases with an increasing of strains and the point where the R_{eq} decreases is associated with the value of reference strain, γ_r. The stress integration approach effectively accounts for this variation of R_{eq} over the range of strains and the soil nonlinearity.

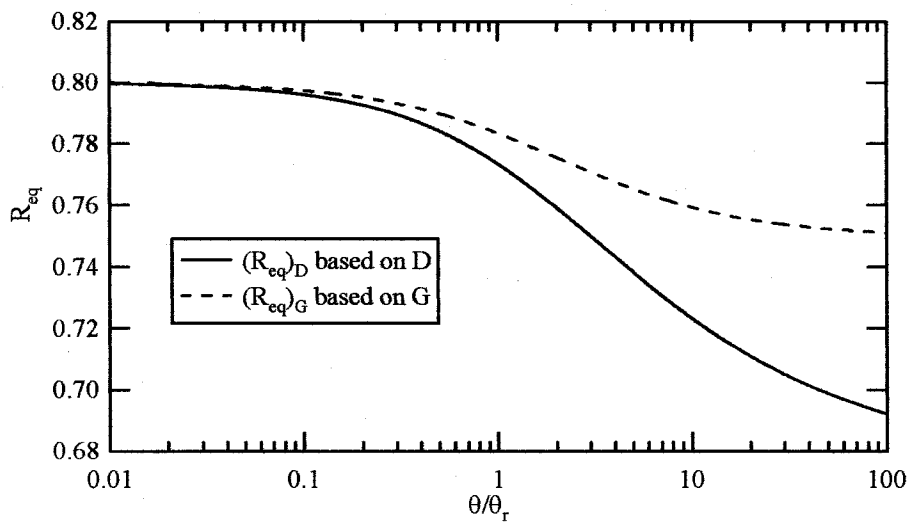

Figure 10.1 R_{eq} curves versus normalized rotation based on G and D

2. The conventional equivalent radius approach was limited at strain level up to 10^{-1}%. While the stress integration can be applied for higher strains.
3. The conventional equivalent radius approach was developed based on the hyperbolic model. The stress integration approach is not limited to only one stress-strain soil model, therefore, the approach provide options to select the best model to match the experimental data.
4. The conventional equivalent radius approach developed the value of R_{eq} on shear modulus and this value is also applied for calculations of strain for damping. By applying the stress integration approach, the R_{eq} value for damping was found to be different than the R_{eq} for shear modulus. The R_{eq} value for damping is less than the R_{eq} ratio for shear modulus and the difference tends to increases as the strain increases. Therefore, the stress integration approach provides more accurate damping curves in RC/TS testing.

One limitation of the stress integration approach is that the method can only be applies with specific stress-strain models. In some special cases, no available stress-strain model provides a good best to the experimental data.

Another limitation of the stress integration approach is that R_{eq} curve for damping was developed assuming that Masing behavior applies according to Masing rules. This assumption requires further study.

10.2.4 Dynamic Properties of Bonneville Clay

RC/TS testing of Bonneville clay was performed on seven soil specimens obtained from sites along the Wasatch front, Utah. High accuracy test results were obtained by applying the correction of equipment generated damping predicted by the electromagnetic model and the application of the stress integration approach.

The effect of plasticity index and confining pressure effect on the nonlinear dynamic properties of Bonneville clay was investigated and compared with the empirical relationships developed by other researchers. Results showed that Bonneville clay exhibits more linearity than predicted using the empirical relationships. The more linear behavior of Bonneville clay might be explained by the aging effects. Effects of plasticity index and confining pressure on modulus reduction and damping curves observed for Bonneville clay was much smaller than that predicted by the empirical relationships.

10.3 RECOMMENDATIONS

Based on this work, the following issues require further investigations:

1. An investigation of the effect of the non-rigid body motion of the drive plate on the polar moment of inertia in this study is only preliminary. Better modeling of

the connection between the drive plate and magnet requires further study. Other factors affecting the non-rigid body motion may need to be considered such as the accelerometer and counter weight.

2. An investigation into the effects of rotation on proximitor behavior is desirable. High accuracy measurement of small rotation angle is required to accomplish this task.
3. An investigation for the variation of k_i with frequency requires further study. A stiffer torque sensor might be used to measure torque at higher frequencies.
4. The uncertainty in k_B value needs to be investigated further. Explanations for the increasing of k_B with frequency also requires further study. A more detailed study of magnetic effects may be required.
5. Increasing capacity of torque generated in RC/TS equipment is recommended as a result of this study by the use of more number of loops in coil or stronger magnets. Alternatively, the connection of coil in parallel can also increase the torque capacity. When coils are in parallel, the voltage potential dropped across each coil is less than for the coils connected in series. This implies that for the same input voltage, higher torque can be generated in case of coils in parallel.
6. Although the back emf effect at frequencies higher than 200 Hz is very small, the values of model parameters could be investigated at higher frequency. This woud require calibration specimens with resonant frequencies above 200 Hz.
7. The problem with the available stress-strain soil models could not predict the soil behavior for the entire range of strain level requires further study. More versatile

soil model that can be fit the experimental data from very low strain level to very high strain level could be developed.

8. Study of the non-Masing behavior in soil is required further study. Masing behavior was assumed in applying the stress integration approach to damping.
9. The effect of plasticity index, confining pressure and cyclic degradation for Bonneville clay requires further study. Other factors affecting dynamic properties of Bonneville clay needs to be considered such as the water content, degree of saturation, cementation etc. More RC/TS testing on specimens with interbedded layers is recommended.

LITERATURE CITED

Cascante, G., Vanderkooy, J., and Chung, W. (2003). "Difference between current and voltage measurements in resonant-column testing." *Can. Geotech. J.*, 40, 806-820.

Chen, A.T. F., and Stokoe, K. H., II (1979). "Interpretation of strain dependent modulus and damping from torsional soil tests." *Rep. No. USGS-GD-79-002*, NTIS No. PB-298479, U.S. Geological Survey, 46.

Darendeli, M. B. (2001). "Development of a new family of normalized modulus reduction and material damping curves," PhD dissertation, Univ. of Texas, Austin, Tex.

Darendeli, M. B., and Stokoe, K. H., II (1997). "Dynamic properties of soils subjected to the 1994 Northridge earthquake." *Geotechnical Engineering Report GR97-5*, Civil Engineering Department, Univ. of Texas, Austin, Tex.

Halliday, D., and Resnick, R. (1981). *Fundamentals of physics.* Wiley, New York.

Hardin, B. O., and Drnevich, V. P. (1972a). "Shear modulus and damping in soils: measurement and parameter effects." *J. Soil Mech. and Found. Div.*, ASCE, 98 (6), 603-624.

Hardin, B. O., and Drnevich, V. P. (1972b). "Shear modulus and damping in soils:design equations and curves." *J. Soil Mech. and Found. Div.*, ASCE, 98 (7), 667-692.

Hwang, S. K. (1997). "Investigation of the dynamic properties of natural soils," PhD dissertation, Univ. of Texas, Austin, Tex.

Idriss, I. M. (1990). "Response of soft soil sites during earthquakes." *Proc., H. Bolton Seed Memorial Symposium*, 2, 273-289.

Idriss, I. M., Dobry, R., and Singh, R. D. (1978). Nonlinear behavior of soft clays during cyclic loading." *J. Geotech. Engrg. Div.*, ASCE, 104 (12), , 1427-1447.

Isenhower, W. M. (1979). "Torsional simple shear/resonant column properties of San Francisco bay mud," MS thesis, Univ. of Texas, Austin, Tex.

Ishibashi, I., and Zhang, X. (1993). "Unified dynamic shear moduli and damping ratios of sand and clay." *Soils and Foundations*, 33(1), 182-191.

Ishihara, K. (1996). *Soil behavior in earthquake geotechnics.* Oxford University Press, Oxford.

Iwasaki, T., Tatsuoka, F., and Takagi, Y. (1978). "Shear modui of sands under cyclic torsional shear loading." *Soils and Foundations*, 18(1), 39-56.

Kim, D. S. (1991). "Deformational characteristics of soils at small strains from cyclic tests," PhD dissertation, Univ. of Texas, Austin, Tex.

Li, X. S., Yang, W. L., Shen, C.K., and Wang, W.C. (1998). "Energy-injecting virtual mass resonant column system." *J. Geotech. and Geoenviron. Eng.*, 124(5), 428-438.

Lodde, P. F. (1982). "Shear modui and material damping of San Francisco bay mud," MS thesis, Univ. of Texas, Austin, Tex.

Meng, J., and Rix, G.J. (2003). "Reduction of equipment-generated damping in resonant column measurements." *Geotechnique*, 53(5), 503-512.

Ni, S. H. (1987). "Dynamic properties of sand under true triaxial stress states from resonant column/torsional shear tests," PhD dissertation, Univ. of Texas, Austin, Tex.

Seed, H. B., and Idriss, I. M. (1970). "Soil modui and damping factors for dynamic response analyses." *Report No. EERC-70-10*, Earthquake Engineering Research Center, Univ. of California, Berkeley, Calif., 37.

Seed, H. B., Wong, R. T., Idriss, I. M., and Tokimuatsu, K. (1986). "Moduli and damping factors for dynamic analyses of cohesionless soils." *J. Soil Mech. and Found. Div.*, ASCE, 112(11), 1016-1032.

Streeter, V. L., Wylie, E. B., and Richart, F. E., Jr. (1974). "Soil motion computations by characteristics method." *J. Geotech. Engrg.*, ASCE, 100 (3), March, 247-263.

Sun, J. I., Golesorkhi, R., and Seed, H. B. (1988). "Dynamic moduli and damping ratios for cohesive soils." *Rep. UCB/EERC-88/15*, Univ. of California, Berkeley, Calif., 48.

Taylor. P. W., and Parton, I. M. (1973), "Seismic torsion testing of soils." *Proc. 8th Int. Conf. on Soil Mechanics and Foundation Engineering,* Moscow, U.S.S.R., 425.

Vucetic M., and Dobry, R. (1991). "Effect of soil plasticity on cyclic response." *J. Geotech. Engrg.*, ASCE, 117 (1), 89-107.

Wang, Y. H., Cascante, G., and Santamarina, J. C. (2003). "Resonant column testing: the inherent counter emf effect." *Geotech. Testing J.*, 26 (3), 1-11.

Zhang, J., Andrus, R. D., and Juang, C. H., (2005). "Normalized shear modulus and material damping relationships." *J. Geotech. and Geoenviron. Eng.*, ASCE. (In press).

VITA

Inthuorn Sasanakul was born in Bangkok, Thailand, on October 5, 1977, the daughter of Werasak Sasanakul and Arunee Sasanakul. She received a Bachelor of Engineering degree in Civil Engineering in February 1998 from Thammasat University, Bangkok, Thailand. Ms. Sasanakul entered Asian Institute of Technology, Bangkok, Thailand and received a Master of Engineering degree in Geotechnical Engineering in April 2000. From May 2000 to July 2000, she worked as a project assistant at Asian Center of Soil Improvement and Geosynthetics, Asian Institute of Technology, Bangkok, Thailand. In August 2000, Ms. Sasanakul enrolled at Utah State University. She worked with Dr. James A. Bay in the area of geotechnical earthquake engineering, with emphasis in field and laboratory measurements of dynamic soil properties. She performed experimental study on drop-weight performance for Spectral-Analysis-of-Surface-Waves (SASW) testing. She conducted SASW testing for multiple sites in Utah and California to characterize soil profiles for site response analysis. Ms Sasanakul also completed part of her dissertation research and one semester of coursework at The University of Texas at Austin. In addition to her research activities, she taught the undergraduate soil mechanic laboratory during spring semester 2004 and 2005.

Permanent address: 280/10 M.13 Soi. Jatuporn
Srihaburanukij Rd. Minburi
Bangkok, Thailand